



**University of
Nottingham**
UK | CHINA | MALAYSIA

LABORATORY-NUMERICAL INVESTIGATION OF
SCALE EFFECTS IN GRANULAR SLIDES

MATTHEW KESSELER, MEng.

STUDENT ID: 4245894

*Thesis submitted to the University of Nottingham
for the degree of Doctor of Philosophy.*

October 2019

Abstract

Granular slides are omnipresent phenomena, occurring in both natural contexts such as avalanches and landslides, and in industrial applications such as blenders, chutes, hoppers, and rotating drums. The correct modelling of these events is paramount to the safety of populations that are at risk from granular slides themselves and other slide-related hazards such as landslide tsunamis. Many granular slides are strongly influenced by their interactions with fluid-phases, such as moisture or entrained snow and ice; nevertheless, this study focuses on "dry" granular slides where the surrounding and interstitial airflow is the dominant fluid phase.

Scale effects are changes in physical behaviour of a phenomenon at different geometrically similar scales, such as between a large event observed in nature and a smaller laboratory representation. These scale effects can be considerable and cause small-scale models to become misleading in their prediction of key slide characteristics including maximum velocity and runout distance. Although scale effects are highly relevant to granular slides due to the multiplicity of time and length scales involved, they are currently not well understood. This study aims to provide evidence of and quantify these scale effects, and to clarify whether these scale effects are inherent to the physical grains and their structure, or whether they are more dependent on other characteristics such as the grain Reynolds number (Re), which quantifies the turbulent or viscous manner in which the drag force acts on particles.

A versatile laboratory set-up has been developed to investigate dry granular slides of different scales and initial conditions, with a scale series of experiments being conducted under Froude similarity. The scale series allowed the slide geometry of different experiments to be directly up- or down-scaled, allowing key slide parameters to be measured, non-dimensionalised, and compared directly to quantify scale effects. While many studies addressed granular slides, none of them directly compare geometrically similar slides in this scale series approach.

This set-up has a configurable channel width of 0.25–1.00 m, with an inclined surface up to 3.00 m in length leading to a flat runout zone via interchangeable transition curves. The slide masses investigated in the scale series ranged from 1–110 kg, while Re varied from 10^2 – 10^3 . Particle image velocimetry was used to measure the slide surface velocity at specific points on the inclined ramp section, while laser-trigonometry was used to measure the slide thickness, and photogrammetry was used to measure the final deposit dimensions. The particles investigated in the present study were polydisperse mixtures of angular sand (quartz) grains, with mean diameters ranging from 0.675–2.7 mm across the scale series. Discrete element modelling (DEM) simulations were also conducted, modelling the laboratory scale series and much larger and smaller granular slides. This DEM approach was validated against an axisymmetric column collapse and a granular slide experiment from the technical literature, showing that these two slide conditions could be described well without the need for coupling with computational fluid dynamics.

The data from the experiments conducted in this study has been compared to many slide events in nature and analysed to quantify the influence of Re on slide dynamics, and to evaluate the match between simulated and laboratory events. Overall, significant scale effects have been identified in the laboratory experiments with respect to the slide surface velocity, total runout distance, and deposit morphology. The slide surface velocity increased by up to 34.8% as the experimental scale increased by a factor of 4, and became increasingly Re -dependent as the slide progressed further down the inclined channel section. Normalisation of the slide surface velocity with the estimated drag force on particles shows that the particle drag force becomes increasingly influential over Re scale effects as the velocity increases.

Meanwhile, the deposit runout distance increased by up to 38.1% as scale increased across the range of initial conditions that were investigated, and morphological parameters show greater dependence on the maximum Re achieved by the slide before it starts to settle. Additionally, the slide deposit volume and porosity decreased by over 10% as scale increased, showing a weak inverse dependence on Re . Normalising key laboratory data by multiplying them by a power α of Re

significantly improved the match of similar experiments of differing scales, allowing the influence of Re to be directly quantified. Simultaneously, characteristics such as the maximum slide thickness in motion remain scale-independent, highlighting that scale effects affect granular slide in heterogeneous and non-linear ways. Furthermore, other physical factors such as increasing dust formation with increasing scale were also observed in the laboratory-scale experiments, which may become increasingly important at geophysical scales. However, the magnitude of the effects induced by these secondary mechanisms is seen to be small compared to the influence of Re , particularly in the deposit position data.

The DEM shows general agreement with the small-scale laboratory experiments. The DEM also provides insight into the processes that may occur in the laboratory slides; analysis of the simulated depth-velocity profiles show the granular slide alternating between Bagnold- and plug-like flow conditions as it traverses the inclined channel. The main difference of the simulations in comparison to the laboratory experiments was the former not being strongly influenced by scale effects. This highlights the importance of laboratory models and experiments in capturing and quantifying scale effects. Overall, the clear importance of Re to these slides suggests that modelling of the airflow surrounding the granular slides is an essential component for capturing scale effects in dry granular slides in numerical contexts.

Furthermore, comparisons of the laboratory data to that of other studies and of relevant natural events show that data calibration with Re is an effective method of correctly upscaling laboratory results to natural events. This upscaling technique can improve hazard assessment in natural contexts and is potentially useful for modelling industrial flows.

Acknowledgements

Firstly, I would like to extend my gratitude towards Dr. Valentin Heller and Dr. Barbara Turnbull for their continued support and interest in my work. I cannot overstate my appreciation of the long discussions we would often share on the granular mechanics of my experiments and the scaling principles involved, and of the opportunities to share my work with others that they provided to me. My two supervisors have helped me to develop my interest in science and research in general, and have been instrumental in facilitating the development of important skills such as project management, independent problem solving, and publishing that will be invaluable in the future. Furthermore, they were always available to help me discuss and deal with personal issues, and always kept my best interests in mind. In the laboratory, Dr. Valentin Heller's willingness to assist with lifting and fixing heavy components (particularly for the largest scale experiments!) as well as performing drilling work was highly appreciated. Meanwhile, Dr. Barbara Turnbull was helpful in particular for providing access and use of the high speed cameras and software required for recording the granular slides and providing accurate velocity data.

This study was supported by the Engineering and Physical Sciences Research Council [grant number EP/M506588/1] (EPSRC). I would like to thank Dr. Mike Swift and Dr. Lis Bowman for their valuable feedback and discussion during the viva for this study. I would also like to thank Mr. Steven Gange and Mr. Balbir Loyla for their assistance and expertise in building the experimental set-up, as well as Dr. Nikolaos Kokkas for providing useful advice on photogrammetry techniques and Mr. Luke Johnson for constructing the electromagnetic trigger for the release shutter. I would also like to acknowledge Prof. Stuart Marsh for his advice and support, and for providing access to the AgiSoft photogrammetry software, as well as Prof. Ricky Wildman for his assistance. With respect to the DEM simulations conducted in this study, I acknowledge the use of HPC Minerva and Augusta at the University of Nottingham, as well as the use of Athena at HPC Midlands+ as part of the HPC Midlands+ consortium. I would like to thank Mr. Colin Bannister for his continued assistance in installing and troubleshooting the LIGGGHTS software

modules on these clusters and migrating older simulation data from HPC Minerva to HPC Augusta as the University of Nottingham replaced the previous system. Finally, I would like to thank Mr. Ming Chung and Mr. Samuel Hammond for expressing interest in my laboratory set-up within their respective MEng and BEng projects, and wish them continued success in their work.

I would also like to thank my partner Ms. Sarah Found for her continued love and support throughout my PhD, and for giving me the strength to move forward, no matter what obstacles may present themselves.

Contents

1	Introduction	1
1.1	Relevance of granular slides and flows	2
1.2	Scaling granular slides and flows	5
1.3	Aims and objectives	7
1.3.1	Objectives	8
2	Literature review	9
2.1	Introduction	9
2.2	Granular slides and flows	9
2.2.1	Characterising granular slides and flows	11
2.2.2	Granular slide and flow principles	16
2.2.3	Granular slide rheology	20
2.2.4	Particle geometry	22
2.2.5	Granular slide geometry	24
2.3	Scale effects and Froude scaling	30
2.3.1	Force ratios and other important dimensionless parameters	33
2.3.2	Strategies for mitigating scale effects	39
2.3.3	Hypermobility: size versus scale effects	42
2.4	Capturing and modelling granular slides	46
2.4.1	Experimental measurement techniques and applications	47
2.4.2	Savage-Hutter continuum model	51
2.4.3	Numerical modelling techniques and applications	54
2.5	Important experimental studies	69
2.6	Summary	80
3	Methodology	82
3.1	Introduction	82
3.2	Experimental set-ups	83
3.2.1	Design and construction of ramp	86
3.2.2	Key geometric parameters	90
3.2.3	Axisymmetric column collapse set-up	101
3.3	Measurement techniques	104
3.4	LIGGGHTS-DEM formulation	110
3.4.1	LIGGGHTS workflow	111
3.4.2	Contact modelling	112
3.4.3	Modelling shape effects	115
3.4.4	Measuring slide porosity	119
3.4.5	Slide wedge generation	120
3.4.6	Selection of simulation time-step	122
3.4.7	DEM implementation on HPC	125
3.4.8	Summary of DEM parameters	128
3.5	Summary	129
4	Results	130
4.1	Introduction	130
4.2	Calibration and validation of DEM	131

4.2.1	Frictional and damping parameters	131
4.2.2	Simulation of size distribution	138
4.3	Main results	140
4.3.1	Comparisons of slide fronts and tails	140
4.3.2	Slide position distribution	147
4.3.3	Slide velocity distribution	155
4.3.4	Slide velocity profiles	159
4.3.5	Slide thickness profiles	167
4.3.6	Deposit dimensions and properties	178
4.3.7	Simulated scale-series extrapolation	193
4.4	Summary	199
5	Discussion	201
5.1	Introduction	201
5.2	Scale-invariance in DEM and secondary mechanisms	202
5.2.1	Influence of acoustic fluidisation	204
5.2.2	Influence of material stiffness	206
5.3	Power-law-similarity of simulated slide velocity profiles	208
5.4	Reynolds-dependency of key slide parameters	215
5.4.1	Reynolds-dependency of surface velocity	215
5.4.2	Drag force normalisation of slide surface velocity	220
5.4.3	Reynolds-dependency of key deposit parameters	229
5.4.4	Comparison of slide runout data to other studies	233
5.4.5	Reynolds-dependency of other deposit parameters	236
5.5	Influence of channel surface roughness	238
5.6	Summary	241
6	Conclusions and Outlook	243
6.1	Conclusions	243
6.2	Outlook	247
A	Additional slide position distribution data	250
B	Additional simulated velocity distribution data	256
C	Additional laboratory-simulation comparisons	264
D	Additional porosity data	268
E	Laboratory measurement error assessment	269
	References	272

List of Figures

Figure 1	Georeferenced aerial photographs of the site of Yungay (outlined in white) (a) before and (b) after the May 31, 1970 debris flow at Mt. Huascarán, Peru (Evans et al., 2009) .	3
Figure 2	Photograph of the aftermath of a large-scale laboratory landslide experiment at the National Research Institute for Earth Science and Disaster Prevention (NEID), Tsukuba, Japan, 2003 (Moriwaki et al., 2004)	5
Figure 3	Natural landslide types (adapted from Lynn Highland Graphics, 2004)	10
Figure 4	Common granular flow configurations: (a) plane shear, (b) annular shear, (c) vertical-chute flows, (d) inclined plane, (e) heap flow, and (f) rotating drum. Black and white arrows indicate applied forces, red arrows indicate velocity profiles (Forterre and Pouliquen, 2008)	11
Figure 5	Comparison of steady and avalanching phases. Straight lines show variation of flow depth over particle diameter h/d and inclination angle θ as the flow rate Q is varied across a fixed channel width $w =$ (a) $19d$ (b) $38d$ (c) $142d$ (d) $283d$ (e) $570d$ (adapted from Jop et al., 2005)	12
Figure 6	Comparison of particle velocity via Eq. (1) (a) and velocity fluctuations (b) with flow depth z/d and ramp angle θ (adapted from G.D.R. MiDi, 2004)	14
Figure 7	Froude number u/\sqrt{gh} as a function of the ratio between current flow depth and critical flow depth h/h_{stop} for different inclination angles θ . The particle diameter is 0.5 mm both in the flow and attached to the surface (adapted from Pouliquen, 1999)	15
Figure 8	Diagram of slide particle phases (Forterre and Pouliquen, 2008)	17
Figure 9	Granular temperature distribution with $\theta = 33^\circ$ (Brodu et al., 2015)	19
Figure 10	Kinematic classification of typical 2D particles (Vangla et al., 2018)	24
Figure 11	Series of side profiles for cylindrical piles of glass beads of initial height 46 mm and base diameter of 142 mm. (a) Loose initial pile with $\Phi = 0.58$ and a time lapse of 0.02 s between consecutive lines. (b) Dense initial pile with $\Phi = 0.65$ and a time lapse of 0.04 s between consecutive lines (adapted from Daerr and Douady, 1999)	25

Figure 12	Radial size distribution in a rotating drum filled with large green (500–750 μm), medium white (400–500 μm) and small red (75–150 μm) particles. (a) Overview of the rotating drum. (b) Close-up of the surface avalanche, shown distinctly from the slowly rotating grains locked in solid body rotation (Gray, 2018))	27
Figure 13	(a) Evidence of self-channelisation in a large-scale controlled debris flow, composed of sand, gravel, and water. Coloured tracer particles were dropped onto the slide surface as it entered the runout area (b-d), showing the deposit motion and formation of static levees to the sides of the central channel flow (Gray, 2018)	29
Figure 14	(a-c) Numerical simulations of segregation-induced fingering solved via a finite-volume scheme, with $\bar{\phi}$ representing the proportion of large particles in the flow. (d) Fingering in a bidisperse mixture of 80% white ballotini (75–150 μm) and 20% brown carborundum (305–355 μm) on a base of turquoise ballotini (750–1000 μm) (adapted from Gray, 2018)	30
Figure 15	Comparison of air entrainment, detrainment and runout length L_r between a large and small slide at the same relative times after slide impact into water between (a) and (b), and between (c) and (d). $\lambda = 2$ between the large and small slide (Heller et al., 2008)	32
Figure 16	Relationship between Re and the drag coefficient C_D for a spherical particle. Streamlines around the sphere are also shown at various Re values (adapted from Bagheri and Bonadonna, 2016)	35
Figure 17	Dependency of normalised drag coefficient of freely falling particles on normalised Reynolds number. See Bagheri and Bonadonna (2016) for experimental data sources (adapted from Bagheri and Bonadonna, 2016)	36
Figure 18	Impact of orientation on the drag coefficient of an ellipsoidal particle compared to an equivalent sphere, with average values for free fall in air and water also displayed. (a) Ellipsoid drag coefficient C_D at different values of Re . (b) Ellipsoid drag coefficient normalised against the sphere drag coefficient $C_{D,s}$ (adapted from Bagheri and Bonadonna, 2016)	37
Figure 19	Similar sand morphologies caused by (a) water ripples in a bridge pier scour model and (b) air ripples on a dune in Swakopmund, Namibia (Heller, 2011)	41

Figure 20	Comparison of runout length L_r against slide volume V_s (shapes are terrestrial data, crosses are Martian data). Inset: Comparison of runout length L_r and inundated area A (adapted from Staron and Lajeunesse, 2009)	43
Figure 21	Comparison of runout length L_r against non-dimensionalised slide volume $V_s^{1/D}$ (shapes are terrestrial data, crosses are Martian data, filled circles are simulation data) (adapted from Staron and Lajeunesse, 2009)	44
Figure 22	Velocity distribution (a) at the free surface and (b) at the bottom of a chute slide (adapted from Pudasaini et al., 2005)	48
Figure 23	Deposit granulometry obtained from core samples, showing the relative abundance of fine (F) and coarse (C) materials, with contours showing deposit thickness at 5 cm spacing (adapted from Johnson et al., 2012)	50
Figure 24	3D unconfined chute geometry and coordinates (Gray et al., 1999)	54
Figure 25	Force networks in sandpiles constructed with different base deflections of (a) 2000 <i>d</i> and (b) 125 <i>d</i> (Zhou et al., 2003)	56
Figure 26	3D reconstruction of a corn seed (top) and clump representations using (a) five, (b) ten, (c) fifteen, and (d) twenty spheres (adapted from Pasha et al., 2016)	60
Figure 27	Front view of a spherical agglomerate breaking in different modes at different impact velocities (Zheng et al., 2015)	61
Figure 28	Comparison of rolling resistance coefficient μ_r and ellipsoid major/minor axis ratio a/b (adapted from Wensrich and Katterfeld, 2012)	63
Figure 29	Comparison of rolling resistance coefficient μ_r and relative spacing of inter-clump spheres δ_s (adapted from Wensrich et al., 2014)	63
Figure 30	Side view of granular slide velocity profile into a water reservoir at (a) 1 s from release and (b) 3 s from release (adapted from Shan and Zhao, 2014)	65
Figure 31	Outline of dynamic load balance based on two-dimensional slice-grid method (Tsuzuki and Aoki, 2016)	66

Figure 32	(a) Perspective view of the chute from Hutter et al. (1995). (1) Frontal side wall, (2) rear side wall, (3) basal surface, (4) curved chute element, (5) rotating shutter, (6) slide loading zone, (7) experiment number, (8) experiment clock. (b) Cross sectional cut through the chute. (1) Frontal side wall, (2) rear side wall, (3) basal surface, (4) aluminium I-beam. (c) Detail of the shutter operating system. All numbers are in mm (Hutter et al., 1995)	70
Figure 33	Side-view image series from experiment #117 of Hutter et al. (1995)	71
Figure 34	Laboratory flume from Okura et al. (2000a)	73
Figure 35	Initial release mass and apparatus from Okura et al. (2000b)	75
Figure 36	Time series of rockfall experiment using 1000 0.1×0.1×0.1 m granite blocks (adapted from Okura et al., 2000b)	75
Figure 37	Experimental flume setup of De Haas et al. (2015) . . .	77
Figure 38	Side view of experimental setup in Haug et al. (2016) . .	78
Figure 39	Overview of experimental set-up for small scale experiments ($\lambda = 4$). (a) Floodlight for illumination. (b) High-speed cameras. (c) Sidewalls attached to sides of main ramp frame. (d) Shutter in open position. (e) Runout area with reference grids and deposit. (f) Shutter attachment point with electromagnet trigger. (g) Laser pointer for thickness measurement	84
Figure 40	Overview of experimental set-up for medium scale experiments ($\lambda = 2$). (a) Floodlights for illumination. (b) High-speed cameras. (c) Sidewalls attached to sides of main ramp frame. (d) Shutter in closed position. (e) Shutter attachment point with electromagnet trigger. (f) Laser pointer for thickness measurement. (g) Runout area with reference grids and deposit	85
Figure 41	Overview of experimental set-up for large scale experiments ($\lambda = 1$). (a) High-speed camera. (b) Ladder used for camera access and maintenance. (c) Shutter in partially open position with electromagnet trigger. (d) Floodlights for illumination. (e) Sidewalls directly attached to main frame. (f) Runout area with reference grids. (g) Laser pointer for thickness measurement	86
Figure 42	Overview of experimental set-up for large scale experiments ($\lambda = 1$). (a) Side view of set-up design schematic. (b) Rear view of shutter with release mechanism	88

Figure 43	Picture of loaded shutter and counterweight mechanism for large scale experiment. (a,b) Attachment points for smooth counterweight cable movement. (c) Shutter rotation axis. (d) Attachment point for post-release shutter restraint. (e) Electromagnet trigger. (f) Counterweight and attachment bar	90
Figure 44	Definition of bulk slide parameters. (a) Side view of the ramp, with x, y, z showing the curvilinear position coordinate system, and u_x being the ramp-wise velocity aligned with x . θ_W is the key control parameter varied between experiments of the same λ . (b) Section of the slide across the channel width	92
Figure 45	Photographs of sand used at (left to right) $\lambda = 4, 2$, and 1	93
Figure 46	Size distribution of sand particles used in the laboratory experiments	94
Figure 47	Representative sand particles that resemble oblate (top) and prolate (bottom) spheroids, at $\lambda = 4$ (left), $\lambda = 2$ (middle), and $\lambda = 1$ (right)	94
Figure 48	Friction angle measurement set-up. Pile of material before mobilisation at $\theta = 16.2^\circ$ (left). Pile of material after mobilisation at $\theta = 33.3^\circ$ (right)	95
Figure 49	Definition of h_i from initial wedge. The two shaded areas are equal	98
Figure 50	Overview of experimental set-up for axisymmetric column collapse	102
Figure 51	Overview of axisymmetric column collapse set-up. The reference grid is visible underneath the polypropylene surface in detailed images used for photogrammetry. (a) Frame used to stabilise cylinder movement, with pulley attached. (b) Digital camera. (c) Illuminated base surface and loaded cylinder. (d) Floodlight for additional illumination for out-of-image high-speed camera	103
Figure 52	Deposit from completed axisymmetric column collapse .	103
Figure 53	Diagram showing thickness measurement laser inclination angle θ relative to the ramp. Laser at x_1 (right) angled parallel to the xz plane. Laser at x_2 (left) angled parallel to the yz plane	104

Figure 54	PIV vectors produced by Digiflow for experiment L5, (a) soon after the slide passes through the x_2 window and (b) 0.5 s later. The closer the colour to purple, the higher the calculated velocity. The reference vector enclosed in the red box = 3.75 m/s. The left side of the images corresponds to the channel sidewall, while the right side corresponds to the channel centre	106
Figure 55	Workflow of Agisoft Photoscan process for generation of slide deposit meshes. (a) Loose point cloud. (b) Dense point cloud. (c) Mesh from dense point cloud. (d) Textured mesh	107
Figure 56	Deposit from experiment L5, with reference gridlines on channel base and channel sidewalls	109
Figure 57	Flowchart of LIGGGHTS engine workflow during simulations	112
Figure 58	Two dimensional cross section of an elliptical particle (adapted from Wensrich and Katterfeld, 2012)	116
Figure 59	Porosity estimation method. The generated surface contacts (black) enclose Monte-Carlo points generated to fill their volume (green). The red outlined cube and blue surface mesh constrain the Monte-Carlo generation volume, while the green outlined cube constrains which particles are included in the calculation	119
Figure 60	Side view of wedge generation procedure, with the loosely packed particles in the generation zone compacting in the release zone. Particles outside the bold triangular wedge were deleted immediately before release	120
Figure 61	Comparison of simulated kinetic energy over different time-step sizes	124
Figure 62	Comparison of laboratory column collapse deposit with simulation	132
Figure 63	Axisymmetric column collapse simulation at (a) $t = 0$ s, (b) $t = 0.283$ s, (c) $t = 0.609$ s (deposition complete), and (d)–(f) corresponding laboratory images. Subfigure in (c) indicates dilute boundary extent (radial co-ordinate < -0.2) in simulation	133
Figure 64	Comparison of laboratory and simulated column collapse outlines at (a) $t = 0$ s, (b) $t = 0.071$ s, (c) $t = 0.141$ s, (d) $t = 0.212$ s, (e) $t = 0.283$ s, (f) $t = 0.354$ s, (g) $t = 0.424$ s, (h) $t = 0.495$ s, and (i) $t = 0.566$ s	134

Figure 65	Simulated (background) position distribution compared with x_f , x_{max} , and x_t values from experiment #117 (symbols) of Hutter et al. (1995), with (a) $\delta = 25.14^\circ$ and $\phi = 23.67^\circ$ and (b) $\delta = 28^\circ$ and $\phi = 26^\circ$	136
Figure 66	Comparison of (a) monodisperse and (b) polydisperse slide velocities throughout a central vertical cross section midway through the slide event	138
Figure 67	Side view of (a) monodisperse and (b) polydisperse slide deposits with the same release geometries	139
Figure 68	Plan view of (a) monodisperse and (b) polydisperse slide deposits with the same release geometries	140
Figure 69	Comparison of slide fronts between left sidewall and centre-line as they approach the x_1 position, increasing in θ_W from left to right, and increasing in λ from top to bottom. Experiment numbers are (a) L6, (b) L12, (c) L17, (d) L21, (e) L25, (f) L29, (g) L37, (h) L45, and (i) L53 (Table 2)	141
Figure 70	Comparison of slide tails between left sidewall and centre-line as they approach the x_1 position, increasing in θ_W from left to right, and increasing in λ from top to bottom. Experiment numbers are (a) L6, (b) L12, (c) L17, (d) L21, (e) L25, (f) L29, (g) L37, (h) L45, and (i) L53 (Table 2)	142
Figure 71	Comparison of slide fronts between left sidewall and centre-line as they approach the x_2 position, increasing in θ_W from left to right, and increasing in λ from top to bottom. Experiment numbers are (a) L6, (b) L12, (c) L17, (d) L21, (e) L25, (f) L29, (g) L37, (h) L45, and (i) L53 (Table 2)	143
Figure 72	Comparison of slide tails between left sidewall and centre-line as they approach the x_2 position, increasing in θ_W from left to right, and increasing in λ from top to bottom. Experiment numbers are (a) L6, (b) L12, (c) L17, (d) L21, (e) L25, (f) L29, (g) L37, (h) L45, and (i) L53 (Table 2)	144
Figure 73	Simulated slide fronts and tails between left sidewall and centre-line passing through x_1 with $\lambda = 2$. (a) Slide front with $\theta_W = 0^\circ$ (S4). (b) Front with $\theta_W = 15^\circ$ (S6). (c) Slide tail with $\theta_W = 0^\circ$ (S4). (d) Tail with $\theta_W = 15^\circ$ (S6)	145
Figure 74	Simulated slide fronts and tails between left sidewall and centre-line passing through x_2 with $\lambda = 2$. (a) Slide front with $\theta_W = 0^\circ$ (S4). (b) Front with $\theta_W = 15^\circ$ (S6). (c) Slide tail with $\theta_W = 0^\circ$ (S4). (d) Tail with $\theta_W = 15^\circ$ (S6)	146

Figure 75	Comparison of position distribution over time between laboratory (L18–L21) and simulation (S4) slides, for $\lambda = 2$ and $\theta_W = 0^\circ$ at (a) channel sidewalls and (b) channel centre	149
Figure 76	Comparison of position distribution over time between laboratory (L26–L29) and simulation (S6) slides, for $\lambda = 2$ and $\theta_W = 15^\circ$ at (a) channel sidewalls and (b) channel centre	151
Figure 77	Comparison of position distribution over time between laboratory (L1–L6) and simulation (S1) slides, for $\lambda = 1$ and $\theta_W = 0^\circ$ at (a) channel sidewalls and (b) channel centre	153
Figure 78	Comparison of position distribution over time between laboratory (L13–L19) and simulation (S3) slides, for $\lambda = 1$ and $\theta_W = 15^\circ$ at (a) channel sidewalls and (b) channel centre	154
Figure 79	Slide velocity distribution over time for simulation S4, with $\lambda = 2$ and $\theta_W = 0^\circ$	155
Figure 80	Slide velocity distribution over time for simulation S6, with $\lambda = 2$ and $\theta_W = 15^\circ$	158
Figure 81	Simulated (S4) slide velocity profiles with $\lambda = 2$ and $\theta_W = 0^\circ$ at (a) x_1 and (b) x_2	160
Figure 82	Simulated (S4) non-dimensional mean slide velocity plotted against slide depth at 400,000 time-step intervals, with t_1 starting 400,000 time-steps after the slide front contacts the (a) x_1 and (b) x_2 measurement points, with $\theta_W = 0^\circ$. Circles denote sidewall surface velocities while squares denote central surface velocities	162
Figure 83	Simulated (S6) non-dimensional mean slide velocity plotted against slide depth at 400,000 time-step intervals, with t_1 starting 400,000 time-steps after the slide front contacts the (a) x_1 and (b) x_2 measurement points, with $\theta_W = 15^\circ$. Circles denote sidewall surface velocities while squares denote central surface velocities	163
Figure 84	Comparison of ensemble-averaged slide surface velocity profiles at x_1 and x_2 . Laboratory (L1–L6, L18–L21, and L30–L37) and simulated (S1, S4, and S7) velocity measurements with $\theta_W = 0^\circ$	165
Figure 85	Comparison of ensemble-averaged slide surface velocity profiles at x_1 and x_2 . Laboratory (L13–L17, L26–L29, and L46–L53) and simulated (S3, S6, and S9) velocity measurements with $\theta_W = 15^\circ$	166

Figure 86	Cross-sections of simulated slide (S6) at 1,600,000 time-step intervals, starting 400,000 time-steps after (left) the slide front contacts the x_1 measurement point and (right) the slide front contacts the x_2 measurement point	168
Figure 87	Comparison of laboratory (L1–L6, L18–L21, and L30–L37) and simulated (S1, S4, and S7) slide thickness profiles at the sidewall position at x_1 , with $\theta_W = 0^\circ$	170
Figure 88	Comparison of laboratory (L13–L17, L26–L29, and L46–L53) and simulated (S3, S6, and S9) slide thickness profiles at the sidewall position at x_1 , with $\theta_W = 15^\circ$	171
Figure 89	Comparison of laboratory (L1–L6, L18–L21, and L30–L37) and simulated (S1, S4, and S7) slide thickness profiles at the centre position at x_2 , with $\theta_W = 0^\circ$	172
Figure 90	Comparison of laboratory (L13–L17, L26–L29, and L46–L53) and simulated (S3, S6, and S9) slide thickness profiles at the centre position at x_2 , with $\theta_W = 15^\circ$	173
Figure 91	Laboratory (L1–L6, L18–L21, and L30–L37) and simulated (S4) non-dimensional slide surface velocity plotted against slide depth at 400,000 simulation time-step intervals, with t_1 starting 400,000 time-steps after the slide front contacts each measurement point, with $\theta_W = 0^\circ$	175
Figure 92	Laboratory (L13–L17, L26–L29, and L46–L53) and simulated (S6) non-dimensional slide surface velocity plotted against slide depth at 400,000 simulation time-step intervals, with t_1 starting 400,000 time-steps after the slide front contacts each measurement point, with $\theta_W = 15^\circ$	177
Figure 93	Plan view of laboratory slides of all conditions, with θ_W increasing from left to right and λ increasing from top to bottom. (a) L6, (b) L10, (c) L13, (d) L21, (e) L23, (f) L29, (g) L31, (h) L41, and (i) L48	179
Figure 94	Comparison of laboratory (L1–L6, L18–L21, and L30–L37) and simulated (S1, S4, and S7) deposit surfaces with $\theta_W = 0^\circ$, at (a) 10% across, (b) 50% across, and (c) 90% across the channel width	180
Figure 95	Comparison of laboratory (L7–L12, L22–L25, and L38–L45) and simulated (S2, S5, and S8) deposit surfaces with $\theta_W = 7.5^\circ$, at (a) 10% across, (b) 50% across, and (c) 90% across the channel width	182

Figure 96	Comparison of laboratory (L13–L17, L26–L29, and L46–L53) and simulated (S3, S6, and S9) deposit surfaces with $\theta_W = 15^\circ$, at (a) 10% across, (b) 50% across, and (c) 90% across the channel width	183
Figure 97	Comparison of laboratory and simulation deposit front and tail positions for (a) $\theta_W = 0^\circ$, (b) $\theta_W = 7.5^\circ$, and (c) $\theta_W = 15^\circ$	185
Figure 98	Local analysis of slide porosity for simulation S4, with $\lambda = 2$ and $\theta_W = 0^\circ$. (a) represents the first 5 mm away from the runout zone surface, with (b) to (i) moving up the deposit in 5 mm intervals	191
Figure 99	Local analysis of slide porosity for simulation S6, with $\lambda = 2$ and $\theta_W = 15^\circ$. (a) represents the first 5 mm away from the runout zone surface, with (b) to (o) moving up the deposit in 5 mm intervals	193
Figure 100	Position distribution over time for simulated slide S10, for $\lambda = 0.2$ and $\theta_W = 0^\circ$ at (a) channel sidewalls and (b) channel centre	195
Figure 101	Position distribution over time for simulated slide S11, for $\lambda = 20$ and $\theta_W = 0^\circ$ at (a) channel sidewalls and (b) channel centre	195
Figure 102	Plan view of slide position and velocity over time at $\lambda = 0.2$ (S11)	196
Figure 103	Plan view of slide position and velocity over time at $\lambda = 2$ (S4)	196
Figure 104	Plan view of slide position and velocity over time at $\lambda = 20$ (S10)	197
Figure 105	Velocity distribution for simulation S10, with $\lambda = 0.2$ and $\theta_W = 0^\circ$	198
Figure 106	Velocity distribution for simulation S11, with $\lambda = 20$ and $\theta_W = 0^\circ$	198
Figure 107	Simulated (S4) particle velocity data (Fig. 82) normalised to maximum velocity and thickness at (a,c) x_1 and (b,d) x_2 at (a,b) the channel sidewall and (c,d) the channel centre, with $\theta_W = 0^\circ$. Data plotted at 400,000 time-step intervals t_1 to t_{11} , with t_1 starting 400,000 time-steps after the front reaches the measurement point	210

Figure 108	Fitting of power-law velocity profiles based on Eq. (48) over the slide depth of simulated (S4) particle velocity data (Fig. 107) at (a,c) x_1 and (b,d) x_2 at (a,b) the channel sidewall and (c,d) the channel centre, with $\theta_W = 0^\circ$. Fit-lines plotted at 400,000 time-step intervals t_1 to t_{11} , with t_1 starting 400,000 time-steps after the front reaches the measurement point	210
Figure 109	Simulated (S6) particle velocity data (Fig. 83) normalised to maximum velocity and thickness at (a,c) x_1 and (b,d) x_2 at (a,b) the channel sidewall and (c,d) the channel centre, with $\theta_W = 15^\circ$. Data plotted at 400,000 time-step intervals t_1 to t_{12} , with t_1 starting 400,000 time-steps after the front reaches the measurement point	213
Figure 110	Fitting of power-law velocity profiles based on Eq. (48) over the slide depth of simulated (S6) particle velocity data (Fig. 109) at (a,c) x_1 and (b,d) x_2 at (a,b) the channel sidewall and (c,d) the channel centre, with $\theta_W = 15^\circ$. Fit-lines plotted at 400,000 time-step intervals t_1 to t_{12} , with t_1 starting 400,000 time-steps after the front reaches the measurement point	213
Figure 111	Comparison of Re-normalised slide surface velocity (data from Fig. 84) profiles over time with $\theta_W = 0^\circ$. Dotted data-lines are described by the legend of Fig. 84. $t_* = t/(d/g)^{1/2} - 28.93$ at x_1 and $t/(d/g)^{1/2} - 41.59$ at x_2 . . .	218
Figure 112	Comparison of Re-normalised slide surface velocity (data from Fig. 85) profiles over time with $\theta_W = 15^\circ$. Dotted data-lines are described by the legend of Fig. 85. $t_* = t/(d/g)^{1/2} - 28.33$ at x_1 and $t/(d/g)^{1/2} - 41.59$ at x_2 . . .	219
Figure 113	Comparison of Re-normalised slide surface velocity profiles over time across all θ_W values. $t_* = t/(d/g)^{1/2} - 28.33$ at x_1 and $t/(d/g)^{1/2} - 41.59$ at x_2	219
Figure 114	Comparison of dimensionless u_f , u_t , and u_d over dimensionless time	224
Figure 115	Comparison of k_D across experimental range of $u_d/(gd)^{1/2}$	225
Figure 116	Comparison of k_D -normalised slide surface velocity (data from Fig. 84) profiles over time with $\theta_W = 0^\circ$. Dotted data-lines are described by the legend of Fig. 84. $t_* = t/(d/g)^{1/2} - 28.93$ at x_1 and $t/(d/g)^{1/2} - 41.59$ at x_2 . . .	226

Figure 117	Comparison of k_D -normalised slide surface velocity (data from Fig. 85) profiles over time with $\theta_W = 15^\circ$. Dotted data-lines are described by the legend of Fig. 84. $t_* = t/(d/g)^{1/2} - 28.33$ at x_1 and $t/(d/g)^{1/2} - 41.59$ at x_2	226
Figure 118	Comparison of volume-normalised slide runout and fall height (see Table 18 for raw data)	233
Figure 119	Re-normalisation of slide runout data from Fig. 118	235
Figure 120	(a) Mean coefficient of friction for single particles pressed against a surface. (b) Mean coefficient of friction for particle tripods sliding down a flat surface. Friction intensity is a graphical representation of the friction coefficient	240
Figure 121	Comparison of position distribution over time between laboratory (L22–L25) and simulation (S5) slides, for $\lambda = 2$ and $\theta_W = 7.5^\circ$ at (a) channel sidewalls and (b) channel centre	250
Figure 122	Comparison of position distribution over time between laboratory (L7–L12) and simulation (S2) slides, for $\lambda = 1$ and $\theta_W = 7.5^\circ$ at (a) channel sidewalls and (b) channel centre	251
Figure 123	Position distribution over time for simulated slide S7, for $\lambda = 4$ and $\theta_W = 0^\circ$ at (a) channel sidewalls and (b) channel centre	251
Figure 124	Position distribution over time for simulated slide S8, for $\lambda = 4$ and $\theta_W = 7.5^\circ$ at (a) channel sidewalls and (b) channel centre	252
Figure 125	Position distribution over time for simulated slide S9, for $\lambda = 4$ and $\theta_W = 15^\circ$ at (a) channel sidewalls and (b) channel centre	252
Figure 126	Comparison of position distribution over time between individual laboratory (L18–L21) and simulation (S4) slides, for $\lambda = 2$ and $\theta_W = 0^\circ$ at (a) channel sidewalls and (b) channel centre	253
Figure 127	Comparison of position distribution over time between individual laboratory (L22–L25) and simulation (S5) slides, for $\lambda = 2$ and $\theta_W = 7.5^\circ$ at (a) channel sidewalls and (b) channel centre	253
Figure 128	Comparison of position distribution over time between individual laboratory (L26–L29) and simulation (S6) slides, for $\lambda = 2$ and $\theta_W = 15^\circ$ at (a) channel sidewalls and (b) channel centre	254

Figure 129	Comparison of position distribution over time between individual laboratory (L1–L6) and simulation (S1) slides, for $\lambda = 1$ and $\theta_W = 0^\circ$ at (a) channel sidewalls and (b) channel centre	254
Figure 130	Comparison of position distribution over time between individual laboratory (L7–L12) and simulation (S2) slides, for $\lambda = 1$ and $\theta_W = 7.5^\circ$ at (a) channel sidewalls and (b) channel centre	255
Figure 131	Comparison of position distribution over time between individual laboratory (L13–L19) and simulation (S3) slides, for $\lambda = 1$ and $\theta_W = 15^\circ$ at (a) channel sidewalls and (b) channel centre	255
Figure 132	Velocity distribution for simulation S5, with $\lambda = 2$ and $\theta_W = 7.5^\circ$	256
Figure 133	Velocity distribution for simulation S1, with $\lambda = 1$ and $\theta_W = 0^\circ$	257
Figure 134	Velocity distribution for simulation S2, with $\lambda = 1$ and $\theta_W = 7.5^\circ$	257
Figure 135	Velocity distribution for simulation S3, with $\lambda = 1$ and $\theta_W = 15^\circ$	258
Figure 136	Velocity distribution for simulation S7, with $\lambda = 4$ and $\theta_W = 0^\circ$	258
Figure 137	Velocity distribution for simulation S8, with $\lambda = 4$ and $\theta_W = 7.5^\circ$	259
Figure 138	Velocity distribution for simulation S9, with $\lambda = 4$ and $\theta_W = 15^\circ$	259
Figure 139	Simulated (S5) non-dimensional mean slide velocity plotted against slide depth at 400,000 time-step intervals, with t_1 starting 400,000 time-steps after the slide front contacts the (a) x_1 and (b) x_2 measurement points, with $\theta_W = 7.5^\circ$. Circles denote sidewall surface velocities while squares denote central surface velocities	260
Figure 140	Simulated (S5) particle velocity data (Fig. 139) normalised to maximum velocity and thickness at (a,c) x_1 and (b,d) x_2 at (a,b) the channel sidewall and (c,d) the channel centre, with $\theta_W = 0^\circ$. Data plotted at 400,000 time-step intervals t_1 to t_{12} , with t_1 starting 400,000 time-steps after the front reaches the measurement point	261

Figure 141	Fitting of power-law velocity profiles based on Eq. (48) over the slide depth of simulated (S5) particle velocity data (Fig. 140) at (a,c) x_1 and (b,d) x_2 at (a,b) the channel sidewall and (c,d) the channel centre, with $\theta_W = 0^\circ$. Fit-lines plotted at 400,000 time-step intervals t_1 to t_{12} , with t_1 starting 400,000 time-steps after the front reaches the measurement point	261
Figure 142	Simulated (S10) non-dimensional mean slide velocity plotted against slide depth at 126,500 time-step intervals, with t_1 starting 126,500 time-steps after the slide front contacts the (a) x_1 and (b) x_2 measurement points, with $\lambda = 0.2$ and $\theta_W = 0^\circ$. Circles denote sidewall surface velocities while squares denote central surface velocities	263
Figure 143	Simulated (S11) non-dimensional mean slide velocity plotted against slide depth at 1,265,000 time-step intervals, with t_1 starting 1,265,000 time-steps after the slide front contacts the (a) x_1 and (b) x_2 measurement points, with $\lambda = 20$ and $\theta_W = 0^\circ$. Circles denote sidewall surface velocities while squares denote central surface velocities	263
Figure 144	Comparison of laboratory (L7–L12, L22–L25, and L38–L45) and simulated (S2, S5, and S8) slide thickness profiles at the channel sidewall position at x_1 , with $\theta_W = 7.5^\circ$	264
Figure 145	Comparison of laboratory (L7–L12, L22–L25, and L38–L45) and simulated (S2, S5, and S8) slide thickness profiles at the channel centre position at x_2 , with $\theta_W = 7.5^\circ$	265
Figure 146	Comparison of ensemble-averaged slide surface velocity profiles at x_1 and x_2 . Laboratory (L7–L12, L22–L25, and L38–L45) and simulated (S2, S5, and S8) velocity measurements with $\theta_W = 7.5^\circ$	265
Figure 147	Comparison of Re-normalised slide surface velocity (data from Fig. 84) profiles over time with $\theta_W = 0^\circ$ and $\alpha = -1$. Dotted data-lines are described by the legend of Fig. 84. $t_* = t/(d/g)^{1/2} - 28.93$ at x_1 and $t/(d/g)^{1/2} - 41.59$ at x_2	266
Figure 148	Comparison of Re-normalised slide surface velocity (data from Fig. 84) profiles over time with $\theta_W = 0^\circ$ and $\alpha = 1$. Dotted data-lines are described by the legend of Fig. 84. $t_* = t/(d/g)^{1/2} - 28.93$ at x_1 and $t/(d/g)^{1/2} - 41.59$ at x_2	266

Figure 149	Comparison of Re-normalised surface velocity (data from Fig. 146) profiles over time with $\theta_W = 7.5^\circ$. Dotted data-lines are described by the legend of Fig. 146. $t_* = t/(d/g)^{1/2} - 28.93$ at x_1 and $t/(d/g)^{1/2} - 42.19$ at x_2	267
Figure 150	Comparison of k_D -normalised surface velocity (data from Fig. 146) profiles over time with $\theta_W = 7.5^\circ$. Dotted data-lines are described by the legend of Fig. 146. $t_* = t/(d/g)^{1/2} - 28.93$ at x_1 and $t/(d/g)^{1/2} - 42.19$ at x_2	267
Figure 151	Local analysis of slide porosity for simulation S5, with $\lambda = 2$ and $\theta_W = 7.5^\circ$. (a) represents the first 5 mm away from the runout zone surface, with (b) to (k) moving up the deposit in 5 mm intervals	268

List of Tables

Table 1	Features, advantages, and disadvantages of DEM engines	68
Table 2	Key experimental and numerical parameters. Parameters kept constant between all experiments include the ramp inclination angle $\theta = 40^\circ$, the internal friction angle $\phi = 30^\circ$, the ramp bed friction angle $\delta_i = 30^\circ$, the runout bed friction angle $\delta_R = 28.5^\circ$, the grain density $\rho_s = 2650 \text{ kg/m}^3$, the simulated coefficient of restitution $e = 0.893$, grain stiffness $E = 70 \text{ GPa}$, grain Bulk modulus $K = 35 \text{ GPa}$, polypropylene stiffness = 2 GPa , and steel stiffness = 210 GPa . .	91
Table 3	Scaling ratios for Froude and Reynolds scaling models . .	97
Table 4	Estimated (Fr_i , Re_i , Ca_i , $N_{Sav,i}$, and $N_{Bag,i}$) and measured (Fr , Re , Ca , N_{Sav} , and N_{Bag}) force and stress ratios for conducted experimental conditions	100
Table 5	Simulation particle counts and run times	127
Table 6	Key DEM calibration parameters	128
Table 7	Non-dimensionalised slide front, peak, and tail positions .	187
Table 7	Non-dimensionalised slide front, peak, and tail positions (continued)	188
Table 8	Slide initial and deposit volumes and porosities	189
Table 9	Laboratory slide spreading and centre of mass movement	203
Table 10	β and r_{min} values for Fig. 108 with $\theta_W = 0^\circ$	211
Table 11	β and r_{min} values for Fig. 110 with $\theta_W = 0^\circ$	214

Table 12	α and R^2 values of the original and Re-normalised slide surface velocity fitted to Eq. (49). Fit improvement refers to the improvement of fit between pure $u_s/(gd)^{1/2}$ scaling and combined $u_s/(gd)^{1/2} \times \text{Re}^\alpha$ scaling	217
Table 13	α , k_D , and R^2 values of the original and normalised slide surface velocities fitted to Eq. (49). Fit improvement refers to the improvement of fit between pure $u_s/(gd)^{1/2}$ scaling and combined $u_s/(gd)^{1/2} \times \text{Re}^\alpha$ or $u_s/(gd)^{1/2} \times k_D$ scaling	227
Table 14	Re-dependency of laboratory slide deposit front positions	229
Table 15	Re-dependency of laboratory slide deposit peak positions	230
Table 16	Re-dependency of laboratory slide deposit mass centroid positions	230
Table 17	Re-dependency of laboratory slide deposit tail positions .	231
Table 18	Important physical parameters of natural granular slides seen in Fig. 118. (1) Cruden and Hungr (1986). (2) McKinnon (2010). (3) Shugar and Clague (2011). (4) Moore (1976). (5) McSaveney (2002). (6) Lipovsky et al. (2008). (7) Sosio et al. (2008). (8) Evans et al. (2001)	234
Table 19	Re-dependency of slide deposit volumes	236
Table 20	Re-dependency of slide deposit porosities	237
Table 21	β and r_{min} values for Fig. 108 with $\theta_W = 0^\circ$	262

Nomenclature

a	= Ellipse major axis	(m)
\mathbf{a}	= Acceleration vector	(m/s ²)
A	= Slide inundated area	(m ²)
\bar{A}	= Mean particle cross-sectional area	(m ²)
b	= Ellipse minor axis	(m)
c	= Coordination number	(-)
c_f	= Frictional coordination number	(-)
c_n	= Non-frictional coordination number	(-)
C_D	= Drag coefficient	(-)
$C_{D,s}$	= Sphere drag coefficient	(-)
Ca	= Grain Cauchy number	(-)
Ca_i	= Initial grain Cauchy number	(-)
d	= Mean particle diameter	(m)

d_{max}	= Maximum particle diameter	(m)
d_{min}	= Minimum particle diameter	(m)
\bar{d}	= Local mean particle diameter	(m)
D	= Number of dimensions	(-)
e	= Restitution coefficient	(-)
$\langle e \rangle$	= Mean contact eccentricity	(-)
e_c	= Contact eccentricity	(-)
E	= Young's Modulus	(N/m ²)
E_k	= Slide kinetic energy	(J)
E_p	= Slide potential energy	(J)
E_t	= Particle settlement energy threshold	(J)
Eu	= Euler number	(-)
f	= Data capture frequency	(1/s)
F_N	= Newton's particle shape factor	(-)
F_S	= Stokes' particle shape factor	(-)
\mathbf{F}_b	= Body force vector	(N)
\mathbf{F}_n	= Normal force vector	(N)
\mathbf{F}_t	= Tangential force vector	(N)
Fr	= Froude number	(-)
Fr _i	= Initial Froude number	(-)
g	= Gravitational acceleration	(m/s ²)
h	= Flow thickness	(m)
h_{max}	= Maximum slide thickness along centre-line	(m)
$h_{start}(\theta)$	= Critical flow stopping thickness	(m)
$h_{stop}(\theta)$	= Critical flow stopping thickness	(m)
H_c	= Height of slide mass centroid above runout area	(m)
H_{COM}	= Vertical change in slide centre of mass position	(m)
$H_{s,0}$	= Initial slide thickness at shutter position	(m)
I	= Inertial number	(-)
$I_{\bar{d}}$	= Local inertial number	(-)
I_m	= Moment of inertia	(kg/m ²)
I_r	= Mean rolling moment of inertia of particles	(kg m ²)
k_D	= Drag force calibration coefficient	(-)
k_n	= Normal spring coefficient	(-)
k_N	= Newton's particle drag correction	(-)
k_r	= Rolling contact stiffness	(-)
k_S	= Stokes' particle drag correction	(-)
k_t	= Tangential spring coefficient	(-)
K	= Bulk Modulus	(N/m ²)
$K_{act/pas}$	= Earth pressure coefficient (active/passive)	(-)
$K_{x,act/pas}$	= Down-slope earth pressure coefficient (active/passive)	(-)

$K_{y,act/pas}$	= Cross-slope earth pressure coefficient (active/passive)	(-)
L	= Characteristic length scale	(m)
L_{COM}	= Horizontal change in slide centre of mass position	(m)
L_M	= Characteristic model length scale	(m)
L_P	= Characteristic prototype length scale	(m)
L_r	= Slide runout length	(m)
L_s	= Slide length	(m)
$L_{s,0}$	= Initial slide length	(m)
L_{sh}	= Distance of axis of rotation from ramp surface	(m)
L_1	= Length of inclined ramp section	(m)
m	= Particle mass	(kg)
M	= Slide mass	(kg)
n	= Tuneable parameter	(-)
n_p	= Number of particles in simulation	(-)
n_t	= Number of time-steps in simulation	(-)
N	= Porosity	(-)
N_d	= Deposit slide porosity	(-)
N_r	= Number of experimental repeats	(-)
N_s	= Initial slide porosity	(-)
N_{Bag}	= Bagnold number	(-)
$N_{Bag,i}$	= Initial Bagnold number	(-)
N_{Sav}	= Savage number	(-)
$N_{Sav,i}$	= Initial Savage number	(-)
P	= Characteristic pressure scale	(N/m ²)
Q	= Flow rate	(m ³ /s)
Q_c	= Critical flow rate	(m ³ /s)
r	= Particle radius	(m)
\mathbf{r}_c	= Particle radius contact vector	(m)
r_{min}	= Mean residual	(%)
R	= Radius of ramp transition	(m)
R_{min}	= Minimum simulated particle radius	(m)
R_q	= Roughness length of material	(nm)
R_r	= Effective rolling radius of particle contact	(m)
R_s	= Slide horizontal runout distance from shutter release	(m)
Re	= Grain Reynolds number	(-)
Re_d	= Drag-influenced grain Reynolds number along incline	(-)
Re_i	= Initial grain Reynolds number	(-)
S	= Volume-area slope	(-)
t	= Time	(s)
$t_{c,0}$	= Time of particle contact	(s)
t_s	= Simulation time-step	(s)

t_{macro}	= Macroscopic timescale	(s)
t_{micro}	= Microscopic timescale	(s)
t_{0-12}	= Specific time interval	(-)
t_*	= Time reference starting at 0 when slide reaches x_1 or x_2	(-)
T	= Topographic parameter	(-)
T_g	= Granular temperature	(°K)
T_r	= Slide runout completion time	(s)
$T_{r,real}$	= Simulated slide runout completion time in real time	(hours)
T_s	= Settlement time	(s)
$T_{s,real}$	= Simulated settlement time in real time	(hours)
T_t	= Total slide completion time	(s)
$T_{t,real}$	= Simulated total slide completion time in real time	(hours)
T_{0-5}	= Polynomial fit coefficient	(-)
\mathbf{T}_r	= Rolling resistance torque	(N m)
$\mathbf{T}_{r,max}$	= Maximum rolling resistance torque	(N m)
\mathbf{T}_r^d	= Viscous damping rolling resistance torque	(N m)
\mathbf{T}_r^k	= Mechanical spring rolling resistance torque	(N m)
u	= Mean flow velocity	(m/s)
u_d	= Particle drag-influenced velocity along incline	(m/s)
u_f	= Particle free-fall velocity along incline	(m/s)
u_i	= Initial characteristic slide velocity	(m/s)
u_s	= Ramp-wise slide surface velocity	(m/s)
u_{sh}	= Shutter-tip velocity	(m/s)
u_t	= Particle terminal velocity along incline	(m/s)
u_x	= Ramp-wise component of slide velocity	(m/s)
U	= Characteristic velocity scale	(m/s)
v_R	= Rayleigh wave speed	(m/s)
V	= Volumetric parameter	(-)
V_s	= Slide volume	(m ³)
w	= Channel width	(m)
x	= Surface down-slope coordinate	(m)
x_c	= Ramp-wise position of slide mass centroid	(m)
x_f	= Ramp-wise position of slide front	(m)
$x_{f,0}$	= Initial ramp-wise position of slide front	(m)
x_{max}	= Ramp-wise position of slide peak	(m)
x_s	= Longitudinal spread of slide deposit	(m)
x_t	= Ramp-wise position of slide tail	(m)
$x_{t,0}$	= Initial ramp-wise position of slide tail	(m)
x_0	= x coordinate on ellipse surface	(m)
x_1	= First measurement position along channel length	(m)
x_2	= Second measurement position along channel length	(m)

y	= Surface cross-slope coordinate	(m)
y_0	= y coordinate on ellipse surface	(m)
z	= Surface normal coordinate	(m)

Greek Symbols

α	= Reynolds-normalisation power constant	(-)
α_m	= Measurable parameter from G.D.R. MiDi (2004)	(-)
α_2	= Density-related drag parameter' (-)	(-)
β	= Velocity depth-normalisation power constant	(-)
β_m	= Measurable parameter from G.D.R. MiDi (2004)	(-)
β_2	= Density-related drag parameter' (-)	(-)
δ	= Bed friction angle	(°)
δ_i	= Ramp bed friction angle	(°)
δ_R	= Runout bed friction angle	(°)
Δt_c	= Rayleigh critical time-step	(s)
$\Delta \mathbf{T}_r^k$	= Change in \mathbf{T}_r^k over time-step	(N m)
$\Delta \theta_r$	= Relative particle rotation over time-step	(°)
η	= Linear ramp co-ordinate in Hutter et al. (1995)	(-)
η_r	= Rolling viscous damping ratio	(-)
γ	= Characteristic shear rate	(/s)
$\dot{\gamma}$	= Mean shear rate	(/s)
γ_n	= Normal damping coefficient	(-)
γ_t	= Tangential damping coefficient	(-)
Γ	= Function of Poisson ratio	(-)
λ	= Scale factor	(-)
Λ	= Ratio of basal pore pressure and slide normal stress	(-)
μ	= Friction coefficient	(-)
μ_f	= Dynamic viscosity	(N s/m ²)
μ_r	= Rolling friction coefficient	(-)
μ_{eff}	= Effective friction coefficient	(-)
ν	= Poisson ratio	(-)
ν_f	= Kinematic viscosity	(m ² /s)
ω_s	= Shutter angular acceleration	(rad/s ²)
$\boldsymbol{\omega}$	= Particle rotational velocity vector	(rad/s ²)
ϕ	= Internal friction angle	(°)
ϕ	= Proportion of large particles	(-)
Φ	= Slide volume fraction	(-)

Φ_i	= Initial slide wedge generation volume fraction	(-)
ρ_f	= Fluid density	(kg/m ³)
ρ_s	= Particle density	(kg/m ³)
σ	= Normal stress	(N/m ²)
τ	= Shear stress	(N/m ²)
θ	= Flow surface angle	(°)
θ_i	= Laser inclination angle	(°)
$\dot{\theta}_r$	= Relative rolling angular velocity between particles	(rad/s ¹)
θ_{start}	= Critical flow starting angle	(°)
θ_{stop}	= Critical flow stopping angle	(°)
θ_W	= Release wedge surface angle	(°)

Abbreviations

CFD: Computational Fluid Dynamics
 CLR: Curvature Length Ratio
 CN: Coordination Number
 CPU: Central Processing Unit
 DEM: Discrete Element Modelling
 EPSRC: Engineering and Physical Sciences Research Council
 GPU: Graphics Processing Unit
 HPC: High Performance Computing
 IW: Interrogation Window
 LIGGGHTS: Large-scale atomic/molecular massively parallel simulator Improved for General Granular and Granular Heat Transfer Simulations
 MPI: Message Passing Interface
 NCAR: Non Corner Aspect Ratio
 NEID: National Research Institute for Earth Science and Disaster Prevention
 OpenMP: Open MultiProcessing
 PIV: Particle Image Velocimetry
 PTV: Particle Tracking Velocimetry
 RDF: Radial Distribution Function
 RIM: Refractive Index Matching
 RMSE: Relative Mean Squared Error
 SH: Savage-Hutter
 SPH: Smoothed Particle Hydrodynamics

1 Introduction

Granular slides and flows are omnipresent in both natural contexts such as avalanches, landslides, debris flows, and pyroclastic flows (Pudasaini and Hutter, 2010) and in industrial applications such as blenders, chutes, hoppers, rotating drums (Zhu et al., 2008; Turnbull, 2011), and heap formation (Zhang and Vu-Quoc, 2000; Markauskas and Kačianauskas, 2011; Bryant et al., 2014). Granular slides can be characterised as assemblies of discrete particles moving together, with the space between particles being filled by an interstitial fluid (Campbell, 2006). Natural slides and flows can differ greatly in composition and behaviour from each other. In this study, avalanches are defined as masses of granular material that break loose from their surroundings, and include rock avalanches (consisting of large blocks of shattered rock), ice and snow avalanches (consisting mostly of water in its various forms), and debris avalanches (consisting of unconsolidated materials such as loose stones and soil). Landslides are similar but are typically characterised by their coherent nature, with interactions between solid and fluid phases (such as groundwater and pore water) governing their motion.

The main difference between granular slides (avalanches, rockfalls, etc.) and flows (debris flows, pyroclastic flows, etc.) as defined in this study is that a slide consists of a finite, discontinuous mass of particles, with clear initial and final configuration states, whereas a flow is a continuous stream of particles where mass is continually added to the granular system until the flow is stopped. Slides are more common in nature while continuous flows are more often seen in industrial processes where their continuous nature provides utility. Granular slides such as avalanches and landslides can exhibit many different types of movements within their structure, including flowing, sliding, spreading, and toppling, either simultaneously or separately at different phases of the slide duration (Gariano and Guzzetti, 2016). These slides can be triggered by perturbations such as temperature changes in either the particles or the interstitial fluid, acoustic propagation, or direct mechanical action on the slide mass. Aradian et al. (2002) discuss an initiation method where a mobile layer forms on the surface and entrains other particles and another where the slide is initiated by local particles rolling and cascading

into a full slide. Juanico et al. (2008) and Montrasio et al. (2016) analyse rain- and vibration-driven granular slides using experimental and computational models. This complexity makes the motion and behaviour of granular slides a challenging and interesting field of study.

While constitutive models have been well developed and validated for static granular materials, the dynamics of granular slides and flows have relatively recently come more into focus as a distinct field. Many of the original granular flow models were based on fluid mechanics principles, with modifications being made over time to better suit the granulometry of these systems. Recently, powerful numerical models have been developed that can model the discrete nature of these granular slides and flows, calculating the motion of individual bodies rather than approximating them via a continuum of differential equations (Zhu et al., 2008). This new perspective has facilitated a drive to better understand how the specific granulometry of granular systems impacts their behaviour, directly modelling effects such as particle shape (Wensrich et al., 2014) and fracture (Jensen et al., 2001; Zheng et al., 2015) that could only be approximated before.

1.1 Relevance of granular slides and flows

The study of granular slides is highly important, with slides in nature having drastic impacts on both the surrounding terrain and local populations. Many injuries and fatalities are caused worldwide by the millions of natural snow and ice avalanches that occur annually; an estimated 1% of avalanches cause issues such as injury, destruction of property, and death. In the US, Armstrong and Williams (1986) indicate around 140 people were caught in avalanches, with almost half being at least partly buried and around 17 being killed. Regarding property damage, the amount of money invested in the direct and indirect prevention of casualties and damage is significantly higher than the amount given out by insurance companies (Singh, 1996). Historic avalanche and landslide events have also caused much higher death tolls, especially in less developed countries where safety protocols were not as rigorous. For instance, approximately 6,000 people died in a catastrophic

debris flow in 1970 on the slopes of Mt. Huascarán, Peru, where an earthquake triggered rock and ice falls that were further fluidised by glacial surface snow, producing highly mobilised material that flowed at 50–85 m/s over 180 km to reach the Pacific Ocean. This event is an example of a granular slide triggering a flow of longer duration, with the destructive capability of the event increasing as a result. Figure 1 shows that the village of Yungay was completely destroyed by this slide event (Evans et al., 2009).

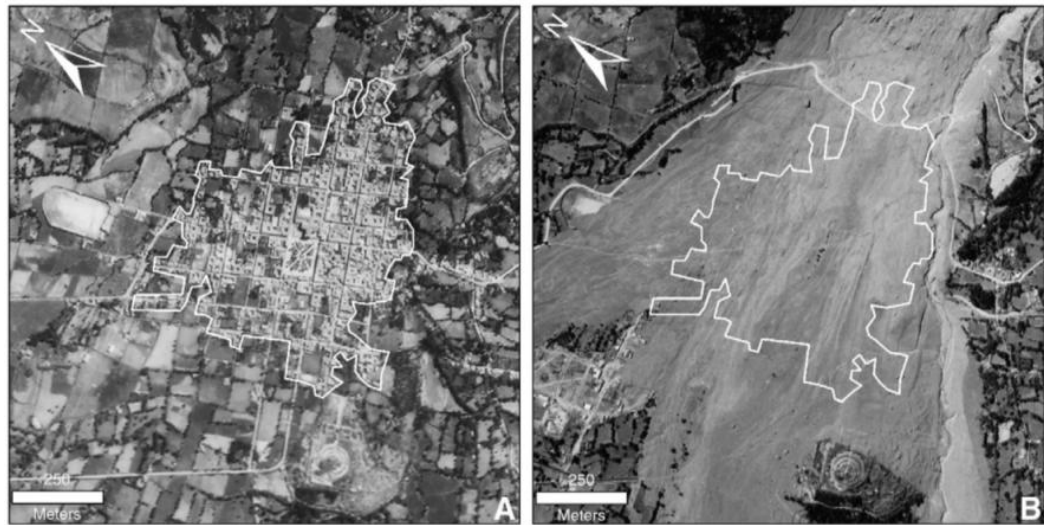


Figure 1 Georeferenced aerial photographs of the site of Yungay (outlined in white) (a) before and (b) after the May 31, 1970 debris flow at Mt. Huascarán, Peru (Evans et al., 2009)

Avalanches and landslides can often run out for several kilometres even on relatively shallow slopes, resulting in areas initially deemed safe for development by older modelling techniques actually being unsafe (Legros, 2002). Granular slides can also induce significant erosion of the flow surface, with this combined behaviour significantly contributing to sedimentation into valleys and rivers, ground water contamination, and seabed topography changes for coastal events. Furthermore, while granular slides can cause catastrophic damage through their bulk motion (Haque et al., 2016), they can also have drastic indirect effects, with slides impacting into bodies of water producing significant impulse waves such as tsunamis (Heller and Hager, 2010; Heller and Spinniken, 2015). Granular slides can also lead

1. INTRODUCTION

to secondary hazards such as unintentional dam formation (Chang et al., 2011), dam overtopping (Yavari-Ramshe and Ataie-Ashtiani, 2016), or flooding of nearby coastal areas or settlements (Glinsdal et al., 2016). For instance, a wave run-up height of 524 m was recorded at Lituya Bay in 1958, destroying much vegetation, animal life, and local infrastructure (Miller, 1960), while a landslide at Monte Toc, Italy, 1962, caused the Vaiont Dam reservoir to overtop and kill almost 2,000 people (Ventisette et al., 2015).

Notably, the impact of climate change is likely to significantly increase the intensity and frequency of avalanche and landslide events, as well as increasing the range of vulnerable areas, in the future (Gariano and Guzzetti, 2016). This is not only due to sustained changes in boundary conditions such as soil moisture, vegetation, temperature cycles, total precipitation and intensity, and wind behaviour, but also due to the resettlement of people from other vulnerable areas and subsequent changes in land use patterns. This further justifies the importance of modelling these large granular slide events.

However, it is usually impractical in terms of expense and resources to replicate and measure full-scale avalanches and landslides, with such studies being scarce (Hutter et al., 1995). On the other hand, in recent times certain sections of mountainside have been designated for predetermined test avalanches, and some tests have been performed on real avalanches (Sovilla et al., 2006). In these large-scale experiments, there can be extreme difficulties in ensuring that environmental conditions remain constant during and between experiments, with Bryant et al. (2014) noting that basal friction and moisture conditions are particularly difficult to control for outdoor tests. Designing an effective measurement system for large-scale slides can also be challenging, particularly due to the heavy loading that measurement equipment such as pressure sensors must be able to withstand. Figure 2 depicts the laboratory set-up of Moriwaki et al. (2004), using one of the largest documented controlled experimental landslide chutes with a built-in rainfall simulator, capable of handling up to 83 m³ of material.



Figure 2 Photograph of the aftermath of a large-scale laboratory landslide experiment at the National Research Institute for Earth Science and Disaster Prevention (NEID), Tsukuba, Japan, 2003 (Moriwaki et al., 2004)

1.2 Scaling granular slides and flows

The impact of large granular events and the difficulty of their measurement justify the use of small-scale experiments for understanding their physical processes and outcomes, allowing for more detailed analysis and better repeatability at lower time and resource requirements. However, this reduction in scale between the real-world events and these smaller models can cause its own problems. Model effects can be caused by improper reconstruction of prototypical features such as the terrain, materials involved, or slide initiation mechanisms, while measurement effects arise in cases where measurements from large-scale events and small-scale models are conducted via different approaches and techniques (Heller, 2011). These two types of effects are fairly simple to correct in principle.

1. INTRODUCTION

Scale effects, the differences in physical behaviour and the forces involved between prototypical and experimental phenomena, are much more difficult to identify, isolate, and correct. For example, smaller avalanches and landslides may run out over less distance in the laboratory compared to corresponding natural events. It is impossible to remove all scale effects from a smaller representation of a real world event; correct scaling of one parameter will often directly result in incorrect scaling of other parameters (Heller, 2011). Therefore, it is crucial to develop a strong understanding of the various scale effects that can impact the behaviour of granular slides, so that the most disruptive scale effects can be mitigated and the remaining effects can be identified clearly within measured data. With this knowledge in mind, scale effects can be identified and taken into account when upscaling laboratory results to natural events. These scale effects can also potentially be quantified and factored into future analytical, numerical, and experimental models, helping to increase the safety of planned future settlements and supporting geohazard assessment by more accurately determining key parameters such as slide velocity and runout distance. Industrial processes such as mining and food processing can also see increased efficiency as key flow behaviours such as velocity profiles and segregation are modelled with these scaling principles in mind.

Notably, the relative difficulty of effectively downscaling granular materials due to the different length scales inherent to the system has made rigorous experimental studies at a variety of physical scales exceedingly rare, especially in comparison to those studying fluid phenomena. Additionally, the many additional properties that granular systems display in comparison to fluid systems (such as stress anisotropy, local and historical effects, and particle fragmentation) make their scaling a more challenging process, requiring a wider range of constraints and variables to be scaled and monitored throughout their duration (Slonaker et al., 2017). As a result, many studies that focus on the scaling of granular systems focus on comparing the micro-scale of individual particle interactions to the macro-scale of the full system (Glasser and Goldhirsch, 2001; Bryant et al., 2014; Brodu et al., 2015; Slonaker et al., 2017), or the relative scales within a granular event (Warnett et al., 2014), rather than addressing the relative scale of similar systems (Iverson, 2015). Furthermore, existing studies of scale effects in granular systems often focus on

steady, continuous flows, due to these circumstances being more easily defined and characterised than discontinuous granular slides (Pouliquen, 1999; Artoni et al., 2012). Finally, the scaling of these granular systems becomes even more complicated as fluid phases are reintroduced; the properties of granular slide behaviour can change drastically as the moisture content of the material is increased (Rombi et al., 2006). The result is a relatively unexplored field of scaling in granular slides.

1.3 Aims and objectives

The main aim of this study is to identify scale effects in granular slides. This aim will be satisfied by applying a scale series approach to the granular slides conducted in this study, in both laboratory experiments and numerical simulations. Accordingly, experiments of matching relative geometry and kinematics will be conducted at a range of scales, with key slide parameters being calculated via a Froude scaling approach. This technique will ensure that the relative influences of slide inertial and gravity forces remain constant between experiments of different scale. Accordingly, scale effects will result from other physical differences and will be directly identifiable and quantifiable compared to the expected behaviour.

The experiments in this study will focus specifically on dry granular slides, with slides being released via a shutter down a channel with a fixed width and confining sidewalls into a confined runout area. The slide material will be kept dry throughout all experiments such that scale effects that are independent of any fluid phase interactions will be identified. Furthermore, the experiments will be conducted at a constant temperature and humidity to minimise any related model effects. The slide channel will be kept inclined at an angle of 40° throughout all experiments.

While there has been much discussion in the literature about the "hypermobility" of granular slides, where extremely large slide volumes start to run out over larger-than-expected distances (Parez and Aharonov, 2015; Johnson et al., 2016), no definitive reason for this phenomenon has been found. Overall, it has proven

impossible to replicate the hypermobility effect at experimental scale. While some numerical models have been able to reproduce this behaviour in the absence of fluid and thermal effects (Campbell et al., 1995; Perez and Aharonov, 2015), the fundamental mechanism of friction reduction in these models is not fully clear. Conducting a series of laboratory experiments at different physical scales will help to identify whether subtle mechanisms and behaviours begin to occur as the scale increases that alter the slide dynamics.

1.3.1 Objectives

These aims will be achieved with the following objectives:

1. Design and construct a versatile laboratory set-up that will allow these granular slides to be investigated without interference from model and measurement effects.
2. Implement a measurement methodology to allow the accurate measurement of key slide parameters such as the surface velocity, front position and shape, and deposit morphology.
3. Conduct confined granular slide experiments for a range of initial release geometries, varying chute and slide dimensions.
4. Run discrete element modelling (DEM) simulations to validate against the laboratory experiments, to develop improved understanding of the underlying physics, and to provide additional data.
5. Characterise scale effects based on the laboratory-DEM data set collected.
6. Compare the laboratory slides to laboratory events from other studies and to natural events, to identify any correlating factors between these data-sets.

2 Literature review

2.1 Introduction

In Section 2.2, some of the most important properties and behaviours of granular slides and flows are described. Insight is provided in Section 2.2.1 on how these granular slides and flows can be defined and characterised. Key principles are identified in Section 2.2.2 that govern the behaviour of granular slides and flows, and the various impacts of particle and bulk slide geometry are described in Sections 2.2.4 and 2.2.5. In Section 2.3, the concept of scale effects is introduced, and their drastic impact on the accuracy of small-scale experimental modelling of phenomena is highlighted. Dimensionless parameters are described in Section 2.3.1 that govern the behaviour of a granular system, and their relative impacts are discussed, while the scale series approach of conducting experiments is also outlined. In Section 2.3.2, commonly adopted strategies for mitigating scale effects are discussed. Meanwhile, the concept of hypermobility, an important effect already identified in granular slides, is described in Section 2.3.3. In Section 2.4, techniques for capturing and modelling granular slides are described, such as experimental measurement techniques and applications (Section 2.4.1), the Savage-Hutter (1989) continuum model (Section 2.4.2), and numerical modelling techniques such as discrete element modelling (DEM) (Section 2.4.3). Finally, key experiments in the literature that formed the basis of the experimental geometry in this study are highlighted in Section 2.5, focusing on Hutter et al. (1995), Davies and McSaveney (1999), Okura et al. (2000a), De Haas et al. (2015), and Haug et al. (2016).

2.2 Granular slides and flows

Granular slides and flows can be seen in many configurations and have been the subject of much investigation, as they are simple, easily controlled systems that allow the rheological properties of particulate systems to be identified precisely (Pouliquen, 1999). Granular slides are typically seen in natural contexts such as

2. LITERATURE REVIEW

rock, ice, snow, and debris avalanches, and landslides, where an initial perturbation mechanism triggers the release of a granular slide from its surroundings. These slides translate their potential energy into kinetic energy as they traverse natural slopes until they reach an obstacle or dissipate the rest of their kinetic energy via frictional mechanisms. Many granular slides start and stop moving several times throughout this traversal process, making characterisation of their movement difficult. Hungr et al. (2013) define the "failure" of a landslide as the most significant movement episode in its known or anticipated history, and outlines a range of landslide types based on a range of failure mechanisms and outcomes. This range includes falls and topples, slides in rock, slides in soil, spreading, flow-like landslides (differentiated from other slides by mobilisation mechanisms that vastly extend their run-time and produce relatively more steady states), and slope deformations. Figure 3 summarises common landslide types in nature.

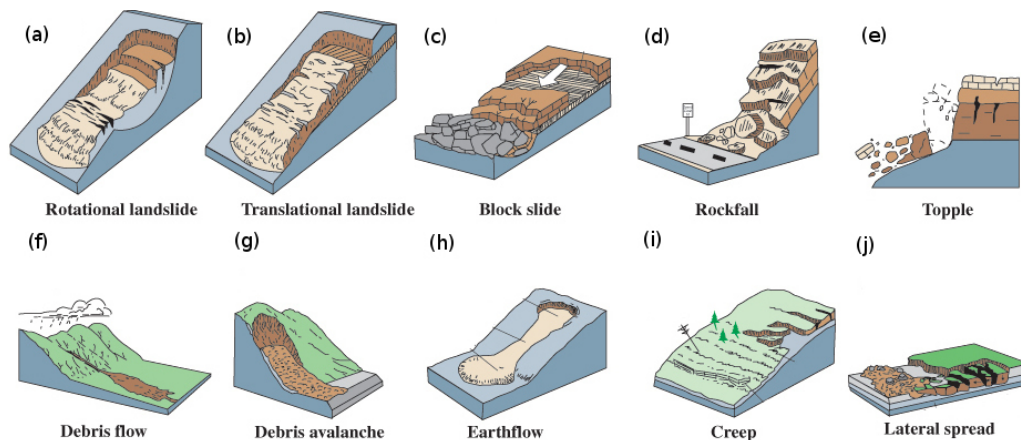


Figure 3 Natural landslide types (adapted from Lynn Highland Graphics, 2004)

While granular slides are inherently unsteady due to their finite nature, steady granular flows can be established where key flow parameters such as mean depth and velocity, are invariant with time. As this requires a continuous input of energy into the system and highly controlled conditions, granular flows are mostly seen in industrial applications, with Fig. 4 summarising some of the most common configurations (Forterre and Pouliquen, 2008).

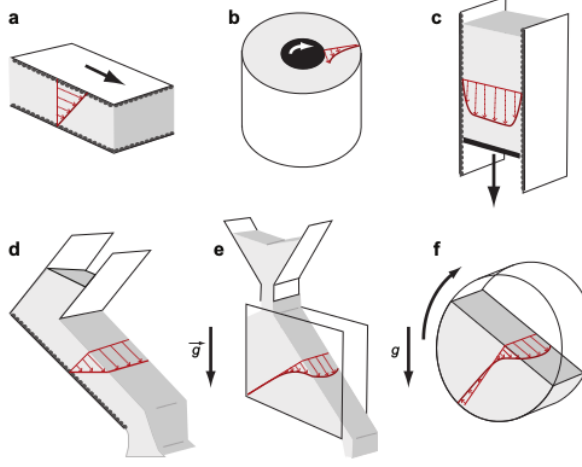


Figure 4 Common granular flow configurations: (a) plane shear, (b) annular shear, (c) vertical-chute flows, (d) inclined plane, (e) heap flow, and (f) rotating drum. Black and white arrows indicate applied forces, red arrows indicate velocity profiles (Forterre and Pouliquen, 2008)

Figure 4(a) represents plane shear where one plate moves over a layer of particles bounded by a stationary base layer. Figure 4(b) describes annular shear where particle motion is driven by a central rotating element and is bounded by a cylinder. Figure 4(c) represents vertical chute flows where a base plate is lowered and particles slide down vertically. Figure 4(d) describes inclined plane flow, which is related to a granular slide and is thus the most relevant case for this study. Figure 4(e) similarly shows heap flow where the slope of the flowing surface is dictated entirely by particle dynamics. Figure 4(f) describes rotating drum flow where the particles are bounded and driven by a horizontally rotating cylinder.

2.2.1 Characterising granular slides and flows

G.D.R. MiDi (2004) performed tests on granular flows with a steady uniform flow thickness down rough inclined planes of different constructions, such as particles being glued to the surface, carpet, and velvet cloth. A critical flow surface angle

2. LITERATURE REVIEW

θ_{start} was identified that, if exceeded, would cause a static layer of particles to start flowing and accelerate continuously if unimpeded. Similarly a second reduced critical angle θ_{stop} was identified at which the flow would start to decelerate and eventually stop (Pouliquen, 1999). Within the domain between these two angles, steady flows can be achieved once they have been triggered. As these critical angles depend on the flow thickness, these starting and stopping thresholds can be interpreted as critical flow depths ($h_{start}(\theta)$ and $h_{stop}(\theta)$) at which a flow becomes or ceases to be steady.

Jop et al. (2005) further noted that a minimum flow rate Q_c was required for steady flow to occur; otherwise, the flow would consist of successive avalanches, with wider channels requiring higher flow rates per unit width for steady flow. Figure 5 clarifies the conditions under which avalanching takes precedence over steady flow in heap flow with d representing the particle diameter; as the ramp angle increases, uniform flow becomes possible at lower flow depths. All experiments seen in Fig. 5 used particles with the same bed and internal friction angles.

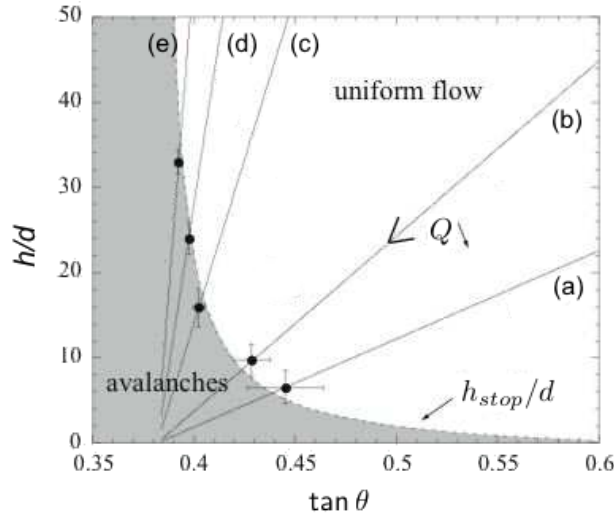


Figure 5 Comparison of steady and avalanching phases. Straight lines show variation of flow depth over particle diameter h/d and inclination angle θ as the flow rate Q is varied across a fixed channel width $w =$ (a) $19d$ (b) $38d$ (c) $142d$ (d) $283d$ (e) $570d$ (adapted from Jop et al., 2005)

G.D.R. MiDi (2004) also identified that flows sufficiently thicker than h_{stop} roughly followed a Bagnold velocity profile, with

$$\frac{u(z)}{\sqrt{gd}} = A(\theta) \frac{(h^{3/2} - (h - z)^{3/2})}{d^{3/2}}, \quad (1)$$

$$A(\theta) = \frac{2}{3} I(\theta) \sqrt{\cos(\theta)}. \quad (2)$$

u is the mean flow velocity, while h is the flow thickness, z is a coordinate normal to the flow direction, and d is the particle diameter. A is a parameter that depends on the flow surface angle θ and the inertial number I , which will be evaluated in Section 2.2.2. The granular slides of this study fit into this category due to the relatively high slope angles used. Importantly, these slides do not exert a fixed flow rate of material over time, but release a single mass of particles. While the conditions are such that a steady flow could develop in the laboratory with continued flow of material, this state is never achieved in the experiments in this study. Eqs. (1) and (2) indicate that, for a constant ramp angle and steady flow depth, the velocity of an individual particle depends solely on its depth within the slide under these conditions.

Figure 6(a) shows the velocity distribution from a numerical simulation of a flow roughly 40 particles deep, with the white symbols representing simulation data and the black continuous lines representing the predictions of Eq. (1). It should be noted that while the Bagnold velocity profile describes the particle velocity distribution in their data well for most of the flow depth, particles near the flow base moved more slowly than predicted, especially at higher inclination angles, while particles on the free surface move slightly more quickly than predicted at lower angles. While many studies focus mostly on relatively slow flows, Holyoake and McElwaine (2012) provide a comprehensive study on faster granular flows at higher ramp angles up to 50° . Pouliquen (1999) concluded that the flow depth

2. LITERATURE REVIEW

$h_{stop}(\theta)$ and flow velocity measurements varied significantly with changes to the roughness conditions, but despite this, scaling laws could be established for flows with matching boundary conditions.

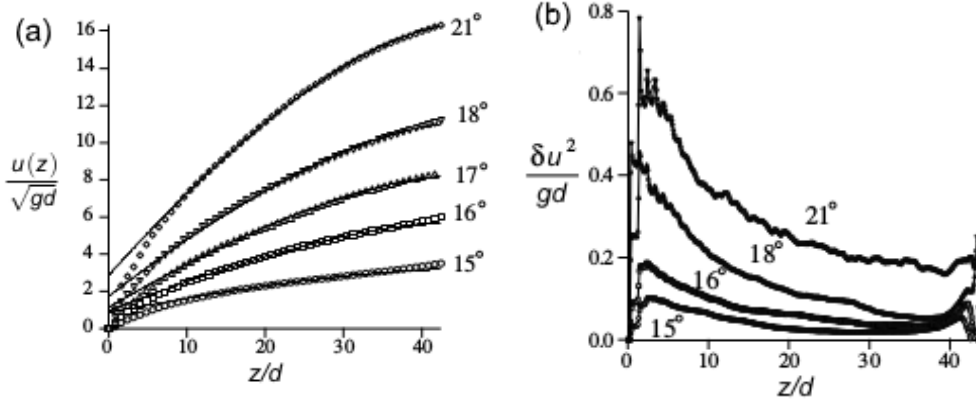


Figure 6 Comparison of particle velocity via Eq. (1) (a) and velocity fluctuations (b) with flow depth z/d and ramp angle θ (adapted from G.D.R. MiDi, 2004)

Figure 7 indicates that the flow Froude numbers u/\sqrt{gh} compared to h/h_{stop} collapse onto a straight line for multiple inclination angles, showing that the variation of mean flow velocity with inclination correlates to the variation of h_{stop} with inclination. Similar agreement was seen for other particle flow and surface configurations, which all showed self-similarity (Barenblatt, 1996; Heller, 2017). This indicated that the Froude number is a linear function of h/h_{stop} regardless of inclination, roughness conditions, or particle diameter, with the influence of these factors being accounted for by the function $h_{stop}(\theta)$. G.D.R. MiDi (2004) present this scaling law with the following expression, where α_m and β_m are measurable constants related to the system in question (Tagaki et al., 2011).

$$\frac{u}{\sqrt{gh}} = \alpha_m + \beta_m \frac{h}{h_{stop}(\theta)}. \quad (3)$$

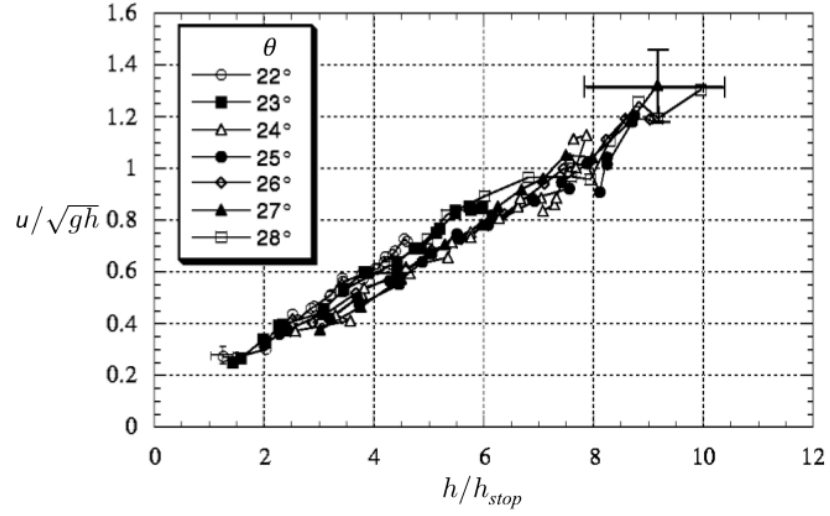


Figure 7 Froude number u/\sqrt{gh} as a function of the ratio between current flow depth and critical flow depth h/h_{stop} for different inclination angles θ . The particle diameter is 0.5 mm both in the flow and attached to the surface (adapted from Pouliquen, 1999)

Meanwhile, integrating Eq. (1) over the flow depth results in Eq. (4).

$$\frac{u}{\sqrt{gh}} = \frac{3}{5} \frac{h}{d} A(\theta). \quad (4)$$

For glass beads, α_m is zero and thus Eqs. (3) and (4) can be combined to provide the following relationship between $A(\theta)$ and $h_{stop}(\theta)$.

$$A(\theta) = \frac{5}{3} \beta_m \frac{d}{h_{stop}(\theta)} \quad (5)$$

Equation (5) can then be combined with Eq. (2) resulting in Eq. (6); a relationship between the depth averaged inertial number I , depth averaged flow velocity, and flow thickness.

$$I = \frac{5}{2} \frac{ud}{h\sqrt{gh} \cos \theta} \quad (6)$$

However, for sand, α_m is non-zero and thus the effective friction coefficient μ_{eff} of the flow is not only dependent on I but also on h/d , as described below.

$$\mu_{\text{eff}}(u, h) = \mu_{\text{eff}}\left(\frac{u/d}{h\sqrt{gh}} - \alpha_m \frac{d}{h}\right) \quad (7)$$

The only forces between cohesionless particles are normal mechanical forces, resulting in the shape of a granular body being determined entirely by its boundaries, the influence of gravity, and forces acting from the interstitial fluid (in dry granular bodies, air) (Jaeger and Nagel, 1996). Depending on the circumstances of the granular system, the fluid forces acting on the body may be insignificant.

2.2.2 Granular slide and flow principles

One of the difficulties of modelling granular slides is that the dynamics of a particle within a slide depend not only on its individual properties in a micro-scale reference frame, but also on the behaviour of the surrounding particles in a macro-scale reference frame. The discrete nature of granular particles makes individual fluctuations that would be irrelevant in molecular fluids have an impact on the macroscopic slide behaviour (Glasser and Goldhirsch, 2001). In dense flow conditions where the flowing surface is several particle diameters thick, granular media can effectively be described with three phases: a solid regime where particles are static and governed by frictional forces, a gaseous regime where particles bounce off each other and are governed by collisional forces, and a liquid regime where a dense layer flows and both frictional and collisional forces have similar influences (Goldhirsch, 2003; Forterre and Pouliquen, 2008). This can be seen in Fig. 8,

where a long exposure image has been taken of a ball-bearing flow to indicate the relative particle velocities.

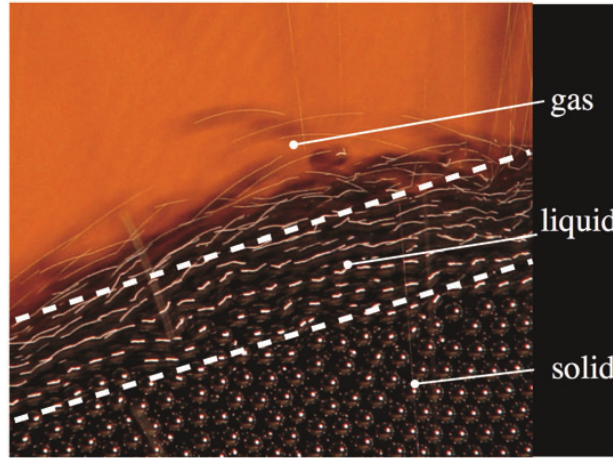


Figure 8 Diagram of slide particle phases (Forterre and Pouliquen, 2008)

It should be noted that even though a granular slide is by definition discontinuous, these three phases can still be seen developing as the slide progresses, with a solid regime usually not forming until the slide starts to deposit and before most of the particles falling into the liquid and gaseous phases respectively. Granular slide behaviour is highly dependent on both the internal friction angle ϕ of the particles and on the bed friction angle δ . This frictional criterion exists not only due to the friction between individual grains but also due to their fluctuating position and interaction within the slide contact network; thus even a slide consisting of frictionless particles would have a macroscopic friction angle (Forterre and Pouliquen, 2008). As a result, the value of ϕ at which a slide will start to flow can vary depending on the initial configuration of the slide mass and potentially its history of previous deformation.

Different formation conditions can result in different slide densities and arrangements, resulting in different flow characteristics (Daerr and Douady, 1999). The behaviour of granular particles flowing in a gaseous state led to comparisons between this regime and molecular gases, with Ogawa (2002) introducing the con-

cept of granular temperature T_g , which represents the fluctuation in kinetic energy of a particle. Note that this has no direct relation to thermal temperature due to the vastly smaller scale of thermal vibrations. The main difference between molecular and granular gases, aside from size of course, is that kinetic energy is lost with each particle collision, resulting in a particle coefficient of restitution e , the ratio of input and output energy after a collision, always being < 1 . For example, a single marble will bounce on a hard surface if dropped, but an assembly of thousands of marbles dropped onto the surface will stop dead due to the vast number of inelastic collisions dissipating the kinetic energy (Jaeger and Nagel, 1996).

Accordingly, a granular slide can only be maintained by the application of an external force (mostly gravity, but vibration can occur in industrial contexts or natural acoustics) to replace the kinetic energy lost from these collisions (Goldhirsch, 2003). Similarly, dilute gaseous regimes become more pronounced on steeper slopes where the gravity force component increases compared to the frictional resistance (Andreotti et al., 2013). This is supported by Fig. 6, where for simulated 2D thick flows of ≈ 50 particle diameters, mean particle velocities and velocity fluctuations increase at all depths with ramp angle.

While the mean particle velocity decreases with depth, the mean velocity fluctuation increases due to the continuous formation of new contacts on these tightly-packed particles. However, similar 3D simulations in Brodu et al. (2015) highlight a slightly different behaviour in Fig. 9, with an overall increase of granular temperature with depth still being seen at the sidewalls, but a core forming in the middle of the channel which is relatively free of fluctuations. This matches descriptions from Cleary and Campbell (1993) where for large landslides the strata in the middle of a slide deposit is often more stable than the boundary layers of the slide compared to initial conditions.

Overall, this demonstrates that the presence of confining sidewalls significantly influences the dynamics of granular slides, and models with periodic boundary conditions will not be able to replicate these dynamics. This will be further discussed in Sections 2.2.5 and 2.4.3.

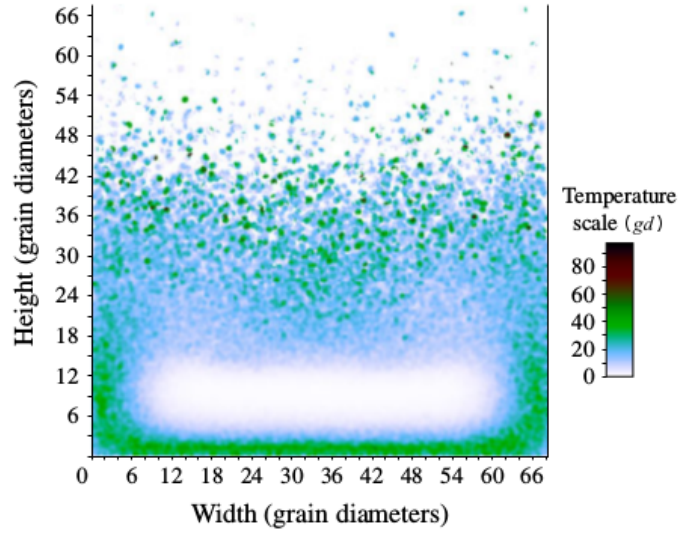


Figure 9 Granular temperature distribution with $\theta = 33^\circ$ (Brodu et al., 2015)

Fluidisation is a phenomenon where a purely solid material phase (such as a bed of granular particles) behaves similarly to a fluid due to upwelling currents of gas or liquid moving through them, initiating when the overall pressure drop (in addition to buoyancy forces) starts to exceed the net downward forces (primarily gravity) (Pudasaini and Hutter, 2010). Granular materials such as sand can become fluidised simply by being set into motion by external forces or vibrations; this leads to the runaway nature of avalanche and landslide formation in nature where earthquakes can set enough granular particles in motion to fluidise more in a cascading process (Xing et al., 2017). Combined with the capability of avalanches and landslides to accumulate more material from their surroundings as they move down the slope, this can lead to much larger runout distances than those predicted by the particle angle of repose (Section 2.3.3).

Similarly, lubrication can occur in granular slides, where the frictional resistance to slide motion is reduced by either liquid-, gas-, solid-, or heat-based lubricants. In natural contexts, the lubricant can be water, air, snow, ice, mud, clay, dust, or powder, while specialised products can be used for industrial purposes. Snow avalanches typically produce a film of water between the solid snow surface and

the ground, with frictional heat melting more snow/ice and perpetuating the layer. Meanwhile, for large scale rock avalanches, landslides, and debris flows, (Erismann, 1986) suggests that frictional heat can cause rock gravels to melt in localised areas, further lubricating the slide. This hypothesis has been evaluated further by Goren and Aharanov (2007) and de Blasio and Elverhøi (2008), with Goren and Aharanov (2007) simulating frictional heating and its impacts on pore pressure and de Blasio and Elverhøi (2008) producing a model for frictional melt generation. However, while frictionite rock samples produced by melting have been found at landslide locations (de Blasio and Elverhøi, 2008), there is little natural data on frictional melting and its effect on fluidising natural slides to validate these models against. The main difference between lubrication and fluidisation in the case of granular slides is that the former affects only the local flow surface directly, while the latter can influence particle dynamics throughout the entire slide mass. Staron and Lajeunesse (2009) also detail that trapped air can minimise energy dissipation at the flow surface, and ground vibrations caused by the movement of larger masses can also further lubricate the flow.

Additionally, cohesive effects can take place between particles that are sufficiently small, often occurring due to surface forces or other phenomena such as liquid bridges that bind particles together via the surface tension of an interstitial fluid (Campbell, 2006). Schaefer et al. (2010) performed granular slides using both large (1.4 mm) and small (0.1 mm) ballotini (glass beads) in air and did not see any cohesive effects for either particle size, suggesting cohesive effects can be ignored in particles larger than a minimum threshold diameter.

2.2.3 Granular slide rheology

Many rheologies and theories have been developed to try and effectively describe granular slides and flows from an analytical and physical basis. However, due to the multitude of length- and time-scales involved, no unifying rheology has been developed that accurately describes granular systems in all circumstances. This section will briefly describe some of the notable theories and rheologies that have

been developed to describe granular slides and flows in specific circumstances.

Kinetic theory was developed to describe the behaviour of granular gases where the interactions in the granular system are mostly collisional (Jenkins and Zhang, 2002). While this theory describes the surface of granular slides and flows where particles are frequently ejected from the slide surface, it can also apply to astronomical phenomena such as planetary ring systems (Goldhirsch, 2003). These granular gases differ most significantly from molecular gases due to their inelastic collisions and thus their constant dissipation of energy. With the interactions of these granular gases filling a small subset of the interactions involved in denser granular systems, constitutive equations and models have been developed that can describe these systems to a high degree of accuracy (Jenkins and Zhang, 2002; Brilliantov and Pöschel, 2004). However, while the kinetic theory does describe rapid and dilute granular flows from their microscopic interactions reasonably well with hydrodynamic equations, it also has some notable disadvantages. These include a lack of scale separation from inelastic particles conflicting with the difference between particle and hydrodynamic scales, clumping behaviour in slides with insufficient energy to maintain flow, and lack of variation of flow velocity with restitution coefficient (Goldhirsch, 2003; G.D.R. MiDi, 2004; Andreotti et al., 2013). Lee and Huang (2012) combine the kinetic theory with a static granular model to more accurately model dense granular flows, and note that additional work needs to be done to address the theoretical inconsistencies of these two approaches.

Another rheology that aims to characterise granular flows and slides is the inertial number theory, which defines the ratio I between the microscopic timescale t_{micro} of particle re-arrangement and the macroscopic timescale t_{macro} of the mean shear rate of a particle layer. This ratio is called the inertial number I , and is controlled by the mean shear rate $\dot{\gamma}$, as shown in Eq. (8). σ represents the normal stress applied to the slide and ρ_s denotes the particle density.

$$I = \frac{t_{micro}}{t_{macro}} = \frac{d}{\sqrt{\sigma/\rho_s}} \times \dot{\gamma} = \frac{\dot{\gamma}d}{\sqrt{\sigma/\rho_s}}. \quad (8)$$

It can be shown via dimensional analysis that the volume fraction Φ of the slide is a function of I only and that the shear stress τ is equal to the product of the normal stress σ and the friction coefficient μ (that is also a function of I only), at any given point in the slide (Andreotti et al., 2013). A higher I corresponds to a more energetic flow, where the confining pressure is low compared to the mean particle velocity. This model can easily be adapted for polydisperse media by defining a local mean particle diameter \bar{d} for a region, leading to a corresponding local inertial number of $I_{\bar{d}}$ (Andreotti et al., 2013).

This local rheology, where a particle's behaviour is dependent solely on its neighbours, captures some of the basic characteristics of inclined-plane flows, but progress is being made towards non-local rheologies that can capture the influence of other parts of the flow on particle behaviour (Pouliquen and Forterre, 2009). Jop (2015) notes that for sufficiently thin flows Bagnold scaling of Eq. (1) starts to break down and even reverse with some particles traversing up the slope due to the bulk slide movement; a non-local effect. They also note that the $\mu(I)$ rheology starts to break down for fast, dilute flows, with transition towards salting grain behaviour occurring once the ratio of shear to normal stress exceeds a certain limit; beyond this, the friction coefficient starts to decrease with $I < 0.8$.

2.2.4 Particle geometry

The particles that comprise granular materials can display a number of complex and varied features that can make them difficult to model. While regular shapes such as spheres and cylinders are occasionally relevant to industrial processes such as pharmaceutical and food manufacturing and processing, irregular shapes are more commonly found both in industrial contexts (such as quarrying and mixing of rocks/sand) and in natural slide events. Particle sphericity can be defined as the ratio of a normalised particle radius to the radius of a circumscribing sphere (Wadell, 1932), and angularity can be defined as the number and sharpness of corners on the particle surface (Sukumaran and Ashmawy, 2001). As this coefficient increases, the torque applied to particles by eccentric contacts increases due to the

increasingly sharp and angular nature of the particles. This increases its influence on the general motion of the particle, either increasing or decreasing the rotational energy of the particle depending on the specific orientation of the contact.

Vangla et al. (2018) highlight three important shape features that dictate the behaviour of a particle; its macro-scale form, its meso-scale roundness (which is measured using convex regions of the particle surface), and its micro-scale surface texture. Particle kinematics such as rolling, sliding, and interlocking are highly influenced by these shape characteristics, which in turn govern the overall strength, deformation, and dilation properties of the granular material as a whole. However, while these characteristics can describe bulk particle behaviour to a degree, they do not easily describe the interactions of specific particles due to their tendency to neglect specific contact geometries. Figure 10 shows a variety of different 2D particle images assessed by two other characterising parameters, the Non Corner Aspect Ratio (NCAR) and the Curvature Length Ratio (CLR), to more appropriately describe how likely a particle is to slide or roll, or to interlock with other particles. Importantly, more angular particles are seen to favour sliding and interlocking over rolling, demonstrating shape-dependent rolling resistance.

Another important characteristic of particle geometry is how the shape of a particle impacts its tendency to fracture. Rough particles can have several stress-concentrators on their surface, where the contacting force of another particle or boundary is applied to a very small area of a particle's surface due to the protrusion of a small convex region. This can result in angular particles fracturing more under similar loading to spherical particles of the same material. Particles may also have pre-existing weaknesses in their structure due to their formation or past behaviour, resulting in splitting fractures that can be triggered by loads far below the typical strength of the material. The relative volume difference between a fracturing rock shelf and the fine particles its fracture produces can be in the order of 10^{18} in natural events (De Blasio and Crosta, 2014), significantly changing the size and mass distribution of the slide as a result. Notably, this phenomenon has also proven impossible to be replicated at experimental scale, due to the limited size of the smallest particles that can be generated from such an event.

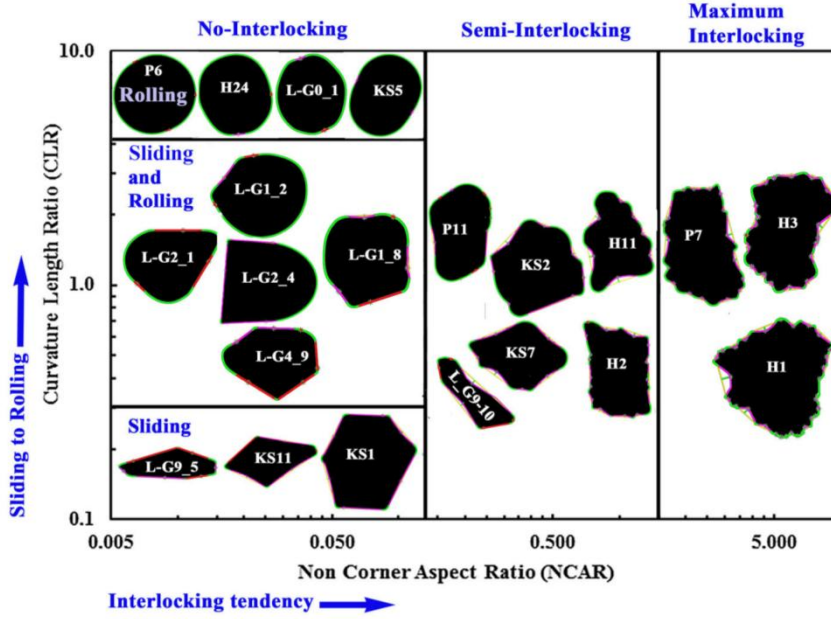


Figure 10 Kinematic classification of typical 2D particles (Vangla et al., 2018)

2.2.5 Granular slide geometry

One of the fundamental states of granular systems is a packed bed of particles; although this is one of the simplest states for a mass of particles, proper description of it is fundamental for the understanding of more complex particle interactions (Zhu et al., 2008). Regarding granular slides, this relates to generating the initial packing of the slide mass before the slide is released, which can have a significant impact on the slide behaviour (Daerr and Douady, 1999). The coordination number (CN) and radial distribution function (RDF) provide some important information about a packed bed, with the CN representing the average number of contacts per particle and the RDF representing the density variation of particles as a function of distance from a reference particle. For frictional particles, the minimal average CN c for a packing to maintain stability is $c_f = 4$, whereas for non-frictional particles the corresponding CN is $c_n = 6$; packings that satisfy these conditions are "isostatic" (Silbert et al., 2002a). Figure 11 shows the difference in flow behaviour of two real cylindrical piles flowing off a platform with different ini-

tial packing fractions; in Fig. 11(a) a rounded tip quickly forms while in Fig. 11(b) the corners of the tip gradually move towards a central tip.

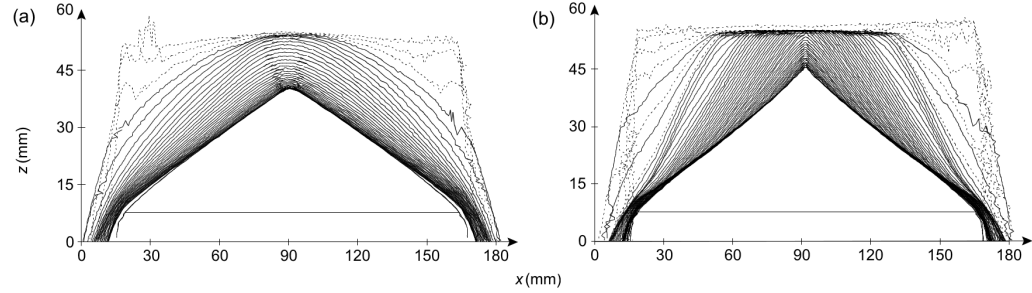


Figure 11 Series of side profiles for cylindrical piles of glass beads of initial height 46 mm and base diameter of 142 mm. (a) Loose initial pile with $\Phi = 0.58$ and a time lapse of 0.02 s between consecutive lines. (b) Dense initial pile with $\Phi = 0.65$ and a time lapse of 0.04 s between consecutive lines (adapted from Daerr and Douady, 1999)

Packings can be formed in a number of different ways to suit the nature of the study. Silbert et al. (2002a) analysed depositing cohesionless particles under gravity to see whether packings readily achieved isostaticity by varying many particle parameters and the construction history. They investigated how the final packing density, CN, and contact natures changed, finding that frictional particles achieve a variety of hyperstatic packings where ($c > c_f$), with the CN reducing smoothly from $c = 6$ as μ increases. Other methods of preparing granular packings include centripetal growth (Liu et al., 1999), where the centripetal force acting on particles affects the densification rate and mean coordination number, and compression (Liu, 2003; Zhang and Makse, 2005), where an initially loose packing is condensed by shrinking boundaries until the desired packing properties are reached.

While the properties of individual granular particles are important, the size distribution of a granular slide's particles can also have significant impacts on its behaviour. For instance, a granular mass consisting of monodisperse particles can behave very differently to one containing two very differently-sized particles, or a well-graded mixture that has particle sizes following a roughly normal distribution.

2. LITERATURE REVIEW

One of the effects that can manifest in these polydisperse mixtures is size segregation, where an initially well mixed material may separate out into layers containing different concentrations of differently sized particles (Johnson et al., 2012; Gray et al., 2015; Gray, 2018). This effect is chiefly caused by the mechanisms of kinetic sieving and squeeze expulsion, where small particles fall between larger ones, levering them upwards in the granular slide and resulting in a coarse grained top layer of large particles. Once these large particles reach the top layer, they are often transported to the slide front due to the slide velocity gradient.

While diffusive remixing occurs in the flow as it progresses due to the nature of random particle collisions, the segregation effects eventually dominate the composition of the flow. Gray (2018) notes that this segregation effect is strongest in granular slides and flows on surfaces angled at close to θ_{stop} , gradually diminishing as the inclination angle increases. Particles can also segregate due to differences in density, with denser particles settling towards the bottom layer of the slide, but this particle-density segregation effect is typically much weaker than particle-size segregation at low inclination angles. Gray (2018) identifies gravity as the key force driving segregation mechanisms, with experiments completed using viscous interstitial fluids drastically reducing the rate of particle-size segregation, and experiments completed using neutrally buoyant flows also showing little evidence of segregation. Figure 12 illustrates segregation in a rotating drum flow; the initially mixed mixture of differently sized particles can clearly be seen to separate into three distinct layers through the action of the continuous surface avalanche (Gray, 2018).

The presence of confining sidewalls, and the relative narrowness of the channel compared to its flow depth, can also have large impacts on the velocity profiles of granular slides and flows. As a chute becomes narrower, the frictional effect of the sidewalls starts to dominate over that of the channel flow, resulting in exponential velocity profiles where the top slide layers flow much more quickly than those in the middle or bottom layers of the slide. This is in contrast to the Bagnold velocity profile (Section 2.2.1) seen in less confined flows where the channel walls are much further apart.

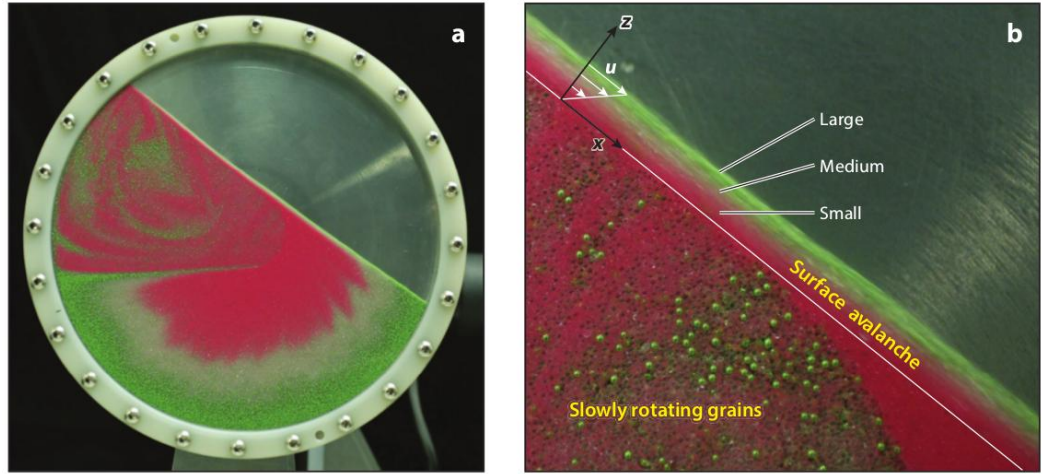


Figure 12 Radial size distribution in a rotating drum filled with large green (500–750 μm), medium white (400–500 μm) and small red (75–150 μm) particles. (a) Overview of the rotating drum. (b) Close-up of the surface avalanche, shown distinctly from the slowly rotating grains locked in solid body rotation (Gray, 2018))

Jop et al. (2005) performed a series of experiments with channels varying from 20–600 d , finding that steady granular flows are entirely controlled by these side wall effects. Jop et al. (2005) also found that, for similar flow rates per unit width, wide channel flows tend to be thicker and slower than narrow channel flows, contrasting with intuitive views. Bryant et al. (2014) identified that the effects of sidewall friction were minimal at the start of a granular slide, but became much more significant as the slide progressed down the chute, with a retarded region of about 50 mm (17 d) from the glass producing a maximum velocity drop of about 0.5 m/s (170 d per second). Schaefer et al. (2010) agreed that this slowing effect was present in their experiments but that it did not affect the overall macroscopic behaviour of the central slide mass. While most experimental studies look at straight chutes, Pudasaini et al. (2008) modelled experiments on curved and twisted channels, showing that many different characteristics of the curvature of the channel affected the final deposit patterns.

In contrast, significant spreading occurs immediately after release for granular slides that are unconfined by sidewalls. McFall et al. (2018) notes that the lateral

2. LITERATURE REVIEW

thickness of an unconfined slide transitions from an initial trapezoidal profile at the exit of a confined chute region to a parabolic profile further downstream. The curvature of this paraboloid increases and becomes flattened as the slide position down the ramp increases. McFall et al. (2018) also notes that the extent of the slide's lateral spreading is governed by the rates of mass and momentum flux in the sliding (i.e. slope-parallel) direction, with a maximum lateral extent being reached in an asymptotic manner. Meanwhile, on a conical ramp surface, the slide width continues to increase linearly as the slide travels further down the slope. Importantly, McFall et al. (2018) also note that rapid, thick slides tend to have reduced maximum slide width. For both planar and conical ramp surfaces, the maximum slide velocity was found alongside the peak slide thickness along the slide centre-line, with faster moving slides maintaining their initial shape for a larger proportion of the overall slide event.

There is also significant evidence that granular slides and flows can self-channelise. This can happen through deposition where, in flows with substantial internal pore pressures, large particles transported to the slide front over time can become more resistant to motion, resulting in these particles slowly moving backwards in the slide and recycling to the top. This resistance can cause the more mobile particles to push these coarse grains to the sides of an unconfined deposit, where they eventually settle and exert friction on the rest of the slide, as seen in Fig. 13 (Johnson et al., 2012; Gray, 2018). Self-channelisation can also occur through erosion where material is entrained into the slide from an erodible base. In both of these cases, the channelisation causes the slide to run out further than it would in a purely unconfined case.

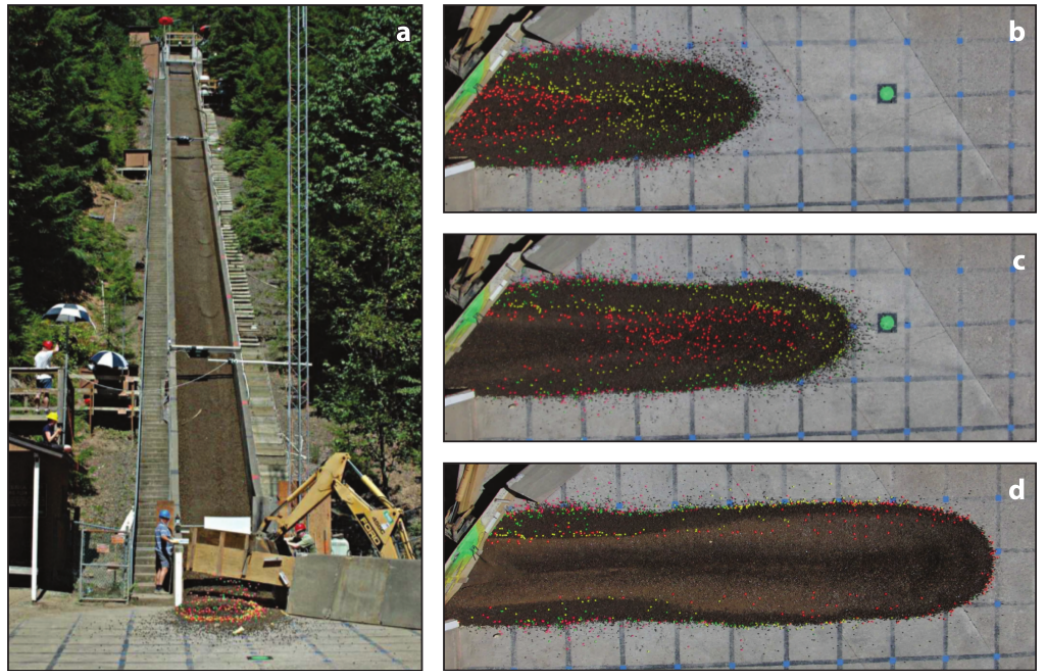


Figure 13 (a) Evidence of self-channelisation in a large-scale controlled debris flow, composed of sand, gravel, and water. Coloured tracer particles were dropped onto the slide surface as it entered the runout area (b-d), showing the deposit motion and formation of static levees to the sides of the central channel flow (Gray, 2018)

Another mechanism seen frequently in granular slides is the splitting of an initially smooth front into a series of granular "fingers" under certain conditions, partly via the recirculation mechanism occurring laterally at a much smaller scale to the overall front recirculation (Jackson, 2014; Baker et al., 2016b; Gray, 2018). The fluid flow surrounding and acting on the slide front as it progresses can play a large part in finger formation even for monodisperse slides, either due to an unstable airflow developing due to random particle motion or due to the formation of larger vortices that act on the slide front. Furthermore, adding a small fraction of differently-sized particles to a monodisperse flow can be enough to cause fingers. Figure 14 shows the formation of fingers in a typical granular slide, captured both numerically and in laboratory experiments (Gray, 2018).

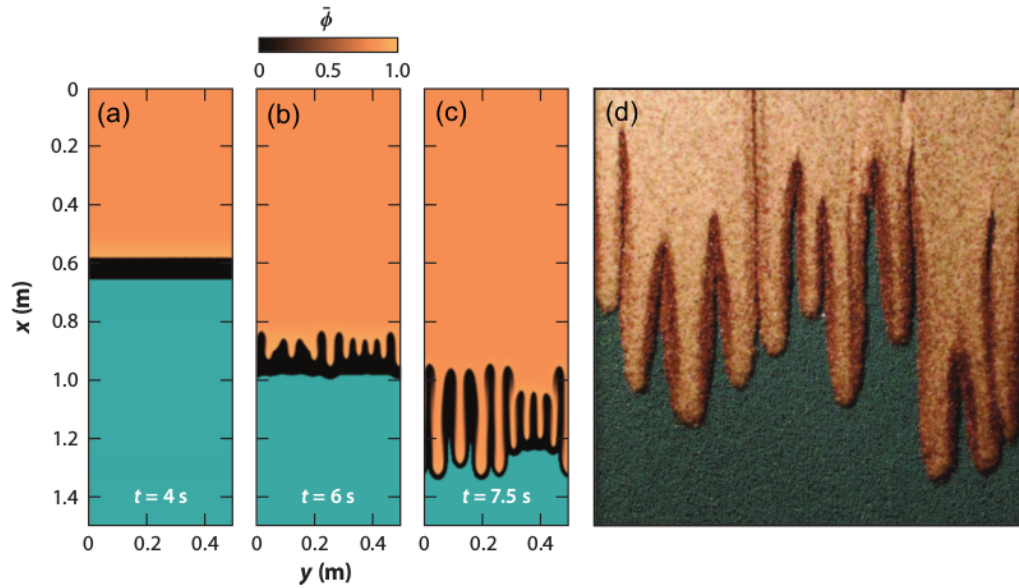


Figure 14 (a-c) Numerical simulations of segregation-induced fingering solved via a finite-volume scheme, with $\bar{\phi}$ representing the proportion of large particles in the flow. (d) Fingering in a bidisperse mixture of 80% white ballotini (75–150 μm) and 20% brown carborundum (305–355 μm) on a base of turquoise ballotini (750–1000 μm) (adapted from Gray, 2018)

2.3 Scale effects and Froude scaling

Scale effects can be identified in many situations, where the properties and behaviour of a phenomenon change significantly as its geometrical scale changes. Due to the difficulty and expense of conducting large-scale experiments, and in particular ensuring those tests are conducted in a controlled environment and with robust, accurate measurement techniques, small-scale experiments are often created to simulate these events. In contrast to scale effects, model effects can be caused by idealised representation of a prototypical feature such as the geometry, slide initiation mechanisms, and particle or material properties. This applies not only to idealised conditions, but also to idealised geometry, with laboratory models potentially being more or less complex than the natural geometry. Additionally, measurement effects can be caused by differences in measurement techniques be-

tween cases; for example, using non-intrusive systems for a real world event and using intrusive systems in a laboratory model.

The scale factor λ represents the ratio between a characteristic length of the prototype L_P and model L_M . In many circumstances, the scale effects that are introduced in a model of a real world event depend strongly on these scale differences. As λ increases, the scale effects present in a model will change in magnitude and nature, so the maximum scale difference between model and nature scale is often based on the maximum permissible influence of scale effects on key parameters. However, the space, time, and cost required to run experiments also decreases with increasing λ , so there are economic considerations at play as well (Heller, 2011). It should also be noted that a scale factor cannot be used in isolation to identify whether scale effects are small enough to be ignored. Different physical situations can result in drastically different behaviour of scale effects with increasing λ , and scaling laws should be defined specifically for the physical phenomenon being studied.

Scale effects in experimental fluid mechanics have been analysed quite thoroughly, with Heller (2011) reviewing scale effects and limiting criteria in many scenarios. However, there has been relatively little research into the scalability of granular slides (Iverson, 2015) and a lack of clear scale separation between the microscopic grain scale and macroscopic flow scale (Andreotti et al., 2013; Armanini, 2013). Slonaker et al. (2017) highlights many of the characteristics that make granular systems especially difficult to develop scaling laws for, including history- and preparation-dependent dilation and strengthening (Daerr and Douady, 1999), local differences in flow structure and variation of confining normal stresses (Bagnold, 1954; G.D.R. MiDi, 2004; Goldhirsch, 2010), and nonlocality due to the discrete nature of the particles involved. These complexities produce many more dimensionless numbers that each describe important aspects of the granular system and the necessary scaling. Furthermore, scaled experiments of granular systems require materials to be produced that match in several important physical parameters while varying drastically in size.

2. LITERATURE REVIEW

Cohesive and electrostatic effects can also make systems with already-small grain sizes (such as sand dune ripples) extremely difficult to downscale without inducing scale effects (Slonaker et al., 2017). Many experimental apparatus used to analyse granular systems, such as chutes or shear cells, must also have smaller or larger replicas built to directly quantify differences in behaviour with scale, which is often an unwanted layer of expense for studies not focused specifically on these differences. This additional difficulty has resulted in a relative gap in understanding of scaling granular systems in comparison to otherwise similar fluid systems, particularly when it comes to physical experiment data.

Scale effects can manifest themselves in many different ways depending on the context. Figure 15 highlights different scale effects manifesting between landslides depositing into bodies of water over a small relative scale difference of $\lambda = 2$.

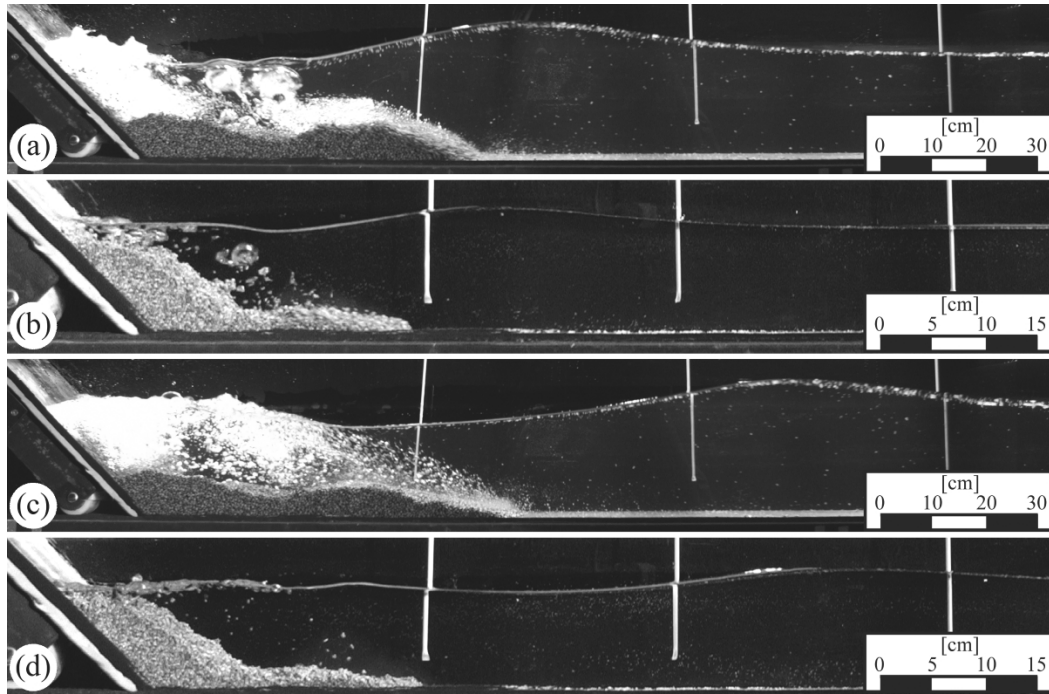


Figure 15 Comparison of air entrainment, detrainment and runout length L_r between a large and small slide at the same relative times after slide impact into water between (a) and (b), and between (c) and (d). $\lambda = 2$ between the large and small slide (Heller et al., 2008)

As λ decreases, a clear increase can be seen in the overall runout length of the slide deposit, as well as a significant change in deposit shape across the submerged body. Additionally, the larger-scale experiment shows significantly increased air entrainment in the region above the slide body. Heller et al. (2008) also notes that the relative wave amplitude is damped at smaller scales, and the wave propagation behaviour also starts to vary between scales after the slide has deposited.

Heller (2011) provides three similarity criteria that can be used to evaluate whether a scaled model is completely similar to its corresponding natural event; geometric similarity, kinematic similarity, and dynamic similarity. A model is geometrically similar if all length dimensions of a model are a factor of λ shorter to its corresponding natural event. In the context of granular slides, kinematic similarity requires both geometric similarity and the correct scaling of particle motion between the two systems. Finally, dynamic similarity requires both geometric and kinematic similarity as well as the correct scaling of all force ratios (Section 2.3.1) between the model and natural event. If a model is dynamically similar to its natural event, then it should represent the natural behaviour accurately without any scale effects being imposed. However, in practise this is unlikely due to the interaction of different dimensionless parameters within the granular slide.

2.3.1 Force ratios and other important dimensionless parameters

Scale effects are primarily caused by differences in force and stress ratios between a scaled model and the real-world event. The Froude number Fr , relating to the ratio between inertial and gravity forces, is the most important force ratio governing the behaviour of granular slides (Choi et al., 2015). This and other significant force and stress ratios are listed below. These force and stress ratios are important tools for quantifying the direct impact of physical forces and stresses on overall slide behaviour. Stress ratios can be compared to force ratios in a similar way to each other by dividing the corresponding forces by their respective area scales.

2. LITERATURE REVIEW

$$\text{Froude Number: } Fr = (\text{inertial/gravity force})^{1/2} = \frac{U}{(gL)^{1/2}} \quad (9)$$

$$\text{Grain Reynolds Number: } Re = (\text{inertial/viscous force}) = \frac{Ud}{\nu_f} \quad (10)$$

$$\text{Grain Cauchy Number: } Ca = (\text{inertial/elastic force}) = \frac{\rho_s U^2}{K} \quad (11)$$

$$\text{Euler Number: } Eu = (\text{pressure/inertial force}) = \frac{P}{\rho_s U^2} \quad (12)$$

$$\text{Savage Number: } N_{Sav} = (\text{inertial/quasi-static shear stress}) = \frac{\rho_s \gamma^2 L}{(\rho_s - \rho_f)g} \quad (13)$$

$$\text{Bagnold Number: } N_{Bag} = (\text{inertial/viscous shear stress}) = \frac{\Phi \rho_s \gamma L^2}{(1 - \Phi)\mu_f} \quad (14)$$

U and L represent characteristic velocity and length scales for a phenomenon, while ν_f is the kinematic viscosity of the surrounding fluid. d is the relevant length scale for the grain Reynolds number, with L relating to the general Reynolds number. P denotes a characteristic pressure scale, such as air or pore pressure depending on the slide. γ is the characteristic shear rate across the slide width (a velocity scale divided by a length scale) and ρ_s and ρ_f denote the solid and fluid phase densities respectively. For N_{Bag} , Φ is the slide volume fraction and μ_f is the dynamic viscosity of a pore fluid with suspended sediment (i.e. the fluid phase of a granular slide).

The grain Reynolds number Re quantifies the type of drag that particles experience against the surrounding air (such as turbulent or laminar flow), and the relative influence of air viscosity on the slide or flow. Meanwhile, the grain Cauchy number Ca represents the influences of particle and surface stiffness within a slide or flow, and the Euler number Eu represents the influences of fluid and particle pressure on the particles. It is expected that between these three numbers, Re

will be the dominant source of scale effects for granular slides. Even in air, Re is relevant for granular slides, with particle drag force being strongly influenced by the grain Reynolds number and representing its influence on the bulk slide dynamics. The drag coefficient C_D is a dimensionless parameter that quantifies the resistance of an object in a fluid environment, with a value of 0 indicating no resistance occurring at all, and larger values indicating greater resistance compared to the dynamic pressure acting over the surface area of the object.

Figure 16 demonstrates the influence of Re on the drag coefficient of a spherical particle, displaying the variation of fluid streamline states seen as Re increases (Bagheri and Bonadonna, 2016). The maximum Re seen in the slides investigated in this study are found in the range 10^2 – 10^3 , staying within the intermediate regime of Fig. 16 where the drag varies significantly.

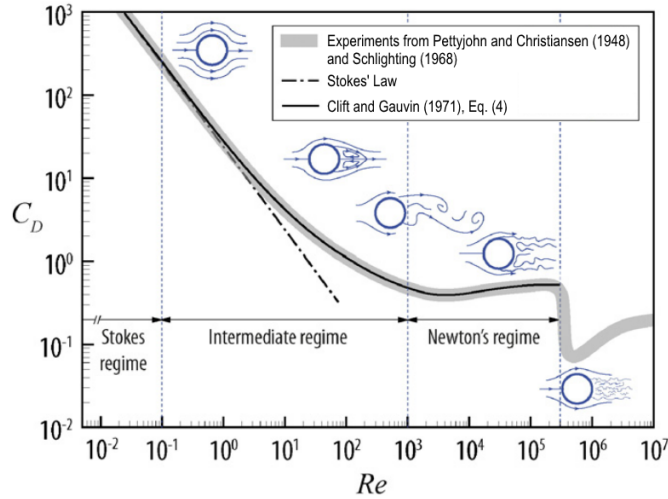


Figure 16 Relationship between Re and the drag coefficient C_D for a spherical particle. Streamlines around the sphere are also shown at various Re values (adapted from Bagheri and Bonadonna, 2016)

However, the shape of a particle can significantly influence the average drag force it experiences; while the instantaneous drag force of an aspherical particle will depend on its orientation and projected area, this average drag force is typ-

2. LITERATURE REVIEW

ically increased compared to that of a spherical particle. Figure 17 highlights a relationship between Re and C_D that is accurate for a wide variety of particle shapes, experimentally validated against cases such as ellipsoids, disks, cylinders, and other regular and irregular shapes. The shape of the particle influences the drag corrections applied to normalised Re and C_D , with k_N primarily influencing Newton's regime of Re and k_S primarily influencing Stokes' regime of Re .

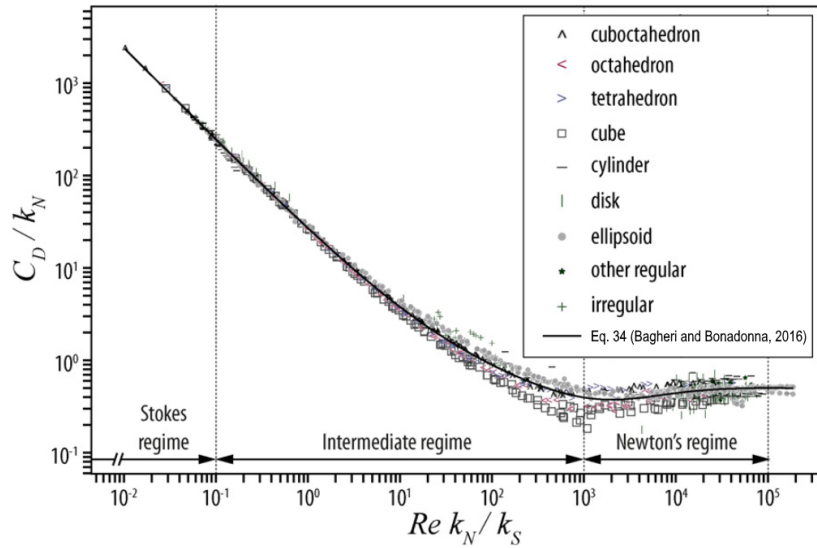


Figure 17 Dependency of normalised drag coefficient of freely falling particles on normalised Reynolds number. See Bagheri and Bonadonna (2016) for experimental data sources (adapted from Bagheri and Bonadonna, 2016)

An initial estimate of the particle drag force in a typical experimental slide of the present study without interstitial liquid is up to 10% of the particle gravity force, although many particles will experience less overall drag force due to the air velocity within the slide approaching the velocity of its particles. This drag is felt on an individual scale by many particles at the more dilute slide front and tail, rather than at the bulk scale seen in the bulk of the slide mass. A more thorough analysis for the particle drag force is conducted in Section 5.4.2, suggesting that this initial estimate may be an underestimate.

A significant fluctuating component is introduced to the drag force due to the particle angularity causing variation in the flow-normal cross-sectional area over time. Loth (2007) and Bagheri and Bonadonna (2016) note that the non-sphericity of the particles may increase the drag coefficient drastically, investigating this effect over a wide variety of particle shapes. Figure 18 demonstrates the effect of particle orientation on drag coefficient, comparing a sphere to an ellipsoid (Bagheri and Bonadonna, 2016).

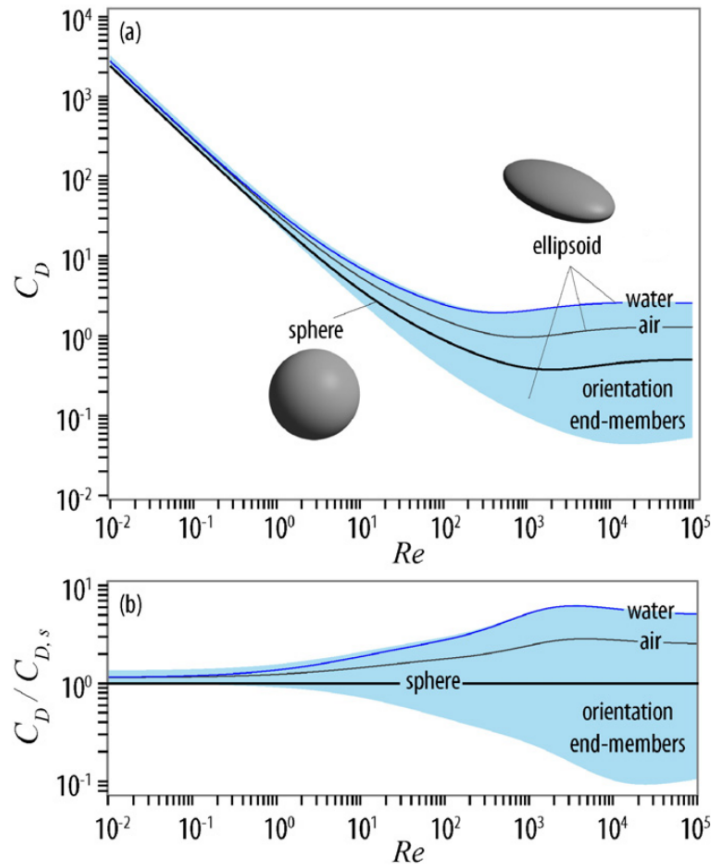


Figure 18 Impact of orientation on the drag coefficient of an ellipsoidal particle compared to an equivalent sphere, with average values for free fall in air and water also displayed. (a) Ellipsoid drag coefficient C_D at different values of Re . (b) Ellipsoid drag coefficient normalised against the sphere drag coefficient $C_{D,s}$ (adapted from Bagheri and Bonadonna, 2016)

2. LITERATURE REVIEW

Small initial differences on the particle drag force may be amplified or diminished by Re scale effects, potentially cascading into large changes in overall slide behaviour over time. Furthermore, differences in Re between scales can correspond to differences in the relative turbulence of the air. This not only affects particles separated from the main slide mass by random collisions; it also affects the probability of this separation and the internal airflow through the bulk slide mass, possibly contributing to the cascading separation of particles throughout the course of the slide event. Looking at Fig. 16 and Fig. 17, it is also reasonable to predict that experiments performed at smaller scales (with lower maximum Re values) will have increased mean particle drag coefficients throughout the slide durations. Thus, scale effects may be seen in the laboratory experiments that may not be picked up by DEM models which neglects the interstitial fluid.

Meanwhile, N_{Sav} represents the influences of shear stresses caused by grain collisions to those associated with enduring grain contacts and Coulomb frictional sliding (Iverson, 1997). Notably, N_{Sav} is also the square of the inertial number I and is proportional to the square of Fr , since the enduring grain contacts are mostly dominated by gravity. Savage and Hutter (1989) identified that slides with $N_{Sav} > 0.1$ are dominated by collisional stresses over frictional stresses. The Bagnold number N_{Bag} represents the relative influences of collisional shear stresses to viscous fluid shear stresses, making this parameter the most relevant in mixtures of grains and liquids. Iverson (1997) identifies that buoyant slide mixtures are dominated by collisional stresses over viscous fluid stresses with $N_{Bag} > 200$.

A commonly-used technique to identify scale effects is using a scale series of experiments, where dimensionless parameters (such as the Froude number) are kept constant between models of different sizes to allow for direct comparison, such as the landslide tsunamis seen in Fig. 15 (Heller et al., 2008). Thus, a scale series of experiments can be designed via a Froude scaling approach such that their geometries and kinematics produce granular slides with identical Fr values, eliminating the interplay of inertial and gravity forces as a source of scale effects. While an experiment can be designed such that a single force ratio is kept constant between scales, differences will result in other force ratios, and it is practically

impossible to keep all force ratios constant between all scales (Heller, 2011). For example, to ensure that both Fr and Re remain constant with varying λ , either the model interstitial fluid must be of different kinematic viscosity to ordinary air, or the experiments must be performed in a centrifuge exerting higher relative gravity on the slide, increasing experimental cost and complexity (Bowman et al., 2010; Bryant et al., 2015). As a result of scaling phenomena at different scales (such as producing a model of a real world phenomenon) so that the slides share the same Fr and N_{Sav} , scale effects will result due to differences in Re , Ca , Eu , and N_{Bag} .

While N_{Sav} and N_{Bag} were primarily designed for characterising simple shears of steady, uniform mixtures of monodisperse spherical particles (Savage and Hutter, 1989), they are also often used to identify limiting flow regimes for debris slides and flows (Iverson, 1997; Santivale and Bowman, 2017). This is done by idealising kinematic parameters such as shear rate and slip velocity and estimating bulk parameters such as surface velocity and flow thickness from observations. In these cases, the characteristic grain diameter is usually taken to be the mean diameter of the flow. While no excess pore pressure is often assumed due to the difficulty of field measurement, Berti et al. (1999) and McArdell et al. (2007) provide accurate measurements of basal normal and shear stresses and pore pressure in debris flows. However, in many circumstances, a wide particle size distribution may be present, with smaller particles being more heavily influenced by contact/viscous stresses and larger particles being more heavily influenced by collisional stresses, and particles may be significantly segregated within the flow or slide as a result (Santivale and Bowman, 2017). Thus, it may be more relevant to characterise a granular slide through the evolution of N_{Sav} and N_{Bag} and the corresponding Fr and Re over time, rather than by characterising them at a single moment.

2.3.2 Strategies for mitigating scale effects

With these important dimensionless parameters being identified, mitigation strategies for reducing the impacts of scale effects on experimental models can be discussed. Heller (2011) provides a thorough discussion of different strategies used in

2. LITERATURE REVIEW

a wide range of experimental contexts, focusing mainly on fluid mechanics experiments, with many principles that can be transferred to the phenomena of granular slides and flows. The ideal strategy for avoiding significant scale effects in a Froude scaling model would be to set limiting criteria on how much the dimensionless force and stress ratios described in Section 2.3.1 can vary from natural values. However, in many cases, these force and stress ratios are not considered and empirical rules are used instead to produce these limiting criteria, restricting experiments to fixed scale ratios or parameter values that have been identified from repeated testing, rather than from physically sound theoretical analysis. For instance, a fluids experiment may be limited to a minimum or maximum water depth, to satisfy an empirical rule within which force ratios lie within acceptable values.

Other than avoidance via limiting criteria, other strategies exist to modify the behaviour or composition of experiments to reduce scale effects. Fluid replacement is often used to circumvent scale effects caused by the different relative influence of kinematic viscosity between scales. For example, air could be used to replace water in experiments where the effects of gravity, surface tension, and cavitation are less important than inertial and viscosity dependent effects (Heller, 2011). Alternatively, mixtures of fluids can be created that have more suitable properties, such as mixing water with alcohol to reduce surface tension effects. Similarly, particle or boundary materials can be replaced to better reflect properties such as stiffness and deformability in scaled models. Heller (2011) attributes the failure of the Sines breakwater in Portugal in 1978/9 (Baird et al., 1980) in part due to the lack of scaling of material properties when conducting model tests of the breakwater. Figure 19 provides an example where fluid replacement could be used appropriately, where similar particle movement can be seen between tailwater ripples in a bridge pier scour test using water and ripples on dunes caused by wind.

If scale effects cannot be avoided entirely via these methods, then a model can compensate for scale effects by using a slightly altered model geometry (i.e. reducing geometric similarity) to produce better kinematic and dynamic similarity between the model and its corresponding natural events. For example, Heller (2011) notes that beach shoreline processes are typically modelled at 1:100 verti-

cal scale and 1:300 horizontal scale, as a compromise between reasonable size and cost and moderate scale effects that may not necessarily be negligible. Likewise, channel roughness can be altered in ways that violate Froude scaling to reduce scale effects caused by surface tension and fluid viscosity in fluid flows.

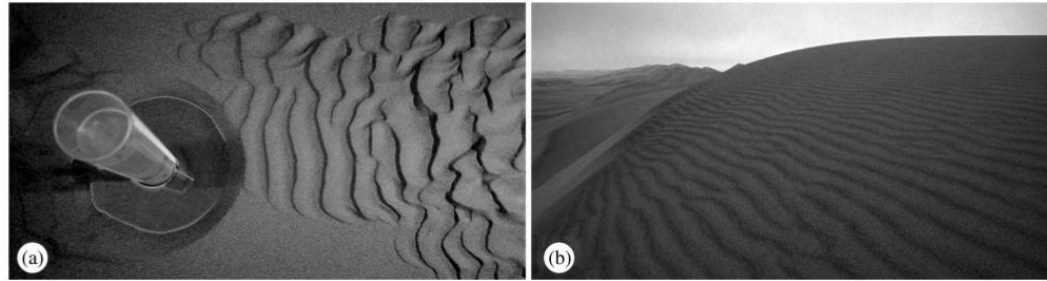


Figure 19 Similar sand morphologies caused by (a) water ripples in a bridge pier scour model and (b) air ripples on a dune in Swakopmund, Namibia (Heller, 2011)

Alternatively, the flow depth can be increased to better satisfy Reynolds similarity at the cost of Froude similarity, which may be useful in some models of fluid phenomena. Sediment transport and the motion of granular material suspended in fluid are also non-trivial issues, depending not only on the Froude number but also on the grain Reynolds number (Ettema et al., 2006) and the bed and particle properties (Kamphuis, 1974; Oumeraci, 1984). Ranieri (2007) and Heller (2011) specify that a length-distorted model can be a good approach for balancing the relative influence of these factors on the sediment entrainment and motion behaviour, while Zarn (1992) discusses modification of the grain size distribution as a correction procedure. However, in the granular slides conducted in this study, the effects of the slide and chute geometry have a greater influence than these viscosity related effects, limiting the usefulness of this compensation approach.

Finally, in cases where these approaches are not applicable but scale models must still be smaller than limiting criteria would allow due to economic reasons, correction factors can be applied to key parameters if enough quantitative information is present on influential scale effects (Ettema et al., 2006; Ranieri, 2007).

2.3.3 Hypermobility: size versus scale effects

The concept of "hypermobility" has been given significant focus in the last few decades, being a phenomenon where avalanches, landslides, and debris flows of volumes over 10^6 m show high dependency between the volume and mobility of the granular slide. As these events exceed this volume, their slide velocities and runout distances see a respective increase (Parez and Aharonov, 2015; Johnson et al., 2016). Natural avalanches, landslides, and debris slides can involve up to 10^{12} m³ of material and can reach velocities of up to 100 m/s. Scheidegger (1973) defines the effective friction coefficient μ_{eff} of a granular slide using the position of the centre of mass, with

$$\mu_{eff} = \frac{H_{COM}}{L_{COM}}. \quad (15)$$

H_{COM} and L_{COM} are the changes in vertical height and horizontal distance of the centre of mass throughout the slide event. The effective friction coefficient of granular slides experiencing hypermobility can be as low as 0.03, proceeding over topographic slopes as shallow as 1° (Pudasaini and Miller, 2013) as a result.

Dade and Huppert (1998) evaluated the relationship between the ratio of H_{COM} and L_{COM} (the relative runout) and the slide volume, as well as the relationship between the inundated area A and the estimated potential energy of the slide material before transport. A key finding of Dade and Huppert (1998) was that the runout of large slide events is constrained by an approximately constant shear stress that resists deformation and transport of the slide material. Legros (2002) produced one of the most extensive sources on landslide runout, including data from over 200 terrestrial and Martian landslides and conducting power-law fits across this data set evaluating the relationships between horizontal runout, vertical fall height, inundated area, and slide volume. Figure 20 compares the runout length and volume across a range of terrestrial and extra-terrestrial granular slide events, highlighting the lack of influence of atmospheric dynamics on this phenomenon.

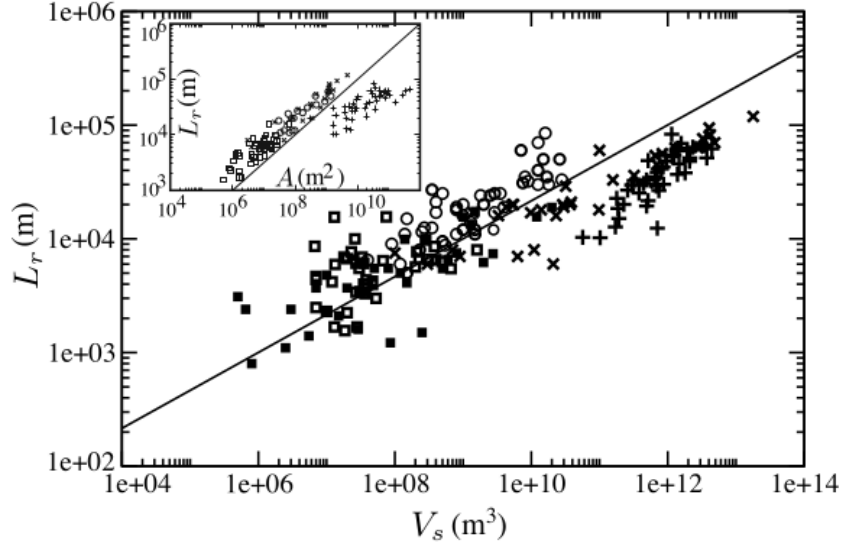


Figure 20 Comparison of runout length L_r against slide volume V_s (shapes are terrestrial data, crosses are Martian data). Insert: Comparison of runout length L_r and inundated area A (adapted from Staron and Lajeunesse, 2009)

In addition to the comparisons of L_r , V_s , and A seen in Fig. 20, Staron and Lajeunesse (2009) also conducted 2D numerical simulations and compared them to the natural data, with simulated values of L_r and $V_s^{1/D}$ (D being the number of dimensions present) correlating somewhat well, as shown in Fig. 21.

The hypermobility phenomenon has often been attributed to secondary factors such as fluidisation via acoustics (Collins and Melosh, 2003) or airflow (Savage and Hutter, 1989), melt-induced self-lubrication (Erismann, 1986), fragmentation (Davies et al., 1999; Lucas et al., 2014), shear-dependent frictional behaviour (Liu et al., 2016), and others. Bowman and Take (2015) discuss the influence of dynamic fragmentation on the long runout of chalk cliff collapses, noting that fragmentation is typically greatest at the distal ends of rock avalanche deposits, contrasting with greater fragmentation at the rear end of chalk cliff collapse deposits. This shows that the influence of dynamic fragmentation on granular slides and similar events depends significantly on the release geometry and material, and suggests that its influence on hypermobility is complex.

Notably, Perez and Aharonov (2015) dispute this and identify that the increase in runout distance is mainly an inherent property of the physics within the granular slide, particularly the gradual mass-spreading from the release condition. The correlation L_r and $V_s^{1/D}$ in Staron and Lajeunesse (2009), combined with a poorer match once L_r is normalised with the fall height (resulting in the slide mobility), also suggests spreading is important in mobilising these large natural slides. However, Kokelaar et al. (2017) note that large-scale granular slides seen at many different positions on the Moon do not provide evidence of scale effects when compared to small-scale experiments, indicating that atmospheric effects could indeed have a significant influence on scale effects (e.g. via the Reynolds number).

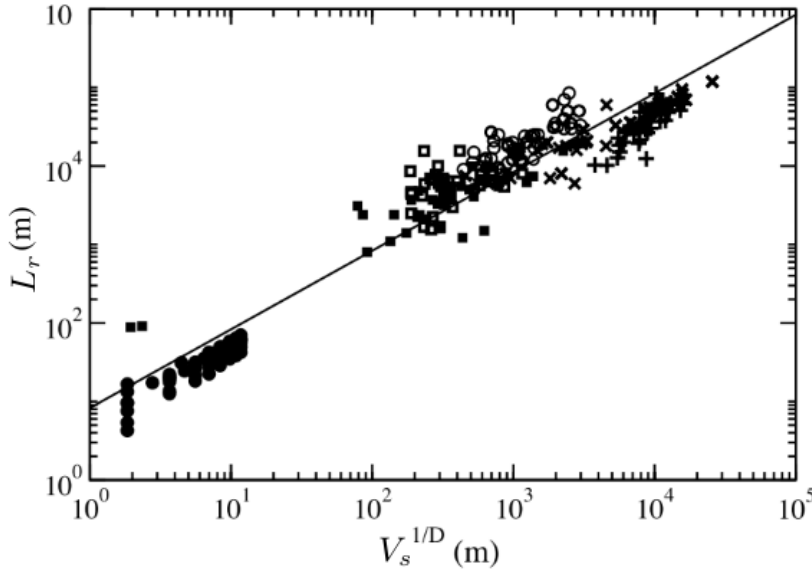


Figure 21 Comparison of runout length L_r against non-dimensionalised slide volume $V_s^{1/D}$ (shapes are terrestrial data, crosses are Martian data, filled circles are simulation data) (adapted from Staron and Lajeunesse, 2009)

Johnson et al. (2016) observed folding behaviour with the basal and top layers of granular slides due to basal friction, ruling out dispersive basal particle flow as a cause for this phenomenon of increasing runout distance with slide volume. Johnson et al. (2016) conclude that short wavelength waves both within the granular material and between the slide and basal surface are primarily responsible for the increase in runout distance with slide volume. Pudasaini and Hutter (2010)

state that a potential explanation for this hypermobility effect is strong shearing in the particle layer immediately above the slide surface, causing enhanced collisions between particles and thus increasing mean particle distance and reducing the effective friction angle of the particles. This leads to the classification of an effective friction angle that is lower than the static external friction angle δ of the particles (Jaeger and Nagel, 1996).

However, while this hypermobility phenomenon is well documented, there has still been no definitive consensus on a mechanism for predicted extreme runout distances as the fundamental physical processes at play are still poorly understood. It should be noted that hypermobility may not necessarily be a scale effect, but may simply prove to be a model effect if it cannot be quantified through the use of force and stress ratios. Identifying the main physical cause of hypermobility is thus highly important for developing the understanding of large-scale granular slides.

Pudasaini and Miller (2013) define hypermobility as the reciprocal to an effective friction coefficient μ_{eff} that is derived as a function of the volumetric, mechanical, and topographical characteristics of a flow or slide. In this coefficient, the dominant term is the degree of fluidisation involved in the flow, with hypermobility being less prevalent in environments with less easily fluidised conditions (such as extraterrestrial slides) and more prevalent in easily fluidised environments (particularly submarine slides). Pudasaini and Miller (2013) state that a realistic rheological model should directly include the volumetric, physical, and topographical effects at play in a slide, and crucially determine the mass-dependence of the flow rheology. The specifics of their model are summarised by the equation

$$\mu_{eff} = \frac{\mu(1 - \Lambda)VTh}{S^{n-1}V_s^{1-\frac{1}{n}}} \quad (16)$$

where μ is the friction coefficient and Λ is the ratio of basal pore fluid pressure and total normal stress. V is a volumetric parameter, while T is the corresponding topographic parameter and h is the mean flow depth. S represents the volume-

area slope, V_s represents the slide volume, and n is a tuneable parameter greater than 1. This model can fit to the volume and mobility of extraterrestrial, volcanic, non-volcanic, and submarine slide events with appropriately selected parameters (Pudasaini and Miller, 2013). However, the significant spread in the natural slide data around the results of the model, combined with the empirical nature of several of these fitting parameters, show considerable scope for improvement of the physical understanding of granular slides and the implementation of this physical understanding in analytical models.

The experiments conducted in the present study may help to identify why this hypermobility behaviour suddenly manifests in larger slides. They may further identify whether this hypermobility is caused by subtle scale effects that can be seen in much smaller laboratory slide geometries. Alternatively, they may identify whether hypermobility is impossible to capture at laboratory scale due to unavoidable model effects that are necessary for practical downscaling.

2.4 Capturing and modelling granular slides

As natural avalanches and landslides can be of extremely large scales and can affect vast areas (Xu et al., 2014), physical modelling at these larger scales can be very difficult but not impossible (McElwaine and Nishimura, 2001; Iverson et al., 2010). Johnson et al. (2012) were motivated to use a 95 m long debris flume in their investigation of levee formation due to the over-representation of grain inertia, fluid viscosity, and fluid yield strength and the under-representation of pore fluid pressure in small-scale experiments. While Coulomb friction rheology is effective for modelling small slide volumes (Iverson, 1997; Jop et al., 2006), modelling large natural mass flows with this approach is inhibited as appropriate values for the effective stress and friction coefficient are unknown.

The implications of scale effects being incorrectly captured by smaller models are clear, with designs based on models that do not properly account for scale effects leading to potentially dangerous outcomes. For instance, a settlement could

be built close to a possible slide zone where previously conducted experiments indicated a certain runout distance, only to find that the real physical event could exceed this runout distance and end up engulfing the settlement. Additionally, the identification and mitigation of scale effects in industrial contexts can result in more efficient systems (Grima and Wypych, 2011), higher profits, and improved safety as scale effects can be taken into account during design and upscaling. This section will summarise some of the modelling and data capture approaches taken for modelling granular slides, relating to both large-scale and small-scale experimental set-ups, as well as corresponding analytical and numerical approaches.

2.4.1 Experimental measurement techniques and applications

With a developed understanding of some of the important parameters that govern granular slide and flow behaviour, this section will detail some of the experimental approaches taken to measuring these parameters and key characteristics such as slide velocity, shape, and stress distribution. In slides consisting of natural debris, it is easiest to directly observe the flow margins, such as the top and basal surface and the channel sides, leaving the internal flow dynamics unmeasured. Schaefer et al. (2010) used optical velocity sensors mounted to the ramp surface to extract basal slide velocities via infrared reflectivity, while they used a force plate to measure shear and normal forces exerted on the channel base, as well as an ultrasonic flow height sensor to measure the flow depth. Recently, non-invasive techniques such as X-ray computed tomography and magnetic resonance imaging have been used to view the interior of concentrated, opaque granular flows in chute slides, hoppers, rotating drum flows, and many other geometries (Santivale and Bowman, 2012). These two techniques are often too complex and expensive for routine use, but many other cheaper methods have also been developed.

Particle image velocimetry (PIV) and particle tracking velocimetry (PTV) are techniques that track the flow motion and extract an array of vectors that describes the flow velocity across images captured in rapid succession. Granular slides generally provide sufficient surface texture for these methods without the use of tracer

2. LITERATURE REVIEW

particles. High levels of illumination must be provided for both methods, either generally or focused in a specific location, to ensure that the relative motion of particles is clear even at the very low exposures required for image capture. PIV tracks the displacement of particles within an array of many small interrogation windows, with the displacement of particles in each interrogation window between two consecutive images being extracted by cross-correlation (Gollin et al., 2017). Velocity vectors are then produced for each interrogation window by dividing each displacement calculated by the time-step between the two images (e.g. the frame rate of a recording camera). This process is fairly robust to noise and can accurately resolve velocities for materials with a varied surface texture such as a granular slide, where individual particles can drop in and out of view in the image. Figure 22 shows example PIV vector fields recorded (a) at the surface and (b) at the base, produced by using cameras on either side of a transparent Plexiglas chute (Pudasaini et al., 2005).

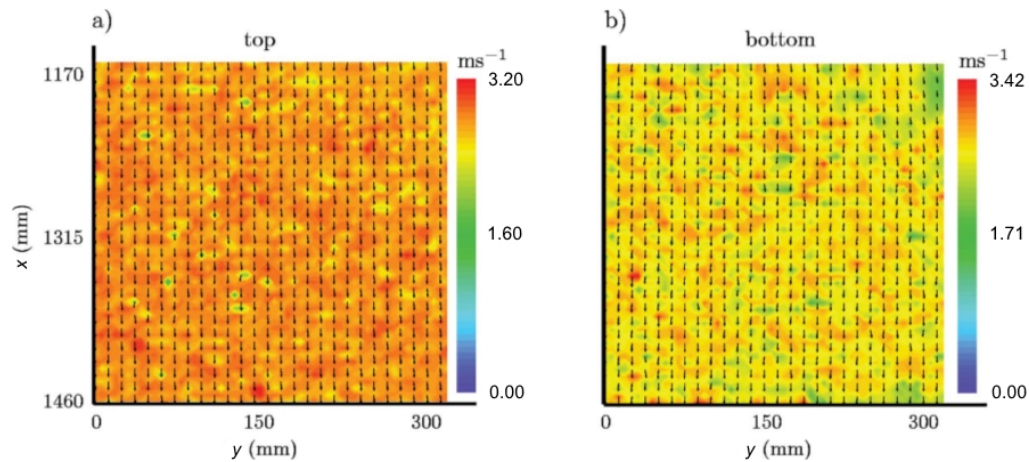


Figure 22 Velocity distribution (a) at the free surface and (b) at the bottom of a chute slide (adapted from Pudasaini et al., 2005)

On the other hand, PTV attempts to track the motion of individual particles, detecting particle centroids in consecutive images by analysing the image brightness pattern and detecting particle edges. This makes PTV more suitable for low density flows where these edges can be identified easily (Gollin et al., 2017). While

both PIV and PTV are powerful, they can also be subject to significant errors without keen optimisation of the most crucial methodological parameters. In PIV, larger interrogation windows typically produce more accurate vectors and experience reduced noise at the cost of detailed resolution. Importantly, while PIV only measures out-of-plane velocity components, some in-plane velocity gradients may be present in granular slides, especially those with rough boundary conditions, and these in-plane gradients can cause a loss of accuracy. Meanwhile, PTV suffers from two major error sources; errors in particle position detection and errors arising from the assumption of linear particle movement between the image time-step. Particle position uncertainty can be reduced by ensuring particle image diameters exceed at least 3 pixels (Gollin et al., 2017). However, both PIV and PTV can occasionally produce spurious outlier vectors even with proper tuning of parameters.

Another approach using optical methods is refractive index matching (RIM), using transparent materials for both solid and fluid slide phases so that internal slide dynamics can be identified and measured. The refractive index of these materials is matched such that the mixture as a whole is transparent without significant refractive distortions. Santivale and Bowman (2012) conducted experiments using this technique in combination with planar laser induced fluorescence to allow the measurement of grain re-arrangement within an interstitial fluid and the overall evolution of granular flows in motion. The effectiveness of RIM can be reduced by factors such as entrapped air, temperature effects on the refractive index of materials, and imperfections and impurities within the solid phases, and Santivale and Bowman (2012) saw reduced effectiveness in systems with finer particles due to the increase in scattered light at particle-fluid interfaces.

Measuring the physical dimensions of the granular slide, both during the slide event and in its deposited state, is also important. Stereophotogrammetry is a useful technique, where the 3D co-ordinates of points on an object can be extracted through the analysis of images taken of the object from multiple different angles and positions (Luhmann et al., 2006). Common points are identified on each image, and lines of sight can be constructed between the cameras and these common points. With enough common points being detected and a set of reference points

2. LITERATURE REVIEW

with known coordinates, the precise shape, location, and dimensions of the object under investigation can be determined. While this technique has been applied only to the slide deposits herein, this technique can also be applied to slides in motion using multiple high-speed cameras aimed at the flow channel at different angles. Valentino et al. (2008) used photogrammetry to track the slide shape as it developed by adding a large number of tracer particles with known initial coordinates to the top surface.

Johnson et al. (2012) measured the grain-size distribution and general granulometry of large-scale chute deposits by inserting thin-walled steel tubes at various points across the deposit length and extracting material cores. They used this technique to identify differences in formulation between the central strip of the deposit and levees that formed midway through the overall deposition process. As seen in Fig. 23, they found increased concentration of coarse particles in the levees and more fine particles in the central strip.

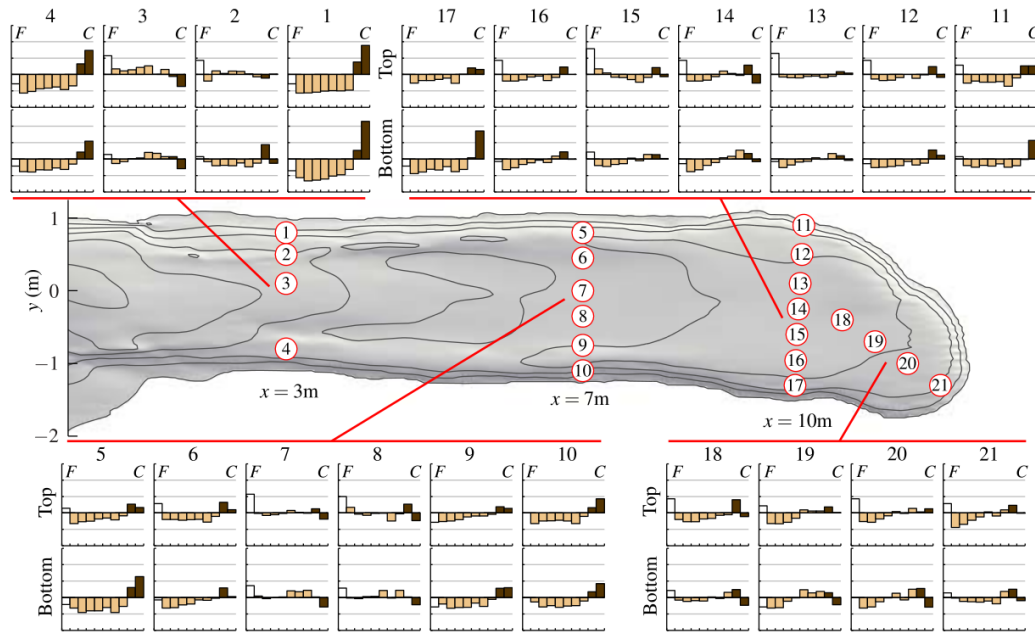


Figure 23 Deposit granulometry obtained from core samples, showing the relative abundance of fine (F) and coarse (C) materials, with contours showing deposit thickness at 5 cm spacing (adapted from Johnson et al., 2012)

In one experiment, white tracer pebbles were attached to the chute base and entrained into the flow to show evidence of segregation and recirculation mechanisms. The intact deposit was marked with pasted contour lines obtained via laser levelling. Lateral layers of particles were then removed via trowels, with the position of tracer pebbles also being measured as they were revealed.

2.4.2 Savage-Hutter continuum model

It is valuable to produce analytical models of granular slides and flows based on theoretical and physically-based principles, not only for the purpose of predicting slide events without requiring complex and expensive laboratory experiments or numerical simulations, but also for developing understanding of how complex processes can be effectively represented by simple principles. Such analytical models provide a foundation upon which numerical simulations can be verified and validated according to physical principles; once a numerical simulation is seen to represent bulk slide behaviour well, the features unique to the numerical scheme can be analysed with more confidence of their physicality.

Savage and Hutter (1989) formulated what many consider to be the first continuum mechanical theory of granular slide motion, describing the geometry and velocity distribution of a finite mass of granular particles as it progresses down an inclined surface. This model became standard for granular slide mechanics due to its basis in physical reasoning making its form simple and highly intuitive. Additionally, it can be implemented practically to even large scale phenomena such as avalanches, landslides, debris flows and pyroclastic flows. However, in its simplest form, the Savage-Hutter (SH) model is scale invariant, meaning it will not capture any scale effects that may manifest in physical experiments of different scales. The following assumptions are used to simplify the model while ensuring sufficient realism (Pudasaini and Hutter, 2010).

- Volume is conserved throughout the slide.
- Granular slide is *dry, cohesionless, isothermal* (or thermal effects can be

2. LITERATURE REVIEW

neglected) and obeys *Mohr-Coulomb* frictional criteria within the mass and along the slide surface.

- Shear stresses lateral from the main flow can be neglected.
- Typical slide thickness is small in comparison to slide length along surface.
- Sliding and shearing velocities are combined into a single sliding law, allowing for depth-averaged approaches.
- Leading equations are integrated through the slide depth.
- Scaling analysis identifies physically significant terms and isolates those that can be neglected.

The SH model is represented by the following set of differential equations.

$$\frac{\partial h}{\partial t} + \frac{\partial(hu)}{\partial x} = 0, \quad (17)$$

$$\begin{aligned} \frac{\partial}{\partial t}(hu) + \frac{\partial}{\partial x}(hu^2) = g\{(\sin(\theta) - \text{sign}(u)\tan(\delta)\cos(\theta))h \\ - \frac{1}{2} \frac{\partial}{\partial x}(K_{act/pas}h^2(x, t))\cos(\theta)\}. \end{aligned} \quad (18)$$

h represents the slide depth, u is the mean slide velocity at a certain longitudinal point x in the flow direction on the slide surface, g is the gravity acceleration and t is the time. Eq. (17) represents conservation of mass, while Eq. (18) represents conservation of momentum and force balancing. The term $(\sin(\theta))h$ represents the driving force of gravity acting on the slide, with the term $(-\text{sign}(u)\tan(\delta)\cos(\theta))h$ representing the basal friction force and the term $-\frac{1}{2} \frac{\partial}{\partial x}(K_{act/pas}h^2(x, t))\cos(\theta)$ representing the variation of longitudinal pressure along the slide. $K_{act/pas}$ is the earth pressure coefficient for whichever of the active (act) or passive (pas) modes is relevant. This last term effectively accelerates the front of the slide in comparison

to the tail, representing physical behaviour (Pudasaini and Hutter, 2010; Schaefer et al., 2010). The active and passive earth pressure coefficients can then be calculated using the following expression, which relates the internal ϕ and external δ friction angles of the material.

$$K_{act/pas} = 2\sec^2\phi\{1 \mp (1 - \cos^2(\phi)\sec^2(\delta))^{1/2}\} - 1 \quad (19)$$

Several generalisations of this model exist: Hutter and Koch (1991) extended the model to an exponential curve while Hutter and Greve (1993) looked at a 2D confined chute surface with both concave and convex regions. This was achieved by transforming the coordinate system into a curvilinear set, with the x coordinate following the ramp surface and the z coordinate being projected perpendicularly above it. Hutter et al. (1993) then looked at 2D spreading across a flat unconfined chute, introducing the new y coordinate to the SH model, while Greve et al. (1994) extended this theory to an unconfined width-uniform curved chute with lateral spreading.

Gray et al. (1999) extended this further to consider a chute with additional curvature along its width in the top section as shown in Fig. 24. This results in a third term being added to Eq. (17) to represent cross-slope slide motion and in Eq. (18) being split into two different equations to represent each horizontal component of the momentum balance. The earth pressure coefficient seen in Eq. (18) is still used to represent the downslope earth pressure, and the resulting value of $K_{x,act/pas}$ is used to calculate the cross-slope earth pressure coefficient $K_{y,act/pas}$.

When the SH equations in this case are smoothed and non-dimensionalised, they bear significant resemblance to the shallow water equations used in fluid mechanics. However, the main difference between these two models is that the SH model is based on Mohr-Coulomb frictional criteria while the shallow water equations apply to ideal and Newtonian fluids. Additionally, the non-dimensional granular slide length-, time-, and velocity-scales depend on the slide length L_s ,

as opposed to the corresponding shallow water scaling that depends on the water depth. As erosion and deposition can significantly influence granular slide dynamics in real scenarios outside of this model, volume-production terms can be added to the SH model, along with changes to the basal boundary conditions, to improve the model's applicability in these cases (Pudasaini and Hutter, 2010). Another example of an analytical model that addresses the lateral spreading of unconfined slides can be seen in Denlinger and Iverson (2004).

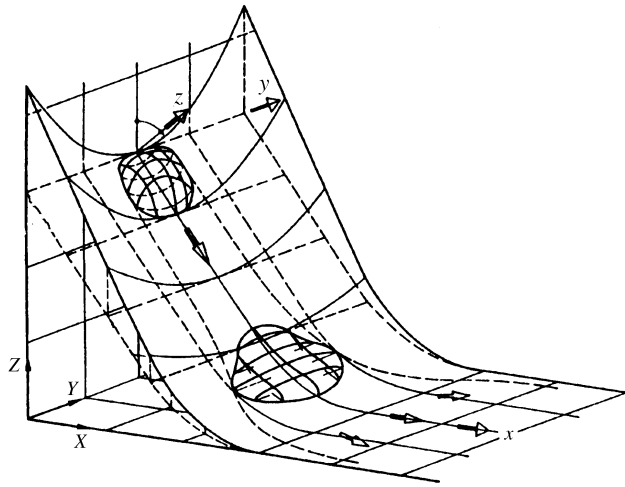


Figure 24 3D unconfined chute geometry and coordinates (Gray et al., 1999)

2.4.3 Numerical modelling techniques and applications

As there are many different approaches to producing a theoretical or analytical model for granular flows and slides, and to experimentally measuring these phenomena, there are also many different numerical techniques that can be used, such as discrete element modelling (DEM) (Zhu et al., 2008), depth-averaged methods (Baker et al., 2016a), and smoothed particle hydrodynamics (SPH) (Nguyen et al., 2017). This study will focus on discrete particle modelling as continuum based methods (such as the Savage-Hutter model (1989) and similar variants) do not directly model the granularity of a slide. In particular, DEM provides a better

representation of phenomena based on particle shape, size, and relative movement to other particles, such as particle segregation, contact force transmission, dilute surface flow regimes, and jamming. A continuum approach approximates a granular slide to a defined volume of infinitely small particles, which may not capture the grain-scale interactions that could produce scale effects, either through their interactions with each other or the atmosphere.

Meanwhile, SPH was originally invented to model astrophysical phenomena (Gingold and Monaghan, 1977) and subsequently adapted for use in fluid mechanics (Colagrossi and Landrini, 2003), solid mechanics (Rabczuk and Eibl, 2003), and geomechanics (Bui et al., 2011) contexts. The basic formulation must be significantly modified with artificial and non-physically-based parameters to model granular slides and flows to a degree of accuracy (Nguyen et al., 2017). Thus, it is unsuitable for a study that attempts to isolate the behaviour of micro-scale particle interactions and behaviour as a potential cause of scale effects. DEM also allows extraction of micro-scale data such as individual particle velocities, precisely-mapped travel paths, and packing densities that can be difficult to measure experimentally, allowing for deeper quantitative understanding of how the aforementioned phenomena inform the bulk behaviour of the granular slide. This data can then be averaged systematically to extract other important macro-scale data such as bulk slide density, velocity, and stress, allowing comparisons to be made with continuum based models (Zhu et al., 2008) and experiments that manage to measure these bulk slide parameters.

Discrete element modelling

Discrete particle simulation has become an increasingly common and practical method for analysing the behaviour of granular flows and slides in recent times, as computer processing has become more powerful. The original invention of DEM in the context of granular bodies can be attributed to Cundall and Strack (1979), using Newton's equation of motion to consider the contact and non-contact forces acting on each particle, which can move rotationally and translationally. One of

this method's main advantages over experimental testing is that particle parameters such as coefficient of restitution and friction angle can be varied directly, which is extremely difficult to achieve practically. Zhang et al. (2001) provide a good example of this, identifying the effect of changing many physical parameters on a resulting gravity-deposited packing of spheres. Additionally, parameters such as inter-particle forces, rotational velocities and stresses can be recorded directly and accurately, which is not feasible with current experimental equipment (Zhu et al., 2008). Figure 25 provides an example of this, showing force contact networks present in granular piles formed on curved surfaces (Zhou et al., 2003).

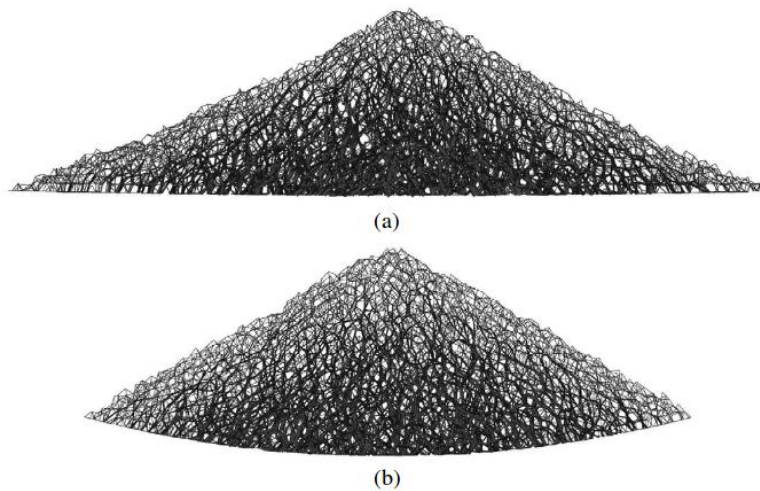


Figure 25 Force networks in sandpiles constructed with different base deflections of (a) $2000d$ and (b) $125d$ (Zhou et al., 2003)

The extra information that can be extracted from DEM can thus provide new insight into mechanisms that may subtly influence granular slides and flows. Of course, as the particles modelled are only crude approximations of real particles, caution should be maintained to avoid interpreting model effects as real physical behaviour. Furthermore, the accuracy of these models in replicating real-world phenomena heavily depends on the effective calibration of simulation parameters. Coetzee (2017) identifies that calibration can form the bulk of the work for many DEM projects, and that the lack of a standardised, robust calibration procedure

for matching DEM to real-world situations leads to many simulations not being validated, reducing the replicability of many studies.

Of course, DEM also has some disadvantages. Most notably, while the applicability of DEM has improved significantly over the years with corresponding increases in computing power, the method remains highly resource intensive due to the large number of particles simulated. In many circumstances, the size distribution of particles has to be altered for simulation to be possible, replacing many small particles with fewer larger particles, having impacts on the dynamic behaviour of the granular slide or flow. Geophysical flows can contain trillions of particles; storing the properties of these particles would be practically impossible, not to mention calculating their movements and interactions. Additionally, geophysical flows often contain an extremely wide range of particle sizes from boulders that can be metres across to clay particles that are fractions of millimetres in diameter. Many of the contact laws used in DEMs break down when involving such size disparities, or at least require excessively small time-steps to simulate the contacts in a stable manner, rendering simulation of these size distributions impossible and requiring them to be truncated (Minh and Cheng, 2013; Thornton, 2015). However, the experiments conducted in this study use a relatively narrow fixed size distribution at each experimental scale, and have a relatively low particle count (in the order of 10^6), diminishing these downsides of the DEM modelling approach.

Validation of DEMs

DEM simulations are usually validated by comparison to measured results from experimental tests under a variety of conditions. Zhang and Vu-Quoc (2000) show good agreement between DEM simulation and experimental chute flows of soybeans, while Hanes and Walton (2000) found similar agreement for glass spheres flowing down a bumpy incline. Silbert et al. (2003) used DEM to identify many flow regions on inclined planes, splitting stable flow into a continuous flow region governed by Bagnold scaling (Section 2.2.1), a continuous flow region with velocity profile proportional to flow depth (for higher inclination angles) and avalanching

flow where the steady state involves creep motion of the entire slide mass with intermittent free surface flow down the incline (at inclinations just above the angle of repose). Silbert et al. (2003) also found good agreement between simulated and experimental values of β in Pouliquen's previous scaling law seen in Eq. (3). While there has been much study on granular packings and flows using DEM, more work is needed to link the microscopic force networks identified by DEM to larger-scale phenomena that govern bulk flow characteristics, such as fluid flow, heat transfer, and mass transfer in porous media. The capability and efficiency of algorithms also needs to be improved so that they can be used to model large phenomena such as industrial or natural contexts directly (Zhu et al., 2008).

Choosing the correct time-step for a DEM is critical, as using a value that is too large will result in inaccurate results and violation of conservation of energy. While hypothetically systems containing a large amount of particles should conserve energy if no energy dissipation mechanisms are activated, the explicit numerical integration techniques used in the DEM can lead to slight numerical errors in grain velocity and position during each iteration. These numerical errors can be caused by the fundamental assumption adopted in DEM that solid particles maintain a constant velocity during one iteration time-step (Thornton, 2015). In contrast, in real granular systems, the forces acting on solid particles can vary continuously; thus, the larger the numerical time-step, the worse the approximation of this force distribution behaviour and the larger the resulting errors introduced to the simulation. These errors can rapidly compound over time, resulting in vastly different results over the course of millions of iterations, which is typical to many simulations of granular systems.

Of course, using a time-step that is too small will result in an increased time requirement for completing the simulation, with no significant difference in results compared to a simulation with a slightly larger time-step. The choice of time-step t_s is thus highly important, and how it varies at different scales as it manifests itself is a potential model effect. Burns and Hanley (2017) and Otsubo et al. (2017) provide in-depth approaches for selecting the appropriate time-step for a granular system based on its parameters.

A DEM time-step should be sufficiently small that a disturbance wave can only propagate from one particle to its immediate contacting neighbours. For the Hertzian spring model used in the DEM in this study, this critical time-step cannot be calculated directly. Miller and Pursey (1955) identifies that Rayleigh waves account for approximately 67% of the energy radiated by the particle contact, while distortional and dilational waves account for roughly 26% and 7% of the total energy respectively. As the difference in speed between Rayleigh and distortional waves is very small and the energy transferred by the dilational waves is relatively negligible, the energy transfer can be safely approximated to be entirely due to Rayleigh waves. Additionally, the average arrival time of a Rayleigh wave to any contact is the same regardless of the contact location. This results in the following expression for the critical simulation time-step Δt_c .

$$\Delta t_c = \frac{\pi R_{\min}}{v_R} = \frac{\pi R_{\min}}{\Gamma} \sqrt{\frac{\rho}{G}} = \frac{\pi R_{\min}}{0.1631\nu + 0.8766} \sqrt{\frac{2\rho(1-\nu)}{E}}. \quad (20)$$

R_{\min} is the minimum particle diameter in the simulation. v_R can be calculated using the particle density ρ_s , the particle shear modulus G , and the value Γ that is a function of the Poisson ratio ν of the material. Γ can be obtained exactly by solving a more complex quartic equation (Thornton, 2015), but the linear approximation used in Eq. (20) is sufficiently accurate for the purposes of this study.

Simulating particle shape

The particle shape is another important DEM parameter that is crucial to accurately modelling real physical systems. Spherical particles are typically used due to the simplicity of modelling their contacts and the resultant low performance requirements allowing larger particle counts to be simulated. However, this approach fails to capture important mechanisms such as interlocking, shear band formation, and eccentric contacts, leading to imperfect representation of bulk slide frictional and collisional behaviour (Section 2.2.4).

2. LITERATURE REVIEW

The multi-sphere "clump" approach is a popular method of simulating rough particles (Matsushima and Saomoto, 1978; Mollanouri Shamsi and Mirghasemi, 2012; Wu et al., 2016), replicating angular surfaces by assembling and overlapping multiple spheres into a non-spherical clump. Zheng and Hryciw (2017) describes an approach of approximating images of real-world particles into precisely tuned 2D multi-circle clumps, fully matching parameters such as roundness and sphericity. However, this increases the resource requirements of the DEM drastically due to both increasing the number of simulated sub-particles and by decreasing the size of the required time-step. Figure 26 provides an example of this; corn particles are approximated with a range of clump sphere counts, with increased sub-particle counts providing a better overall match in shape to the laboratory measurements of the corn grains.

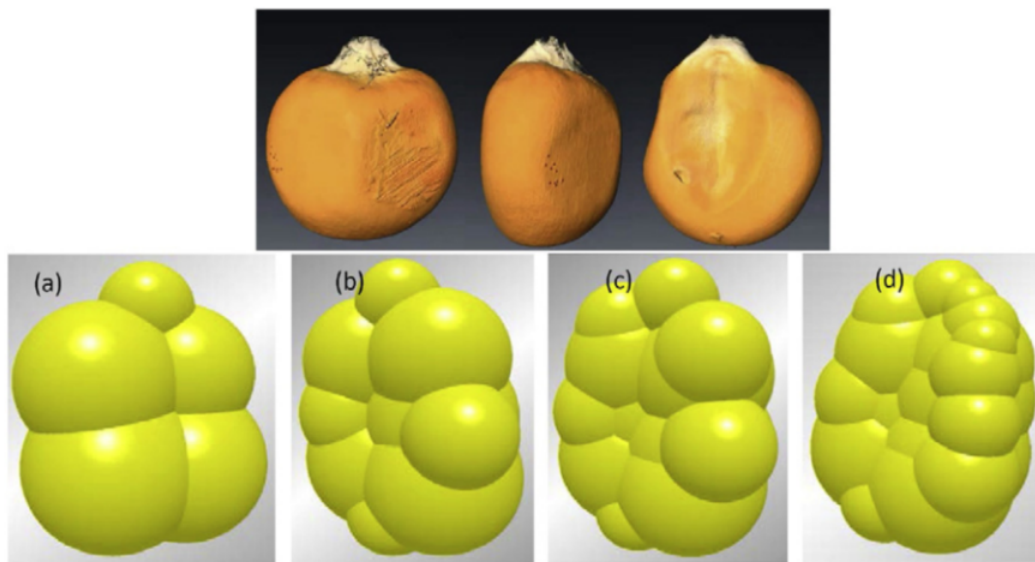


Figure 26 3D reconstruction of a corn seed (top) and clump representations using (a) five, (b) ten, (c) fifteen, and (d) twenty spheres (adapted from Pasha et al., 2016)

The multi-sphere technique is powerful, allowing almost any object or particle to be represented in a DEM (Jerier et al., 2010), including bodies that can fracture into many smaller sub-bodies, reflecting real-world rock avalanches, debris avalanches and flows, and other complex phenomena through the use of break-

able bonds between sub-particles (Zheng et al., 2015; Zhao et al., 2017; Goel et al., 2018). However, Song et al. (2006) found that the multi-sphere model failed to correctly model the magnitude of angular velocity in particle collisions. They approximated the shape of a tablet with a range of sphere counts and found that, in all cases, the simulated angular velocity was much higher than experimentally measured. They also found that the magnitude of the error increased as more spheres were added to the model, showing a trade-off between resolution of surface detail and modelling of mass and inertia properties. This makes sense, as overlapping particles necessitate a reduced sub-particle density to match the density of the "real" particle counterpart, resulting in an unavoidable difference in inertial behaviour. Figure 27 shows an example of a coal particle simulated as an agglomerate of thousands of spheres, showing different fracture behaviour at different impacts velocities.

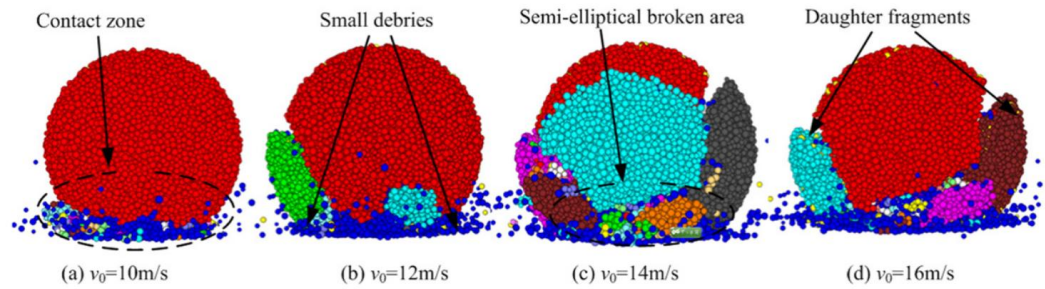


Figure 27 Front view of a spherical agglomerate breaking in different modes at different impact velocities (Zheng et al., 2015)

In contrast, a multi-sphere clump without overlapping particles is likely to have an unphysical surface unless extremely high particle counts are used. Kruggel-Emden et al. (2008) showed similar concerns, simulating the collisions of a spherical clump approximated by increasing numbers of sub-spheres. In particular, they found that the angular velocity of the particle depended significantly on the orientation of the clump, limiting the applicability of the multi-sphere approach for modelling flat contact surfaces. It remains unclear whether these differences in individual particle behaviour translate to differences in bulk slide behaviour. Markauskas et al. (2010)

2. LITERATURE REVIEW

seemed to find little variation in bulk behaviour of on the fineness of resolution of elliptical "rice grains" in hopper flow and pile formation.

Other computationally expensive but powerful methods of representing particle shape include ellipsoidal (Ouadfel, 1998; Campbell, 2011; Yan and Regueiro, 2018), polygonal (Walton, 1982; Mirghasemi et al., 1997; Latham and Munjiza, 2004; Wu and Cocks, 2006), and superquadric (Podlozhnyuk et al., 2017) particles, while Mollon and Zhao (2013) generated realistic 3D sand particles by revolving 2D cross-sections of real sand particles around three axes using Fourier descriptors.

As an alternative to simulating complex, rough particles, a "rolling friction" parameter can be applied to spherical grains to uniformly resist particle rotation and achieve the desired bulk slide behaviour (Wensrich and Katterfeld, 2012; Wensrich et al., 2014). The coefficient of rolling resistance μ_r is defined as the tangent of the angle at which the rolling resistance torque \mathbf{T}_r is balanced by the torque produced by gravity acting on the particle (Ai et al., 2011). Wensrich and Katterfeld (2012) define μ_r as a ratio between the mean contact eccentricity $\langle e \rangle$ of a particle contact from its centre of mass, and the rolling radius R_r of an idealised sphere with the particle volume. The value of μ_r reflects the angularity and sphericity of a particle, increasing with particles with sharper contacts. The result is a powerful, physically based model for simulating the rolling resistance of aspherical particles with a DEM consisting of spherical particles. Figure 28 shows how μ_r varies for ellipsoids with a major/minor axis ratio a/b . Figure 29 shows how μ_r varies for multi-sphere clumps with relative spacing δ_s between sub-spheres.

However, this technique also has some disadvantages. Notably, the rolling resistance torque applied to the particles always resists the direction of motion in a uniform manner, while in reality the aspherical and angular nature of rough particles causes the torque to fluctuate significantly around a mean value. Depending on the position of the particle contact, the particle centre-of-mass, and its trajectory, the torque can occasionally even act with the direction of motion, rather than against it. As a result, while the rolling-resistance coefficient can model bulk granular systems well, the individual particle dynamics are simplified compared to those of the real, angular particles. Wensrich and Katterfeld (2012) note that this

abstracted uniform resistance of motion results in approximately half the amount of rolling friction being required to model the same angle of repose of a collapsing pile as an "equivalent" amount of shape. Additionally, while this technique has been validated for many types of multi-sphere clump (Wensrich et al., 2014), it has not been validated against particles with the capability to interlock; this would require clumps of higher particle count and increased size range of clump sub-spheres.

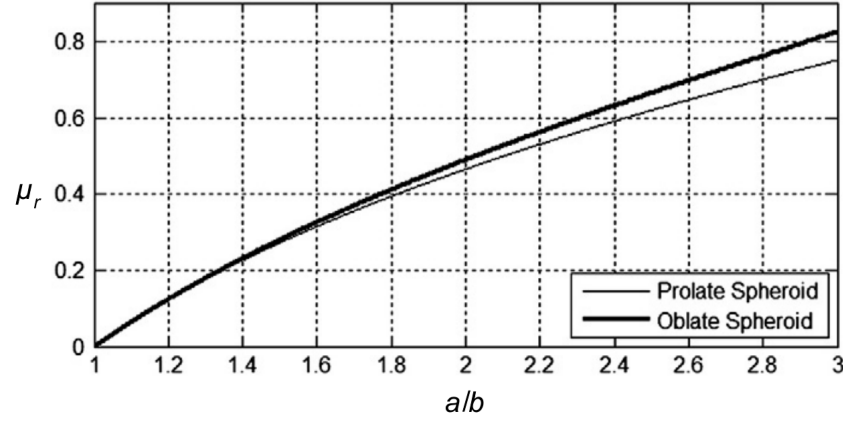


Figure 28 Comparison of rolling resistance coefficient μ_r and ellipsoid major/minor axis ratio a/b (adapted from Wensrich and Katterfeld, 2012)

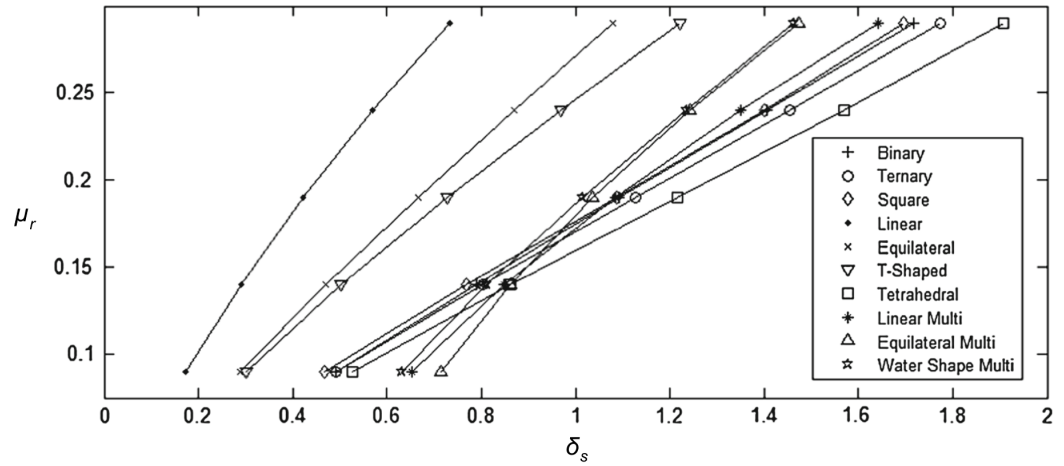


Figure 29 Comparison of rolling resistance coefficient μ_r and relative spacing of inter-clump spheres δ_s (adapted from Wensrich et al., 2014)

Coupling DEM with fluid dynamics models

Models have also been developed that directly couple the DEM approach to a separate model for the interstitial fluid, usually computational fluid dynamics (CFD), resulting in a hybrid CFD-DEM approach. This approach solves locally averaged Navier-Stokes equations for the flow of the fluid phase via continuum-based CFD, while DEM is handled using Newton's equations of motion. Meanwhile, the coupling between these two models incorporates fluid-particle interaction forces that are exchanged between the two mediums. Shan and Zhao (2014) states that CFD-DEM can be more computationally efficient and numerically convenient than other coupled models such as the lattice Boltzmann-DEM coupling method.

Shan and Zhao (2014) coupled the LIGGGHTS-DEM code with OpenFOAM (forming the CFDEM package) to handle the fluid phase, while also modelling the buoyancy force, drag force, and a virtual mass force. In their study, a granular slide was released down a chute, moving from an air body into a water body, both of which are modelled by the CFDEM package. The surface tension forces that become relevant as solid particles transition from the air phase to the water phase are also captured. The solid and fluid phases are not solved simultaneously, but iteratively, with the particle forces being solved via the DEM and interaction forces being calculated and then imposed on the fluid system via the CFD, which then updates the interaction forces and translates these back to the DEM in the subsequent time-step. Figure 30 shows the slide geometry they simulated both (a) before and (b) after the slide contacts the water reservoir.

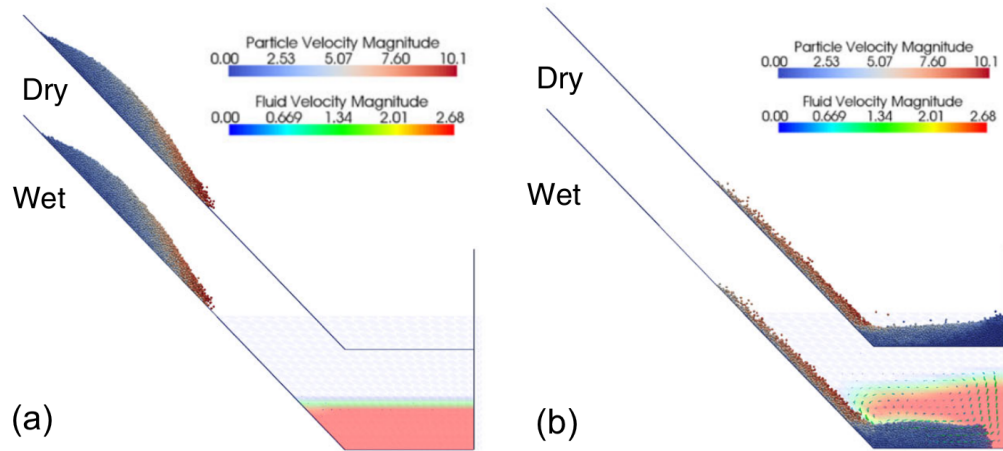


Figure 30 Side view of granular slide velocity profile into a water reservoir at (a) 1 s from release and (b) 3 s from release (adapted from Shan and Zhao, 2014)

Optimising DEM performance

Reducing the resource requirements of a DEM simulation without reducing the utility and fidelity of the simulation can be challenging. With simulations involving millions of particles, one of the most efficient methods is to use a cluster of processors, either central processing units (CPUs) or graphics processing units (GPUs) depending on the simulation nature (Tsuzuki and Aoki, 2016; Yan and Regueiro, 2018). Each processor handles the calculations required in a specific sub-domain in parallel. To co-ordinate these processors and ensure that particles can move between domains without errors, data on particles close to the domain boundaries is transferred to connecting domains. Open MultiProcessing (OpenMP) and Message Passing Interface (MPI) are popular parallelisation techniques for CPUs, while CUDA is typically used for Nvidia GPUs (Furuichi and Nishiura, 2017).

The spatial arrangement of these sub-domains is important, with the aim being to distribute particles evenly between the assigned processors for the duration of the simulation. While this is relatively easy for continuous flows and other cases such as shear cells, mixers, or hoppers where the particles fill the geometry relatively evenly, discontinuous slides will impose different loads on sub-domains during each

phase of their movement. In some cases, the domains can be arranged specifically for the geometric set-up to distribute processor load evenly (e.g. column collapses), but in some cases this will prove impossible or impractical (e.g. chute slides with obstacles or winding chutes). In these circumstances, some DEM codes allow for "dynamic" load rebalancing, where the processor domains are reassigned after a regular interval of time-steps to ensure similar particle counts throughout. Figure 31 provides an example of a simple slice-grid method, but more efficient divisions can be obtained through the use of space-filling curves (Tsuzuki and Aoki, 2016).

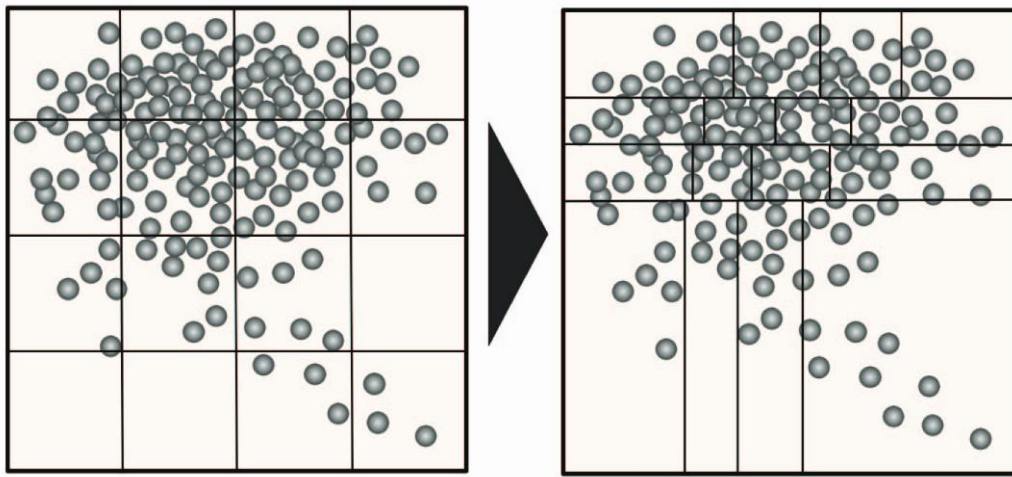


Figure 31 Outline of dynamic load balance based on two-dimensional slice-grid method (Tsuzuki and Aoki, 2016)

Another technique that can be used to improve the performance of DEM simulations, particularly those containing many particles across a relatively homogeneous domain, is the use of periodic boundary conditions. In these schemes, instead of fixed boundaries that repel and confine particles, some or all of the boundaries may loop with particles exiting one and re-entering the domain at the opposite boundary. This essentially allows a granular system to be analysed with semi-infinite motion of the same particles in one or all directions. While this is often used to save resources in triaxial tests (Huang et al., 2014), hopper flows (Cleary and Sawley, 2002), rotating cylinders (Yang et al., 2014), and many other circumstances, the behaviour often differs slightly from scenarios with fixed boundaries

that should theoretically yield the same results (Yang et al., 2014; Huang et al., 2014). However, the technique is poorly suited to simulating granular systems where fixed boundaries are replaced by periodic ones, due to the lack of side-wall frictional effects. Additionally, the technique is less useful for circumstances with low counts of highly complex particles, as the effects of non-random particle placement start to dominate the system behaviour.

Overall, the capabilities and advantages of DEM as a modelling approach prove to be tremendous, and it was decided that a DEM should be included in this study to provide better qualitative understanding of the behaviour of the experimental granular slides conducted, and to provide quantitative data that would be impossible to measure and discern otherwise. Table 1 provides a summary of many of the DEM engines currently being developed and used to model granular slides and flows, highlighting their features and evaluating their strengths and weaknesses and evaluating their suitability for this study. LIGGGHTS (LIGGGHTS, 2016) was ultimately chosen as the most suitable DEM for use in this study due to its open-source nature, its capability of modelling complex ramp and particle geometry, its ability to efficiently simulate slides containing millions of particles using MPI on a HPC cluster, and its implementation of a rolling resistance model to simulate particle shape in a less resource-intensive manner than the multi-sphere clump approach. The formulation of the DEM used in this study can be seen in Section 3.4.

Table 1 Features, advantages, and disadvantages of DEM engines

DEM code	Features	Advantages	Disadvantages	Suitability
EDEM (EDEM, 2018)	GPU solver engine. Variety of contact models. Handles complex phenomena including sticky solids, breakage, flexible fibres and membranes, charged and magnetic particles.	Internally coupled with Finite Element Analysis. Multi-body Dynamics, and CFD engines. EDEM Creator provides intuitive interface and allows a large range of import files for geometry and particles. Designed around and validated against the multi-sphere model. EDEM Analyst provides extensive internal post-processing, visualisation, and analysis tools. GPU solver is extremely powerful for solving well-suited problems.	Code is not open source.	EDEM is not open source, making it unsuitable for this study.
ESyS-Particle (Weatherley et al., 2010, 2014; Zhao, 2015)	Linear contact model. Scriptable model geometry with spherical particles. Rigid and deformable bonds for multi-sphere clumps.	Open source Linux-based C++ code. Designed to use MPI for efficient parallelisation and has demonstrated low reduction in efficiency at high particle counts. Python wrapper API provides flexibility in model design and ease of access. Designed specifically for generating granular packings with specific properties and simulating rock fracture and fragmentation. Can be coupled with OpenFOAM for fluid modelling.	Lacking of rolling friction model. Capability of modelling complex geometry is lacking.	ESyS seems suitable for modelling large granular slides on the HPC, but lacks the capability of imposing a rolling resistance model on spherical particles. Fragmentation is not a key simulation concern.
LIGGGHTS (LIGGGHTS, 2016; Shan Zhao, 2014)	Spring-dashpot contact model. Moving mesh geometry, force and stress analysis. Coupling with OpenOAM in CFDEM configuration. Also capable of SPH simulations. Multi-sphere particle clumps, superquadratic particles.	Open source C++ code. Many different contact and rolling models for different applications. Complex geometries can be imported via STL and VTK files. Outputs to standard VTK files, easy to post-process in ParaView and MATLAB. Designed for efficient parallelisation via MPI.	Important features (dynamic load balancing and processor-domain resizing, improved multi-sphere restitution modelling) locked behind premium version. Lack of non-terminal interface and post-processing.	Suitable for modelling high particle counts in timely manner via HPC. Can be adapted very specifically to the desired laboratory geometry and particle modelling. Can be coupled efficiently with other capabilities.
PFC (PFC 5.0, 2018)	Variety of contact models. Particle-fluid coupling. Wide range of particle and geometry models and capabilities.	Advanced and intuitive interface and post-processing capabilities. Rhino CAD front end allows for straightforward and powerful particle and boundary geometry design. Highly optimised for parallel computing environments. Custom FISH scripting language used alongside Python commands. Batch mode allows efficient parametric studies.	Code is not open-source.	PFC is not open-source, making it unsuitable for this study.
YADE (Smlauer and Chareyre, 2015; Haustein et al., 2017)	Deformable contact model. Particle-fluid coupling, FEM-coupling. Deformable particles and interaction with deformable structures. Polyhedral particles.	Open source Linux-based C++ code with intuitive Python interface. Good in-built post-processing capabilities. OpenMP takes advantage of systems with many processors. Batch mode allows efficient parametric studies. Deformation-based approach conserves volume of colliding particles and structures.	Currently missing MPI, limiting applicability to efficient HPC usage. Depends on many external packages being installed. Deformation engine is computationally expensive.	Lack of MPI makes YADE unsuitable for timely simulation of granular slides of over 10^6 particles, which is necessary for correctly matching laboratory size distributions. Ease of use and internal post-processing make it a highly valuable learning tool.

2.5 Important experimental studies

Several experimental studies have been analysed, forming the basis of the approach taken in this study to investigate scale effects in dry granular slides. Hutter et al. (1995), Davies and McSaveney (1999), Okura et al. (2000a), De Haas et al. (2015), and Haug et al. (2016) provided examples of suitable chute configurations due to both the large amount of information provided on their design and construction and due to the large amount of results collected from many different granular slides via these set-ups. Additionally, the set-up of Hutter et al. (1995) was one of the first developed to record snapshots of granular slides throughout their duration, and many other experiments were later developed by other researchers based on these principles. Heller et al. (2008) was used as an example of conducting an laboratory scale series with the aim of identifying scale effects, while Perez and Aharonov (2015) provide a numerical model that was capable of simulating granular slides with behaviour that depended on the scale of the slide.

The experiments performed in Hutter et al. (1995) were conducted in a 0.10 m wide chute with 0.20 m high sidewalls, one of which was transparent 10 mm thick Plexiglas and the other being 10 mm thick black PVC to allow high quality images to be taken of slides from the side. The chute base consisted of an inclined section that could vary between 40–60°, a flat runout section, and a replaceable curved section specific to each experiment type. The base material was PVC, but was coated with drawing paper and sandpaper to influence its frictional properties between experiments. A counterweight was directly attached to the arm of a rotating shutter, with a restraining bolt being removed to release the shutter and trigger the granular slides. They varied the shutter speed by increasing the counterweight, presumably increasing velocity by counteracting the frictional resistance of the rotational axis up to a fixed maximum shutter velocity. This maximum velocity was such that the slide would fully detach from the shutter very shortly after release. Figure 32 provides further clarification of the chute schematics and specific linear chute co-ordinates η at important locations. To measure the slide velocity and position, several photographs were taken using standard film cameras, providing an effective frame rate of 6 images per second.

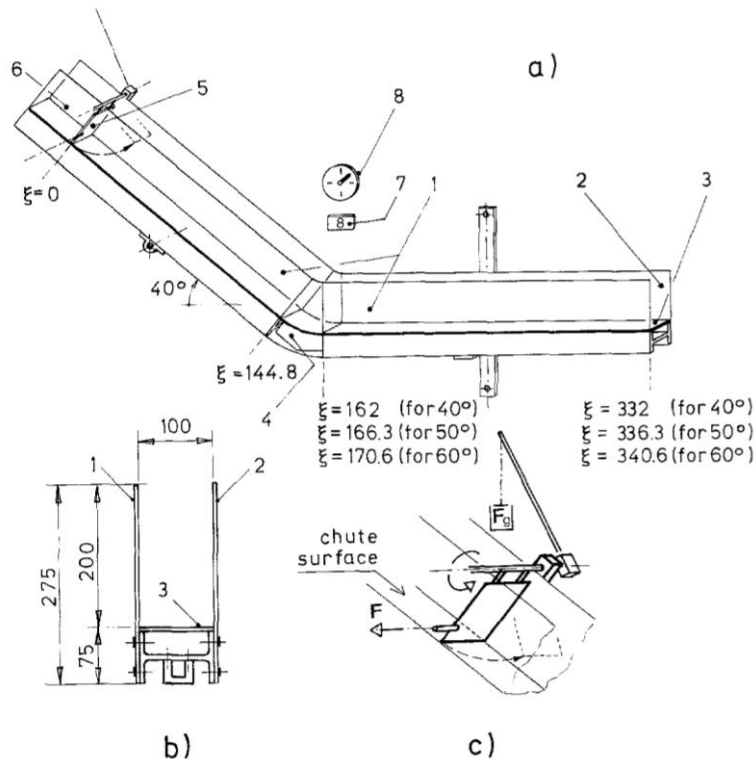


Figure 32 (a) Perspective view of the chute from Hutter et al. (1995). (1) Frontal side wall, (2) rear side wall, (3) basal surface, (4) curved chute element, (5) rotating shutter, (6) slide loading zone, (7) experiment number, (8) experiment clock. (b) Cross sectional cut through the chute. (1) Frontal side wall, (2) rear side wall, (3) basal surface, (4) aluminium I-beam. (c) Detail of the shutter operating system. All numbers are in mm (Hutter et al., 1995)

Two types of granular material were used in the experiments of Hutter et al. (1995); lens-type plastic Vestolen particles with a density of 950 kg/m^3 , diameter of 4 mm, and height of 2.5 mm, and spherical glass beads with a density of 1730 kg/m^3 and diameter of 3 mm. Hutter et al. (1995) determined that these particles were optimal choices for experiments on their chute geometry, as they achieved avalanching slide behaviour on all tested surface types, produced flows of measurable thickness, and left deposits with clearly defined fronts that stayed within the runout zone of their chute. While many experiments were performed by Hutter et al. (1995), experiment #117 was seen as a particularly useful case

to attempt to replicate with the DEM developed in this study. This experiment used a relatively large release mass of 4 kg, resulting in a thick flow and deposit highly suitable for modelling. Furthermore, the spherical glass particles could be easily replicated in the DEM in comparison to the lens-type Vestolen particles, and the use of drawing paper as the flow surface ensured that a DEM with smooth surfaces could be used. The sidewall friction played an important part in the slide dynamics. The particles used in experiment #117 had an internal friction angle of 28° , and a measured bed friction angle of 26° throughout the channel, while the chute had a steep inclination angle of 60° . Figure 33 provides a series of snapshots of the granular slide from its release to its deposition.

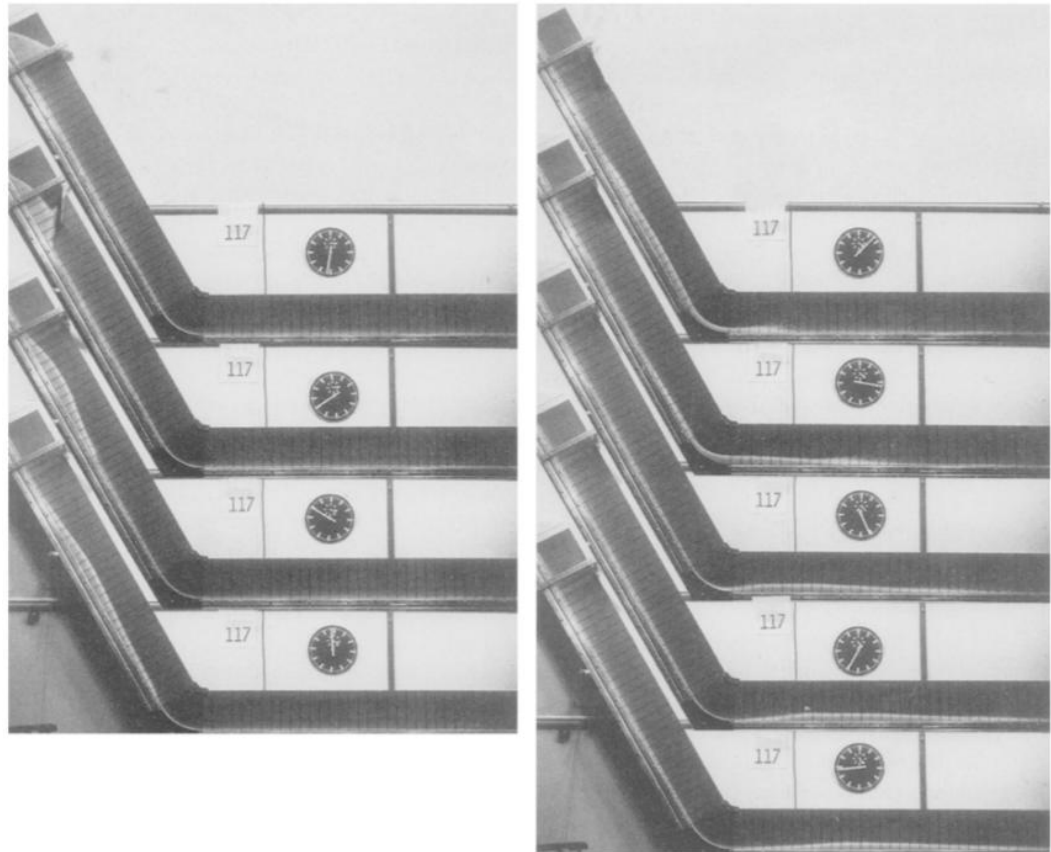


Figure 33 Side-view image series from experiment #117 of Hutter et al. (1995)

2. LITERATURE REVIEW

Overall, this experiment has many characteristics that make it suitable for validating the DEM used in this study. In particular, the use of spherical particles allows the DEM to be validated in a context free of potential shape effects caused by the rolling friction model. Meanwhile, the use of a narrow chute with a steep inclination angle allows the DEM to be evaluated in a different chute geometry to the main experiments of this study, which will use a relatively wide chute and a relatively shallow inclination angle. This is crucial for ensuring that the simulation is not overfitted to the laboratory chute geometry, verifying that the DEM can adequately model granular slides regardless of the chute geometry used.

Davies and McSaveney (1999) conducted a series of laboratory experiments on dry granular slides across a large range of slide volumes (0.1 to 1000 L) and fall heights (0.057 to 4.6 m), two different fall slopes (35° and 45°), and two different material types (well graded silica sand with $d = 0.2$ mm and well-graded gravel with $d = 2.0$ mm). These slide volumes were initially restrained via semi-cylindrical containers with spring-loaded rapid-action bottom gates allowing for the undisturbed release of material, with the containers being mounted at various positions on the inclined plane. The inclined plane was a smooth steel plate, which transitioned directly into a flat smooth concrete runout zone with no transitional curve. Davies and McSaveney (1999) concluded that the grain density, grain size, and grain-size distribution did not contribute significantly to runout distance (at least within the given experimental parameters), while friction angle, fall geometry, and volumes all had significant impacts.

Importantly, Davies and McSaveney (1999) normalised the fall height and runout distance of the experimental slides with $V_s^{1/3}$, providing a linear correlation between these variables within an experimental scale range. Natural events are also included in this correlation, providing a precedent for directly comparing the characteristics of laboratory and natural slides. This technique will be applied in Section 5.4.2 to compare the laboratory results of this present study to those of Davies and McSaveney (1999) and a wider range of natural events.

Okura et al. (2000a) validated a DEM against laboratory experiments of dry granular slides with variable particle types and slope angles. This DEM was used

to evaluate how the travel distance of the slides varied with factors such as slide volume and particle count, slope angle, and friction coefficients. In particular, the particle count varied from 100 to 600 particles, representing systems of lower granularity than the slides of this present study. The DEM from Okura et al. (2000a) is based on the principles of Cundall and Strack (1979), using 3D particles and calculating normal and tangential components of particle velocity. The velocity change caused by normal contacts uses a static restitution coefficient, while that caused by tangential contacts uses a dynamic restitution coefficient that allows the determination of sliding or rolling contacts. The angular velocity of the particles is then calculated based on this data.

The laboratory experiments in Okura et al. (2000a) were conducted in an inclined channel of 3.0 m length, 0.1 m width, and of inclination angle varying from 15° to 25° . The slope then led into a flat runout zone of up to 6.0 m length with no transitional curve. Particles were stacked between two plates 2.0 m and 2.2 m from the transition point across all experiments, with the slides being triggered by the removal of the lower plate. Figure 34 provides an overview of this set-up.

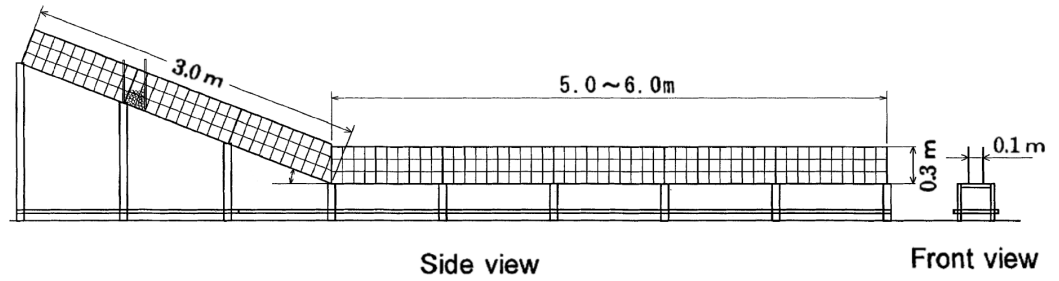


Figure 34 Laboratory flume from Okura et al. (2000a)

The entire channel surface was covered in glued glass beads with $d = 2$ mm to provide uniform roughness, while the sidewalls were coated with Teflon spray to reduce sidewall friction. The slide particles all had $d = 14$ mm but were varied considerably between experiments, with spherical glass, alumina, and zirconia beads being used, as well as glass beads with rubber surfaces or with smaller glass beads glued to their surfaces. This resulted not only in a wide range of μ , μ_r ,

2. LITERATURE REVIEW

and e , but also cases where particles shared the same μ but had different μ_r or ρ_s . e was measured rigorously by performing grain-to-grain and grain-to-surface colliding tests ten times for each particle type, showing low variance in e from the mean, except in the case of the rubber-coated glass beads.

The experiments of Okura et al. (2000a) showed that particle density did not influence the effective friction of the slide, with this effective friction increasing as slope angle increased due to the dissipation of energy from particles colliding with the runout zone. The effective friction also increased as the particle count increased due to collisional dissipation. Okura et al. (2000a) demonstrate the suitability of DEM as a tool for modelling and developing the understanding of granular slide physics, particularly fluidisation mechanisms, with these behaviours matching well between the DEM and the respective laboratory experiments. This motivates the use of DEM as a modelling and evaluation tool in this present study.

Okura et al. (2000b) expands on the work of Okura et al. (2000a) and focuses more specifically on the influence of slide volume on runout distance. Okura et al. (2000b) used a much larger and more complex outdoor set-up, with a channel consisting of a main inclined section of 4.2 m length and 35° inclination angle, a transitional incline of 1.6 m length and 20° inclination angle, and a 9.9 m flat runout section. The channel width varied over its length, from 2.4 m at the slide release zone to 6.6 m in the runout zone, to allow for lateral spreading of the post-release slide mass. The surface consisted of granite slabs, while the slide mass consisted of cubic granite blocks of 0.1 to 0.2 m side length, representing a rockfall. These rockfalls had cubic release conditions, varying from 1 to 10 sub-cubes in side length, and were stacked above the inclined channel on a flat surface that could be released to match the channel inclination by the removal of a column (Fig. 35). These blocks were coloured according to their position in the release match, to allow the relations of the initial condition to the deposit to be analysed more thoroughly.

The DEM used in Okura et al. (2000a) was also applied in Okura et al. (2000b), with the cubic physical particles being represented as spheres in the DEM. e was calculated by colliding two cubic granite blocks from the laboratory experiments

suspended from a common point by wires, with the pre- and post-collisional velocities being measured via high-speed camera. μ was calculated by using a force gauge to measure the force required to initiate the movement of a cubic granite block on a granite slab and comparing this to the gravity force acting on the block. μ_r was calculated by measuring the inclination angle at which a cubic block would start to roll as opposed to sliding down the inclined surface. Figure 36 shows a time series of images taken from the moment of rockfall release to its deposition.



Figure 35 Initial release mass and apparatus from Okura et al. (2000b)

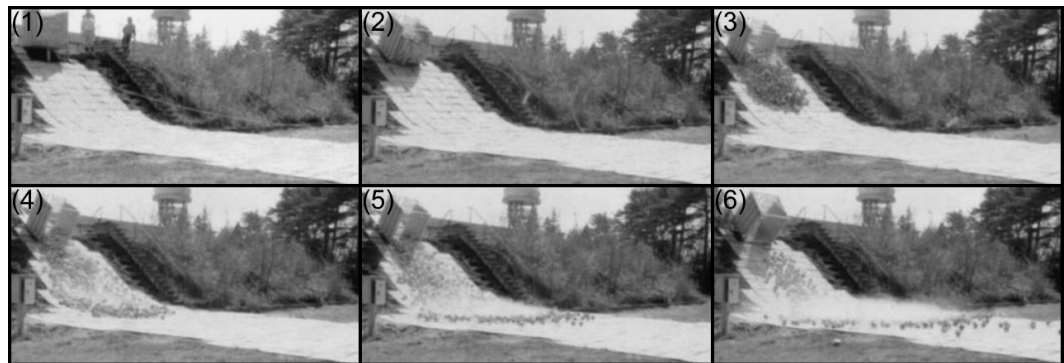


Figure 36 Time series of rockfall experiment using 1000 0.1×0.1×0.1 m granite blocks (adapted from Okura et al., 2000b)

2. LITERATURE REVIEW

Overall, the experiments from Okura et al. (2000b) showed that while the runout of the slide centre of mass decreased as the number of particles increased, the runout distance of the front increased, showing a significant increase in spreading behaviour as the granularity of the system increased, with this behaviour being matched by the DEM. The use of extremely large particle counts in the experiments of this present study should therefore facilitate large degrees of spreading behaviour, and thus scale effects on this spreading behaviour in the deposits can be quantified effectively.

De Haas et al. (2015) conducted a series of laboratory experiments assessing the role of debris flow composition on runout, depositional mechanisms, and deposit morphology. These debris flows consisted of varying ratios of gravel (0 to 72% volume), clay (0 to 38% volume), and water content (39 to 57% volume), with volumes ranging from 1.0 to 5.8 L. The topography of the channel was also varied significantly, with channel slopes ranging from 22° to 34° , runout zone slopes ranging from 0° to 15° , channel width varying between 0.045 and 0.12 m, and channel length varying between 2 and 3 m. Figure 37 provides details of the experimental flume set-up used in De Haas et al. (2015). The inclined channel base and walls used sandpaper to replicate the roughness of a natural channel bed. The composition of the runout zone was varied between an initial unconsolidated bed of sand with thickness of 0.01 m, a fixed rough bed with sand glued to a plate, and a fixed smooth plastic bed.

Experiments were repeated at least 3 times for each configuration of variables, providing precedent for numerous experimental repeats in this present study. A rotating shutter was used to release the material via electromagnetic trigger, allowing the material to be released in a consistent and repeatable manner after mixing in the mixing tank. A release hatch was triggered 1.5 s into the slide events to prevent the flow tail from obscuring the sorting of the rest of the flow deposit and the levees that formed around it, similarly to Johnson et al. (2012). The debris flow deposits were captured with a combination of digital camera photos and 3D scanning, the latter of which produced a point cloud that could be refined into an accurate digital elevation model that captured important features such as

the self-channelising levees that formed. The deposit dimensions and composition measured in De Haas et al. (2015) were then compared to natural slides as well as those from a set of laboratory experiments using a larger flume.

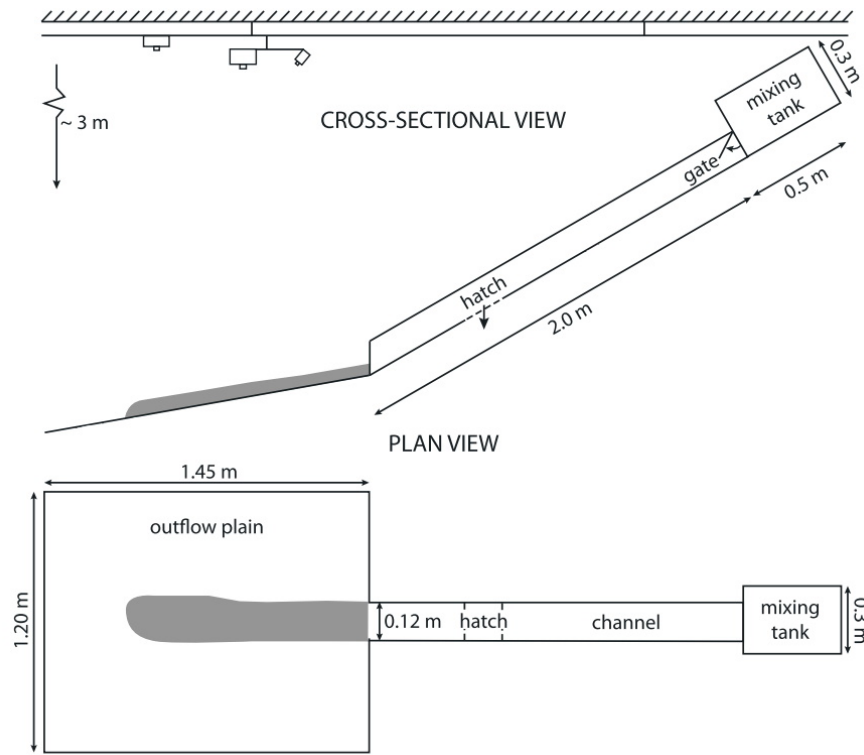


Figure 37 Experimental flume setup of De Haas et al. (2015)

In contrast to the dry granular slides in Davies and McSaveney (1999), the wet debris flows of De Haas et al. (2015) were most strongly influenced by the flow composition, with the initial topographical conditions and slide volumes having little impact. The laboratory experiments conducted in this present study should help to clarify the influence of scale effects on dry granular slides with identical scaled topography and identical composition.

Haug et al. (2016) conducted over 100 laboratory experiments investigating the influence of fragmentation on the runout distance and energy balance of granular slides. These experiments focused on the breakup of one large release mass into several smaller blocks, as opposed the dynamic fragmentation of individual particles

2. LITERATURE REVIEW

due to comminution and grinding (Imre et al., 2010). Figure 38 provides a side view of the experimental setup used in Haug et al. (2016), also showing the use of a rotating shutter as a release mechanism.

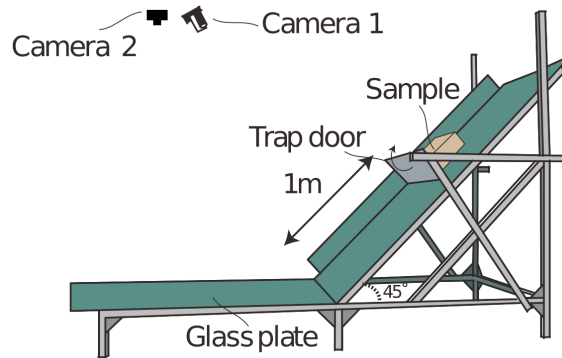


Figure 38 Side view of experimental setup in Haug et al. (2016)

In the experiments of Haug et al. (2016), the initial sliding block was released down an inclined channel into a flat runout area, again with no transition curve, with the block fracturing upon impact with the runout zone. The slide blocks themselves consisted of well-sorted sand with $d = 0.3$ mm mixed with gypsum powder (1 to 5% weight) or potato starch (0.125 to 1% weight), with 10% weight of water being added. After setting, these mixtures became cohesive, rigid blocks, with properties being measured via triaxial and ring shear tests. The cohesive of these blocks could be controlled by varying the type and quantity of the binding agents added to the sand before setting.

Both the slide front positions and centres of mass were measured throughout the slide events, with key slide parameters were non-dimensionalised, to allow direct comparison between experiments with different geometries. While Haug et al. (2016) does not conduct a Froude number scale series with complete geometric similarity, the definition of dimensionless parameters (such as the relative fall height, the aspect ratio (length versus thickness), and the relative runout distances) is instructive as an approach for directly comparing the experiments of this present study. To compare the fragmentation behaviour of the different slide masses, Haug et al. (2016) also used dimensionless numbers such as the ratio of slide potential

energy to internal cohesion (the energy necessary for fracture), and the ratio of slide mass to largest final fragment mass (the degree of fragmentation).

The experiments conducted in Haug et al. (2016) were split into three series based on which dimensionless parameter was varied; one series varied the aspect ratio, while the other two varied the ratio of potential energy and cohesion, with two different runout zone friction coefficients. The friction coefficients of the materials were verified by measuring the force required to move slide material samples over them, using force sensors. Most experimental conditions were repeated 3 to 6 times to ensure reliability; this seems a suitable threshold for this present study.

The data from the experiments of Haug et al. (2016) was measured using two digital cameras, with one capturing the slide event at $f = 50\text{Hz}$ and the other capturing the final deposits. These cameras were positioned such that the pixel length was 0.5 mm, ensuring that each pixel contained 2 to 3 particles and that image correlation could be conducted effectively. Fragments greater than 10 pixels in area were tracked across the entire channel surface using this technique, with the slide centre of mass being calculated from the centres of mass of each tracked fragment, with smaller fragments not contributing significantly to changes in the centre of mass. The fragment velocity was then calculated using PIV, and cross-checked against the motion of fragment centre of mass between subsequent images. Overall, these measurement techniques were sufficient for calculating the kinematics and energy balance of a wide variety of slide conditions, with varying degrees of fragmentation.

In conclusion, the experiments of Hutter et al. (1995), Davies and McSaveney (1999), Okura et al. (2000a), De Haas et al. (2015), and Haug et al. (2016) provide a strong foundation for the design of experiments in this present study, with the aim of conducting repeatable and consistent dry granular slides, modelling these slides with DEM, and producing accurate measurements of the slide runout and deposit morphology. Meanwhile, Pudasaini and Hutter (2010) and Gollin et al. (2017) highlight the robustness of the PIV technique in measuring the velocity of granular slides at the slide surface and channel sidewalls, respectively.

2.6 Summary

In this work, some of the most important dynamics and characteristics of granular slides have been identified, and the influences of key factors such as particle shape and granular slide and boundary conditions and geometry have been evaluated. It can clearly be seen that the behaviour of individual particles depends not only on their own characteristics, but of the particles surrounding them and the bulk motion of the granular slide or flow as a whole. The flow of granular particles also shows some notable characteristics, such as a dependence on different surface inclination angles for starting and stopping, regimes where steady flow becomes impossible and a series of avalanching fronts results, and the segregation of particles of different sizes over time.

The concept of scale effects has also been defined and clarified, with clear implications on the modelling of large-scale real-world phenomena at smaller, more economical experimental scales. A series of dimensionless parameters have been defined that describe various aspects of granular slide behaviour and how they vary with scale, and an experimental design approach has been identified that ensures that the most important force ratio, the Froude number Fr , is preserved between scales. The scale effects resulting from differences in other force ratios have been assessed from a theoretical viewpoint, with the aim of quantifying these scale effects in later sections. The hypermobility phenomenon has also been thoroughly discussed and may be further elucidated by the identification of scale effects in small-scale experiments.

Many different experimental techniques have been evaluated in the context of granular slides, with particle image velocimetry (PIV) and stereophotogrammetry proving to be useful techniques in the laboratory experiments conducted in this study. Meanwhile, discrete element modelling (DEM) proves to be a powerful numerical tool for analysing granular slide dynamics that has become increasingly more accessible in recent years, providing a resolution of grain-scale interactions that other numerical models fail to capture. A variety of DEM engines have been discussed and evaluated with regards to their suitability to this study, with EDEM

(EDEM, 2018) and LIGGGHTS (LIGGGHTS, 2016) proving to be strong open-source candidates. The Savage-Hutter model, one of the most important fundamental analytical models, has also been discussed and has been seen to not address key mechanisms that may cause scale effects. Furthermore, the experiments of Hutter et al. (1995), Davies and McSaveney (1999), Okura et al. (2000a), De Haas et al. (2015), and Haug et al. (2016) provide solid examples that facilitate the design of the experiments seen in Section 3.

3 Methodology

3.1 Introduction

Physical laboratory experiments and numerical simulations have been conducted to model granular slides of a suitable chute geometry at various different scales, with the aim of clearly identifying differences in key slide parameters such as surface velocity, slide positions and shapes over time, and deposit granulometry and dimensions between scales. A discrete element model (DEM) has been developed to evaluate the suitability of the technique for capturing the physical granular slides conducted and its behaviour, and to extract detailed information on the slide behaviour that cannot be captured using the laboratory experiments.

In Section 3.2, the specifics of the newly-developed laboratory set-up are focused on, with the design and construction approaches taken for the laboratory set-up being described in Section 3.2.1. In Section 3.2.2, specific geometric parameters are introduced that dictate the boundary conditions of the granular slides produced, in addition to the qualities of the granular material used (sand and gravel) and how the scale series approach discussed in Section 2.3.1 has been applied to the experiments in this study. Section 3.2.3 describes an axisymmetric column collapse set-up used for validation, while Section 3.3 is focused on the measurement techniques used to identify key experimental parameters and to extract key data from the granular slides during and after their release and deposition.

In Section 3.4, insight is provided into the formulation of the chosen DEM engine (LIGGGHTS, 2016), with Section 3.4.1 describing the general workflow of the engine. Section 3.4.2 is focused on the modelling of particle and wall contacts, while two different approaches taken to model particle shape effects with the engine are discussed in Section 3.4.3. Section 3.4.4 describes techniques used to estimate the local porosity of the simulated slides, while Section 3.4.5 is focused on the macro-scale process of simulating a laboratory granular slide from initial loading to final deposition. Insight is provided in Section 3.4.6 on the process of selecting a suitable time-step for the DEM. In Section 3.4.7, details are given on

the approach taken to implement and complete the DEM simulations in the parallel architecture of the University of Nottingham's Minerva and Augusta HPC services and later on Athena at HPC Midlands+. Section 3.4.8 provides a summary of the key parameters used to calibrate the simulations throughout this study.

3.2 Experimental set-ups

The experimental evaluation of scale effects in granular slides required a set-up that would not only facilitate conducting granular slides in any desired geometric configuration to a high degree of consistency and reliability, but also to being reconfigurable to represent identical geometries at multiple scales. Following the scale series approach applied by Heller et al. (2008), it was decided to evaluate three different experimental sizes. The largest size was such that it was as large as could practically be conducted in the laboratory, and the smallest size was similarly the smallest that could be conducted with the modular building components used.

The scale factor λ is defined as the ratio between a characteristic length in of a large reference scale (such as the largest experimental scale or a natural event being modelled), and the corresponding length in a smaller, representative model. As such, the largest experiments in this study are characterised with $\lambda = 1$, while the smallest experiments are characterised with $\lambda = 4$. A third set of intermediate experiments is characterised by $\lambda = 2$. Using three different sets of experiments, it was expected that correlations could be drawn from experimental data that could show a converging or diverging trend in key slide parameters, providing insight on the extent to which scale effects may start to impact the experiments as λ increases. Figures 39, 40, and 41 provide broad overviews of the experimental set-ups used at each scale.

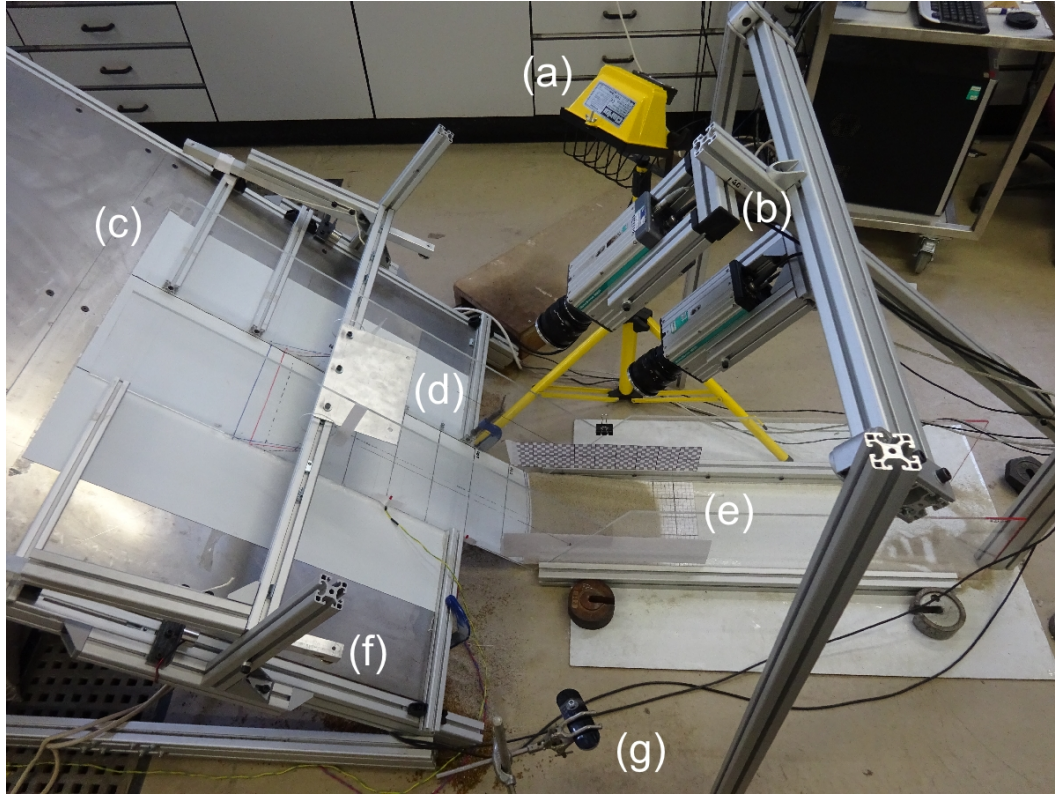


Figure 39 Overview of experimental set-up for small scale experiments ($\lambda = 4$). (a) Floodlight for illumination. (b) High-speed cameras. (c) Sidewalls attached to sides of main ramp frame. (d) Shutter in open position. (e) Runout area with reference grids and deposit. (f) Shutter attachment point with electromagnet trigger. (g) Laser pointer for thickness measurement

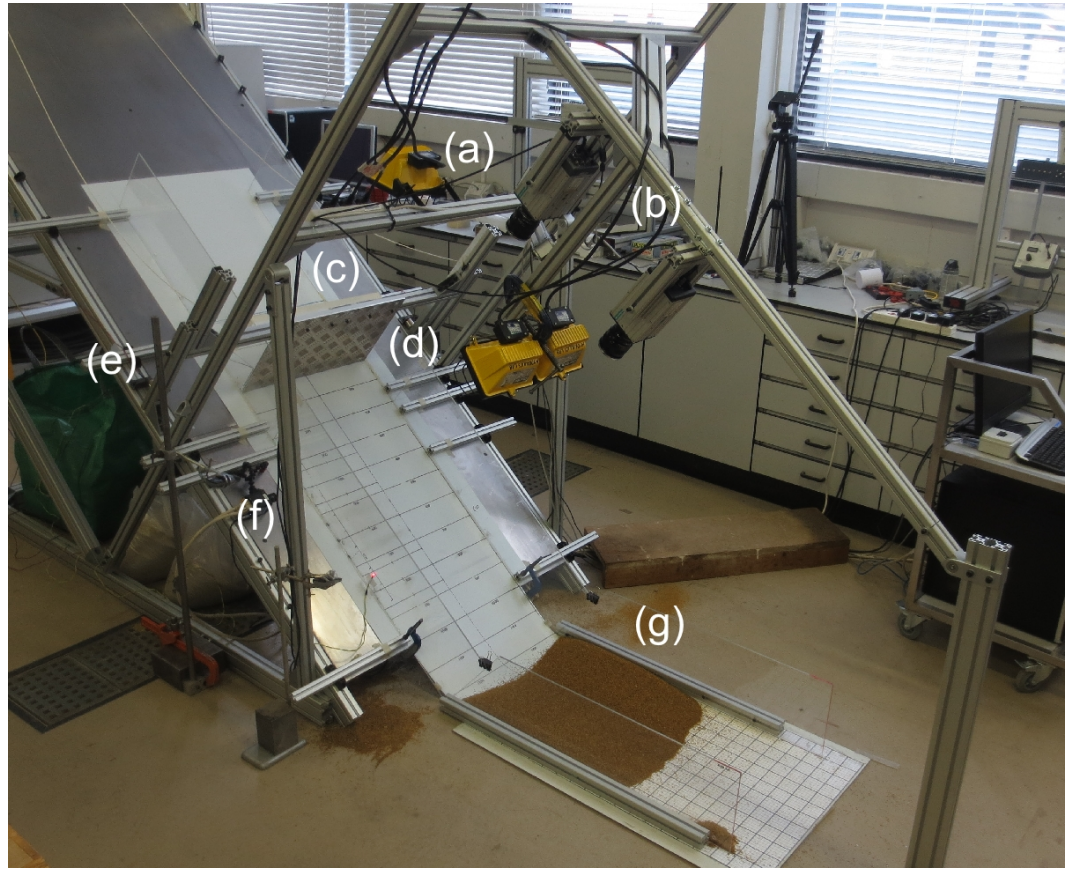


Figure 40 Overview of experimental set-up for medium scale experiments ($\lambda = 2$). (a) Floodlights for illumination. (b) High-speed cameras. (c) Sidewalls attached to sides of main ramp frame. (d) Shutter in closed position. (e) Shutter attachment point with electromagnet trigger. (f) Laser pointer for thickness measurement. (g) Runout area with reference grids and deposit

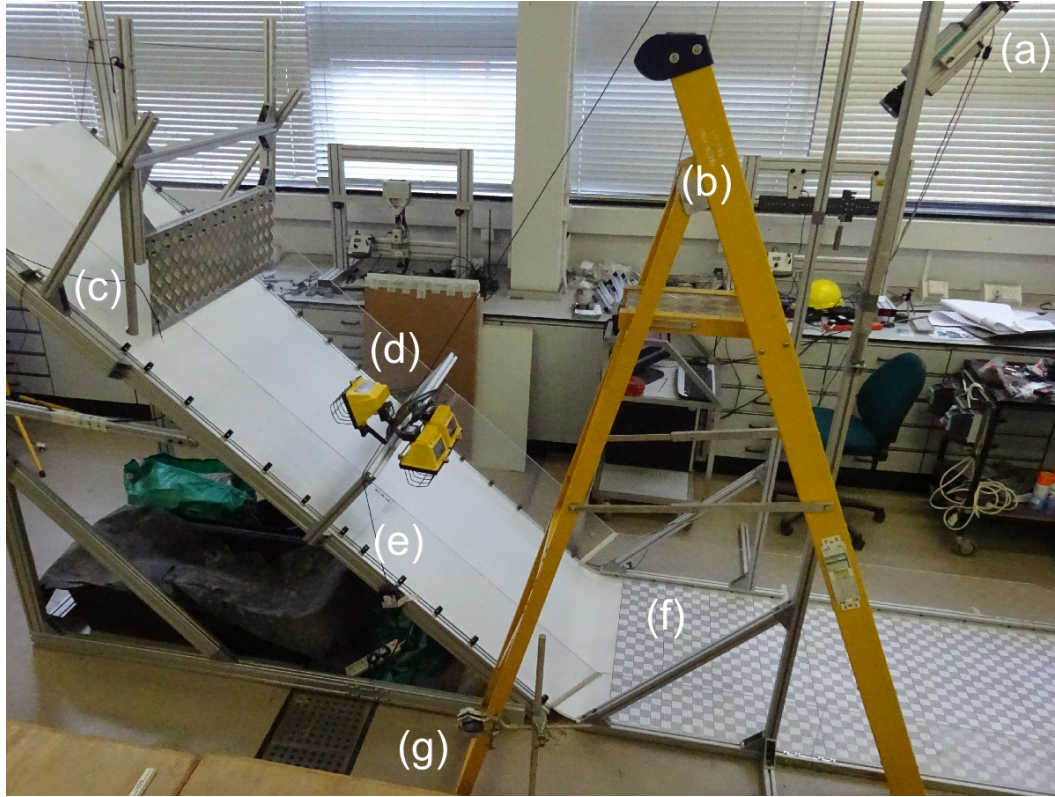


Figure 41 Overview of experimental set-up for large scale experiments ($\lambda = 1$). (a) High-speed camera. (b) Ladder used for camera access and maintenance. (c) Shutter in partially open position with electromagnet trigger. (d) Floodlights for illumination. (e) Sidewalls directly attached to main frame. (f) Runout area with reference grids. (g) Laser pointer for thickness measurement

3.2.1 Design and construction of ramp

Fig. 42 provides a detailed schematic of the set-up at $\lambda = 1$. While the positions of non-critical components (such as floodlights) may vary between set-ups of different scales, the key positions of all critical components (such as high-speed cameras, laser pointers, and ramp components) are scaled appropriately. The main structure of the laboratory set-up comprised of 3 mm mild steel plating supported by a modular frame consisting of aluminium profiles. This structure was sufficiently strong to hold the maximum granular mass without deformation and was modular

enough to allow components to be redesigned to better suit the needs of experiments at different scales. The frame supports an inclined ramp section with a maximum channel width of 1.0 m and a total length of 3.0 m. This inclined section transforms via a curved transition into a flat runout area. The angle of the inclined section can be varied between 30–60°. Circular transition curves were used in this study to minimise the energy loss caused by the slide mass impacting the flat runout zone, as this phenomenon was beyond the scope of the study. The flat runout area consisted of an additional layer of steel plate that was secured to the main structure and the laboratory floor to prevent any slippage. All sections of the ramp were levelled with the use of an inclinometer, ensuring that no transverse slope was present.

The ramp sidewalls were made of 6 mm thick acrylic and were 250 mm high, sufficient for supporting the lateral pressure of the slides. The sidewalls were attached directly to the main structure for the largest experiment via additional support members for the smaller scales so that the channel could remain positioned in the centre of the ramp (Fig. 39). The surface on the inclined channel section and transition curve was covered with a 0.8 mm thick polypropylene sheet, with each scale of experiments using a different set of sheets to minimise the effects of wear and tear. Meanwhile, the runout section used steel plates that were covered by reference grids and plastic laminate, to ease deposit measurement as discussed in Section 3.3. Both of these surfaces were corrosion resistant and maintained their properties well after repeated slide events, dust generation, and subsequent cleaning, and the surfaces were smooth enough to avoid any model effects related to the surface roughness length interfering with the granular slide motion. The plastic laminate was less durable than the polypropylene sheet, particularly at the largest experimental scale, so it was replaced between every experimental condition to ensure its frictional properties remained consistent.

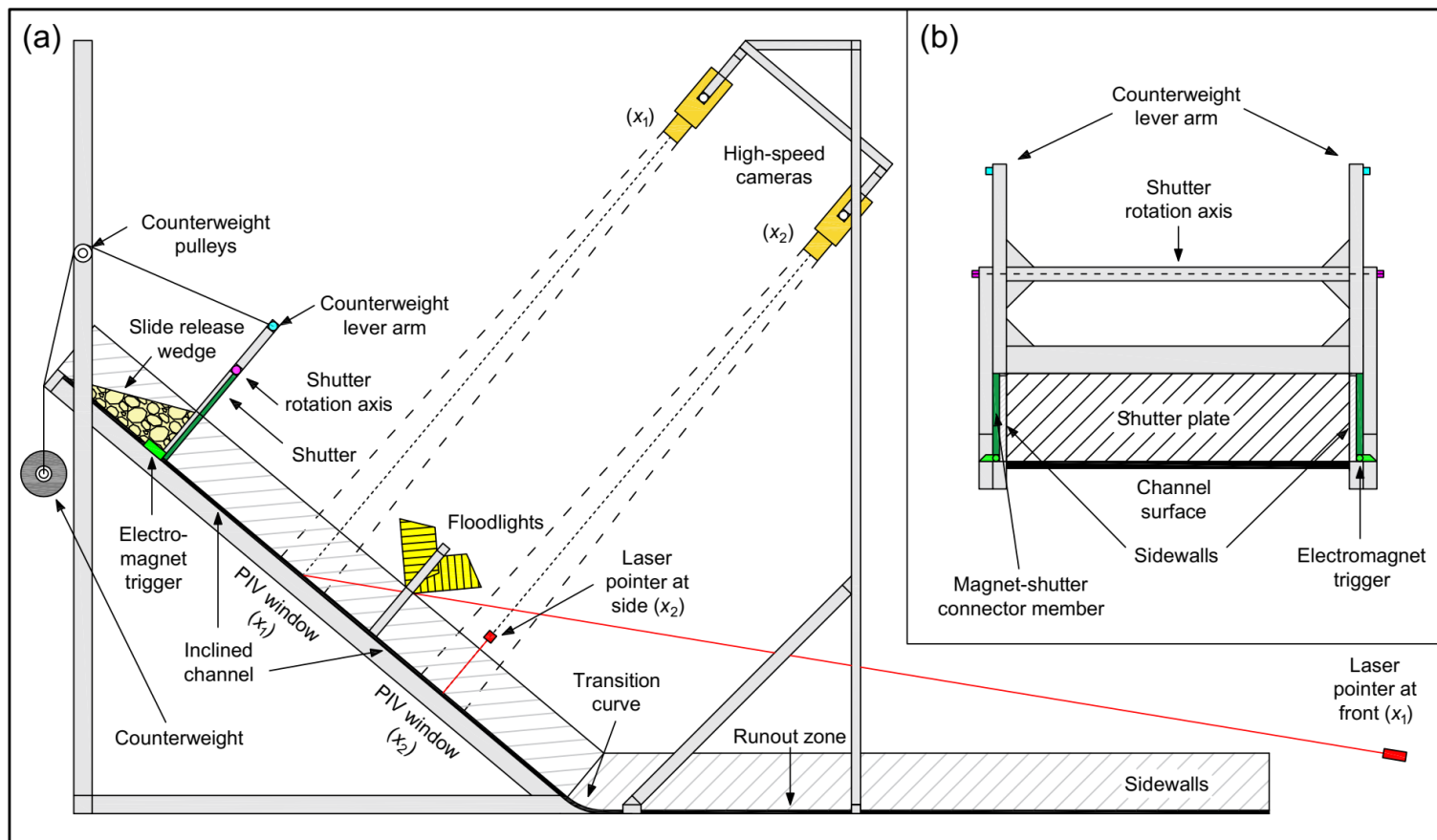


Figure 42 Overview of experimental set-up for large scale experiments ($\lambda = 1$). (a) Side view of set-up design schematic. (b) Rear view of shutter with release mechanism

A rotating shutter triggered by a counterweight was used as the release condition for the granular slides in this study for a number of reasons. Firstly, it allowed the slides to be released without shear forces being applied to the front of the release mass, ensuring that the dominant force acting on the slide at all times was the gravity force. Secondly, the rotational acceleration ω_s of the shutter could easily be varied using this mechanism by varying the distance between the rotational axis and the counterweight-attachment points at the side of the shutter. This ensured that the shutter motion can be correctly scaled across all experiments in the scale series. Care was taken to ensure that the friction between the rotating shutter and the counterweight mechanism was as small as possible, which was particularly relevant at the smallest experimental scale, where the shutter needed to open and approach maximum velocity very quickly. Accordingly, the shutter was held in place by electromagnets that connected to the ramp surface during loading, and swung around with the shutter after the electromagnets were switched off, driven by the counterweight.

Figure 43 shows a close-up of the shutter and counterweight mechanism used at the largest scale. The shutter plates themselves consisted of 6 mm thick aluminium plates. The shutter mechanism was attached to the main ramp structure by aluminium profiles, and thus it could easily be moved up and down to any desired position. Repeated tests were completed to ensure that the shutter opened at a constant acceleration ω_s throughout the slide release. ω_s was achieved sufficiently quickly after release to not disturb the timing of the slide release or its behaviour. Additionally, the shutter did not start to decelerate until it was detached from all of the slide material.

The slide geometry was simply chosen as a triangular wedge stacked behind the shutter evenly across the channel width. After being released, the front tip of the triangular wedge quickly contacted the ramp surface and combines with the front formed by the bottom corner of the wedge, forming a smooth slide body that continued to spread out over time as the front accelerated away from the tail. Accordingly, the slide rapidly approached a shallow flow depth, before reaching the transition curve and depositing thereafter.

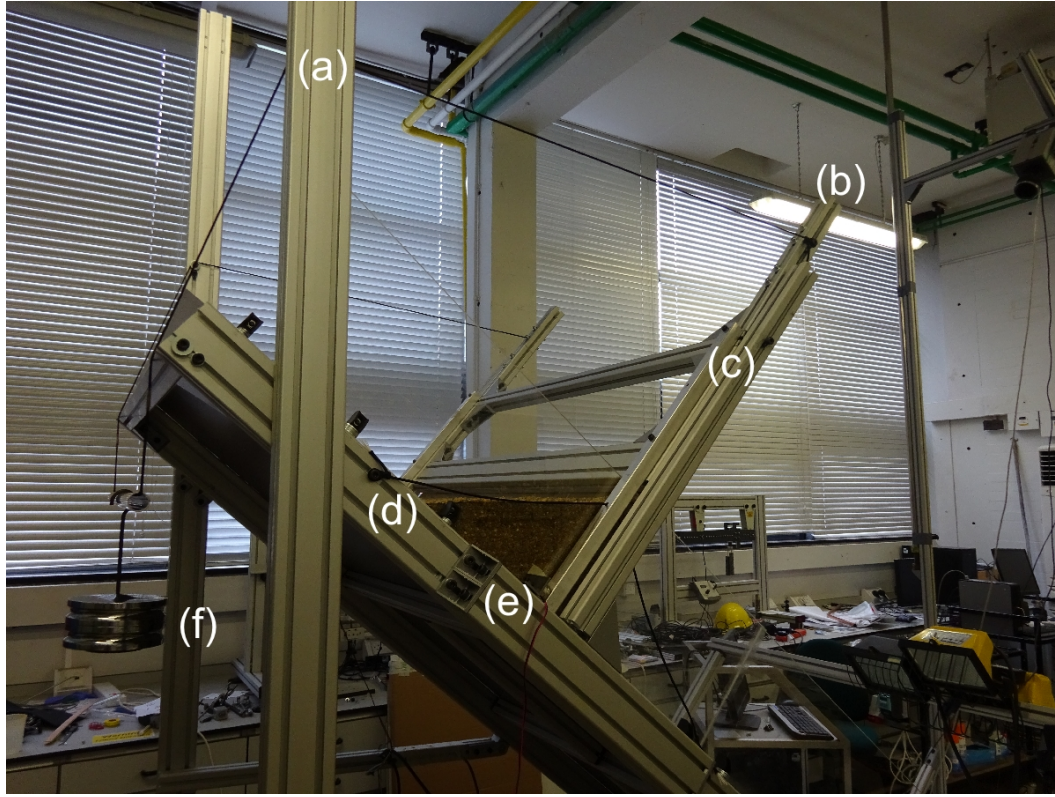


Figure 43 Picture of loaded shutter and counterweight mechanism for large scale experiment. (a,b) Attachment points for smooth counterweight cable movement. (c) Shutter rotation axis. (d) Attachment point for post-release shutter restraint. (e) Electromagnet trigger. (f) Counterweight and attachment bar

3.2.2 Key geometric parameters

Table 2 shows the key geometric parameters that vary between experiments, and Fig. 44 defines some further key parameters in relation to the ramp geometry. Froude scaling was used to scale all relevant parameters such that experiments of different sizes could be compared quantitatively. The x coordinate represents the direction along the ramp surface, with x_f , x_{max} , and x_t representing the channel-wise positions of slide front, peak, and tail respectively. The y coordinate represents the cross-ramp direction with W being the channel width, while the z coordinate represents the direction perpendicular to the channel section at all times.

Table 2 Key experimental and numerical parameters. Parameters kept constant between all experiments include the ramp inclination angle $\theta = 40^\circ$, the internal friction angle $\phi = 30^\circ$, the ramp bed friction angle $\delta_i = 30^\circ$, the runout bed friction angle $\delta_R = 28.5^\circ$, the grain density $\rho_s = 2650 \text{ kg/m}^3$, the simulated coefficient of restitution $e = 0.893$, grain stiffness $E = 70 \text{ GPa}$, grain Bulk modulus $K = 35 \text{ GPa}$, polypropylene stiffness $= 2 \text{ GPa}$, and steel stiffness $= 210 \text{ GPa}$

Exp.	Exp. Type	λ	d	L_1	R	L_{sh}	ω_s	u_{sh}	w	θ_W	$L_{s,0}$	$H_{s,0}$	x_1	x_2	V_s	M	f
(-)	(-)	(-)	(mm)	(m)	(m)	(m)	(rad/s ²)	(m/s)	(m)	(°)	(m)	(m)	(m)	(m)	(m ³)	(kg)	(Hz)
L1-L6	Laboratory	1	2.7	2.310	0.246	0.500	19.6	1.93	1.00	0	0.298	0.250	0.80	1.60	3.7×10^{-2}	60.30	1000
L7-L12	Laboratory	1	2.7	2.310	0.246	0.500	19.6	1.93	1.00	7.5	0.392	0.250	0.80	1.60	4.9×10^{-2}	79.42	1000
L13-L17	Laboratory	1	2.7	2.310	0.246	0.500	19.6	1.93	1.00	15.0	0.536	0.250	0.80	1.60	6.7×10^{-2}	108.51	1000
L18-L21	Laboratory	2	1.35	1.155	0.123	0.250	39.2	1.37	0.50	0	0.149	0.125	0.40	0.80	4.7×10^{-3}	7.54	1414
L22-L25	Laboratory	2	1.35	1.155	0.123	0.250	39.2	1.37	0.50	7.5	0.196	0.125	0.40	0.80	6.1×10^{-3}	9.93	1414
L26-L29	Laboratory	2	1.35	1.155	0.123	0.250	39.2	1.37	0.50	15.0	0.268	0.125	0.40	0.80	8.4×10^{-3}	13.56	1414
L30-L37	Laboratory	4	0.675	0.578	0.062	0.125	78.5	0.97	0.25	0	0.074	0.063	0.20	0.40	5.8×10^{-4}	0.94	2000
L38-L45	Laboratory	4	0.675	0.578	0.062	0.125	78.5	0.97	0.25	7.5	0.098	0.063	0.20	0.40	7.7×10^{-4}	1.24	2000
L46-L53	Laboratory	4	0.675	0.578	0.062	0.125	78.5	0.97	0.25	15.0	0.134	0.063	0.20	0.40	1.0×10^{-3}	1.70	2000
S1	Simulation	1	2.7	2.310	0.246	0.500	19.6	1.93	1.00	0	0.298	0.250	0.80	1.60	3.7×10^{-2}	56.25	1000
S2	Simulation	1	2.7	2.310	0.246	0.500	19.6	1.93	1.00	7.5	0.392	0.250	0.80	1.60	4.9×10^{-2}	74.16	1000
S3	Simulation	1	2.7	2.310	0.246	0.500	19.6	1.93	1.00	15.0	0.536	0.250	0.80	1.60	6.7×10^{-2}	101.29	1000
S4	Simulation	2	1.35	1.155	0.123	0.250	39.2	1.37	0.50	0	0.149	0.125	0.40	0.80	4.7×10^{-3}	6.99	1414
S5	Simulation	2	1.35	1.155	0.123	0.250	39.2	1.37	0.50	7.5	0.196	0.125	0.40	0.80	6.1×10^{-3}	9.27	1414
S6	Simulation	2	1.35	1.155	0.123	0.250	39.2	1.37	0.50	15.0	0.268	0.125	0.40	0.80	8.4×10^{-3}	12.63	1414
S7	Simulation	4	0.675	0.578	0.062	0.125	78.5	0.97	0.25	0	0.074	0.063	0.20	0.40	5.8×10^{-4}	0.88	2000
S8	Simulation	4	0.675	0.578	0.062	0.125	78.5	0.97	0.25	7.5	0.098	0.063	0.20	0.40	7.7×10^{-4}	1.16	2000
S9	Simulation	4	0.675	0.578	0.062	0.125	78.5	0.97	0.25	15.0	0.134	0.063	0.20	0.40	1.0×10^{-3}	1.58	2000
S10	Simulation	0.2	13.5	11.55	1.232	2.500	3.92	4.33	5.00	0	1.490	1.250	4.00	8.00	4.655	6985.1	447
S11	Simulation	20	0.135	0.116	0.012	0.025	392.0	0.43	0.05	0	0.015	0.013	0.04	0.08	7.0×10^{-6}	7.4×10^{-3}	4472

3. METHODOLOGY

h_{max} denotes the maximum slide thickness along the channel centre-line ($y = 0$). $L_{s,0}$ and $H_{s,0}$ represent the initial slide wedge geometry, which can also be defined by a surface angle θ_W . θ_W was the main control parameter by which experimental conditions with the same λ were varied; as θ_W increased, the slide centre of mass was positioned further from the shutter and slide front. This facilitated the study of how scale effects manifested differently in slides of different forms, particularly where slide front behaviour is similar between all configurations.

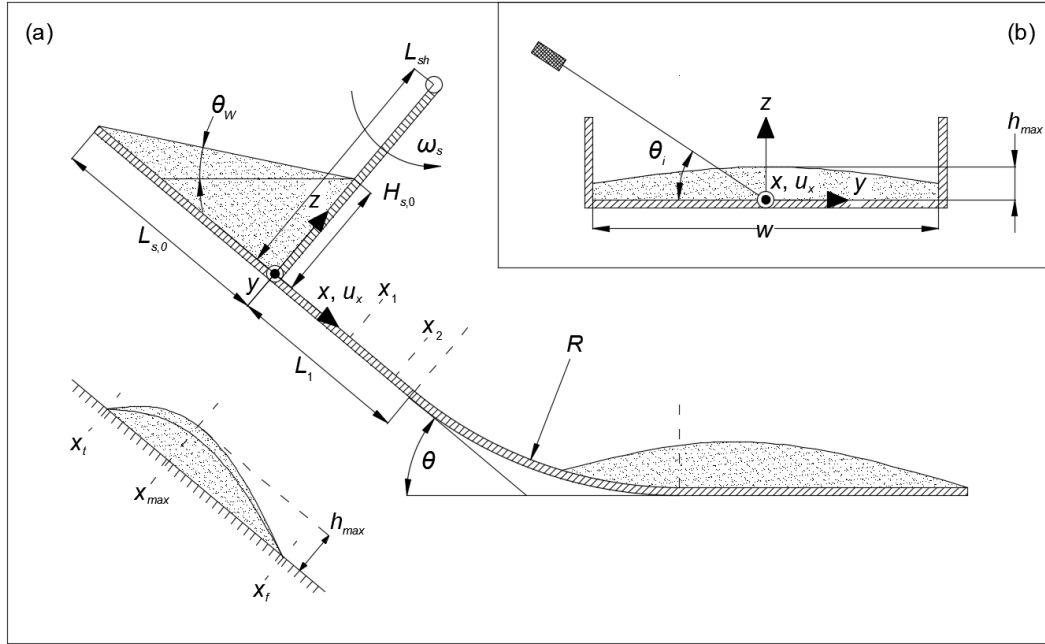


Figure 44 Definition of bulk slide parameters. (a) Side view of the ramp, with x, y, z showing the curvilinear position coordinate system, and u_x being the ramp-wise velocity aligned with x . θ_W is the key control parameter varied between experiments of the same λ . (b) Section of the slide across the channel width

V_s and M are the slide volume and mass; V_s was determined by the release wedge defined in Fig. 44, while laboratory values of M were determined by weighing a 500 ml container of sand at each scale, counting the number of whole containers required to fill the release wedge, and weighing the remainder of material in the final container used. L_1 denotes the distance between the shutter release point and the start of the transition curve, with radius R , while L_{sh} denotes the position of the

shutter axis of rotation from the ramp surface. The shutter angular acceleration ω_s results in a shutter-tip velocity u_{sh} after a rotation of 90° . x_1 and x_2 relate to measurement positions from the shutter release point. Finally, f denotes the image frame rate for each experiment. All experiments for a specific scale and wedge geometry were conducted over a period of 1 to 2 days, with use of a climate controlled laboratory, to minimise the effect of environmental conditions such as room temperature and humidity on slide behaviour.

Natural polydisperse granular mixtures of sand particles were used. Garside Sands aggregate was graded to scale with the experiment, with Gaussian size distributions and with grain diameters ranging from 0.5–1.0 mm (using 16/30 sand) for $\lambda = 4$, 1.0–2.0 mm (using 8/16 sand) for $\lambda = 2$, and 2.0–4.0 mm (using 5/8 sand) for $\lambda = 1$, as shown in Figs. 45 and 46. d represents the mean grain diameter. All particles were sourced from the same material, with the particles at $\lambda = 4$ only differing from those at $\lambda = 1$ and $\lambda = 2$ in colour. The particle density did not vary with λ , and after sieving, the porosity N_s of uncompacted samples varied minimally from 0.385 to 0.393 as λ increased, suggesting that scale does not strongly influence porosity for static material samples. These samples were produced using containers filled with scaled volumes of sand (0.5 kg at $\lambda = 2$), filled from the same height as for the main slides. This correlates well with expectations based on a poured random packing of spheres (Dullien, 1991) and a loose packing of polydisperse spheres (Baranau and Tallarek, 2014).

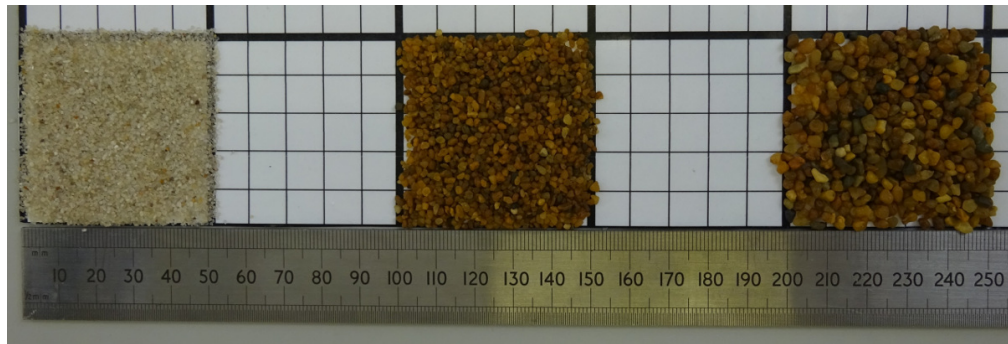


Figure 45 Photographs of sand used at (left to right) $\lambda = 4$, 2, and 1

3. METHODOLOGY

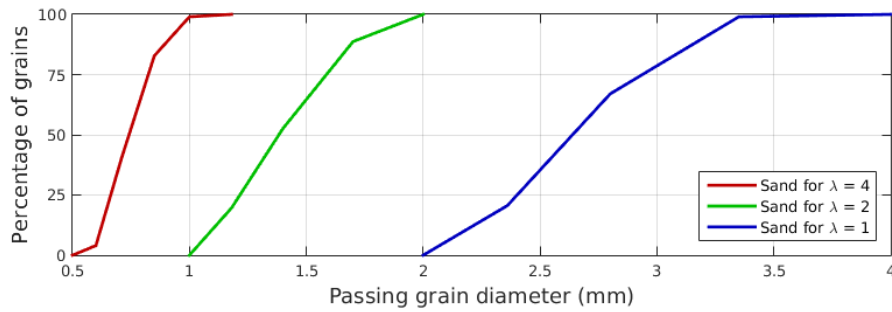


Figure 46 Size distribution of sand particles used in the laboratory experiments

Figure 47 highlights the sphericity and angularity of representative particles for each value of λ . While some particles were more spherical and others were more flattened (resembling oblate spheroids) or elongated (resembling prolate spheroids), and a minority of particles were more angular (resembling multi-sphere clumps), the particles shown in Fig. 47 represent the mean shape well.

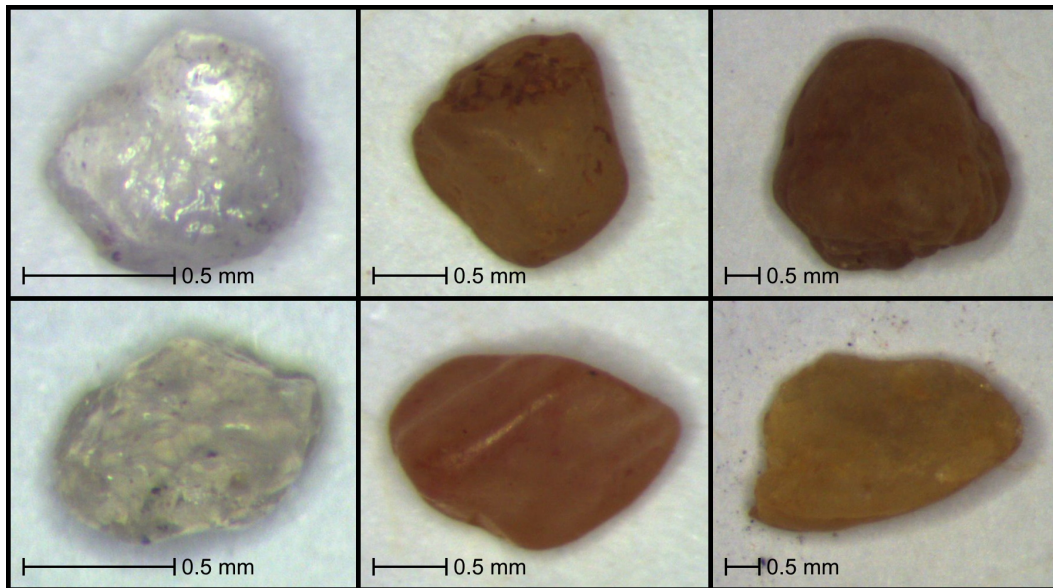


Figure 47 Representative sand particles that resemble oblate (top) and prolate (bottom) spheroids, at $\lambda = 4$ (left), $\lambda = 2$ (middle), and $\lambda = 1$ (right)

Microscope measurements confirmed that particles of quasi-ellipsoid form had major/minor axis ratios a/b varying from 1.0 to 4.0, for both prolate and oblate forms, with the mean value being 1.55 for both. While the particles shown in Fig. 47 display minor angularity, this angularity was typically too low to facilitate particle interlocking, and thus a spheroidal approximation of their shape would be sound. The mean particle angularity and sphericity, as well as the proportions of different particle shapes and forms, are the same across all scales, minimising differences in rolling resistance and shape factors (Section 2.2.4).

The bed friction angles in the inclined channel section and transition curve (δ_i) and in the flat runout zone (δ_R) were identified by settling piles of particles on a flat surface that was inclined until the bulk mass started to mobilise as shown in Fig. 48. The internal friction angle of the sand (ϕ) was similarly measured by tilting static cylinders of particles until their top surfaces started to mobilise. These techniques seemed appropriate for use in this study (Savage and Hutter, 1989; Hutter et al., 1995).



Figure 48 Friction angle measurement set-up. Pile of material before mobilisation at $\theta = 16.2^\circ$ (left). Pile of material after mobilisation at $\theta = 33.3^\circ$ (right)

Measurements were performed with both "natural" piles and flat cylinders of particles restrained by a thin paper cylinder, varying between 10 and 30 d in thickness and measured between all experimental scales. All of these cases produced very similar estimates for the material friction angles, showing no relationship between particle size and frictional behaviour. δ_i and ϕ were both 30° for all of the

3. METHODOLOGY

sand samples at all values of λ , with individual measurements varying by up to 1° . Meanwhile, δ_R was consistently measured as 28.5° due to the smoother nature of the plastic laminate used to cover the reference grids underneath the channel.

These measurements were repeated 5 times for each configuration of material using the same particles, and did not consistently increase or decrease after each repeat, with the minimal changes of friction angle seen being randomly distributed over time. This demonstrates that the frictional behaviour of the material did not vary significantly with scale, and suggests that this behaviour does not vary significantly with material history, facilitating the reproducibility of experimental results. Additionally, the influence of cohesion on the particles at each value of λ was also verified, with no significant cohesion being seen at any scale, for any configuration of material, and for any reasonable level of humidity.

Table 3 shows how the most important parameters must be upscaled such that those of a smaller model match those of a larger prototype; in this case, the largest experiment at $\lambda = 1$. Additionally, it relates these parameters to the similarity criteria described in Section 2.3. The appropriate scaling for matching the grain Reynolds number between scales is also provided for context, highlighting the impracticality of fulfilling both scaling criteria simultaneously (Section 2.3).

By designing experiments such that they all share the same Froude number, it can be ensured that the gravity force driving the slide has the same relative influence at all geometric scales. Thus, scale effects based on the Froude number can be eliminated. Accordingly, any differences seen in the slides at different scales must result from other factors that violate dynamic similarity, such as differences in the grain Reynolds number. In the experiments in this study, the Froude number is defined as $Fr = u/\sqrt{gh}$, where u is the slide velocity and h is the slide thickness. h was chosen as a characteristic length for the slide in analogy to Pouliquen and Forterre (2009) and G.D.R. MiDi (2004), as it represents the criticality of the flow, providing insight into the influence of wave-speed relative to flow-speed and general flow dynamics (Heller, 2011; Gray and Edwards, 2014).

Table 3 Scaling ratios for Froude and Reynolds scaling models

Parameter	Important contexts	Dimension	Froude scale factor	Reynolds scale factor
Geometric similarity				
Length	$d, h, H_c, H_{s,0}, L_r, L_s, L_{s,0}, L_{sh}, L_1, r, R, w, x, x_1, x_2, y, z$	[L]	λ	λ
Area	A	[L ²]	λ^2	λ^2
Volume	V_s	[L ³]	λ^3	λ^3
Kinematic similarity				
Time	f^{-1}, t	[T]	$\lambda^{1/2}$	λ^2
Velocity	u, u_s, u_{sh}	[LT ⁻¹]	$\lambda^{1/2}$	λ^{-1}
Acceleration	g	[LT ⁻²]	1	λ^{-3}
Angular acceleration	ω, ω_s	[T ⁻²]	λ^{-1}	λ^{-4}
Flow rate	Q	[L ³ T ⁻¹]	$\lambda^{5/2}$	λ
Shear rate	$\dot{\gamma}$	[T ⁻¹]	$\lambda^{-1/2}$	λ^{-2}
Kinematic viscosity	ν_f	[L ² T ⁻¹]	$\lambda^{3/2}$	1
Dynamic similarity				
Mass	m, M	[M]	λ^3	λ^3
Force	$\mathbf{F}_b, \mathbf{F}_n, \mathbf{F}_t$	[MLT ⁻²]	λ^3	1
Stress	σ, τ	[ML ⁻¹ T ⁻²]	λ	λ^{-2}
Energy	E_k, E_p	[ML ² T ⁻²]	λ^4	λ
Torque	\mathbf{T}_r	[ML ² T ⁻²]	λ^4	λ

An initial Froude number with a characteristic velocity based on the energy balance of a frictional block sliding down a slope was used to define the scale series in this study. This results in

$$u_i = \sqrt{2gH_c(1 - \mu/\tan\theta)}, \quad (21)$$

where H_c is the height of the mass centroid above the flat runout zone, μ is the bed friction angle of the sand, and θ is the ramp inclination angle. The characteristic

3. METHODOLOGY

length h_i is based on the mean thickness of the slide mass spread evenly along the inclined channel length after the shutter (Fig. 49), resulting in

$$h_i = \frac{H_{s,0}^2 \tan(90 - \theta + \theta_W)}{2L_1}. \quad (22)$$

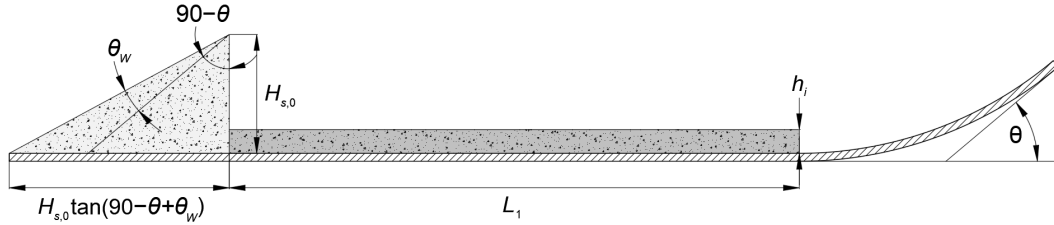


Figure 49 Definition of h_i from initial wedge. The two shaded areas are equal

The resulting Fr_i , Re_i , and Ca_i can thus be defined as

$$Fr_i = \frac{u_i}{\sqrt{gh_i}} = \frac{2}{H_{s,0}} \sqrt{\frac{H_c L_1 (1 - \mu/\tan\theta)}{\tan(90 - \theta + \theta_W)}}, \quad (23)$$

$$Re_i = \frac{u_i d}{\nu_f} = \frac{d}{\nu_f} \sqrt{2gH_c(1 - \mu/\tan\theta)}, \quad (24)$$

$$Ca_i = \frac{\rho_s u_i^2}{K} = 2\rho_s g H_c (1 - \mu/\tan\theta) / K, \quad (25)$$

The grain Reynolds number Re is a quantification of the type of particle-air interaction, where ν_f is the kinematic viscosity of the surrounding air ($15.11 \times 10^{-6} \text{ m}^2/\text{s}$). Similarly, the grain Cauchy number Ca parameterises the effects of particle compressibility on the slide dynamics, where K is the Bulk modulus of the material (taken as 35 GPa for quartz particles (AZoM, 2001)). Notably, K does not scale linearly with λ after Froude scaling and may thus be a source of scale effects as the particle inertia increases relative to the particle's resistance to elastic deformation. However, particle fracture and dust generation are not directly linked to

K and are better characterised by the Weibull modulus of a particle (Brzesowsky et al., 2011), the calculation of which is much more involved. Nevertheless, Ca demonstrates the relative difference in compressibility between scales and may be responsible for scale effects in contexts isolated from particle fracture, such as in the DEM.

Meanwhile, N_{Sav} and N_{Bag} typically use the mean particle diameter d as their characteristic length scale. The characteristic shear rate γ is taken in this case as the surface velocity (u_i for initial estimates and u_s for the experimental values) relative to the velocity at the ramp base (which is assumed to be zero for this assessment) divided by the flow thickness, with h_i being used for initial estimates and h_{max} for the experimental values. This leads to

$$N_{Sav,i} = \frac{\rho_s u_i^2 d}{(\rho_s - \rho_f) g h_i^2}, \quad (26)$$

$$N_{Bag,i} = \frac{\Phi \rho_s u_i d^2}{(1 - \Phi) \mu_f h_i}. \quad (27)$$

Table 4 shows how these characteristic force ratios (Fr_i , Re_i , Ca_i) and stress ratios ($N_{Sav,i}$, $N_{Bag,i}$) vary between the experiments, and how they compare to values produced from experimental data. These force and stress ratios are calculated at $t = 400$ camera frames after the slide front arrives at x_2 , at which point the slide is well developed and the force ratios are representative of typical slide conditions. This demonstrates that Fr_i and $N_{Sav,i}$ are constant between experiments of the same initial slide shape and follow the same scaling laws, and any differences that appear as the slide develops may be attributed to scale effects. Φ is assumed to be 0.55 for this calculation, as the slide volume fraction was not measured at this point. ρ_f is taken as 1.225 kg/m^3 .

Table 4 Estimated (Fr_i , Re_i , Ca_i , $N_{sav,i}$, and $N_{Bag,i}$) and measured (Fr , Re , Ca , N_{sav} , and N_{Bag}) force and stress ratios for conducted experimental conditions

Exp. No.	λ	H_c	u_i	h_i	Fr_i	Re_i	Ca_i	$N_{sav,i}$	$N_{Bag,i}$	u_s	h_{max}	Fr	Re	Ca	N_{sav}	N_{Bag}
(-)	(-)	(m)	(m/s)	(-)	(-)	(-)	(-)	(-)	(-)	(m/s)	(m)	(-)	(-)	(-)	(-)	(-)
L1-L6	1	1.664	3.19	0.0161	8.02	570	7.72×10^{-7}	10.81	3.10×10^5	3.15	0.0149	8.24	563	7.51×10^{-7}	12.31	3.30×10^5
L7-L12	1	1.684	3.21	0.0212	7.03	574	7.80×10^{-7}	6.31	2.37×10^5	3.19	0.0155	8.18	570	7.72×10^{-7}	11.66	3.22×10^5
L13-L17	1	1.716	3.24	0.0290	6.07	579	7.96×10^{-7}	3.44	1.75×10^5	3.24	0.0162	8.13	579	7.96×10^{-7}	11.01	3.13×10^5
L18-L21	2	0.832	2.26	0.0081	8.02	202	3.86×10^{-7}	10.81	1.10×10^5	2.06	0.0088	7.01	184	3.21×10^{-7}	7.54	9.14×10^4
L22-L25	2	0.842	2.27	0.0106	7.03	203	3.90×10^{-7}	6.31	8.37×10^4	2.11	0.0094	6.95	189	3.37×10^{-7}	6.94	8.77×10^4
L26-L29	2	0.858	2.29	0.0145	6.07	205	3.98×10^{-7}	3.44	6.17×10^4	2.15	0.0101	6.83	192	3.50×10^{-7}	6.24	8.32×10^4
L30-L37	4	0.416	1.60	0.0040	8.02	71	1.93×10^{-7}	10.81	3.91×10^4	1.39	0.0052	6.15	62	1.46×10^{-7}	4.92	2.61×10^4
L38-L45	4	0.421	1.61	0.0053	7.03	72	1.95×10^{-7}	6.31	2.97×10^4	1.40	0.0059	5.82	63	1.48×10^{-7}	3.88	2.32×10^4
L46-L53	4	0.429	1.62	0.0073	6.07	72	1.99×10^{-7}	3.44	2.17×10^4	1.42	0.0066	5.58	63	1.53×10^{-7}	3.19	2.10×10^4
S1	1	1.664	3.19	0.0161	8.02	570	7.72×10^{-7}	10.81	3.10×10^5	3.03	0.0192	6.97	540	6.95×10^{-7}	6.86	2.47×10^5
S2	1	1.684	3.21	0.0212	7.03	574	7.80×10^{-7}	6.31	2.37×10^5	3.10	0.0228	6.55	554	7.28×10^{-7}	5.09	2.12×10^5
S3	1	1.716	3.24	0.0290	6.07	579	7.96×10^{-7}	3.44	1.75×10^5	3.17	0.0288	5.96	566	7.61×10^{-7}	3.34	1.72×10^5
S4	2	0.832	2.26	0.0081	8.02	202	3.86×10^{-7}	10.81	1.10×10^5	2.14	0.0096	6.97	191	3.47×10^{-7}	6.86	8.71×10^4
S5	2	0.842	2.27	0.0106	7.03	203	3.90×10^{-7}	6.31	8.37×10^4	2.19	0.0114	6.55	196	3.63×10^{-7}	5.09	7.50×10^4
S6	2	0.858	2.29	0.0145	6.07	205	3.98×10^{-7}	3.44	6.17×10^4	2.24	0.0144	5.96	200	3.80×10^{-7}	3.34	6.08×10^4
S7	4	0.416	1.60	0.0040	8.02	71	1.93×10^{-7}	10.81	3.91×10^4	1.51	0.0048	6.97	68	1.73×10^{-7}	6.86	3.07×10^4
S8	4	0.421	1.61	0.0053	7.03	72	1.95×10^{-7}	6.31	2.97×10^4	1.55	0.0057	6.55	69	1.82×10^{-7}	5.09	2.66×10^4
S9	4	0.429	1.62	0.0073	6.07	72	1.99×10^{-7}	3.44	2.17×10^4	1.58	0.0072	5.96	71	1.89×10^{-7}	3.34	2.14×10^4
S10	0.2	8.320	7.14	0.0806	8.02	6376	3.86×10^{-6}	10.81	3.48×10^6	6.77	0.0960	7.48	6040	3.47×10^{-6}	6.86	2.75×10^6
S11	20	0.083	0.71	0.0008	8.02	6	3.86×10^{-8}	10.81	3.48×10^3	0.68	0.0010	6.97	6	3.47×10^{-8}	6.86	2.75×10^3

3. METHODOLOGY

3.2.3 Axisymmetric column collapse set-up

Axisymmetric column collapse tests were conducted prior to the main experiments, with the aim of validating the numerical simulation before its application to the main experimental geometry. These column collapses were completed using a long transparent acrylic cylinder that was raised rapidly via a pulley system. Figure 50 provides a schematic of the equipment used for the column collapse, while Figs. 51 and 52 show the layout of the axisymmetric column collapse set-up in the laboratory and the resulting deposit after a collapse.

Many studies have been completed analysing the dynamics of two-dimensional column collapses confined by sidewalls, as well as the cylindrical case without sidewalls evaluated here, using a variety of measurement techniques (Lajeunesse et al., 2004; Lube et al., 2004; Cleary and Frank, 2006; Thompson and Huppert, 2007; Warnett et al., 2014). While Grima and Wypych (2011) describe a more complex set-up using a separating clamshell system to initiate the collapse, the simplicity of the vertical cylinder was preferred in this study. The cylinder used in this study had an internal diameter of 100 mm and was filled to a height of 200 mm using the same particles used for the main chute tests at $\lambda = 2$ ($d = 1.35$ mm). This geometry was deemed suitable as it developed a sufficiently thick flow that produced Bagnold-like (Bagnold, 1954) velocity profiles in the regions above the static central core. The set-up also captured important flow features such as creep underneath a moving boundary, the development of shear flow, and an unconfined runout area.

The column collapse itself was recorded at 1414 Hz, matching the corresponding frame rate for the chute experiments (Table 2). High-speed footage of the column was recorded from the side using one of the IDT Nano-Sense cameras used in the main experiments, focusing on the middle of the column. Backlights and a main floodlight illuminating the camera-facing surface of the column ensured good contrast in the high-speed camera images, and a digital camera was used to record the system as a whole. To trigger the collapse, the cylinder was pulled upwards rapidly by hand using the attached pulley system. The pull velocity

3. METHODOLOGY

was high enough to ensure that the cylinder collapse was governed by the pile collapse and not by flow around the cylinder boundaries. Additionally, the friction coefficient of the cylinder material was low, reducing the shear force on the column during release. An aluminium support frame was used to ensure the cylinder moved vertically during release, without any disruptive lateral motion being caused by the pulley system. These design considerations facilitated effective modelling of the column collapse in the DEM.

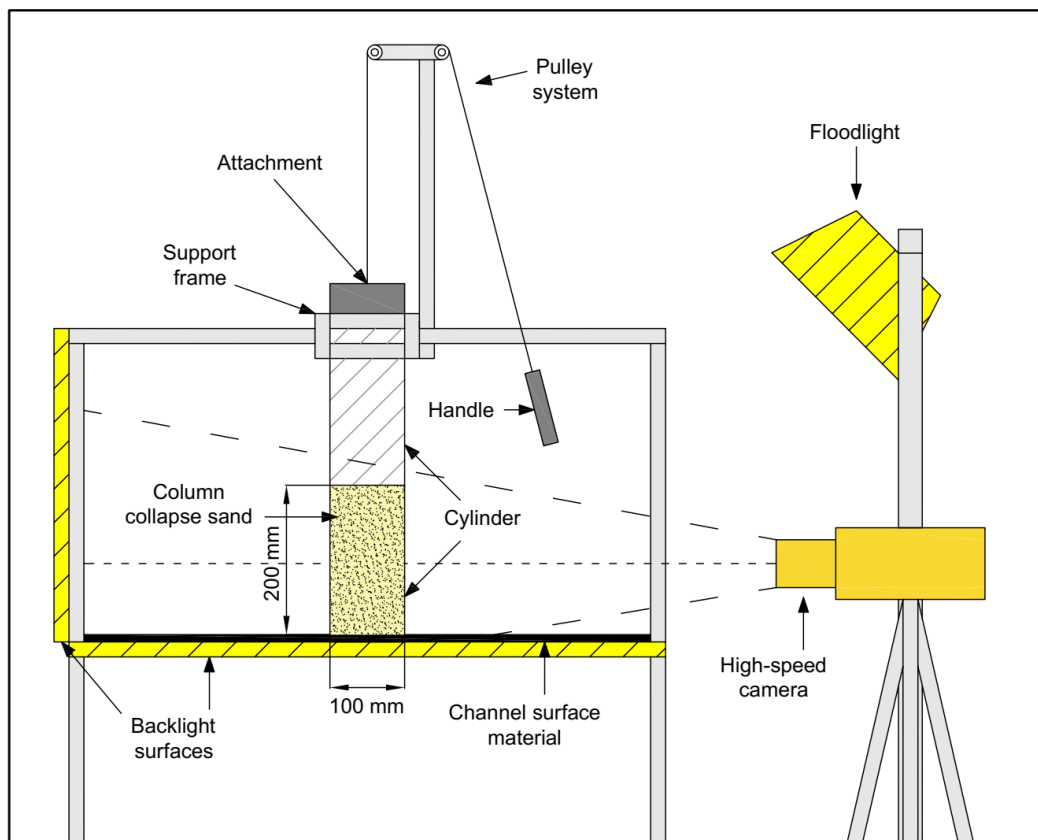


Figure 50 Overview of experimental set-up for axisymmetric column collapse

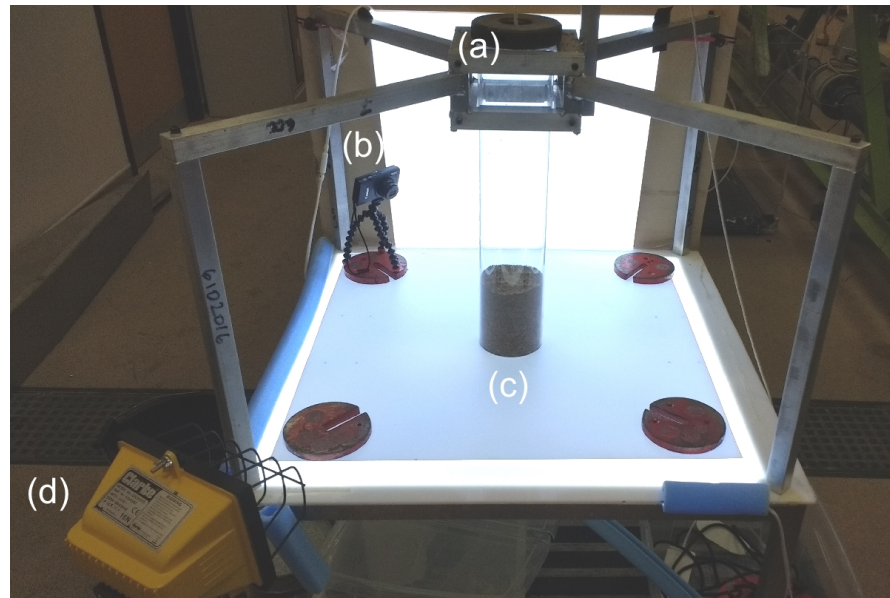


Figure 51 Overview of axisymmetric column collapse set-up. The reference grid is visible underneath the polypropylene surface in detailed images used for photogrammetry. (a) Frame used to stabilise cylinder movement, with pulley attached. (b) Digital camera. (c) Illuminated base surface and loaded cylinder. (d) Floodlight for additional illumination for out-of-image high-speed camera



Figure 52 Deposit from completed axisymmetric column collapse

3.3 Measurement techniques

The main measurements taken in the experiments are the ramp-wise surface velocities u_s at two distance intervals down the channel length (Table 2), as well as slide thickness at these points and measurements of the slide deposit. Measurements were taken only along the y -negative half of the chute given that the slide is symmetrical, using two IDT Nano-Sense high-speed cameras recording at a scale specific frame rate (Table 2) and with a magnification factor of 0.042 between the image and object planes. The slide thickness was measured using laser trigonometry, where laser pointers were pointed at angles from the ramp surface and the beam paths are interrupted by the granular slide, resulting in displacement that is visible in the image plane. This method is based on Börzsönyi et al. (2009) and Saingier et al. (2016). The laser pointers were positioned such that both the central and side slide thicknesses were measured in each experiment. In this case the side slide thickness was measured at x_1 with the laser pointer in line with the channel. Meanwhile the central slide thickness was measured at x_2 with the laser pointer pointing perpendicular from the flow direction. This principle can be seen more clearly in Fig. 53.

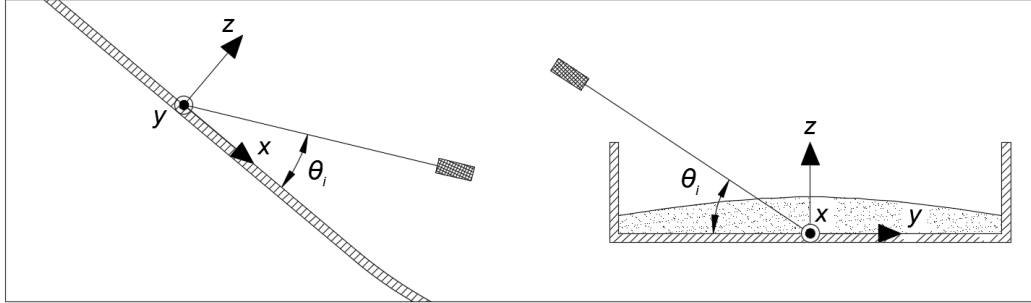


Figure 53 Diagram showing thickness measurement laser inclination angle θ relative to the ramp. Laser at x_1 (right) angled parallel to the xz plane. Laser at x_2 (left) angled parallel to the yz plane

While the angles varied between experimental scales to suit the ramp geometry, it was shown that the laser trigonometry technique provided the same thickness estimates regardless of the angle used, with the angles being kept approximately

at 30° throughout. The accuracy of coordinates taken from the ramp is estimated at $\pm 2.5\%$ of the distance from the centre of the image plane, due to parallax and positioning uncertainty, while the accuracy of the laser displacement method is estimated at $\pm 10\%$ of the correct slide thickness due to occasional interference from stray particles blocking the line-of-sight, spreading the laser point over a wider strip of the channel width than the desired single point.

The camera footage from the two main cameras was analysed via particle image velocimetry (PIV) using DigiFlow image processing software (Dalziel, 2009). PIV was selected as the preferred method of measuring the slide surface velocity profiles, due to its robustness against noise and suitability to capturing a fluctuating granular surface of opaque particles (Section 2.4.1). While only flow features on the slide surface can be identified with PIV, these features will provide significant insight into the overall behaviour of the slide, and DEM simulations seen later in this study provide some insight on the slide kinematics.

PIV velocity vectors were produced across a 512×1024 pixel grid (in the respective x and y directions) at each camera position, with each vector representing an interrogation window (IW) of 45×45 pixels² (12.5×12.5 mm²). As the cameras recorded a slightly larger object area than the area to be analysed, 11×21 vectors resulted. It was necessary to use large interrogation windows in this study to ensure that particles remained within consecutive images for long enough to produce stable vectors, due to relatively high slide velocities. Using a conservative estimate of a maximum measured slide velocity of 3 m/s, at the given frame rate in Table 2, this resulted in a maximum particle velocity of 2.1 mm/frame, or 7.5 pixels/frame across all experimental scales. As a result, the IW side length was roughly 5 mean particle diameters, allowing stable PIV vectors to be calculated reliably.

The PIV algorithm completed three forward passes followed by one reverse subpixel pass to minimise the correlation difference function between successive camera frames. This provided the best match between the velocity vectors calculated at each IW and the overall shift of the camera images. Outlier vectors (greater than $1.2 \times$ the median vector value compared to adjacent vectors) and vectors generated from windows with insufficient texture or intensity range were

3. METHODOLOGY

replaced with interpolated values. Roughly 5% of the vectors were replaced by this procedure, which was deemed satisfactory in comparison to other studies (Eckart et al., 2003; Thielicke and Stamhuis, 2014). Figure 54 shows the PIV vectors calculated across a slide at different time intervals, showing the general variation in velocities and directions recorded over the channel width and over time.

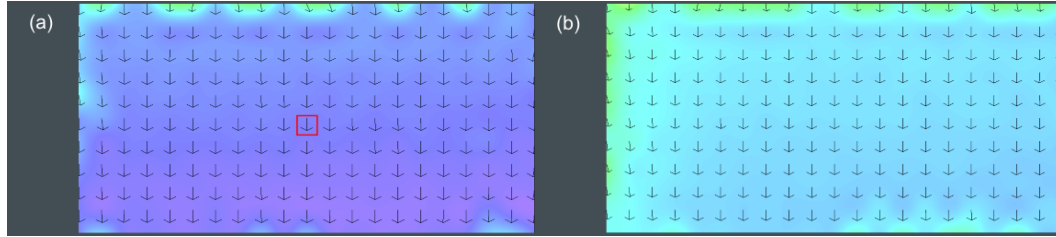


Figure 54 PIV vectors produced by Digiflow for experiment L5, (a) soon after the slide passes through the x_2 window and (b) 0.5 s later. The closer the colour to purple, the higher the calculated velocity. The reference vector enclosed in the red box = 3.75 m/s. The left side of the images corresponds to the channel sidewall, while the right side corresponds to the channel centre

Deposit surface dimensions were measured via the stereophotogrammetry technique using AgiSoft PhotoScan software (AgiSoft-LLC, 2016). Figure 55 provides details of the mesh in the Agisoft workflow process. (a) shows the initial alignment of camera positions (blue boxes) and generation of an initial loose point cloud for camera position calibration. (b) shows the dense point cloud produced if the cameras are placed with sufficiently low error, while (c) shows the resultant surface mesh and (d) shows the final coloured texture.

The technique first assembled a loose point cloud by matching common reference points between 10–20 images taken from different angles. These images were taken with the same focal length and camera to ensure that image distortion is uniform across the images and can be calibrated out in the photogrammetry process to ensure accurate dimensions are produced. These images were taken from many different locations, such as directly over the deposit, at various inclination angles from over the sidewalls, as close to horizontal as possible across the deposit surface, and from different angles relative to the flow direction. This variety was

necessary to ensure that unique deposit features such as the structure at the side-walls and at the transition curve are captured accurately in all dimensions. Clear reference points were marked out throughout the chute runout zone and on the base of the column collapse test to allow a local coordinate system to be easily applied to the images. These reference points were located both on the flat runout surfaces with $z = 0$, as well as on the sidewalls at $x = 0$ and $x = W$ in the main experiments and on the back wall during the column collapse.

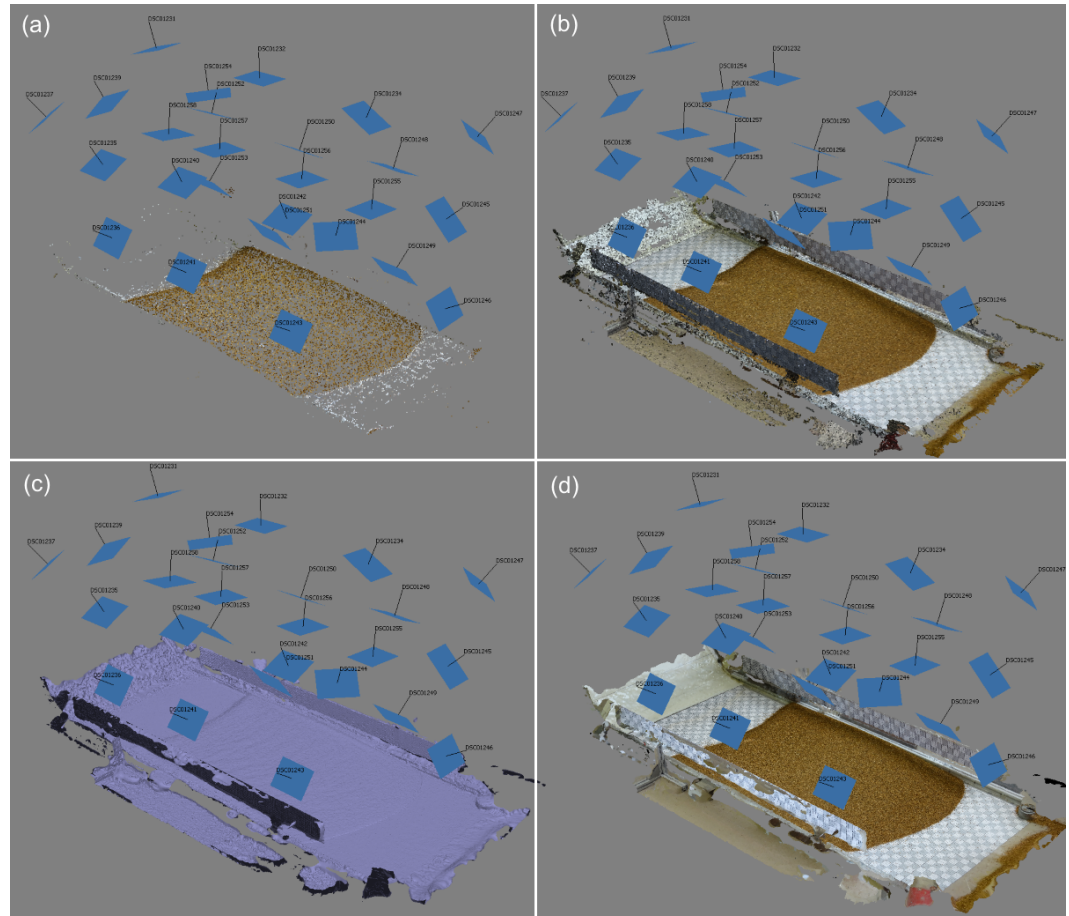


Figure 55 Workflow of Agisoft Photoscan process for generation of slide deposit meshes. (a) Loose point cloud. (b) Dense point cloud. (c) Mesh from dense point cloud. (d) Textured mesh

3. METHODOLOGY

Initially, a loose point cloud was produced to ensure that the reference points and images used in the photogrammetry process are sufficiently accurate and provide sufficient coverage to produce an accurate model. Once the loose point cloud was produced, it was checked for obvious outliers before the dense point cloud was produced. This dense point cloud takes much longer to generate but significantly increases the resolution of the model, allowing the surface roughness to be captured effectively. Mild depth filtering was used in this study so that the roughness of the deposit surface was preserved. This resulted in geometric models corresponding to the real deposit dimensions with an estimated measurement accuracy of ± 0.5 mm. This is roughly equivalent to a particle diameter at the smallest experimental scale. After the dense point cloud was produced, a mesh was constructed from these points, and a texture was applied to it based on the colour data from the images. This texture was analysed to ensure that the positions of individual sand grains were caught successfully by the mesh.

Figure 56 shows the extent of the reference grids used in the largest scale experiments, with similar coverage being used throughout the other experimental scales. It was important to have many reference points in all three directions, to ensure that the scale of the granular deposit is accurately captured and not skewed or distorted. Accordingly, reference grids were used across the flat runout area and above the slide travel path across each sidewall. In the medium- and small-scale experiments, using a laminated paper grid attached to the runout zone was sufficient. For the large-scale experiments, this was replaced with an unlaminated grid overlaid by a 3 mm thick transparent acrylic sheet, which was much more durable and shared the same frictional properties as the laminated grids.

Finally, as the volume of the deposits was captured accurately by this photogrammetry technique, the packing density of the deposits was calculated by dividing the measured slide mass by the slide volume estimated by the surface of the photogrammetric mesh, and then by dividing this by the particle density ρ_s . This could then be subtracted from unity to get the mean porosity N_d of the laboratory deposit, and compared to the initial sample porosity N_s measured directly from the laboratory.



Figure 56 Deposit from experiment L5, with reference gridlines on channel base and channel sidewalls

Overall, this photogrammetry technique allows for efficient and accurate measurement of the slide deposits, providing 3D data that allows key deposit features such as the front, tail, and sidewall structure to be non-dimensionalised and compared across experiments within a scale series. This technique did not require the use of specialist equipment such as laser scanners, making it practical for a wide range of experimental applications. In combination with the other measurement techniques described, this study will allow many key slide parameters to be measured accurately, efficiently, and consistently.

3.4 LIGGGHTS-DEM formulation

The aim of using a numerical simulation in this study was to compare the numerical to the experimental results to understand which physical behaviours could be accurately modelled. In particular, it was important to see whether numerical simulations were capable of capturing scale effects in laboratory experiments. Discrete element modelling (DEM) was chosen due to its ability to capture particle-scale interactions directly, providing a closer physical representation of the slide event than continuum approaches (Section 2.4.3). The DEM simulations in this study were conducted using the Large-scale atomic/molecular massively parallel simulator Improved for General Granular and Granular Heat Transfer Simulations (LIGGGHTS) code from Kloss et al. (2012). As discussed in Section 2.4.3, LIGGGHTS was chosen over other DEM engines due to its open source nature and ease of access compared to codes such as EDEM (EDEM, 2018) and PFC (PFC 5.0, 2018), in addition to its ability to handle rolling friction in particles in comparison to ESyS Particle (Weatherley et al., 2014). Additionally, LIGGGHTS was selected due to its high degree of parallelisation allowing for the full particle counts of laboratory experiments to be simulated in a timely manner using a HPC cluster, which was problematic in previous tests using YADE (Smilauer and Chareyre, 2015).

The LIGGGHTS engine may also be coupled with OpenFOAM to form the complete CFDEM package seen in Shan and Zhao (2014), expanding the array of future research avenues that could be taken with the models formed in this study. The only fluid phase involved in the laboratory slides would be airflow generated by their motion; while this airflow imposes significant forces on the laboratory slide particles, the influence of the main gravity force is dominant throughout the slide events. This study has examined the DEM in isolation of the surrounding and interstitial airflow to identify whether scale effects manifest in granular slides purely due to the scaling of the slide geometry, such as that described by Parez and Aharonov (2015).

3.4.1 LIGGGHTS workflow

While Section 2.4.3 describes many of the facets, advantages, and challenges of DEM in general, this section will rigorously describe the workflow used by the LIGGGHTS engine to calculate particle trajectories and behaviour. LIGGGHTS operates by first reading in an input file, which specifies the simulation domain, the particle and surface types and characteristics, the contact and interaction models to use, and the time-step. This input file also specifies the granular slide geometry, release behaviour, and conditions upon which the slide geometry changes, e.g. when to release the shutter or when to determine that the deposit has settled. Finally, the input file also tells the DEM what information to save (such as particle characteristics) and how often to save this data.

After initialisation with the input file, the granular system is then built and information about the slide event is periodically saved to a log file, with particle characteristics such as position and velocity being saved to separate output files with this save interval. Restart files are also produced at this save interval that can be used to restart the simulation at that moment in time in the event of a crash. Once the simulation and slide event are complete, the final system state is saved to the log file, as well as general timing and performance information. Figure 57 describes the general workflow of the LIGGGHTS engine.

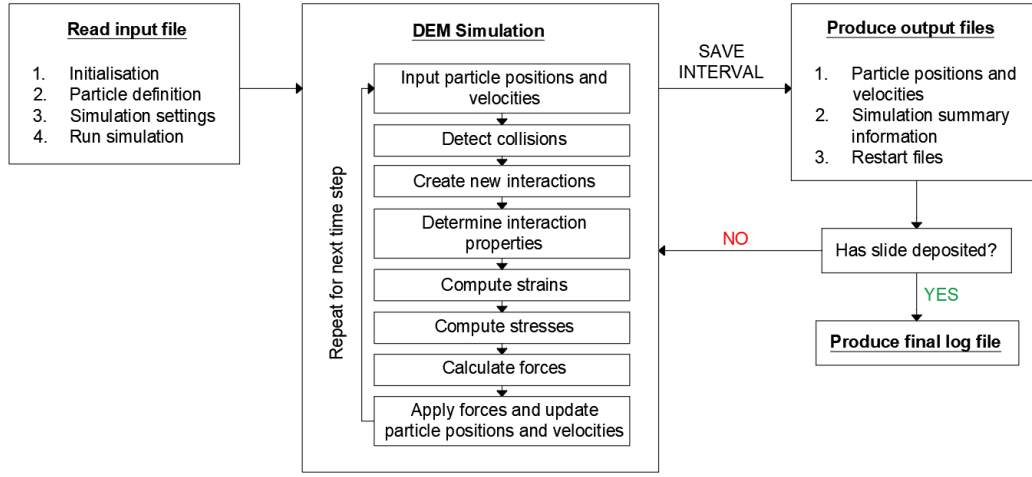


Figure 57 Flowchart of LIGGGHTS engine workflow during simulations

3.4.2 Contact modelling

LIGGGHTS uses a Lagrangian particle solver, explicitly solving particle trajectories throughout the domain. Particle-particle and particle-wall contacts were modelled using a linear spring-dashpot model that determined the normal (\mathbf{F}_n) and tangential (\mathbf{F}_t) contact forces through their respective spring (k_n and k_t) and damping (γ_n and γ_t) coefficients. These forces govern the sliding frictional behaviour of particles, both over themselves and over surfaces. The channel surface and sidewalls act as frictional surfaces that dissipate the forces applied by particles in the same way as other particles in this respect, essentially being treated as particles of infinite radius. These coefficients were calculated from properties such as the Young's Modulus, the Shear Modulus, the Poisson ratio, the restitution (relating to how much kinetic energy is dissipated during a collision) and friction (representing the ratio of the friction force and the normal force acting on the contact) coefficients via a linear contact model using Hertz contact laws. The normal force is

$$\mathbf{F}_n = -k_n \delta_n + \gamma_n \Delta \mathbf{u}_n, \quad (28)$$

while the magnitude of the tangential contact force is given by

$$\mathbf{F}_t = \min\left\{\left|k_t \int_{t_{c,0}}^t \Delta \mathbf{u}_t dt + \gamma_t \Delta \mathbf{u}_t\right|, \mu \mathbf{F}_n\right\}. \quad (29)$$

During collisions, particles were allowed to overlap slightly, with the corresponding repulsive forces between particles being determined by the overlap distance (δ_n being the normal component) and the respective contact normal velocity vector $\Delta \mathbf{u}_n$, while $\Delta \mathbf{u}_t$ is the corresponding tangential velocity vector (Kloss et al., 2012). In Eq. (29), the integral term describes a spring that stores the energy of the relative tangential motion between particles, representing the elastic tangential deformation of the particle surfaces since the contact time $t = t_{c,0}$. The second part describes the energy dissipation of the tangential contact itself. The tangential overlap distance was curtailed to meet the Coulomb friction criterion for a friction coefficient of μ . The exact expressions used to define the spring and damping coefficients can vary, but the expressions used in this study are

$$k_n = \frac{4}{3} E^* \sqrt{r^* \delta_n} \quad (30)$$

$$\gamma_n = -2 \sqrt{\frac{5}{6}} \zeta \sqrt{S_n m^*} \geq 0 \quad (31)$$

$$k_t = 8 G^* \sqrt{r^* \delta_n} \quad (32)$$

$$\gamma_t = -2 \sqrt{\frac{5}{6}} \zeta \sqrt{S_t m^*} \geq 0 \quad (33)$$

$$S_n = 2 E^* \sqrt{r^* \delta_n} \quad (34)$$

$$S_t = 8 G^* \sqrt{r^* \delta_n} \quad (35)$$

$$\zeta = \frac{\ln(e)}{\sqrt{\ln^2(e) + \pi^2}} \quad (36)$$

$$\frac{1}{E^*} = \frac{(1 - \nu_1^2)}{E_1} + \frac{(1 - \nu_2^2)}{E_2} \quad (37)$$

$$\frac{1}{G^*} = \frac{2(2 - \nu_1)(1 + \nu_1)}{E_1} + \frac{2(2 - \nu_2)(1 + \nu_2)}{E_2} \quad (38)$$

$$\frac{1}{r^*} = \frac{1}{r_1} + \frac{1}{r_2} \quad (39)$$

$$\frac{1}{m^*} = \frac{1}{m_1} + \frac{1}{m_2} \quad (40)$$

In Eqs. (30)–(40), parameters with superscript asterisks (*) are the aggregate values between both particles involved in a collision, while parameters with numbered subscripts relate to the first or second particle involved in the collision. r is the particle radius, E the particle Young's Modulus, and G the particle shear modulus. e is the coefficient of restitution of the collision, the particle Poisson ratio $\nu = 0.17$ (AZoM, 2001), and m the particle mass. In this study, a single representative value of e was used for all contacts, as the DEM was fairly insensitive to changes in e within a physically reasonable range. While the spring coefficients k_n and k_t are fixed based on the particle properties, the damping coefficients γ_n and γ_t were tuned through the selection of an appropriate value of e . This value was selected within a reasonable range of values $e = 0.8$ to 0.95 .

Once the normal and tangential forces were calculated, the force balance was then evaluated for each particle by summing \mathbf{F}_n and \mathbf{F}_t with the remaining body force vector \mathbf{F}_b (including gravity, magnetic, and electrostatic forces), given by Eq. (41) and (42) respectively for each specific particle.

$$m\mathbf{a} = \mathbf{F}_n + \mathbf{F}_t + \mathbf{F}_b. \quad (41)$$

$$I \frac{d\boldsymbol{\omega}}{dt} = \boldsymbol{\Sigma}(\mathbf{r}_c \times \mathbf{F}_t) + \mathbf{T}_r. \quad (42)$$

In this study, the additional force vector exerted by the surrounding fluid is zero. m denotes the particle mass while \mathbf{a} denotes the particle translational acceleration vector. I_m denotes the particle moment of inertia, $\boldsymbol{\omega}$ the particle rotational velocity vector, and \mathbf{r}_c the contact radius vector. The momentum balance seen in Eq. (41) thus defines the angular and translational particle accelerations. While this approach is an approximation of real behaviour (real particles do not overlap, for instance), it is adequate for describing the most relevant and important particle behaviour accurately. Overall, this model effectively captures both frictional sliding and rolling of spherical particles.

3.4.3 Modelling shape effects

Two approaches were considered for modelling particle shape effects in this study; multi-sphere particles, and a rolling resistance model applied to spherical particles. As described in Section 2.4.3, the rolling resistance model approximates the energy loss in particle rotations through the application of a coefficient of rolling friction μ_r , related to the coefficient of sliding friction μ . μ_r is defined as the tangent of the angle at which the rolling resistance torque \mathbf{T}_r acting on a particle contact is balanced by the rolling torque produced by gravity acting on the particle (Ai et al., 2011); i.e., the angle at which rolling is fully resisted. While many mechanisms can contribute to rolling resistance in reality (Ai et al., 2011), in the context of the DEM, μ_r solely models the rolling resistance caused by particle shape effects, such as asphericity and angularity. Wensrich and Katterfeld (2012) defines μ_r as a ratio between the mean contact eccentricity $\langle e \rangle$ of a particle contact from its centre of mass, and the rolling radius R_r of an idealised sphere with the particle volume. The value of μ_r reflects the angularity and sphericity of a particle, increasing with particles with sharper contacts and decreasing with more spherical particles.

To produce an estimate of the rolling-resistance coefficient μ_r for particles used in the laboratory experiments, which was necessary for both approaches of approximating shape effects, they were approximated as spheroids. This was a sound approach as a large majority of the sand particles used were appropriately

3. METHODOLOGY

described as spheroids, with only a small minority of super-angular particles that would be better described by multi-sphere clumps. These approximating spheroids are the shape of ellipses revolved around a third dimension, and thus the eccentricity of a contact anywhere on their surfaces can be calculated analytically. Microscope measurements confirmed a mean major/minor axis ratio a/b of 1.55 across all scales, with considerable variation between individual particles (Fig. 47). By placing an ellipse centre at the origin of a set of Cartesian coordinates, as seen in Fig. 58, the expression for the magnitude of a contact eccentricity e_c on the surface of an ellipse is given by

$$e_c = \left| \frac{y_0(1 - \frac{a^2}{b^2})}{\sqrt{\frac{a^2 y_0}{b^2 x_0} + 1}} \right| \quad (43)$$

Revolving this ellipse around the horizontal axis, the point (x_0, y_0) traces a circular line around the surface that has the same eccentricity across it. This allows the mean contact eccentricity of the ellipsoid to be calculated by integrating this expression across the surface, and thus a coefficient of rolling resistance can be assigned to it. For a ratio $a/b = 1.55$, this results in $\mu_r = 0.28$.

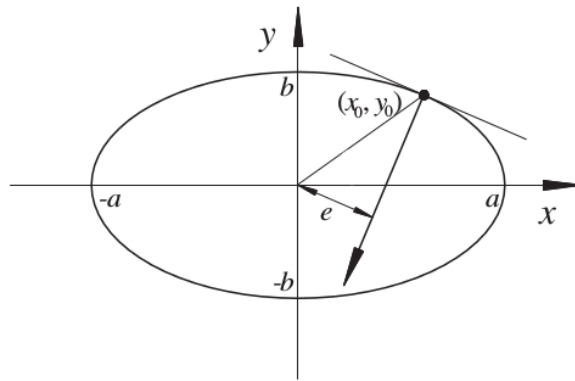


Figure 58 Two dimensional cross section of an elliptical particle (adapted from Wensrich and Katterfeld, 2012)

The rolling resistance model was ultimately chosen for this study due to concerns about the proper modelling of particle angular velocity and inertia via the multi-sphere method, as discussed in Section 2.4.3. Additionally, this method was seen to save significant computational time and resources while still being sufficient for modelling the bulk frictional behaviour of the slide. This system is suited to both kinematically free systems such as granular gases and kinematically restricted systems such as dense granular slides. This rolling resistance was modelled by applying rolling friction as a torque \mathbf{T}_r to particles in collision, either with each other or a surface. This rolling resistance torque is the sum of a mechanical spring torque \mathbf{T}_r^k and a viscous damping torque \mathbf{T}_r^d , and the maximum magnitude of the rolling resistance torque $\mathbf{T}_{r,max}$ is given by

$$\mathbf{T}_{r,max} = \mu_r r_* |\mathbf{F}_n| \quad (44)$$

where r_* is the effective rolling radius of the particle contact. Notably, \mathbf{T}_r always acts against the direction of rotation, resulting in a slight overestimate of rolling resistance compared to actual non-spherical particles. Nevertheless, it models the bulk effects of particle sphericity fairly well (Wensrich and Katterfeld, 2012; Wensrich et al., 2014). \mathbf{T}_r^k is determined using the rolling contact stiffness k_r , which is given by

$$k_r = 2.25 k_n \mu_r^2 r_*^2 \quad (45)$$

where 2.25 is determined as a suitable pre-factor for 3D simulations by Ai et al. (2011). The change in \mathbf{T}_r^k over a single time-step $\Delta \mathbf{T}_r^k$ is then given by Eq. (46), where $\Delta \theta_r$ is the incremental relative rotation between the particles over the time-step. Importantly, the new value of \mathbf{T}_r^k is curtailed by the value of $\mathbf{T}_{r,max}$ seen in Eq. (44). $\Delta \mathbf{T}_r^k$ is then added to the value of \mathbf{T}_r^k from the previous time-step.

$$\Delta \mathbf{T}_r^k = -k_r \Delta \theta_r \quad (46)$$

Meanwhile, \mathbf{T}_r^d is determined using Eq. (47), with a rolling viscous damping ratio η_r being calibrated to adjust the importance of \mathbf{T}_r^d in the rolling resistance model. Importantly, if $\mathbf{T}_r^k = \mathbf{T}_{r,max}$ at a single time-step, \mathbf{T}_r^d is set to 0 for that time-step. $\dot{\theta}_r$ is the relative rolling angular velocity between the particles, while I_r is the mean rolling moment of inertia of the particles (Ai et al., 2011).

$$\mathbf{T}_r^d = -2\eta_r \dot{\theta}_r \sqrt{I_r k_r} \quad (47)$$

While the multi-sphere method ultimately proved to be too resource intensive to simulate the laboratory slides in a timely and accurate manner, tetrahedral clumps were designed that matched the estimated μ_r of the sand, based on the principles of Wensrich and Katterfeld (2012) and Wensrich et al. (2014). This demonstrated that the technique could be applied to studies with reduced particle counts with relative ease. In both of these rolling resistance models, contacts are detected via periodically constructed neighbour lists, which are checked and evaluated based on actual contacts at each time-step, excluding particle pairs that are too distant to have any interaction based on the Verlet parameter (Verlet, 1967).

In this study, the distance at which particle collisions start to be considered was set to two particle diameters, which achieved a good balance between suitability and performance. The size distribution of particles was modelled using a Gaussian distribution with a mean and standard deviation as close as possible to that of the experimental particles for each scale (i.e. 1.35 mm and 0.2 mm respectively at $\lambda = 2$, Table 2). Table 6 in Section 3.4.8 summarises all of the key parameters used in the simulations.

3.4.4 Measuring slide porosity

The slide porosity could also be calculated on a local basis by dividing the slide during a specific time-step into a grid of cubic sub-domains. The Monte-Carlo method was then applied, identifying the ratio of particle space to empty space in each sub-domain. This process could be applied across the whole slide or to a specific volume of interest. This method searched for any particle that had a centre within the maximum particle radius of the specific sub-domain being evaluated, ensuring that even particles that only briefly overlapped the domains were considered. A concave surface mesh was also generated for the slide that further constrained the regions used for porosity calculation, allowing for reasonably accurate estimation of porosity for grid cells that captured the slide surface. Figure 59 shows this process being executed over a single grid cell of 5 mm side length.

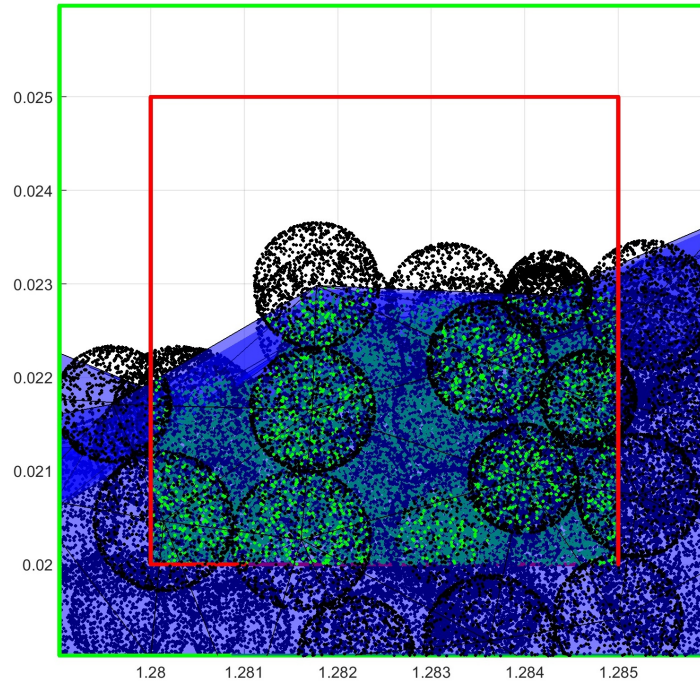


Figure 59 Porosity estimation method. The generated surface contacts (black) enclose Monte-Carlo points generated to fill their volume (green). The red outlined cube and blue surface mesh constrain the Monte-Carlo generation volume, while the green outlined cube constrains which particles are included in the calculation

3.4.5 Slide wedge generation

The particles were gravity deposited in the simulations to match the experimental pre-release conditions as closely as possible, such as the coordination number and radial distribution function (Silbert et al., 2002b; Liu, 2003; Yu et al., 2006). Figure 60 shows the deposition process for the main experiments. The same method was applied to the cylinder tests, where the cylinder itself was the boundary. A very similar process can be seen in a chute geometry in Lo et al. (2010). The process for generating the chute slide wedge up to its release is as follows.

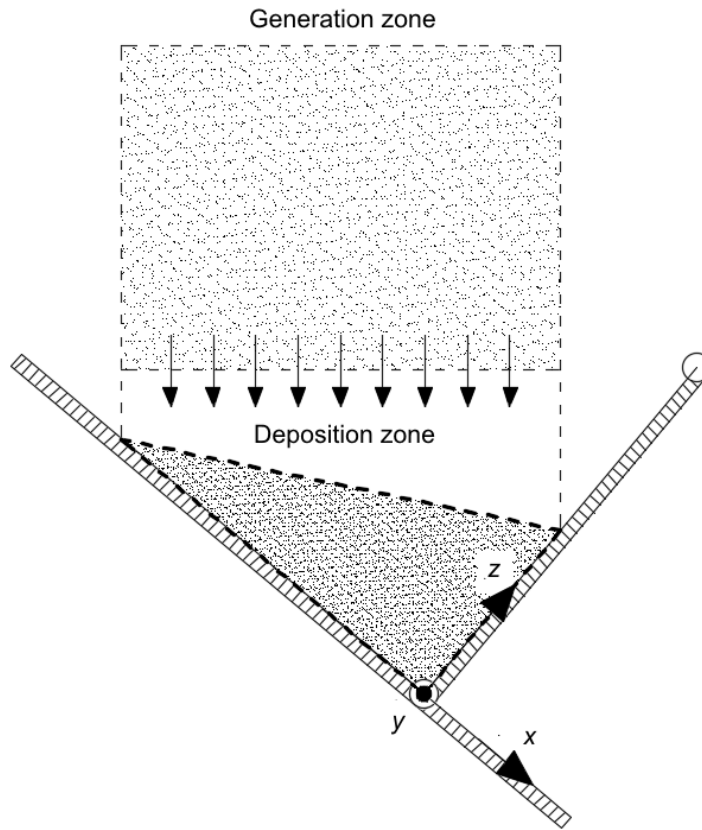


Figure 60 Side view of wedge generation procedure, with the loosely packed particles in the generation zone compacting in the release zone. Particles outside the bold triangular wedge were deleted immediately before release

1. Define the ramp geometry (including shutter in starting position).
2. Add temporary walls at the maximum and minimum position along the length of the ramp at which the slide wedge should be generated. The minimum wall will be some distance behind the shutter, while the maximum wall will intersect the shutter itself.
3. Generate a loose packing ($\Phi = 0.18$) of particles of the desired size distribution just above the chute, confined by the temporary walls and the permanent channel sidewalls.
4. Apply a large, uniform, downward initial velocity to the particles.
5. Run the simulation until the particles have settled, fully covering the desired release wedge domain. The kinetic energy of all particles within this region is tracked throughout the settlement period, and the settlement period ends when this kinetic energy drops below a predetermined value.
6. Delete any particles with centres that lie outside of the release slide wedge domain.
7. Set the velocity of any remaining particles to zero.

While this method did not enforce a set packing density, it allowed the granular system to settle to the lowest stable porosity expected of natural pouring conditions. As the angular laboratory particles are represented as non-interlocking spheres, this resulted in the final release wedge porosities being slightly higher than those seen in the laboratory. An alternative generation method was tested that inserted smaller particles at random initial positions in the deposition zone (Fig. 60) that would grow over time until the desired particle sizes and packing density that matched the laboratory conditions exactly were achieved. However, this configuration did not prove to be stable once the confining shutter was released. At the laboratory packing density, the spheres in the DEM overlapped with each other and exerted a constant pressure on the confining walls. This resulted in a sudden jet of particles being released from under the shutter after release, at

unphysical velocities an order of magnitude greater than expected from gravitational acceleration. This demonstrated that the laboratory packing density could not be achieved in a stable manner with simulated particles in a random packing.

While it is possible that an ordered packing could be designed that better matches the laboratory packing density, the order of this packing could impose additional model effects. Similarly, although the mass of the resulting release wedges differed slightly, compensating for this difference by changing the simulated release wedge dimensions would likely cause greater model effects than the difference in porosity. Overall, given that the difference in porosity between the simulation and laboratory is small, and given that the porosity of both of these systems is representative of a similarly-dense random packing of their respective materials, the simulation was deemed to be sufficiently representative of the laboratory conditions in this regard. More details on the porosity differences between the simulations and laboratory experiments can be found in Section 4.3.6. To model the shutter opening motion, the instantaneous rotational velocity was calculated at regular intervals based on the acceleration rate defined in Table 2. The inherent error caused by using this discrete approach instead of one that updated every time-step was deemed insignificant. Table 6 in Section 3.4.8 provides the settlement parameters used, such as the initial solid volume fraction before gravity deposition Φ_i , and the mean energy threshold per particle required for settlement E_t .

3.4.6 Selection of simulation time-step

An important model effect was the choice of t_s , and how it varied at different scales. Time-steps that are too large result in calculation errors that compound rapidly over time, resulting in unphysical behaviour and violation of conservation of energy, while time-steps that are too small result in inefficient use of time and resources. An initial aim was thus to identify a critical time-step at which the DEM simulations could be run such that calculation errors become negligible. The Rayleigh wave speed v_R transmitted through a particle is a good threshold to use when determining this time-step (Section 2.4.3), and Eq. (20) can be used

to calculate v_R for the particles used in the laboratory experiments of this study. Notably, this critical time-step is proportional to the particle diameter and thus violates the Froude scaling approach taken with the experiments. This is necessary, as matching Δt_c to Fr (i.e. making it proportional to slide velocity) would result in a differing degree of calculation error between experiments of different scales. Accordingly, this means that small scale simulations must take a larger number of time-steps to complete to ensure that no model effects are present in a numerical scale series.

In practise, it was determined that a reduction factor needed to be applied to Δt_c to successfully mitigate calculation errors from the DEM process. This may be due to error caused by discrete approximation of particle motion instead of continuous motion still being significant, despite the threshold for Rayleigh-wave speed being satisfied. To determine this reduction factor, simulations were performed using fully elastic collisions in a 0.05 m cubic box filled with particles of the size distribution of the main simulations at $\lambda = 2$. These particles were randomly placed within the box and set random initial velocities varying in direction and in magnitude from 0 to 1.73 m/s; reasonable values for the intended slide conditions. All particle collisions, both particle-wall and particle-particle collisions, are purely elastic with a coefficient of restitution of 1.0, and gravity, friction coefficients, rolling and damping parameters are all set to zero. Thus with no energy dissipation mechanisms being present, it is expected that the initial energy of the simulated particles in the first time-step will be kept constant, regardless of how long the simulation runs for. Figure 61 shows the kinetic energy of this granular system over time simulated with four different time-steps, ranging from 56% of Δt_c (the final value used in the simulations) to 200% of Δt_c .

It can clearly be seen that an increase in kinetic energy over time occurs in simulations with larger time-steps, with kinetic energy not being conserved despite the lack of any dissipation mechanisms. While this increase is fairly minor at a time-step size of Δt_c , it still becomes significant after 10^7 time-steps, a threshold that could realistically be reached by the main simulations of this study. At larger time-step sizes, the kinetic energy increases much more quickly, with the simulation

3. METHODOLOGY

collapsing completely with 200% of Δt_c . This lack of energy conservation can be entirely ascribed to the numerical calculations in the DEM. In the context of a granular slide in an open channel geometry, these calculation errors and the corresponding kinetic energy "creep" of the simulation could result in increased slide velocities, especially after the initial release period, resulting in higher slide velocities during the spreading and deposition phases, as well as an increase in front position and runout distance due to the "added" kinetic energy. It should be noted that for the main simulations of granular slides conducted in this study, individual particle velocities will vary greatly, both due to their locations within the slide and due to the various dissipation mechanisms that are active, and as a result the potential for a collision energy to be calculated "correctly" is much less predictable than in this idealised validation.

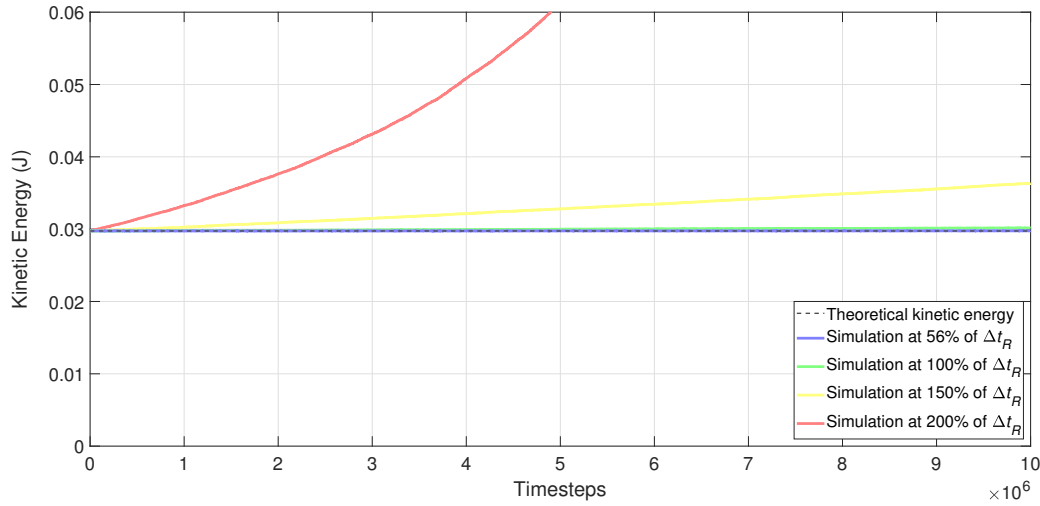


Figure 61 Comparison of simulated kinetic energy over different time-step sizes

Overall, the value determined by this validation can be seen as a conservative estimate, as this validation represents a dissipative gas where particles are colliding with a normal distribution of relative velocities. In the granular slides of this study, the vast majority of particle contacts will be between particles of similar velocity moving as part of the slide mass, and the mean collision energy is much lower, resulting in a lower degree of influence of kinetic energy instability. Similarly, while the kinetic energy in the validation is more strongly influenced by

particle-to-particle and particle-surface collisions than by the frictional sliding seen in granular slides and on the slide channel, the timescale of frictional contacts prevents the kinetic-energy calculations from becoming unstable. This is due to the source of the instability being the shorter contact durations of highly kinetic collisions. Thus the particles in the simulations should not show any of the instability associated with improper time-step selection. The final time-step values selected for the simulations, as well as Δt_c , are provided in Table 6 in Section 3.4.8.

3.4.7 DEM implementation on HPC

The DEM simulations were relatively computationally expensive due to the high particle counts and small time-steps used. This necessitated the use of High Performance Computing (HPC) to run the simulations in a timely manner. CPUs were used to run the simulations as no GPU-based granular solver is yet publicly available as a package for LIGGGHTS, and development of such a solver was beyond the scope of this study. The cylinder validation test contained 658,000 particles and used 12 Dell C6220 computing nodes of 32GB of RAM, each with 2×8 -core processors (Intel Sandybridge E5-2670 2.6GHz) and a Message Passing Interface (MPI) thread for each core. These 192 processors were assigned in a $12 \times 16 \times 1$ grid, representing tall vertical columns dividing the cylinder domain. The simulation time T_s required for the column to settle correctly via gravity deposition was 0.042 s, while the duration T_r of the collapse itself was 0.566 s. The corresponding timings for the chute tests can be seen in Table 5.

Simulations S4 to S6 were completed using the same computing architecture as the cylinder validation, with 6 computing nodes (a total of 96 processors) being arranged in a $1 \times 96 \times 1$ grid in the xyz coordinate system. These simulations were completed using the University of Nottingham's Minerva HPC Service, but simulations S1 to S3 were completed using Athena at HPC Midlands+, which used nodes consisting of 128GB of RAM across 2×14 -core processors (Intel Xeon E5-2680v4 2.4GHz). Meanwhile, simulations S7 to S11 were completed using the University of Nottingham's Augusta HPC Service, which used nodes consisting of 196GB

3. METHODOLOGY

of RAM across 2×20 -core processors (Intel Xeon Gold 6138 20C 2.0GHz CPU). These simulations used a number of nodes that scaled with the particle count for greater efficiency, which was shown to have no effect on the slide dynamics after the initial generation and settlement period. For both HPC configurations, the chute geometry allowed the processors to be divided in a way that ensured each domain was filled with an equal amount of particles, resulting in greater efficiency than the cylinder test.

Notably, particles must be initially generated such that they fit completely within the sub-domain of a single processor, with no overlap. This results in slight gaps forming between particle "strips" in processors upon initial generation. However, these are quickly dissipated during the settlement phases of both the cylinder and chute simulations and due to the randomly generated particles did not seem to have any stratifying effect in the resulting slide motion upon release. After generation, particles can freely flow between domains, with a particle's information being supplied to processors in both domains as it reaches the border between them.

Table 5 provides information on the simulated and real-time run times of the simulations conducted in this study. The particle count n_p and time-step count n_t of the chute slide simulations, along with the settlement time T_s , the respective runout completion time T_r , the total simulation time T_t , as well as the real-time run times $T_{s,real}$, $T_{r,real}$, and $T_{t,real}$, are provided. The simulated settlement times varied due to the thresholds set for the wedge to be considered uniformly settled varying with θ_W . The real-time run-times do not scale consistently with each other due to the different hardware combinations used over the course of the study, but Table 5 still provides a useful comparison of their orders of magnitude.

Table 5 Simulation particle counts and run times

Exp. no.	λ	n_p	n_t	T_s	T_r	T_t	$T_{s,real}$	$T_{r,real}$	$T_{t,real}$
(-)	(-)	(-)	(-)	(s)	(s)	(s)	(hours)	(hours)	(hours)
S1	1	1.95×10^6	8874264	0.181	2.957	3.138	9.820	107.377	117.197
S2	1	2.56×10^6	8993040	0.140	3.040	3.180	12.928	162.024	174.951
S3	1	3.51×10^6	9196656	0.140	3.112	3.252	17.302	222.339	239.641
S4	2	1.94×10^6	12640000	0.128	2.107	2.235	12.644	147.271	159.915
S5	2	2.56×10^6	12800000	0.092	2.171	2.263	13.633	203.540	217.173
S6	2	3.49×10^6	13032000	0.099	2.205	2.304	23.030	297.125	320.155
S7	4	1.94×10^6	17680656	0.090	1.473	1.563	19.579	208.884	228.462
S8	4	2.56×10^6	17906896	0.065	1.518	1.583	20.820	290.756	311.576
S9	4	3.49×10^6	18348064	0.070	1.552	1.622	35.906	422.194	458.100
S10	0.2	1.95×10^6	4098600	0.628	6.617	7.245	7.400	48.688	56.088
S11	20	1.94×10^6	39468000	0.038	0.660	0.698	39.893	417.160	457.052

3.4.8 Summary of DEM parameters

Table 6 provides a summary of all of the calibrated parameters used in the simulations of this study, including the minimum (d_{min}) and maximum (d_{max}) particle diameters generated in the simulations. The time-step sizes t_s and critical time-step thresholds Δt_c are provided, with Section 3.4.6 elaborating on the process used to determine the most suitable time-step for each simulation. Many input parameters remained constant between all simulations; for the quartz particles used throughout, these include the grain Poisson ratio $\nu = 0.17$, the surface Poisson ratio $\nu_s = 0.25$, the grain density $\rho_s = 2650 \text{ kg/m}^3$, the particle Young's modulus $E = 70 \text{ GPa}$ (AZoM, 2001), and the surface Young's modulus $E_s = 210 \text{ GPa}$. Parameters used to determine the settlement of the initial slide wedges and the final deposits are also provided, such as Φ_i and E_t (Section 3.4.5). Values of e , μ , μ_r , and η_r are also provided; the validation for these parameters is provided in Section 4.2.

Table 6 Key DEM calibration parameters

Exp. no.	λ	d_{min}	d	d_{max}	e	μ	μ_r	η_r	Φ_i	E_t	Δt_c	t_s
(-)	(-)	(mm)	(mm)	(mm)	(-)	(-)	(-)	(-)	(-)	(J)	(s)	(s)
S1	1	1.5	2.7	3.9	0.893	0.577	0.28	0.30	0.18	8.0×10^{-11}	6.12×10^{-7}	3.54×10^{-7}
S2	1	1.5	2.7	3.9	0.893	0.577	0.28	0.30	0.18	8.0×10^{-11}	6.12×10^{-7}	3.54×10^{-7}
S3	1	1.5	2.7	3.9	0.893	0.577	0.28	0.30	0.18	8.0×10^{-11}	6.12×10^{-7}	3.54×10^{-7}
S4	2	0.75	1.35	1.95	0.893	0.577	0.28	0.30	0.18	5.0×10^{-12}	3.06×10^{-7}	1.77×10^{-7}
S5	2	0.75	1.35	1.95	0.893	0.577	0.28	0.30	0.18	5.0×10^{-12}	3.06×10^{-7}	1.77×10^{-7}
S6	2	0.75	1.35	1.95	0.893	0.577	0.28	0.30	0.18	5.0×10^{-12}	3.06×10^{-7}	1.77×10^{-7}
S7	4	0.375	0.675	0.975	0.893	0.577	0.28	0.30	0.18	3.1×10^{-13}	1.53×10^{-7}	8.84×10^{-8}
S8	4	0.375	0.675	0.975	0.893	0.577	0.28	0.30	0.18	3.1×10^{-13}	1.53×10^{-7}	8.84×10^{-8}
S9	4	0.375	0.675	0.975	0.893	0.577	0.28	0.30	0.18	3.1×10^{-13}	1.53×10^{-7}	8.84×10^{-8}
S10	0.2	7.5	13.5	19.5	0.893	0.577	0.28	0.30	0.18	5.0×10^{-8}	3.06×10^{-6}	1.77×10^{-6}
S11	20	0.075	0.135	0.195	0.893	0.577	0.28	0.30	0.18	5.0×10^{-16}	3.06×10^{-8}	1.77×10^{-8}

3.5 Summary

In this study, a modular and versatile laboratory set-up has been designed and constructed to be capable of modelling dry granular slides at a range of experimental conditions. A Froude scaling approach was taken to design the key slide parameters for these experiments, with the smallest slide conducted being 0.94 kg in weight and the largest being 108.51 kg. This laboratory set-up was designed such that the slide surface velocity and thickness at positions close to the channel sidewall and centre could be measured accurately and precisely at various distance intervals down the ramp. The particle image velocimetry (PIV) technique was used for velocity measurement. Furthermore, the set-up was designed such that the dimensions of the granular slide could be recorded during motion and measured in detail in its deposited state using stereophotogrammetry, with the workflow required for accurate 3D models being detailed.

The Froude scaling approach was used to calculate the key geometric parameters for the ramp and slide geometry, evaluating how these parameters must be scaled to ensure similarity between all scales as much as possible. Details were also provided of an axisymmetric column collapse set-up which was used to validate a discrete element model (DEM) to provide further qualitative analysis into the granular slide dynamics. The slide generation procedure was described, using a combination of techniques to save simulation time and resources while still achieving a packing in a similar manner to the laboratory experiments. The time-step was also selected for all of the numerical simulations in this study, according to the Rayleigh wave-speed principles identified in Section 2.4.3. The simulation implementation on the University of Nottingham's Minerva and Augusta HPC services and Athena at HPC Midlands+ was also provided.

4 Results

4.1 Introduction

In this chapter, the most important results from this study will be presented. In Section 4.2, focus is placed on some initial results and validations conducted to confirm the validity of the DEM in assessing multiple different granular slide conditions. Comparisons are included in Section 4.2.1 to an axisymmetric column collapse conducted with the sand described in Section 3.2.2, as well as a reproduction of the experimental data recorded from experiment #117 in Hutter et al. (1995). In Section 4.2.2, a comparison is provided between initial simulations that confirms the importance of correctly modelling the size distribution of particles, highlighting vast differences in settlement behaviour between monodisperse and polydisperse simulations with identical mean particle diameters.

Moving on to the main results in Section 4.3, a qualitative comparison is provided in Section 4.3.1 between the shapes and forms of the slide fronts and tails recorded throughout the laboratory and simulated scale series, highlighting differences that manifest as the release wedge surface angle θ_W and experimental scale factor λ are varied. A more comprehensive quantitative comparison of the changes in slide position and dimensions throughout the course of the slide events is provided in Section 4.3.2, with simulation data highlighting the relative slide thicknesses throughout and comparisons being made to laboratory front and tail measurements, displaying clear scale effects. A qualitative assessment of cross-sections from the simulated slides is also conducted. In Section 4.3.3, insight is provided into the distribution of individual particle velocities measured from the simulations. In Section 4.3.4, the differences in slide velocities recorded from different regions of the slides are highlighted, giving insight into how the surface velocity measured in the laboratory experiments can be correlated to other velocities such as the base velocity and the mean slide velocity. Quantitative comparison is also drawn between the simulated and laboratory surface velocities, highlighting clear scale effects.

In Section 4.3.5, the slide thickness recorded at the x_1 and x_2 measurement points is described, highlighting scale effects that impact both the thickness dimension and its fluctuation over time at both the sidewall and central locations. In Section 4.3.6, a qualitative comparison is provided of the laboratory deposits conducted at different scales and initial conditions, before providing further quantitative comparison to the numerical simulation and between experimental repeats. Cross sections of the deposits are provided at channel sidewall and central locations, while the fronts and tails are also recorded. In Section 4.3.7, the capacity of the simulation to capture scale effects is evaluated by providing comparisons between simulations much larger and smaller than their respective laboratory experiments.

4.2 Calibration and validation of DEM

Pilot tests were conducted before the main experimental scale series were carried out, in order to effectively calibrate the DEM to match the laboratory experiments as closely as possible, particularly with respect to frictional and damping parameters. Additionally, these pilot tests were conducted to further evaluate the effects of the particle size distribution and roughness modelling approach.

4.2.1 Frictional and damping parameters

After the correct time-step was selected for the DEM in Section 3.4.6, the axisymmetric column collapse test described in Section 3.2.3 was completed to validate the DEM simulation; in particular, to establish the viability of the rolling resistance approach taken in the DEM formulation. Figure 62 compares the surface of the simulated column collapse deposit to that of the laboratory experiments, with the friction coefficient $\mu = 0.577$, the rolling friction coefficient $\mu_r = 0.28$ and the rolling viscous damping ratio $\eta_r = 0.30$ modelling the rolling resistance and $e = 0.893$ as the coefficient of restitution (Table 6). The laboratory deposit surface was identified via the photogrammetry described in Section 3.3.

4. RESULTS

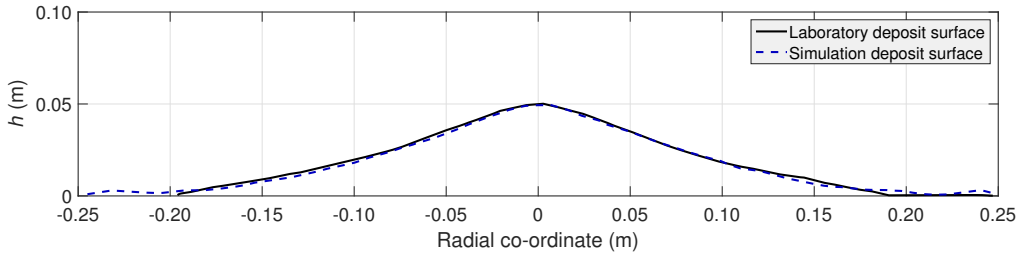


Figure 62 Comparison of laboratory column collapse deposit with simulation

Figure 62 indicates a good match between the simulated and laboratory-measured angles of repose at both the deposit edge (9.5° and 9.9° respectively) and close to the deposit peak (20.7° and 20.1° respectively). The main difference between the laboratory and simulated deposits is the extension of the outer rim into a dilute mono-layer of particles that spreads away from the main mass. This can be attributed to the imperfect nature of using a rolling resistance coefficient to model particle sphericity and angularity. Although the method is suitable for modelling the bulk energy transfer throughout the granular slide, individual particle motion is still less constrained without the presence of physical corners and irregularities.

Figure 63 follows the laboratory and simulated cylinder collapse events over several points in time, with Fig. 63(c) highlighting the dispersive mono-layer in the outer rim. The front of the collapsed pile is defined as the point at which the solid volume fraction of the dispersed front becomes less than half of that of a monolayer of packed particles. There is generally a good match between the evolution of laboratory and simulated column collapses over time, with some small differences caused by slightly non-uniform cylinder acceleration in the laboratory and some of the laboratory particles being freed from the cylinder mass by electrostatic effects. These electrostatic effects are caused by the shearing motion experienced between the sand particles and the acrylic cylinder, and are unlikely to be replicated in the main scale series of this study, where no significant shearing of the slide mass is caused by the rotation of the release shutter.

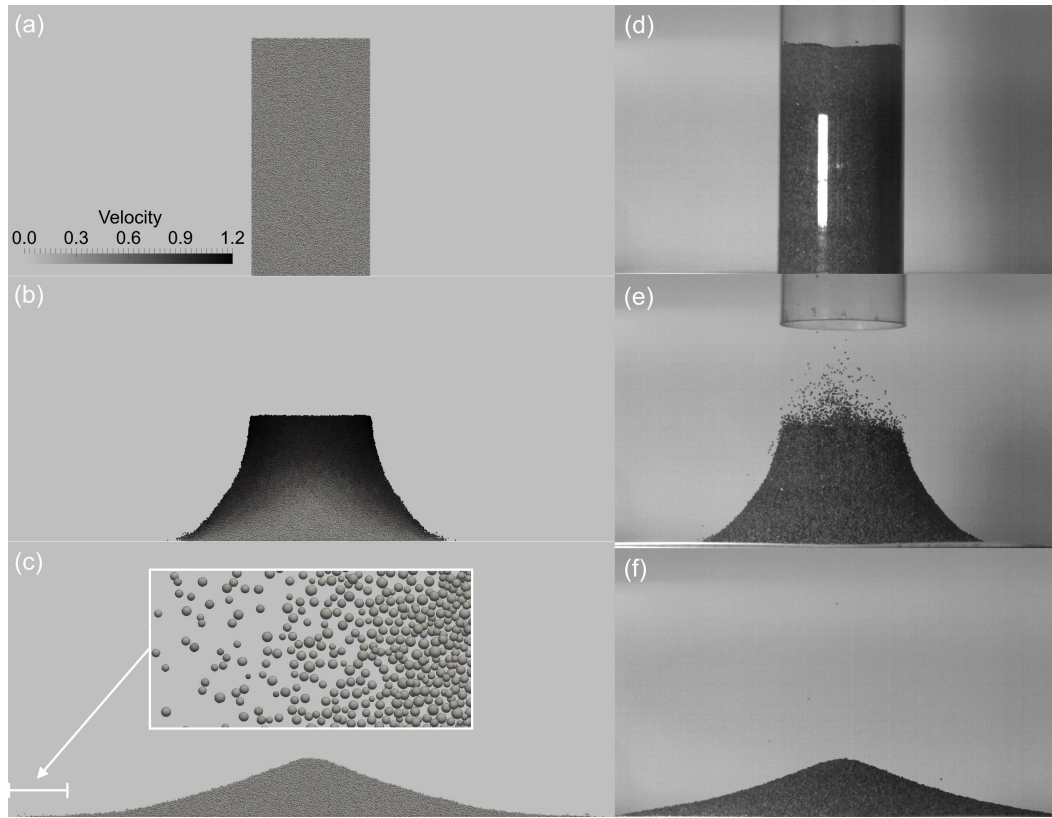


Figure 63 Axisymmetric column collapse simulation at (a) $t = 0$ s, (b) $t = 0.283$ s, (c) $t = 0.609$ s (deposition complete), and (d)–(f) corresponding laboratory images. Subfigure in (c) indicates dilute boundary extent (radial co-ordinate < -0.2) in simulation

To further compare the fit of the column collapse during the collapse event, edge detection was conducted on the high-speed camera images using MATLAB to produce laboratory collapse outlines that could be compared to the simulation data, in a similar manner to Fig. 62. Figure 64 provides this comparison at 0.071 s intervals from the moment of release, providing additional resolution in comparison to Fig. 63. While the accuracy of the outlines produced by this technique is worse than that of the deposit photogrammetry, it is sufficient to show the match of the laboratory and simulated collapse outlines. Generally the match is good throughout the event, with the mismatch seen in Fig. 64 (e) being caused by the spray of loose particles seen in Fig. 63 being included within the surface edge detected.

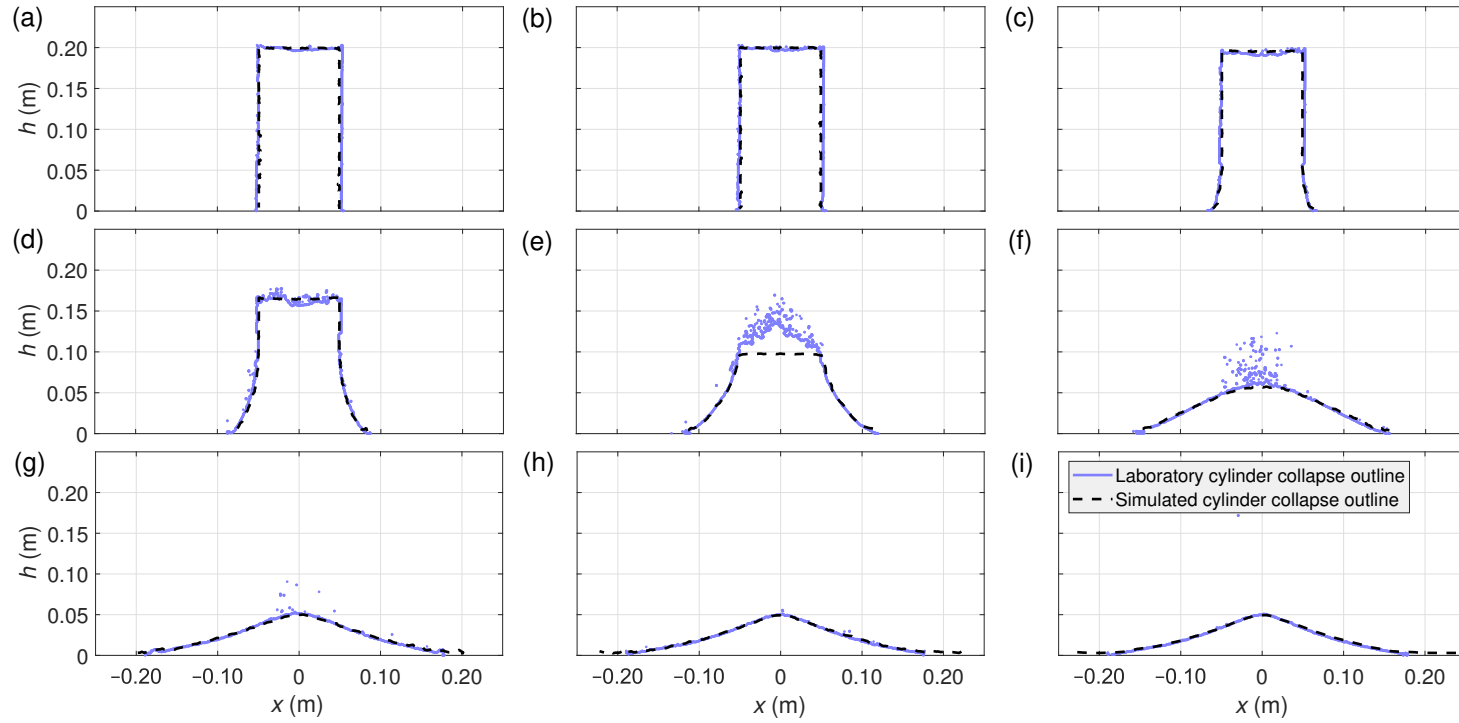


Figure 64 Comparison of laboratory and simulated column collapse outlines at (a) $t = 0$ s, (b) $t = 0.071$ s, (c) $t = 0.141$ s, (d) $t = 0.212$ s, (e) $t = 0.283$ s, (f) $t = 0.354$ s, (g) $t = 0.424$ s, (h) $t = 0.495$ s, and (i) $t = 0.566$ s

As the laboratory and simulated column collapses match well over time, $\mu = 0.577$, $\mu_r = 0.28$, $\eta_r = 0.30$ and $e = 0.893$ were deemed representative values for the granular material. These values were used for all simulations in the main scale series of this study. Although the slide behaviour showed little dependence on e for physically reasonable values, a value of 0.893 was selected due to being the average of the values tested. As the rolling-resistance coefficient and the rolling viscous damping ratio are the only remaining relevant free simulation parameters, the parameters of the DEM were considered validated by this procedure.

To further validate the DEM in the context of modelling real spherical particles, simulations were completed with matching geometries and parameters to experiment #117 from Hutter et al. (1995) (Section 2.5). Comparing the simulations in this study to those of Hutter et al. (1995) allowed them to be tested in a context without the rolling resistance system described in Section 3.4 and for a much different chute geometry. Figure 65 quantitatively compares the simulated slide dimensions and the data points recorded for the corresponding physical experiment in Fig. 22 of Hutter et al. (1995). The position distribution diagram highlights regions of greater thickness with increasing darkness and changing colour. This allowed the slide front, peak, and tail positions to be predicted while also providing context on the shape of the slide as it runs out across the narrow channel. Although the initial release from Hutter et al. (1995) could not be precisely matched due to a lack of information, the predicted slide front, peak and tail positions match well to the laboratory data.

The most notable difference seen in Fig. 65 between experiment #117 of Hutter et al. (1995) and the corresponding simulation is the behaviour of the release wedge immediately after the shutter is triggered. While Fig. 9 in Hutter et al. (1995) shows that a typical undisturbed slide profile was achieved approximately $t = 0.15$ s after release, the simulated wedge front took slightly longer to reach this standard slide configuration despite being fully detached from the shutter. This is despite the shutter acceleration also being calibrated to match that from the laboratory photos in Hutter et al. (1995) as closely as possible, which suggests that this difference is caused by the simulated particle dynamics. Regardless, the

4. RESULTS

bulk slide dynamics seen after this release phase were largely unaffected, with the main difference in timing of the slide runout being easily adjusted for.

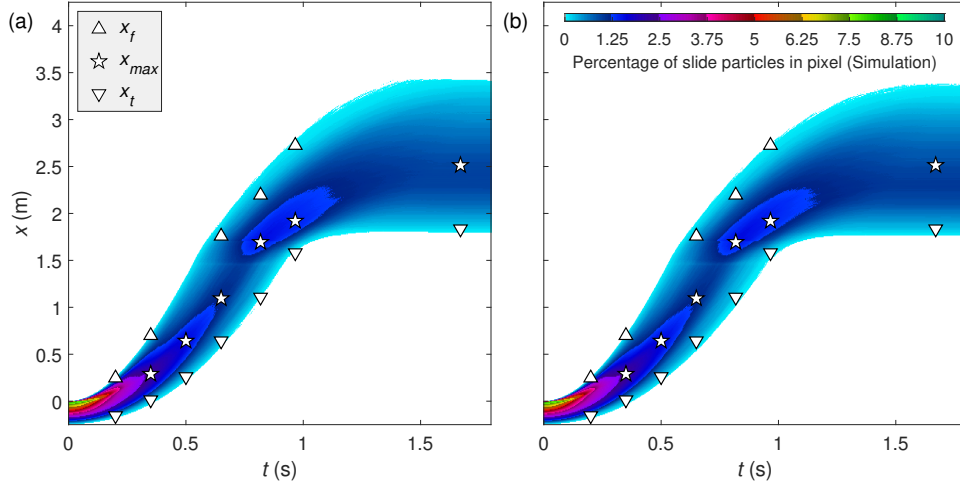


Figure 65 Simulated (background) position distribution compared with x_f , x_{max} , and x_t values from experiment #117 (symbols) of Hutter et al. (1995), with (a) $\delta = 25.14^\circ$ and $\phi = 23.67^\circ$ and (b) $\delta = 28^\circ$ and $\phi = 26^\circ$

As a result, Fig. 65 shows a good match between the simulation and the laboratory results, even better than that provided by the continuum model used in Hutter et al. (1995) and than that seen in the similar comparison of experiment #87 of Hutter et al. (1995) and the DEM simulations of Banton et al. (2009). This confirms that the DEM models the spherical particle dynamics well; in combination with the validation of the rolling resistance model and key simulation parameters seen in the axisymmetric column collapse, this confirms that the DEM is validated and ready for comparison to the main scale series of this study.

Two different sets of friction angles were used in this validation; one using the parameters reported in Hutter et al. (1995), and one using slightly reduced friction angles to investigate the sensitivity of the chute slide to such factors. This approach improves understanding of the potential impacts of error in measurement of frictional parameters in the laboratory experiments of the present study. Figure 65 highlights the differences between these two validation simulations; Fig. 65(a) de-

scribes a simulation using reduced frictional parameters of $\delta = 25.1^\circ$ and $\phi = 23.7^\circ$, while Fig. 65(b) uses the correct respective values of 28° and 26° .

Overall, some slight differences can be seen between Fig. 65(a) and (b), with the deposit front and tail both being about 5 cm closer to the transition curve and the peak being slightly thicker and closer to the transition curve in Fig. 65(b). The front velocity initially remains the same as the slide descends down the inclined channel portion, but notably the slide region immediately after the front remains thinner for a longer distance than in Fig. 65(a). After reaching the transition curve, the front decelerates more quickly in Fig. 65(b), with the slide tail similarly showing decreased acceleration compared to Fig. 65(a) during this time period. These changes all make sense given the increased friction applied to the simulation in Fig. 65(b). Generally, the tail region is more sensitive to the difference in friction coefficients than the front during the slide event, with these differences evening out as the front starts to settle on the flat runout section.

However, it should be noted that the fit to the laboratory data of experiment #117 of Hutter et al. (1995) is still largely preserved, highlighting that these noted differences are relatively minor in terms of how the bulk slide behaviour can be characterised. Specifically, these differences are much less than the differences between experimental scales seen in the laboratory experiments of this study in Section 4.3. Furthermore, these differences are not likely to be influenced by scale effects in the numerical simulation, as the friction coefficients are non-dimensional parameters. Thus, it is reasonable to assume that the influence of minor changes in friction angle on the main laboratory experiments of the present study would be minor. However, it is possible that the differences in chute geometry between the two studies may alter this influence.

4.2.2 Simulation of size distribution

With the DEM being successfully validated, the specific importance of the granular slide material size distribution was evaluated. Preliminary simulations were conducted using monodisperse particles at the mean diameter within the given size distribution at $\lambda = 2$ (Table 6). These monodisperse simulations diverged significantly from simulations with the correct polydisperse particles. In particular, clear differences could be seen in the overall settlement behaviour of the slide front once it had passed the transition curve. Figure 66 highlights this, showing a tendency for the monodisperse particles to settle in a more horizontal manner, with the bottom layer of particles stopping first and subsequent layers of particles building up on top of it. This can be attributed to the bottom layer of particles closely resembling a close-hexagonal packing upon settlement and having a distinct surface upon which another layer can rest. This settled bottom layer quickly extends from the slide front up the transition curve of the ramp, eventually meeting the slide tail as it descends into this region.

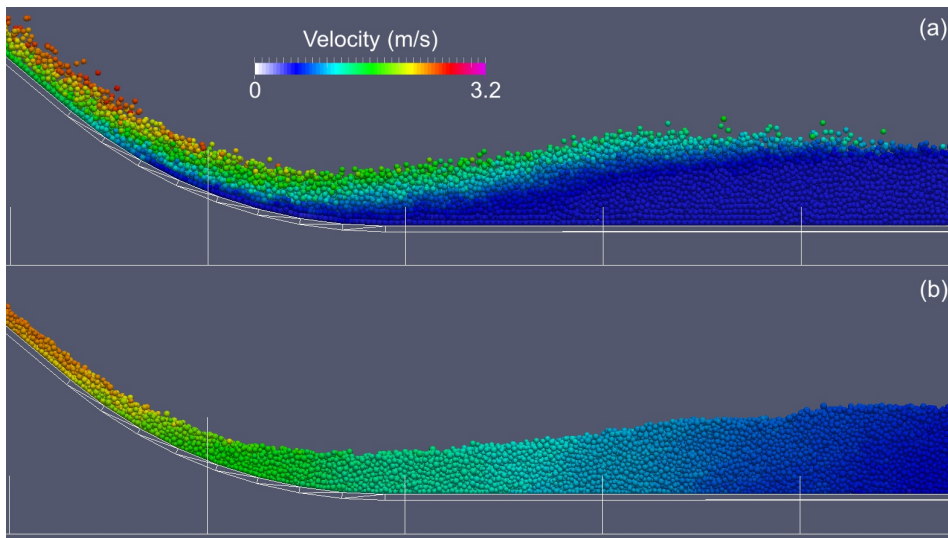


Figure 66 Comparison of (a) monodisperse and (b) polydisperse slide velocities throughout a central vertical cross section midway through the slide event

In contrast, in the polydisperse simulation, the particles can be seen to settle in a more vertical manner, with the particles at the slide front settling first and columns of particles settling thereafter. In this case, there is no uniform packing on the bottom layer for particles to easily settle on or be impeded by. Evidence of kinetic sieving and squeeze expulsion could also be seen in the polydisperse simulation. As the smaller particles fill gaps in the contact network and distribute contact forces, they also dissipate some of the slide energy; the absence of this effect can be seen in the monodisperse granular slide, which has a much more dispersive top layer. More evidence of less energy being dissipated in the thin regions of the monodisperse slide can be seen in its increased runout length. The distances between the slide peak and the front and tail are also significantly increased in the monodisperse slide, as highlighted by Figs. 67 and 68.

Overall, by the time the two slides have deposited, the static monodisperse bottom layer has caused the slide tail to stay confined within the transition curve, while in the polydisperse slide, the tail settles after it clears the region, with no bottom layer settling out before the slide tail arrives. The implications of poorly modelled size distributions are clear.

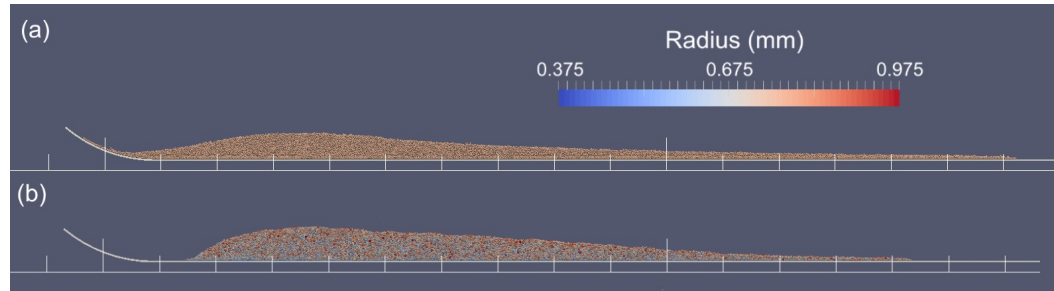


Figure 67 Side view of (a) monodisperse and (b) polydisperse slide deposits with the same release geometries

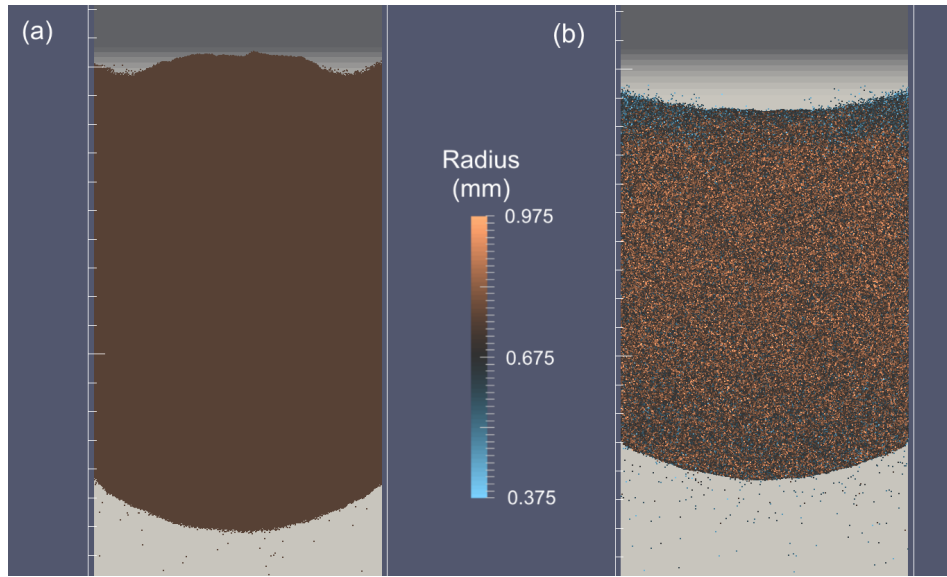


Figure 68 Plan view of (a) monodisperse and (b) polydisperse slide deposits with the same release geometries

4.3 Main results

4.3.1 Comparisons of slide fronts and tails

The main purpose of capturing images of the slide surface at the x_1 and x_2 measurement points (Fig. 44) was to produce estimates of the slide surface velocity. However, these images also allow for qualitative evaluation of many of the features and behaviours that are present in the slides, such as the shape and form of slide fronts and tails. Figures 69 and 70 describe the slide front and tail as it passes through the x_1 measurement point, while Figs. 71 and 72 focus on the x_2 position. In these figures, the channel sidewall is on the left side of each subfigure, while the channel centre-line is on the right side. The slide front is shown as it passes exactly through the measurement point, highlighted with a dashed white line, while the slide tail is shown as it leaves the camera frame at the channel centre. The images shown in Figs. 69 to 72 are representative of the overall slide behaviour and form across laboratory repeats. These images were captured using the high-speed

cameras, with each camera being focused on an interrogation area scaled with λ ; the focus area is $0.5 \text{ m} \times 0.25 \text{ m}$ in subfigures with $\lambda = 1$, $0.25 \text{ m} \times 0.125 \text{ m}$ in subfigures with $\lambda = 2$, and $0.125 \text{ m} \times 0.0625 \text{ m}$ in subfigures with $\lambda = 4$. While the slide colour is brighter at $\lambda = 4$ than at other scales, this is purely due to the colour of the particles used; colour does not indicate any significant differences between fronts and tails at different scales.

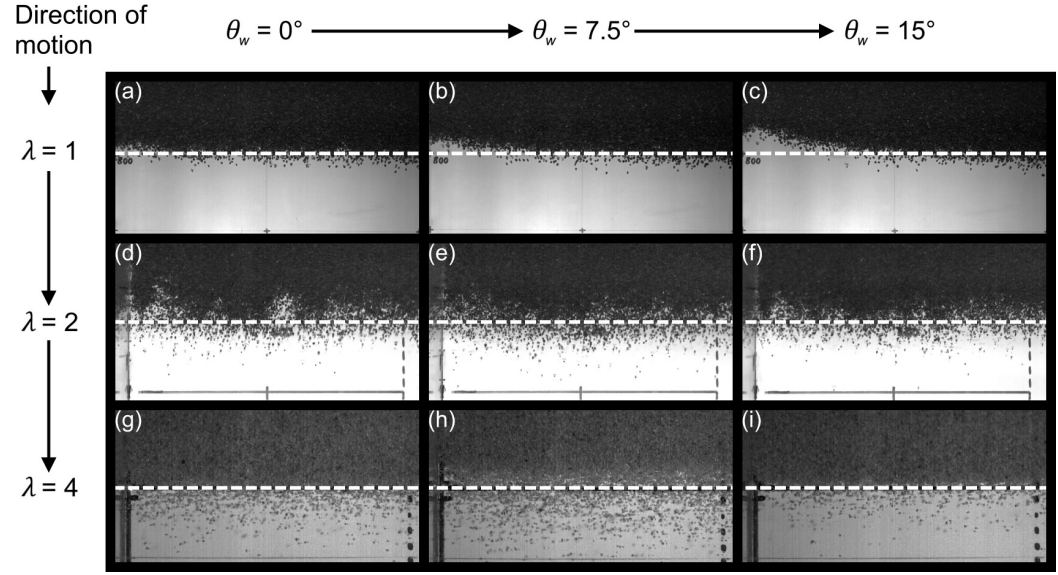


Figure 69 Comparison of slide fronts between left sidewall and centre-line as they approach the x_1 position, increasing in θ_w from left to right, and increasing in λ from top to bottom. Experiment numbers are (a) L6, (b) L12, (c) L17, (d) L21, (e) L25, (f) L29, (g) L37, (h) L45, and (i) L53 (Table 2)

At x_1 , the slide front and tail are clear and defined due to the relatively small travel distance. Figure 69 shows a clear trend at $\lambda = 1$ of increasing front curvature with increasing θ_w , implying that sidewall friction becomes more relevant with increasing slide mass and thickness, despite the release wedge fronts being identical. Additionally, the slide front becomes increasingly dispersed as λ increases. The slide fronts seen in Figs. 69(a), (b), and (c) are relatively clear-cut and the most distant particles remain within about 5 particle diameters of the front, compared to 10 particle diameters in Figs. 69(d), (e), and (f) and 15 particle diameters in Figs. 69(g), (h), and (i). This variation in front structure shows little dependence

4. RESULTS

on θ_W and high dependence on λ , and thus this phenomenon may be a scale effect. This is counter-intuitive, as decreasing Re at smaller scale corresponds to more laminar flow, and thus the random influence of the turbulent airflow surrounding is reduced. Accordingly, the increased front dispersion at the smaller scales can be attributed more closely to the random nature of angular particle collisions. Alternatively, it may be that the increased turbulence at larger scale damps the effects of these individual particle collisions, causing the front and tail to become more uniform and for the airflow to surround the slide body as a whole rather than be steady around individual particles.

As these slides progress, the slide tails diverge significantly as they reach x_1 , with many trends seen in Fig. 69 being exaggerated in Fig. 70. Figure 70 shows a much larger increase in tail curvature with increasing θ_W than that seen at the slide fronts. While the central slide tail region in Fig. 70(a) is relatively flat up to about halfway towards the sidewall, this flat region is about half the size in Fig. 70(b) and barely present at all in Fig. 70(c).

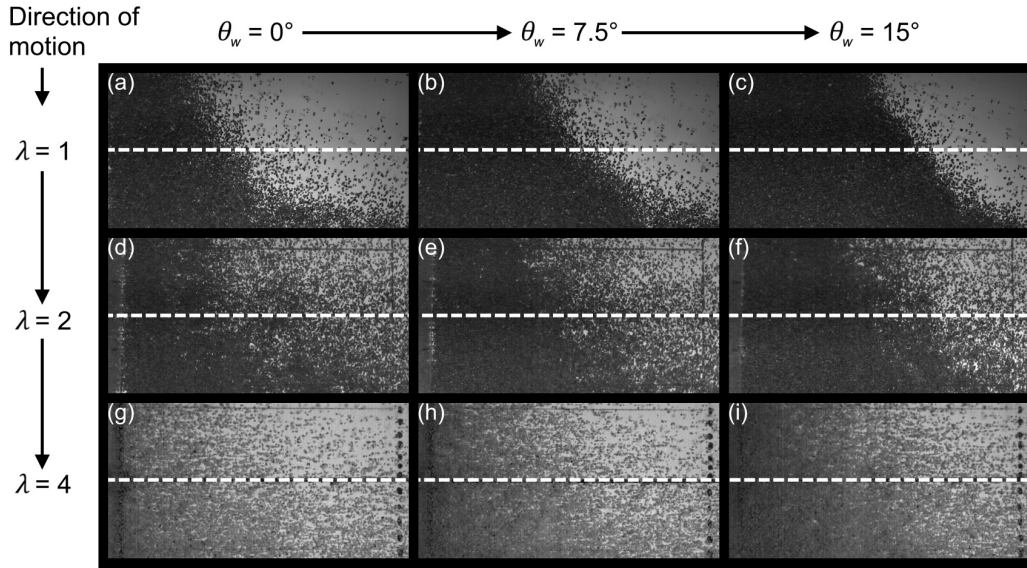


Figure 70 Comparison of slide tails between left sidewall and centre-line as they approach the x_1 position, increasing in θ_W from left to right, and increasing in λ from top to bottom. Experiment numbers are (a) L6, (b) L12, (c) L17, (d) L21, (e) L25, (f) L29, (g) L37, (h) L45, and (i) L53 (Table 2)

This reflects that the slide tail is held further back at the sidewalls as θ_W increases, highlighting the increased influence of sidewall friction on the larger release wedges. Overall, the tail dispersion appears to be relatively equal across all θ_W values but increases as λ increases, showing that differences in air turbulence still affect the slide tail. While difficult to capture due to the extreme dispersion, the increased tail curvature is still visible at increasing θ_W for higher values of λ in Figs. 70(d) to (i).

Meanwhile at x_2 , the slide fronts and tails show similar developmental behaviour as shown at x_1 . Figure 71 shows that the front dispersion increases across all experimental scales and release conditions due to the increased runout time and thus increased particle velocities. Although the front curvature increases in Figs. 71(a), (d), and (g) compared to Fig. 69(a), (d), and (g), this difference is smaller than the difference seen with increasing θ_W , which is still clearly present in Figs. 71(a), (b), and (c).

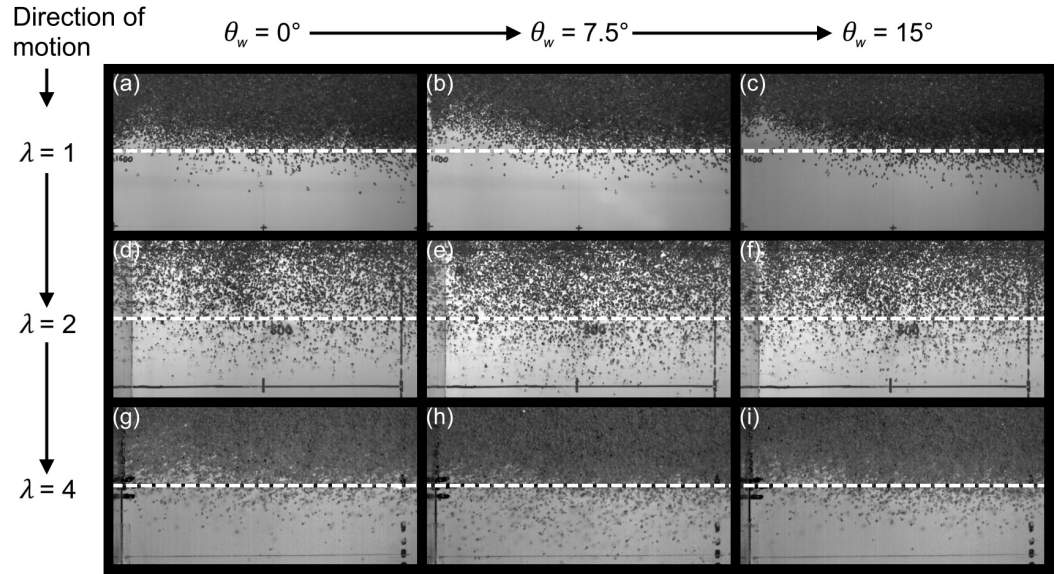


Figure 71 Comparison of slide fronts between left sidewall and centre-line as they approach the x_2 position, increasing in θ_W from left to right, and increasing in λ from top to bottom. Experiment numbers are (a) L6, (b) L12, (c) L17, (d) L21, (e) L25, (f) L29, (g) L37, (h) L45, and (i) L53 (Table 2)

4. RESULTS

The small rate of curvature increase in Figs. 71 compared to Fig. 69 suggests that the influence of confining pressure that causes this difference reduces over time, which makes sense as the slide spreads out significantly as the front travels between the two measurement points. However, the front dispersion in Fig. 71 is increased at $\lambda = 2$ compared Fig. 69 relative to the other experimental scales, with the physical cause for this behaviour being unclear.

The tail behaviour at x_2 in Fig. 72 matches expectations based on Fig. 70, with tail curvature and dispersion increasing uniformly between the measurement points. The tail curvature increase is minor compared to Fig. 70 but still correlates to increasing θ_W , as seen in Figs. 72(a), (b), and (c) and less clearly at the smaller scale experiments.

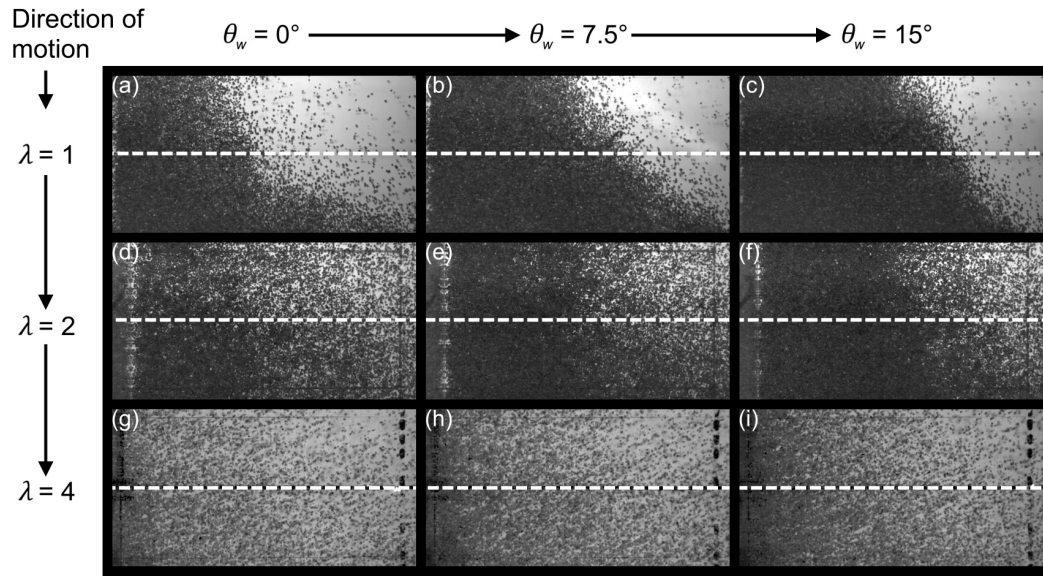


Figure 72 Comparison of slide tails between left sidewall and centre-line as they approach the x_2 position, increasing in θ_W from left to right, and increasing in λ from top to bottom. Experiment numbers are (a) L6, (b) L12, (c) L17, (d) L21, (e) L25, (f) L29, (g) L37, (h) L45, and (i) L53 (Table 2)

Figures 73 and 74 provide corresponding images of the simulated slide fronts and tails at $\lambda = 2$ passing over x_1 and x_2 respectively, with (a) and (c) showing the slide with $\theta_W = 0^\circ$ (S4) and (b) and (d) showing the slide with $\theta_W = 15^\circ$ (S6) in

both figures. Looking first at x_1 , the lack of front curvature seen in the simulation in Fig. 73(a) matches that seen in the laboratory well in Fig. 69(d). However, the front curvature seen in Fig. 73(b) is greatly reduced to that seen in Fig. 69(f). This suggests that the sidewall influence increased slightly with θ_W in the laboratory mechanism via a mechanism that was not captured by the simulation, potentially particle shape effects. The front dispersion is similar between the simulation and laboratory experiments, at least for $\lambda = 2$.

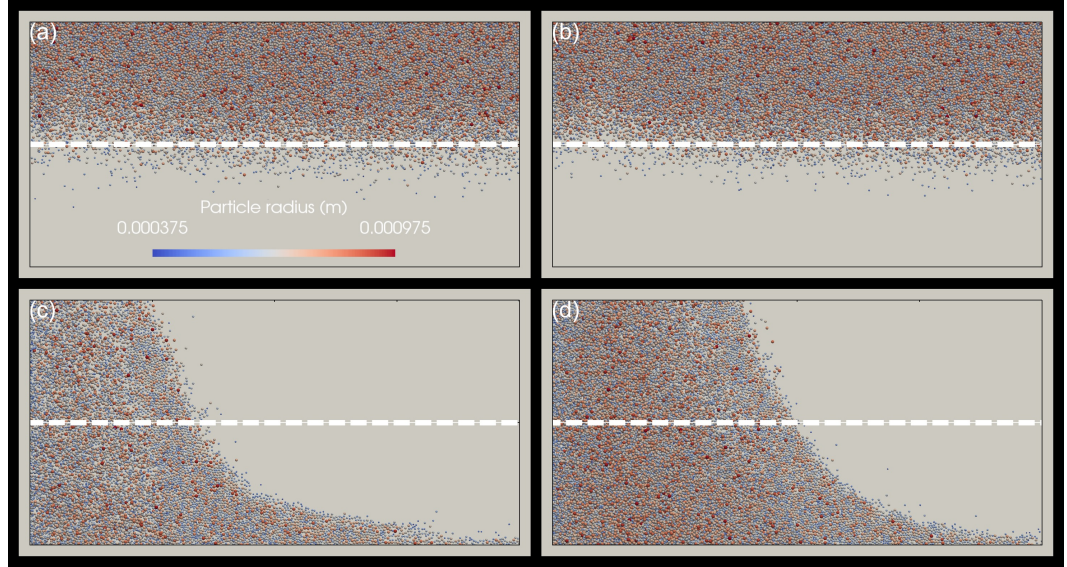


Figure 73 Simulated slide fronts and tails between left sidewall and centre-line passing through x_1 with $\lambda = 2$. (a) Slide front with $\theta_W = 0^\circ$ (S4). (b) Front with $\theta_W = 15^\circ$ (S6). (c) Slide tail with $\theta_W = 0^\circ$ (S4). (d) Tail with $\theta_W = 15^\circ$ (S6)

This highlights that a degree of front dispersion is expected at x_1 even in isolation of particle angularity, which further highlights the Reynolds-related damping effect seen in the larger scale laboratory experiments. However, the tail dispersion at x_1 is far reduced in the simulation (Figs. 73(c) and (d)) compared to the laboratory data at all scales, displaying a clear paraboloid curve and relatively discrete mono-layer consisting mostly of small particles that is only occasionally interrupted. This suggests that the tail dispersion seen in the laboratory experiments can be largely attributed to airflow effects, rather than particle angularity. Additionally, the tail curvature is slightly reduced in the simulations compared to

4. RESULTS

the laboratory slides at even $\lambda = 1$, with this disparity increasing with λ . This suggests that particle shape and airflow effects may start to reduce the sidewall velocity in the laboratory slides as the slide traverses the measurement point, despite not manifesting at that location earlier. Nevertheless, the difference in tail dispersion is stronger than this difference in apparent curvature.

Meanwhile at x_2 , Figs. 74(a) and (b) show similar front dispersion compared to Figs. 71(d) and (f), with the simulations even showing a slightly greater degree of dispersion. This implies that the high relative front dispersion seen in the laboratory experiments at $\lambda = 2$ is not necessarily an outlier. While the fronts display little curvature in either the simulations or the laboratory experiments, the tails seen in Figs. 74(c) and (d) still display the paraboloid curve seen previously, with the mono-layer starting to break up, while the laboratory tail curvature continues to exceed that of the simulated tails. Overall, the influence of air interactions on the laboratory fronts and tails in comparison to the simulation data should be investigated more closely.

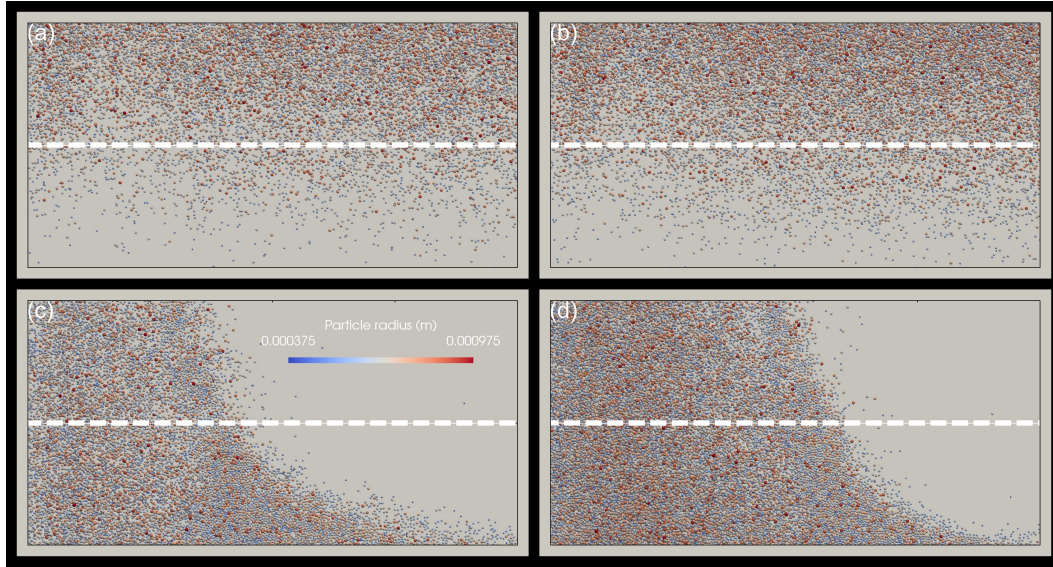


Figure 74 Simulated slide fronts and tails between left sidewall and centre-line passing through x_2 with $\lambda = 2$. (a) Slide front with $\theta_W = 0^\circ$ (S4). (b) Front with $\theta_W = 15^\circ$ (S6). (c) Slide tail with $\theta_W = 0^\circ$ (S4). (d) Tail with $\theta_W = 15^\circ$ (S6)

Directly quantifying the differences seen between the slide fronts and tails across Figs. 69 to 74 is difficult due to the vastly different structural forms that are present. Edge detection (as seen in Section 4.2) can be applied to the laboratory images to define the boundaries of the dilute region and the dense monolayer region of the fronts and tails. However, due to the different lighting conditions and particle colours seen at the different scales, the parameters required for such edge detection to be accurate are difficult to determine and vary drastically with λ and θ_W . The result is not much more useful than a qualitative comparison of the images. Experiments conducted that capture accurate images across a larger section of the channel length, in more uniform lighting conditions and with identically coloured particles, may allow for a more useful quantitative comparison of the diverging front and tail behaviour seen in Figs. 69 to 74. In particular, capturing the entire tail structure as opposed to a small window allows quantitative analysis of its structure to be much more useful.

4.3.2 Slide position distribution

The position distribution of the simulated granular slides was calculated from the moment of initial release and triggering of the shutter to the final deposition phase, for each condition. While this section focuses on quantitatively comparing the laboratory and simulation data on slide position distribution, Section 4.3.7 qualitatively describes the 3D nature of the slides in simulations S4, S10, and S11 with $\theta_W = 0^\circ$ as it evolves. Overall, the simulated slide front rapidly spreads out upon release, with the slide peak and tail taking significantly longer to mobilise as the slide event progresses. Sidewall friction causes some curvature in the slide mass, particularly close to the slide tail, and the slide front region starts to deposit long before the slide tail reaches the transition curve. Slides with higher θ_W share the same general form but with notable differences in the magnitude and duration of certain slide features and behavioural phases. This study will continue to elaborate quantitatively on how these features develop differently in the laboratory and in the simulations.

4. RESULTS

Figures 75 to 76 compare the simulated position distribution for $\lambda = 2$ and increasing values of θ_W to the corresponding laboratory measurements of the slide front and tail positions. The laboratory values were ensemble-averaged from the test repetitions; the data spread from individual experiments for $\lambda = 1$ and 2 can be seen in Section A. With respect to Fig. 65, there are clear differences in the runout behaviour and motion of the slide configuration in this study and that of Hutter et al. (1995). In particular, the slide in this study spreads out significantly more over the course of the initial runout due to the relatively low ramp angle, and the slide peak is shallower overall. Additionally, the slide in experiment #117 of Hutter et al. (1995) clears the transition curve entirely and experiences most of its spreading behaviour after this moment, whereas the tail of the slide in Fig. 75 remains partially in the transition curve, and the front spreads out over a much smaller relative distance, starting to settle long before the slide tail arrives at the transition curve. The deposited slide peak is also much closer to the slide tail and much sharper in general than seen in experiment #117 (Hutter et al., 1995). However, despite the clear changes in geometry and particle type between the two set-ups, the numerical model employed in this study still adequately describes the laboratory slide events.

Figure 75 shows that the simulation accurately describes much of the laboratory behaviour, with the front position matching closely from the initial release up to the point where the slide front starts to settle. The divergence between the laboratory and simulated slide front positions seems to start after the front has passed the transition curve and starts to decelerate. This match appears to be strongest at the channel sidewalls in Fig. 75(a), where the laboratory slide front position exceeded the simulated front position by 4.8%, compared to an increase of 7.1% at the channel centre in Fig. 75(b). The discrete front of the simulated slides occurs where the cyan in the colour-map is strongest, with the loose front region being represented by fainter shades tending towards white. The relative dimensions of the loose front region were similar between the simulation and the laboratory experiments. It can be seen in the laboratory data that the central region of the slide front starts to creep ahead of the sidewall regions in the final deposition phase, while this difference (and thus front curvature) is reduced in the simulations.

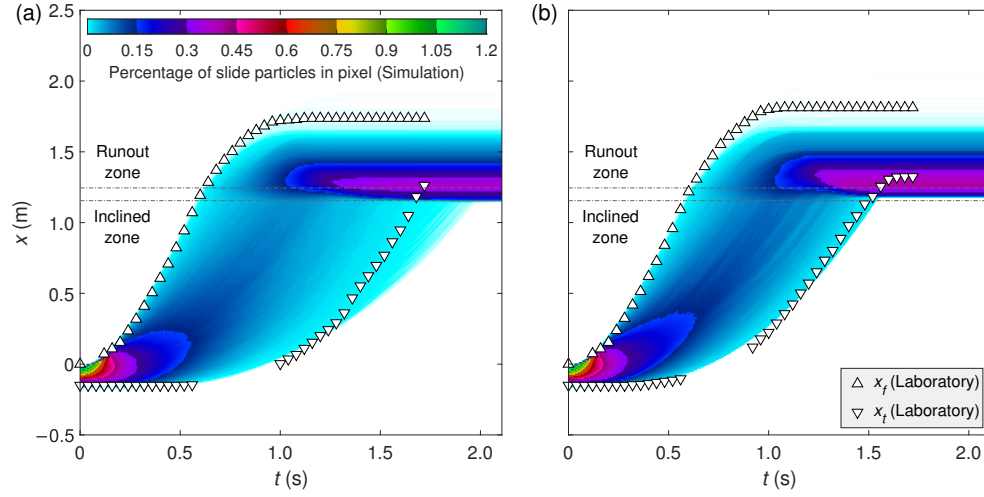


Figure 75 Comparison of position distribution over time between laboratory (L18–L21) and simulation (S4) slides, for $\lambda = 2$ and $\theta_W = 0^\circ$ at (a) channel sidewalls and (b) channel centre

It should be noted that although the simulated slide tail positions appear to be finalised once the bottom cyan region starts to level out in Fig. 75(a), many of the particles are still settling within this small distance interval during this time, increasing the overall settlement time. This factor is diminished in the laboratory experiments due to the nature of angular, interlocking particles restricting this final settlement period; thus the timescales in Figs. 75 to 76 end when the sidewall regions of the laboratory slide tails settle according to camera images.

Overall, there is significantly more difference between the simulated and laboratory slide tail positions, particularly at the channel sidewalls as seen in Fig. 75(a). At the sidewalls, the laboratory and simulated tail positions match well until roughly 1.2s into the slide; at this point, the laboratory tail continues to accelerate past the simulated tail until it approaches a higher constant velocity just before the transition curve. This contrasts with the simulation data, where the slide tail accelerates more slowly down the ramp before impacting the deposit. In Fig. 75(b), the simulated tail position matches the laboratory position more closely at the channel centre, but a clear difference in settlement behaviour is seen, with the

4. RESULTS

simulated slide depositing within the transition curve while the laboratory deposit fully clears this region.

The tail shows significant increased curvature in the simulation, in addition to an overall slower slide tail and deposit buildup closer to the transition curve, despite relatively reduced differences in front position. This may be a reflection of particle shape effects not being captured accurately in the simulation, despite successful validation of the cylinder-collapse case in Section 4.2. While the rolling-resistance approach in LIGGGHTS aims to capture the broad reduction in velocity caused by eccentric particle contacts (Section 3.4.3), this approach does not physically model the interlocking between rough particles, which is most pronounced in the slide tail where particles have less overall energy than in the slide front. Regardless, despite differences in tail behaviour during the slide motion, the final distance between the slide front and tail positions seems to match relatively well between the laboratory and simulated slides.

Looking at Fig. 76, the match between the simulated slide fronts and those in the corresponding laboratory experiments continues to diverge as θ_W increases. The simulated front seems to accelerate very slightly ahead of the laboratory front at $\theta_W = 15^\circ$ as the shutter is released, but this difference seems to dissipate before the transition curve is reached. This phenomenon appears to be equal at both the channel sidewalls and centre, and suggests that the additional mass at the rear of the slide contributes to slight differences in front motion between the laboratory and simulations. At all values of θ_W , the laboratory slide fronts continue to settle further ahead of those in the simulations, with the difference being more pronounced at the sidewalls as θ_W increases, while the difference at the centre is similar for all values of θ_W . Looking at the slide tails, the mismatch seen at $\theta_W = 0^\circ$ in Fig. 75 appears to be replicated in Fig. 76, throughout the slide events and across all values of θ_W . In all cases, the laboratory tails lag behind those of the simulations, but as θ_W increases, the difference in position between the central and sidewall tails also increases. This increases the total time it takes for the slide tail to settle against the deposit mass and significantly increases the overall runout time of the slide events.

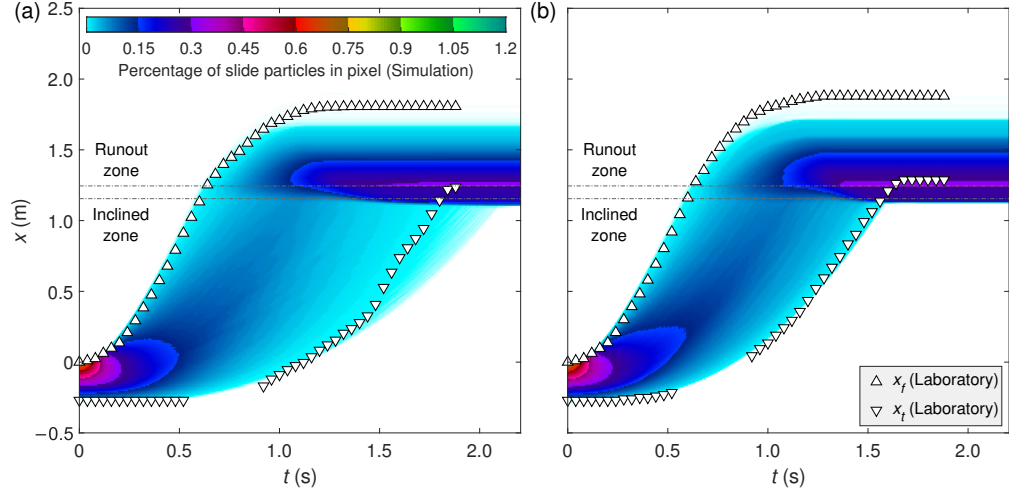


Figure 76 Comparison of position distribution over time between laboratory (L26–L29) and simulation (S6) slides, for $\lambda = 2$ and $\theta_W = 15^\circ$ at (a) channel sidewalls and (b) channel centre

Between $\theta_W = 0$ to 15° , the total slide runout and settlement time increased from 2.10 s to 2.20 s in the simulation; a relative increase of 4.8%. Considering the slide runout time to complete when the simulated slide tail particles first hit the deposit, then this time increases with θ_W from 1.97 s to 2.09 s; a relative increase of 6.1%. However, in the laboratory measurements, the total slide runout time increased from 1.72 s to 1.88 s; a relative increase of 9.3%. This highlights different spreading behaviour in the tail region of the simulated slides that delays the onset of the slide tail and reduces its velocity relative to the laboratory data. Furthermore, the appearance of this increased post-runout settlement period in the simulations seems to be unphysical and not replicated by the laboratory slides, which became completely stationary after the final tail particles impacted the main deposits.

It is likely that this is a consequence of using the DEM, and in particular, the overlap-distance method of evaluating contact dynamics discussed in Section 3.4. As the simulated particles overlap over extremely small time intervals to effectively simulate contact force transmission, particles never become completely stationary

4. RESULTS

in the DEM, but rather the duration and magnitude over these overlap events decrease exponentially over time, until the limits based on system stability are reached. Once this stable configuration is reached, the particles oscillate in position with extremely low amplitude rather than remaining completely still. This is in contrast to real-world systems where the kinetic energy transfer between particles is more complicated and additional energy dissipation mechanisms such as sound and heat quickly diminish the "settlement" energy and time. These additional mechanisms eventually result in the complete dissipation of the kinetic energy, often over a shorter time period than it takes the DEM to reach its low-energy final configuration. It is unclear how much energy from the laboratory slides is lost throughout the course of the slide events, but it appears that this amount is minimal, and only significantly impacts the final settlement behaviour.

Finally, Figs. 75 and 76 confirm that the simulated slide peak occurs closer to the slide front with increasing θ_W as the slide spreads out. Across both initial conditions, clear patterns can be seen in the development of the slide peak, from its initial development as the triangular release wedge stabilises into a typical slide shape. As the slide runs out across the inclined channel section, the peak lags significantly behind the front but starts to accelerate away from the release point much more quickly than the slide tail. Notably, as the slide front passes over the transition curve, the development of a second slide peak occurs in the flat runout zone, characterised by the curvature of the colour contours on Figs. 75 and 76 around $x = 1.2$ m. The peak in the inclined region diminishes in relative thickness as the slide progresses, while the peak in the runout region increases as the deposit mass starts to settle. At all values of θ_W , this second peak seems to stabilise close to the end of the transition curve long before the tail reaches the rest of the deposit, with this peak thickness occurring slightly closer to the transition curve at the channel centre when compared to the sidewalls.

However, looking at the results from other experimental scales, some clear differences can be seen in the slide positioning over time. Figure 77 compares the simulated particle distribution at $\lambda = 1$ to the corresponding laboratory front and tail positions at $\theta_W = 0^\circ$, while Fig. 78 compares them at $\theta_W = 15^\circ$.

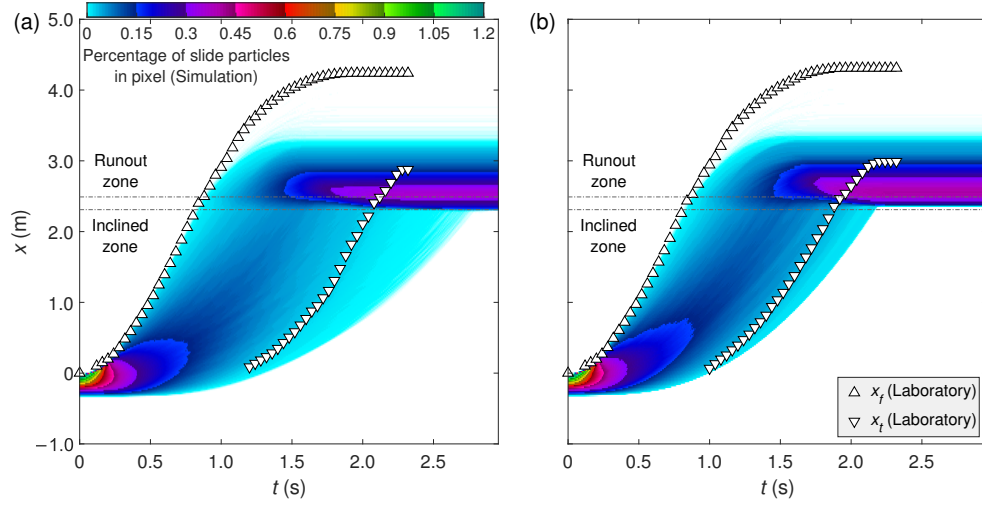


Figure 77 Comparison of position distribution over time between laboratory (L1–L6) and simulation (S1) slides, for $\lambda = 1$ and $\theta_W = 0^\circ$ at (a) channel sidewalls and (b) channel centre

Looking at Fig. 77 first, it is immediately obvious that the match between the laboratory and simulated front and tail positions is much worse once the simulated slide starts to decelerate along the flat runout area. By the time the slides have deposited, the laboratory fronts ran out 26.0% further on average at the channel centre than in the simulation, while the central slide tail ran out about 26.2% further than predicted. This difference increases at $\theta_W = 15^\circ$ to 38.1% at the front and 32.0% at the tail. This contrasts with the front positions recorded at $\lambda = 2$, where the difference between the simulations and laboratory data remains relatively similar between different slide masses. At $\lambda = 1$, despite the obvious overall mismatch, the front positions actually seem to match more closely during the initial release phase of the slide, at least until the slide passes over the transition curve. It remains plausible that air interactions based on Re may be responsible for the increased runout lengths seen at larger scales.

However, the laboratory tails run out significantly further for all measured data points, with Fig. 77(b) showing that this difference again starts to manifest after the slide front has traversed the transition curve. This suggests that the divergent

4. RESULTS

spreading behaviour in the simulated slides restrains the slide tail in a manner not seen in the laboratory experiments, with this phenomenon also causing large differences in deposit settlement and final tail location. More investigation into the difference in tail velocity is presented in Section 4.3.4.

Looking at increasing values of θ_W , Fig. 78 shows some of the same trends at $\lambda = 1$ that were seen at $\lambda = 2$. Both the laboratory and simulated slide masses were more spread out in general, with increased overall slide runout time and separation between the settlement of the slide front and the deposition of the slide tail. Notably, the laboratory slide tail took relatively longer to settle into a fixed position than in Fig. 77, indicating a possible difference in final tail structure. This is supported by the difference in particle distribution seen in Figs. 77 and 78, where the region between the deposit tail and peak regions is implied to be slightly less steep by the increased gap between the cyan and dark-blue colour bands. Additionally, the difference between the central and sidewall front and tail positions throughout the slide events at $\lambda = 1$ are roughly equal in comparison to those at $\lambda = 2$, suggesting that the sidewall friction imposes relatively similar influence on the slides throughout their motion as the experimental scale increases.

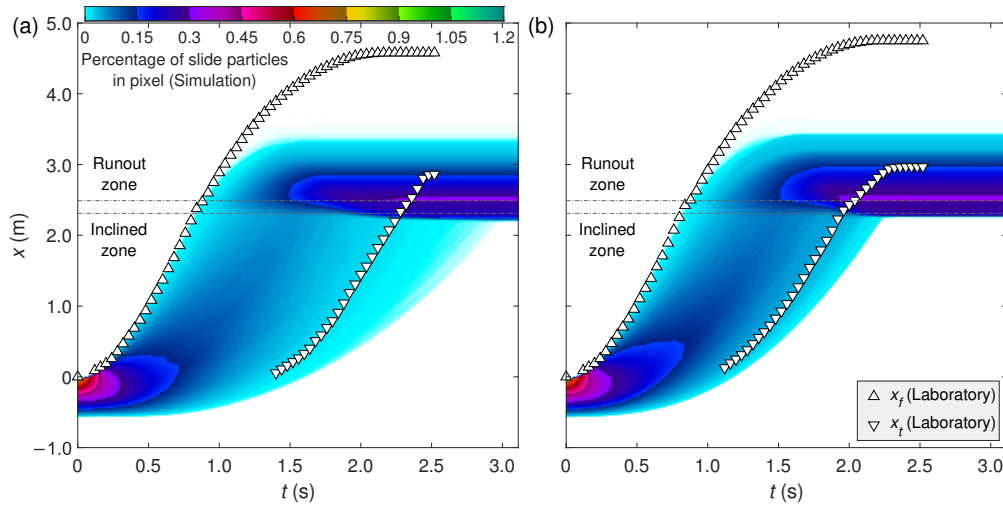


Figure 78 Comparison of position distribution over time between laboratory (L13–L19) and simulation (S3) slides, for $\lambda = 1$ and $\theta_W = 15^\circ$ at (a) channel sidewalls and (b) channel centre

The simulated position distributions of the small-scale simulations at $\lambda = 4$, as well as the laboratory-simulation comparisons at $\theta_W = 7.5^\circ$, can be seen in Section A. The small-scale simulations show continued similarity to the simulations at the other experimental scales, while the data at $\theta_W = 7.5^\circ$ lies approximately at the midpoint between the smaller and larger release wedges.

4.3.3 Slide velocity distribution

Figure 79 provides a description of the simulated slide velocity distribution throughout the course of a slide event, for $\lambda = 2$ and $\theta_W = 0$. Several key features of the slide event can be identified from this technique, allowing for the comparison of these features across different initial conditions and experimental scales.

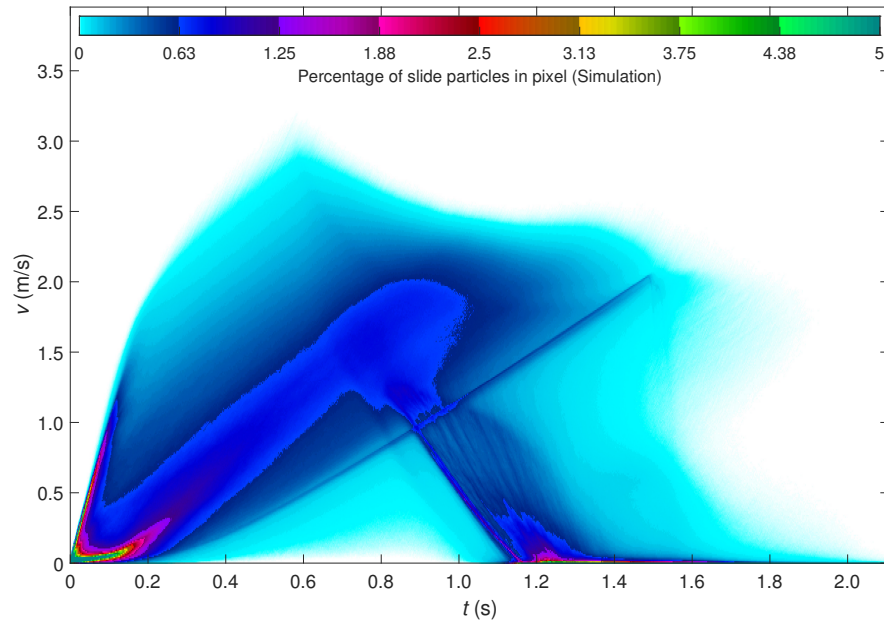


Figure 79 Slide velocity distribution over time for simulation S4, with $\lambda = 2$ and $\theta_W = 0^\circ$

Figure 79 provides some important insight into how the slide velocity behaviour is impacted by λ and θ_W , and will clearly identify any notable features that the

4. RESULTS

simulation captures in ways that would be impossible or impractical to measure in the laboratory. At the initial moment of release ($t = 0$), all of the particles are stationary. Shortly after this moment, for a period of roughly 0.1 s, a clear peak of particles can be seen accelerating very rapidly, due to the relative lack of collisions and frictional behaviour at this phase. This represents the tip of the release wedge most distant from the ramp base but touching the shutter, detaching almost immediately from the shutter as it accelerates rapidly away upon release. These particles then drop under free-fall until they merge with the slide front running along the base of the channel; this event apparently completes at roughly $t = 0.125$ s. Many particles after this moment are still accelerating rapidly; these are particles that have detached themselves from the main slide mass and are colliding infrequently with the ramp surface and sidewalls.

By approximately $t = 0.25$ s, the triangular release wedge has fully transformed into a typical slide mass, with the majority of slide particles now accelerating at a rate of roughly $0.25\ g$ being represented by the central thick blue strip. This strip represents particles in the bulk of the slide mass, close to the slide peak; this is supported by Fig. 75, indicating that the slide peak remains closer to the slide tail than the slide front at this time, and should thus be moving at less than half of the front velocity. Most of the particles at the slide front accelerate at similar rates from $t = 0.25$ s onward, despite their increased overall velocity, while some particles in the slide tail still remain stationary.

Around $t = 0.6$ s, the fastest moving particles can be seen to suddenly decelerate, corresponding to the collision of the slide front with the transition curve of the channel. The particles close to the slide peak are still accelerating uniformly at this point, but slower particles show some different behaviour during this time interval. A clear narrow strip of particles appears, and continues to accelerate slowly at roughly $0.125\ g$ until roughly 1.5 s into this slide; it is reasonable to assume that this corresponds to the discrete region of the simulated slide tail. However, many particles are travelling even more slowly even before the slide reaches the transition curve; this suggests that shearing behaviour within the slide causes individual particles to move more slowly than the slide tail as the shear continues. These par-

ticles may be concentrated at the channel sidewalls, where the additional friction increases the influence of shear flow on the slide dynamics. From $t = 0.6$ s, onward, the slide front starts to rapidly decelerate as it traverses the flat runout zone, with isolated particles at the slide front starting to decelerate below the tail velocity at roughly $t = 0.85$ s. This is highlighted by a dark band that arcs downwards from the maximum velocity, running through the main band representing the majority of particles.

This behaviour leads to the formation of two effective slide peaks between $t = 0.6$ to 1.2 s, with one peak being located in the runout zone close to the slide front (indicated in Fig. 79 by the downwards narrow purple strip) and the original slide peak remaining on the inclined channel section, represented by the diminishing wide blue band. Over time, the particles in this original slide peak start to impact the transition curve, rapidly decelerating as this region impacts the slide front, which is now moving slowly in comparison as seen in Fig. 66(b). This is characterised in Fig. 79 by the subtle vertical stripes that can be seen forming between the two peak stripes. By $t = 1.2$ s, many particles at the slide front have become completely stationary, and many particles in the corresponding slide peak are approaching that state. At this point, the original slide peak has also passed over the transition curve, and as a result the vast majority of particles start to settle quickly, decelerating at between 0.5 – 1 g . The discrete slide tail is still clearly visible, with the last particles contacting the deposit at approximately $t = 1.5$ s and decelerating sharply, although dispersed particles in the slide tail are still seen until roughly $t = 1.9$ s. The main slide mass has become completely stationary at this point, with the dispersed tail particles settling until roughly $t = 2.1$ s.

Figure 80 provides a similar overview of the slide velocity distribution at $\lambda = 2$ for $\theta_W = 15^\circ$, with the main trends and patterns seen in Fig. 79 being reproduced. For instance, the maximum particle velocity occurs at roughly the same time and magnitude for all three release masses, with only a 1% increase in time taken compared to the data at $\theta_W = 0^\circ$. This makes sense, as the fastest moving particles in these slides are detached from the main slide mass and thus would not be influenced by differences in initial release geometries. The moment at which

4. RESULTS

the minimum particle velocity returns to 0 also remains constant at roughly 1 s for all values of θ_W . However, many other aspects of the particle velocity distribution shift subtly as θ_W , particularly those that could be attributed to the peak and tail regions of the slide. For instance, at $\theta_W = 0^\circ$, some particles remain static until about 0.4 s after release, at which point all particles are in motion.

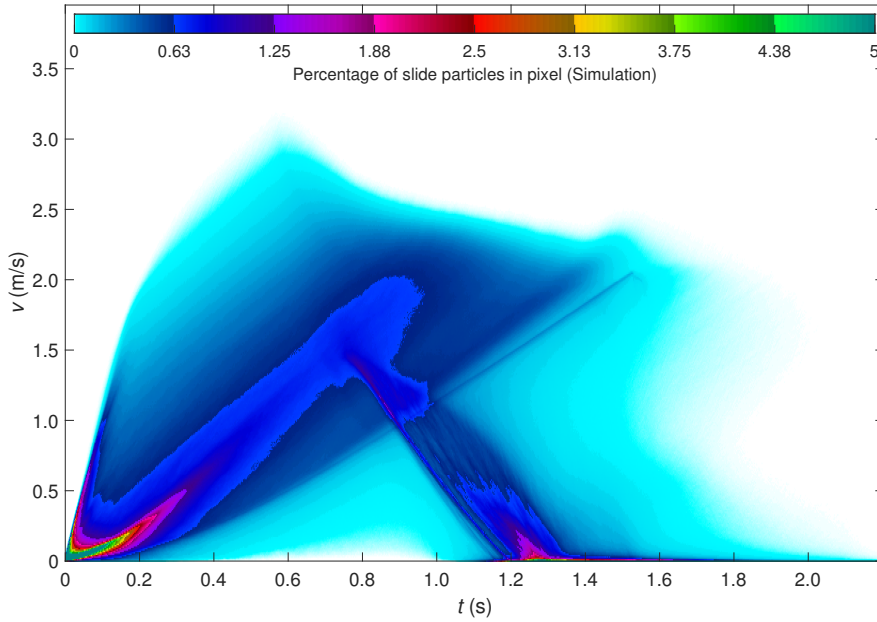


Figure 80 Slide velocity distribution over time for simulation S6, with $\lambda = 2$ and $\theta_W = 15^\circ$

Meanwhile, at $\theta_W = 15^\circ$, this moment does not occur until roughly 0.48 s into the slide event; an increase of roughly 20%. This may be related to changes seen with the green band in the earliest phases of the slide, which mobilises to a greater extent at $\theta_W = 15^\circ$ before the uneven triangular wedge starts to normalise. Additionally, the dark blue band corresponding to the particle velocity at the thickest slide region contracts slightly in thickness, suggesting that the velocity behaviour at peak thickness at higher values of θ_W is less distinct than the velocity behaviour of the surrounding regions. The dark descending band corresponding to the slide front impacting the transition curve in Fig. 79 is much clearer in Fig. 80

but seems to manifest at roughly the same time for both values of θ_W , which is again expected as the slide front behaviour should be independent of θ_W .

The velocity distribution in this core slide region diverges with θ_W after this front impact occurs, suggesting some differences in the shear flow of the settling deposit with θ_W . The discrete slide tail accelerates slightly more slowly as θ_W increases, impacting the deposit at 1.49 s at $\theta_W = 0^\circ$ compared to 1.54 s at $\theta_W = 15^\circ$; a relatively minor change considering the large increase in slide release wedge length between these two conditions. Another clear feature seen in Fig. 80 is a thicker, less distinct dark band of particles slightly faster than those of the discrete tail; as this feature is not visible in Fig. 79, this suggests that the tail structure differs greatly with increasing θ_W .

Similar data from the simulations at $\lambda = 1$ and $\lambda = 4$, as well as those at $\theta_W = 7.5^\circ$, can be seen in Section B, with the simulations showing similar particle velocity distributions throughout the slide events. When non-dimensionalised, these figures confirm that the simulations show little dependence between experimental scale and velocity distribution and slide behaviour.

4.3.4 Slide velocity profiles

While only the slide surface velocity could be measured with PIV in the laboratory at the x_1 and x_2 positions, the simulation provides information on many different aspects of the slide velocity. This helps to provide a better understanding of the physics at play within the granular slides. Figure 81 describes a range of different velocity profiles at the x_1 and x_2 measurement points, detailing simulated values from the moment the slide front arrives at the measurement point to the moment at which the last particles in the slide tail pass through it. Red lines correspond to particles close to the sidewalls, dark blue lines correspond to those near the centre, purple lines represent particles near the channel base, cyan lines correspond to those on the slide surface, and black lines describe all particles. All of these lines represent particles within 1 particle diameter of the region of interest.

4. RESULTS

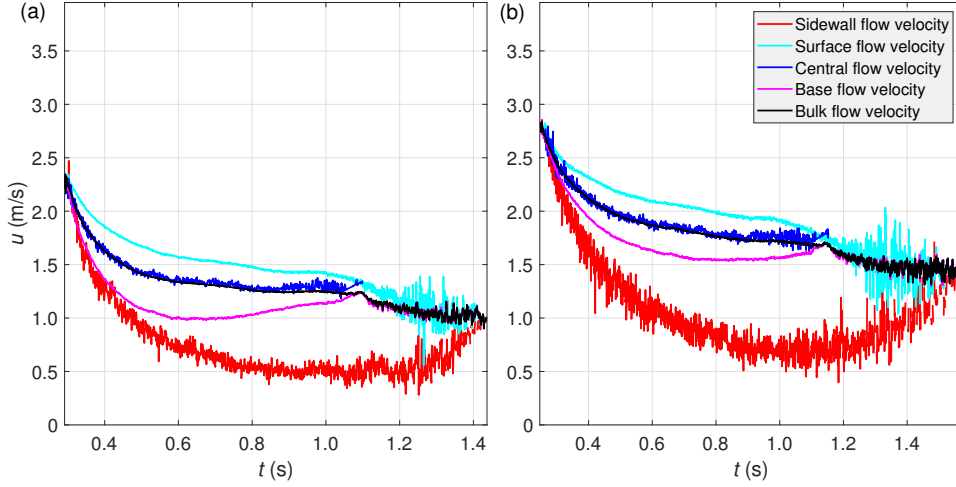


Figure 81 Simulated (S4) slide velocity profiles with $\lambda = 2$ and $\theta_W = 0^\circ$ at (a) x_1 and (b) x_2

Overall, Fig. 81 shows that the slide front enters both measurement points significantly faster than the rest of the slide, with all of the previously described velocity profiles showing deceleration immediately afterwards. While these profiles all start from very similar velocity values when the front arrives as a mono-layer of particles, divergence occurs quickly afterwards. This divergence is strongest at the x_1 measurement point, where after 0.2s of flow, the side flow velocity is 63.3% of the mean velocity of the slide, while the central flow velocity is strongly linked to the mean velocity at this time. Meanwhile, the base flow velocity is roughly 76.5% of the mean velocity, and the surface velocity is roughly 117.8% of the mean velocity. This suggests the presence of a Bagnold-like (Bagnold, 1954) slide velocity profile, albeit with a significant non-zero slip velocity. The base and surface velocity diverge as the slide thickness increases and converge once the slide peak passes the measurement point.

After the initial deceleration, the mean slide velocity enters a "constant" regime where it decreases very slowly as the slide continues to pass. Over time, the side flow velocity at x_1 continues to decrease until it approaches a "constant" minimal value, which in this case is roughly 41.6% of the mean velocity. This minimum is

reached as the central tail region starts to approach the measurement point; after the central tail region has passed, the side velocity starts to climb again due to the lack of confining pressure from adjacent particles. This results in a decrease of roughly 21.7% in the mean slide velocity between the passing of the slide tail at the channel centre and sidewalls respectively. The divergence between the side and central flow velocities justifies the behaviour recorded in the laboratory experiments in Figs. 69 and 70, where small initial differences seen in the slide fronts at the side and centre locations eventually transform into a curved tail.

Similar trends can be seen at the x_2 position, with a few notable differences. Firstly, while the overall velocity of the slide is increased at this point, the initial deceleration rate of the mean slide velocity is slightly lower than that at x_1 , but the deceleration rate remains higher during the "constant regime" until the slide tail arrives. The side flow velocity at x_2 decreases to its minimum value in a similar manner to that at x_1 , but shows increased fluctuation from its mean trend in comparison to the other slide velocity profiles at this measurement point. Additionally, the side velocity almost immediately starts to increase again once it reaches its minimum value. Meanwhile, the divergence of the surface and base velocity profiles is relatively reduced at x_2 compared to x_1 , with the slide peak passing relatively closer to the tail. These two changes can be attributed to the increased longitudinal spreading and reduced thickness of the slide mass as it passes through x_2 . This suggests that the curvature of the Bagnold-like velocity profile decreases as the slide travels down the ramp, converging towards a constant velocity profile.

Figures 82 and 83 provide some indication of the slide velocity profiles in the simulations, looking through a ramp-wise section of the slide. The dotted lines represent the sidewall slide velocity at each measurement point, while the solid lines represent the central slide velocity. These lines are moving averages that are taken from simulation time-steps within $\pm 20,000$ time-steps of the specified simulation time. This is to reduce the influence of outlier particles detached from the slide surface and to provide more accurate averages that are less skewed by the relatively thin slide depth, and thus the coarseness of individual particle velocities at specific time-steps. Even using this method, it can be seen that the mean

4. RESULTS

particle velocity steps up significantly at $z/d = 1$ and 2, where the particles are locked into semi-regular positions due to their proximity to the channel base. This step magnitude decreases further from the channel base as the particle depths are less predictable. The velocity of the particles closest to the slide surface is also represented by circles at the sidewall and squares at the centre respectively.

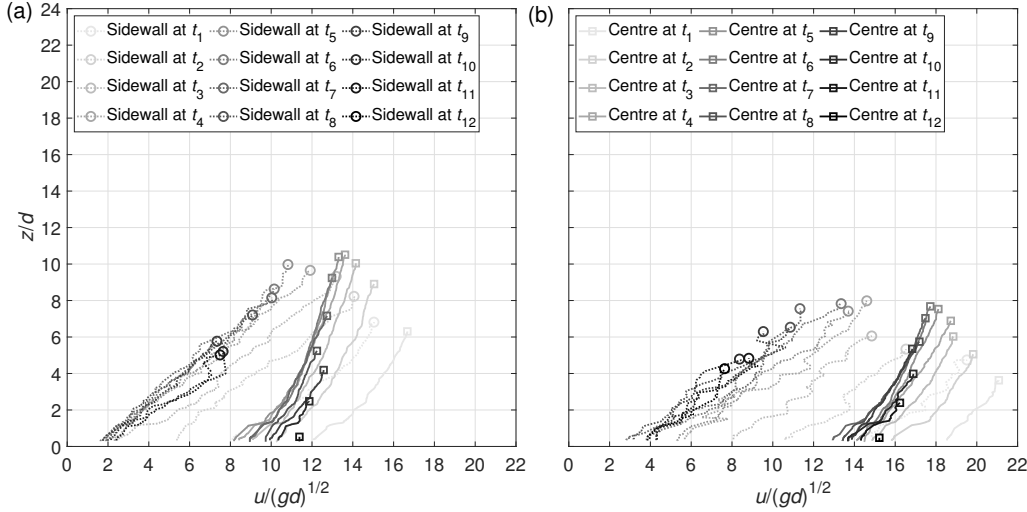


Figure 82 Simulated (S4) non-dimensional mean slide velocity plotted against slide depth at 400,000 time-step intervals, with t_1 starting 400,000 time-steps after the slide front contacts the (a) x_1 and (b) x_2 measurement points, with $\theta_W = 0^\circ$. Circles denote sidewall surface velocities while squares denote central surface velocities

Some clear trends can be seen in how the slide velocity varies over time throughout the simulations at the two measurement points. At the sidewalls, looking at Figs. 82 and 83, the surface velocity typically greatly exceeds the base velocity, with roughly linear trends being seen between velocity and thickness, especially during the middle phases of the slide passing through the measurement point. The gradient of these trends is time-independent at the sidewall location for both values of θ_W , but the gradient reduces with time at the central slide position. As the fronts pass over the measurement points at the channel centre, the rate of change of velocity with thickness remains less than that seen at the sidewalls, although the velocity magnitude is greater due to the lack of sidewall friction.

As time progresses, the rate of change of central velocity decreases with thickness far from the channel base, with the base region seeing greater reduction in velocity. This is especially apparent at $\theta_W = 15^\circ$ in Fig. 83, where this phenomenon only starts to dissipate as the slide tail approaches and the slide surface approaches the channel base. However, this phenomenon is not present at all at the channel sidewalls for either value of θ_W . Additionally, at the sidewalls, the surface velocity decreases rapidly as the front passes, with the rate of decrease reducing as the slide peak starts to move over the measurement point and increasing again once the peak passes through. This contrasts with the behaviour seen at the channel centre, where the rate of decrease of surface velocity reduces continuously from the passing of the front to the arrival of the tail. These behaviours are consistent across all values of θ_W .

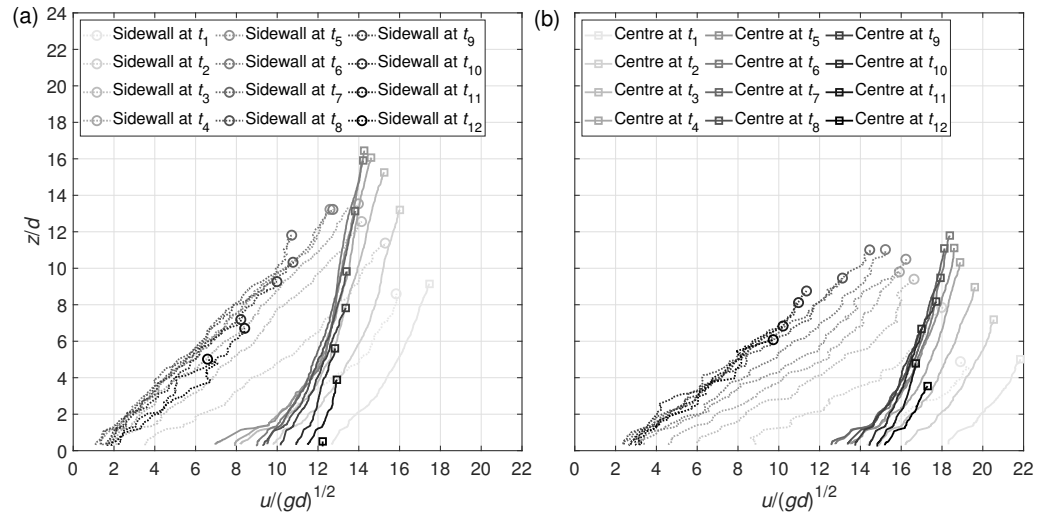


Figure 83 Simulated (S6) non-dimensional mean slide velocity plotted against slide depth at 400,000 time-step intervals, with t_1 starting 400,000 time-steps after the slide front contacts the (a) x_1 and (b) x_2 measurement points, with $\theta_W = 15^\circ$. Circles denote sidewall surface velocities while squares denote central surface velocities

Meanwhile, at the x_2 position, some notable changes can be seen across the two values of θ_W seen in Figs. 82(b) and 83(b). At this point further down the ramp, the slide velocities are increased at all time-steps while the slide thicknesses

4. RESULTS

are reduced. In contrast to Figs. 82(a) and 83(a), the rate of velocity decrease with thickness is more constant with time at the central position, with similar behaviour to that at x_1 at the sidewalls. The rate of surface velocity decrease is increased overall at x_2 at both the sidewall and central positions. These velocity profiles appear to be linear towards the surface across Figs. 82 and 83, in contrast to the expectation of the Bagnold modelling approach, which suggests that the velocity should depend on the slide thickness to a power of 1.5, as seen in Section 2.2.1. However, the sharp reduction in velocity a few particle diameters from the base suggests a power-dependence greater than 1. Additionally, a significant slip velocity can be seen in all of these contexts, while the Bagnold model is designed to be applied to slides without slip velocities, in contexts such as channels with rough boundaries and slides with much finer particles relative to the slide thickness. The match of these velocity profiles to a Bagnold-like model will be evaluated further in Section 5. Overall, these velocity profiles demonstrate a considerable degree of shear flow that is strongest at the sidewalls and diminishes somewhat at the channel centre. The relative influence of this shear (as well as the absolute difference between surface and base velocities) is strongest at x_1 where the mean slide velocities are reduced.

Figure 84 provides a more comprehensive comparison of the surface velocity profiles from the simulations (corresponding to the surface velocity profile in Fig. 81 for $\theta_W = 0^\circ$) to those identified from the laboratory experiments via PIV analysis. These laboratory measurements are ensemble averaged across all experiments for each initial condition. The simulation data is represented as a moving average over a time period of 25 corresponding laboratory camera frames, to clarify the large spread seen as the dilute tail passes through in Fig. 81 for $\theta_W = 0^\circ$. All velocities are mean values across the channel width, closely linked to the channel centre velocity seen in Figs. 82 and 83. Between $\theta_W = 0$ and 15° , some clear trends can be seen for how the simulations compare to the laboratory measurements at the three experimental scales across both measurement points. The velocity and time scales are again non-dimensionalised so that experiments conducted at different scales can be compared quantitatively, based on Froude scaling.

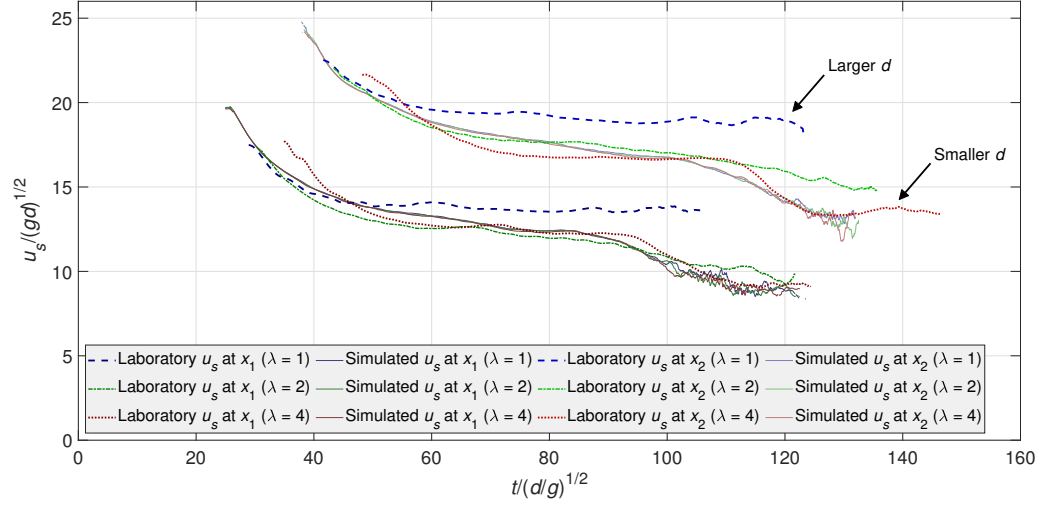


Figure 84 Comparison of ensemble-averaged slide surface velocity profiles at x_1 and x_2 . Laboratory (L1–L6, L18–L21, and L30–L37) and simulated (S1, S4, and S7) velocity measurements with $\theta_W = 0^\circ$

It can be seen in Fig. 84 that the laboratory-measured surface velocity at x_1 and x_2 matches closely when the slide first arrives at the measurement points, at least for $\lambda = 1$ and $\lambda = 2$. The laboratory surface velocity at $\lambda = 4$ implies that the slide arrived at the measurement point slightly later, which could potentially be caused by an air-pressure related effect caused by the relatively fast shutter motion at this scale. However, the behaviour of the slide after it initially passes through the measurement points is more notable. At both measurement points, the laboratory surface velocity at $\lambda = 1$ quickly becomes greater than that of the smaller laboratory scales shortly after the slide front passes over the measurement point. For example, the laboratory surface velocity at the slide tail at x_1 increased by up to 34.8% at $\lambda = 1$ compared to that at $\lambda = 2$, and at x_2 by up to 35.1% at $\lambda = 1$ compared to that at $\lambda = 4$. However, the laboratory surface velocity recorded at x_1 at $\lambda = 2$ and $\lambda = 4$ roughly matches when accounting for the difference in timing, with the laboratory surface velocity at x_2 at $\lambda = 4$ decreasing by only 7.5% compared to that at $\lambda = 2$ during the middle of the slide's passing. This indicates that a scale effect may be manifesting between $\lambda = 2$ and 4 between the two measurement points, only becoming significant after the laboratory slides

4. RESULTS

have ran out to a certain relative velocity. This implies that there may be some critical Re that, if exceeded, results in a reduction in surface velocity.

Figure 85 shows that these behaviours are largely reproduced for a higher value of θ_W , but some distinct differences can be seen as θ_W increases. First of all, while the initial surface velocities recorded as the laboratory slides pass the measurement points remain similar, the rate at which these slides decelerate to the "constant" velocity reduces as θ_W increases. This difference is especially notable for higher values of λ and particularly at x_1 , where the confining pressure from the slide mass is greater than at x_2 . The differences in the longitudinal pressure distribution caused by the ramp-wise component of the slide weight pushing the slide front further down the ramp thus manifest as increased relative velocity.

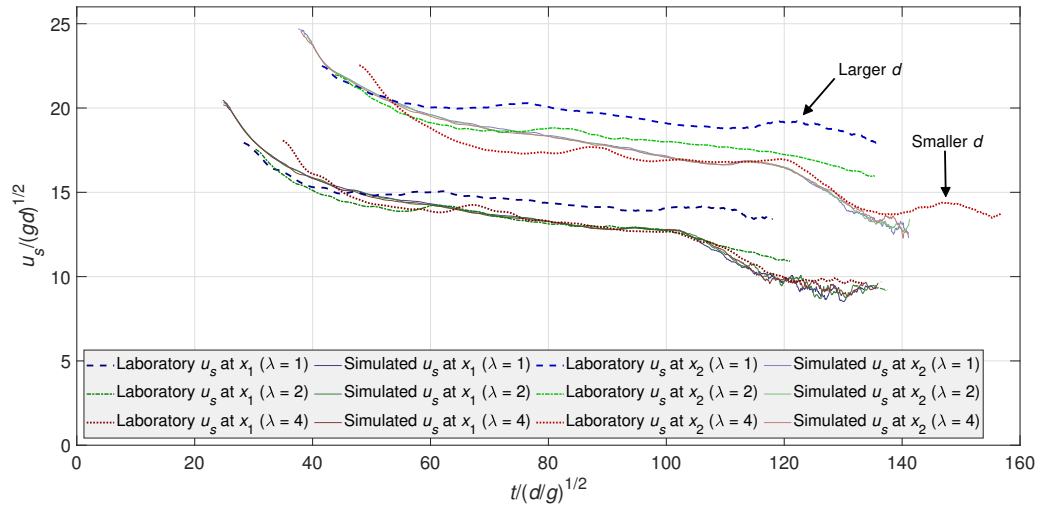


Figure 85 Comparison of ensemble-averaged slide surface velocity profiles at x_1 and x_2 . Laboratory (L13–L17, L26–L29, and L46–L53) and simulated (S3, S6, and S9) velocity measurements with $\theta_W = 15^\circ$

Additionally, the presence of an unusual feature can be seen to develop as θ_W increases; a ridge where the laboratory surface velocity increases temporarily before dipping back down to the "constant" value. This ridge appears to occur increasingly late into the slide event as λ increases across all initial conditions, with the timing remaining largely the same but the magnitude increasing for increasing values of

θ_W . The fact that this ridge shows a positive correlation with the slide mass implies that it is caused by increasing pressure acting on the slide at these moments. This implies that the relative steepness of the slide peak may be causing this ridge, with some particle shape effect or slide shape-dependent airflow interaction causing this ridge to manifest in the laboratory experiments.

Overall, the simulated surface velocity did not vary significantly with λ , with small differences at the slide tail being caused by the random motion of the dilute tail particles increasingly impacting the average velocity as the particle count decreased. Generally, the simulated surface velocity behaves as a mixture of the laboratory velocity measurements at $\lambda = 1$ and $\lambda = 2$ at both x_1 and x_2 . The initial front velocity appears to be slightly higher, but quickly reduces to levels comparable to the laboratory data at $\lambda = 2$. The development of the ridge seen in the laboratory data does not seem to occur in the simulation, suggesting the phenomenon may be caused by shape effects, acoustic effects, or airflow-related mechanisms. As the simulated tail starts to approach the measurement points, the surface velocity rapidly decreases in a manner similar to the laboratory data at $\lambda = 1$, with minimal simulated surface velocities only being slightly lower than that of the laboratory data and occurring with similar timing for all values of θ_W . The influence of air interactions on the slide surface velocity should be investigated further. Related data for $\theta_W = 7.5^\circ$ can be found in Fig. 146 in Section C.

4.3.5 Slide thickness profiles

While the laboratory images and Figs. 75–76 provide a good top-down perspective on the slide behaviour, the laboratory set-up could not capture the complete shape of the slide looking through the slide direction, i.e. providing a cross-section of the slide. However, the simulation can easily provide data that may be useful for understanding later results collected with the laboratory set-up.

Figure 86 shows a series of typical sections of the simulated slides passing through the x_1 and x_2 measurement points, with particle centres being represented by black circles and the detected surface being highlighted by the red line in each

4. RESULTS

case. In this case, $\theta_W = 15$, resulting in a relatively thick slide of roughly $18d$ at peak thickness.

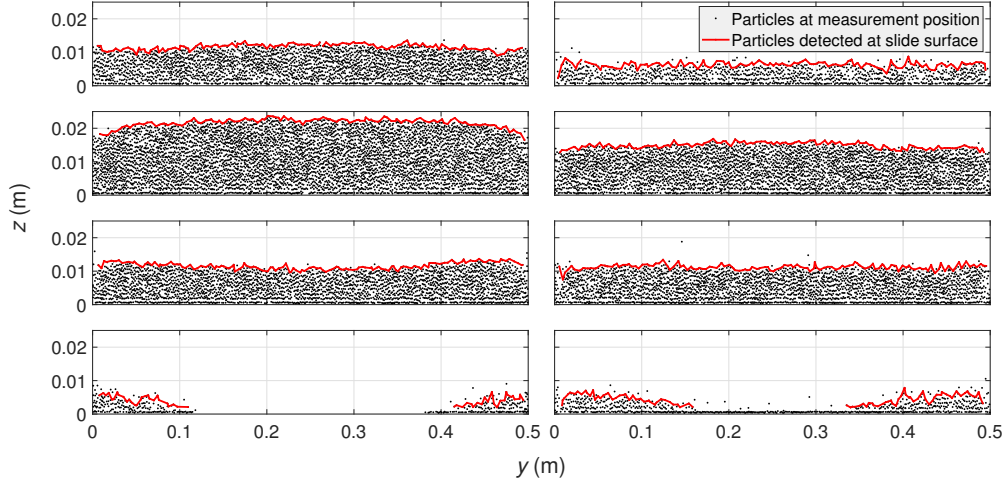


Figure 86 Cross-sections of simulated slide (S6) at 1,600,000 time-step intervals, starting 400,000 time-steps after (left) the slide front contacts the x_1 measurement point and (right) the slide front contacts the x_2 measurement point

Several features can be identified from this comparison. Firstly, when the simulated slide front passes over each measurement point, the surface of the slide starts off relatively flat, but with significant fluctuations caused by particularly energetic particles detaching themselves from the slide mass. Particles that were sufficiently detached from the slide mass were generally ignored in the surface approximation. As the slide progresses across the measurement points and approaches peak thickness, a clear transition can be seen into a curved surface, with the slide being thickest in the middle and decreasing slightly in thickness directly adjacent to the sidewalls.

Notably, as the slide thickness starts to decrease and the tail approaches the measurement points, the surface transitions from a convex into a concave shape. This is due to the influence of sidewall friction, which initially impedes the motion of the slide particles and reduces the thickness that can accumulate at the sidewalls, but simultaneously prevents the thickness from diminishing as quickly as that in the

central region. Once the central slide tail passes, raised concave wedges continue to pass through the measurement points.

The thickness of the slide was measured in the laboratory using the laser trigonometry method described in Section 3.3, with the sidewall thickness being measured at the x_1 position and the central thickness being measured at the x_2 position. Figures 87 to 90 compare the laboratory measurements to the simulated thickness, at both measurement positions and for all values of θ_W . There was a small degree of variance in the position of the laser points due to the granularity of the slide surface and the occasional interference of loose particles, as demonstrated by the simulation in Fig. 86. Accordingly, scatter clouds are portrayed showing the recorded thickness values at regular intervals of 25 camera frames across all experiments in each respective data-set, with a local mean then being calculated and plotted for comparison to the simulated thickness, which could be tracked more precisely. The time and thickness scales are again non-dimensionalised to ensure that data at different experimental scales can be compared directly. Generally, the simulated slide thickness measurements showed no consistent variation with λ .

Figure 87 describes the variation of thickness at the channel sidewall at x_1 , with $\theta_W = 0^\circ$. In general, both the simulated and laboratory slides rapidly increased in thickness from the passing of the initial front to a peak thickness at this sidewall location, occurring about a quarter of the way through the simulated slide event and closer to the slide tail passing in the laboratory events, particularly with increasing λ . After reaching this peak sidewall thickness, the slide maintains this peak thickness for a short period before diminishing in a linear trend until the dispersed tail region reaches the measurement point.

Overall, the rate of decrease matches well between the numerical simulation and the laboratory experiments at $\lambda = 2$ and 4, with the rate of decrease being increased at $\lambda = 1$. This is consistent with the surface velocity matching well between the smaller-scale simulations and the simulation, as seen in Figs. 84 and 85. While there is no clear correlation between the eventual peak thickness in this sidewall region and λ , the simulated slide demonstrated an increase in overall thickness compared to the laboratory slides at the sidewall location. During the

4. RESULTS

initial build-up, the peak laboratory thickness was between 2–3 particle diameters below the simulated value, before the difference in thickness decrease rate begins to dominate at the smaller laboratory scales. This demonstrates that scale effects mainly influence the slide velocity rather than its maximum thickness. However, the simulated slide peak thickness starts to diminish much more quickly.

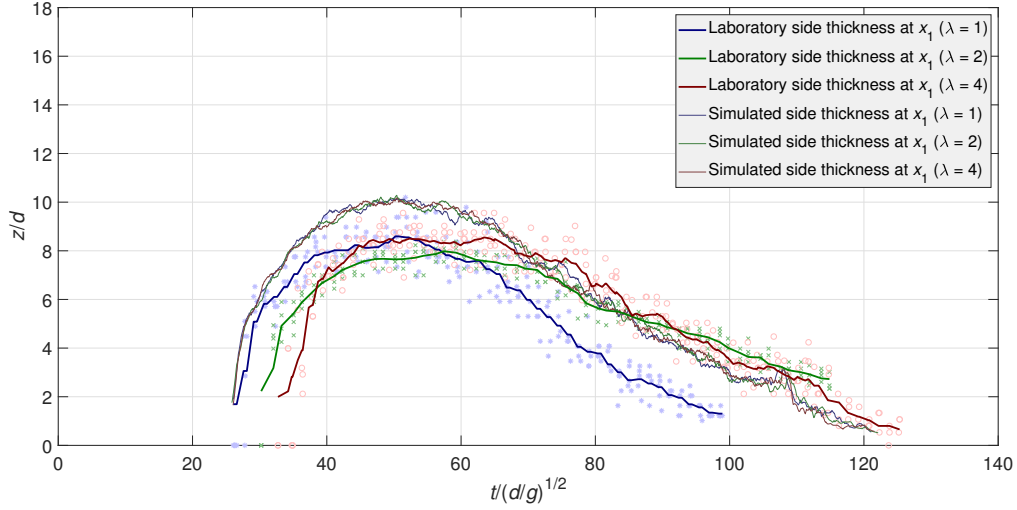


Figure 87 Comparison of laboratory (L1–L6, L18–L21, and L30–L37) and simulated (S1, S4, and S7) slide thickness profiles at the sidewall position at x_1 , with $\theta_W = 0^\circ$

Looking at Fig. 88, the correlation between the simulated and laboratory slides shows similarity with increasing θ_W . Firstly, it can clearly be seen that the peak slide thickness at the sidewall region increases with θ_W , with this peak thickness occurring at roughly the same point in time across the simulated slides. For instance, the peak thickness at $\theta_W = 15^\circ$ is roughly 50% greater than that seen at $\theta_W = 0^\circ$. However, when looking at the laboratory experiments, the peaks occur significantly later (about halfway through the slide event) at $\theta_W = 15^\circ$. Notably, the peaks for this release condition occur well after the initial period of sharp increase in thickness, after a period of much slower thickness increase rate, across all experimental scales. The data relating to $\theta_W = 7.5^\circ$ can be found in Fig. 144 in Section C, and confirms the linear development of these behaviours.

Furthermore, these peaks in slide thickness match in timing with the corresponding peaks in surface velocity seen in Fig. 85. As θ_W increases, the disparity between the simulated and laboratory peak thickness increases to roughly 2 particle diameters. While the rate of decrease of simulated sidewall thickness still seems to match the laboratory experiments at $\lambda = 2$ and $\lambda = 4$ the best, the initial increase in thickness seems to correspond better to $\lambda = 1$, similarly to Fig. 87. The scatter of laboratory measurements from the mean values also increases with θ_W , indicating that the sidewall region becomes increasingly rough and dispersive as the slide thickness increases. The magnitude of the scatter for these laboratory measurements was typically less than $2d$.

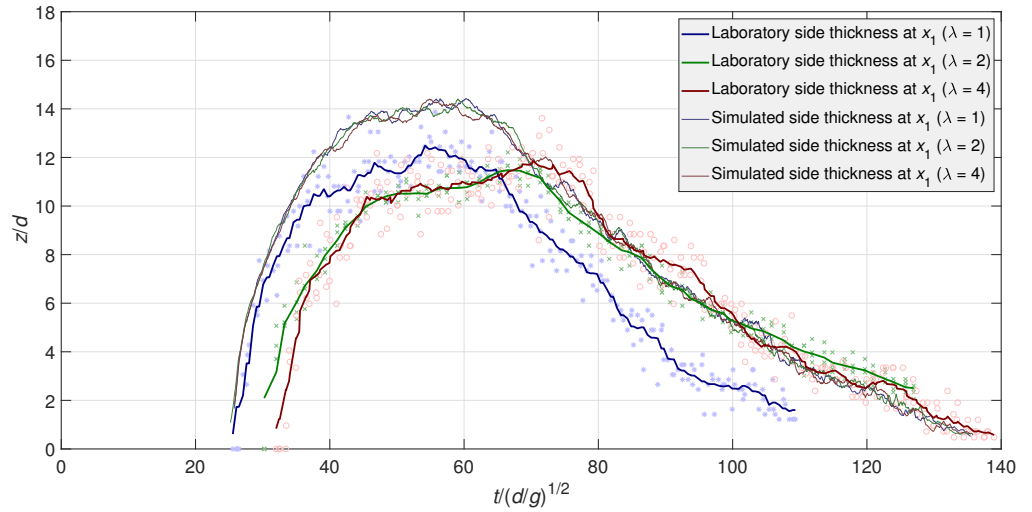


Figure 88 Comparison of laboratory (L13–L17, L26–L29, and L46–L53) and simulated (S3, S6, and S9) slide thickness profiles at the sidewall position at x_1 , with $\theta_W = 15^\circ$

Moving on to the thickness measurements at the channel centre at x_2 , Fig. 89 demonstrates some significant changes in behaviour, some caused by the movement away from the channel sidewalls and some caused by the extra distance the slides have traversed to reach this measurement point. Again, the simulated slide thickness at x_2 did not vary consistently with λ . The recorded slide thicknesses are lower throughout at x_2 , as the slide bodies have spread considerably as they travel down the ramp. The recorded laboratory peak thicknesses are all roughly

4. RESULTS

the same magnitude as the simulated value, with the peak at $\lambda = 2$ being higher than the other laboratory scales by roughly 1 d , 13% of the simulated thickness.

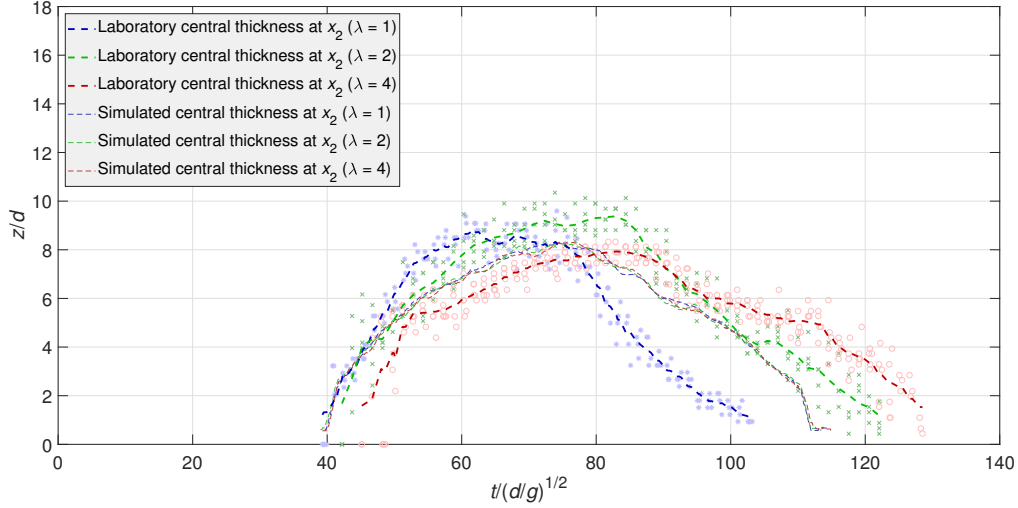


Figure 89 Comparison of laboratory (L1–L6, L18–L21, and L30–L37) and simulated (S1, S4, and S7) slide thickness profiles at the centre position at x_2 , with $\theta_W = 0^\circ$

Furthermore, the variation in slide thickness as it passes through the measurement point at the central region also varies in a more uniform and paraboloid manner, with the thickness increasing as rapidly after the slide front passes as it decreases before the slide tail passes. This makes physical sense as the tail particles are slowed less by the compounding effects of sidewall friction throughout the edge regions, which characterise the slow decreases in slide thickness seen in Figs. 87–88. As expected, the timing of the laboratory slide at $\lambda = 2$ matches the simulated slide best.

While it remains difficult to find a correlation between the peak laboratory thickness and the experimental scale, the timing of the terminal phases of the slide match slightly better in Fig. 89 than those seen at x_1 . The central regions of smaller scale slides clearly seem to take relatively longer to run out, showing further consistency with Figs. 84 and 85. This provides yet more evidence that a scale effect is manifesting between the x_1 and x_2 measurement points that

influences the slide behaviour and results in overall reduced slide velocity at $\lambda = 4$ during the terminal phase.

Looking at increasing values of θ_W in this central x_2 region, many of the trends seen in Fig. 88 are confirmed in Fig. 90, but some clear differences in thickness magnitude and variation over time can also be seen. Firstly, the peak slide thickness depends much more strongly on θ_W in this region, with the simulated peak thickness at $\theta_W = 15^\circ$ being up to 50% greater than that seen at $\theta_W = 0^\circ$. This suggests that the variation in slide thickness across the channel width is roughly equivalent down the ramp. At $\theta_W = 15^\circ$, the smooth curves of the laboratory data are clearly interrupted by a second peak. This peak protrudes rapidly away from the more typical centre of the paraboloid after a short moment, and the slide thickness enters a steep decline shortly afterwards at all experimental scales. This peak is not present at all in the simulation data, suggesting the physical mechanism that causes this difference is not captured in the DEM. Again, these peaks in measured slide thickness correspond to similar peaks in slide surface velocity seen in Fig. 85.

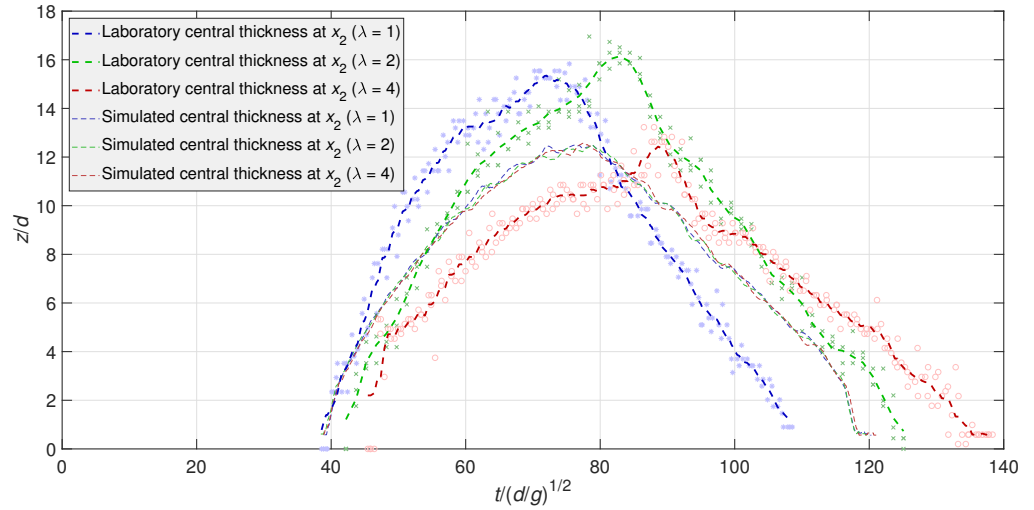


Figure 90 Comparison of laboratory (L13–L17, L26–L29, and L46–L53) and simulated (S3, S6, and S9) slide thickness profiles at the centre position at x_2 , with $\theta_W = 15^\circ$

4. RESULTS

This confirms the earlier hypothesis based on Fig. 88 that this peak in thickness and velocity occurs across the entire slide width. Additional evidence of the development of this peak can be seen at $\theta_W = 7.5^\circ$ in Fig. 145 in Section C. Furthermore, there is significantly less variation in the laboratory measurements of the slide thickness at the x_2 region, with consistently low fluctuations across all experimental scales and initial release conditions of around 1 particle diameter on average. The scatter of the laboratory measurements at x_2 either remain constant or decrease as θ_W increases, in direct opposition to the behaviour seen at x_1 in Figs. 87 and 88. Looking at the thickness profiles across all values of θ_W , a correlation between peak slide thickness and λ becomes apparent that was not as clear when just looking at the data for $\theta_W = 0$. At the centre-line of the slide, the peak thickness slightly increases as λ increases from 1 to 2, but then experiences a sudden drop as λ increases to 4.

The velocity and thickness data seen throughout this section can also be compared in combination, across the range of laboratory and simulated experiments and experimental scales to further identify scale effects. Figure 91 compares the simulation and laboratory velocity (Figs. 82 and 84) and thickness data (Figs. 87 and 89) for the slides with $\theta_W = 0^\circ$, with the data at x_1 relating to the sidewall position and the data at x_2 relating to the central position, where the laboratory data was recorded. Meanwhile, Fig. 92 compares the simulation and laboratory velocity (Figs. 83 and 85) and thickness data (Figs. 88 and 90) for the slides with $\theta_W = 15^\circ$. The laboratory data used in Figs. 91 and 92 is included in the averaged data seen in Figs. 84 and 85 respectively. Only the simulation data at $\lambda = 2$ is shown in Figs. 91 and 92, as no significant variation of the simulated data with λ was seen in the previous sections.

In both cases, the laboratory data was averaged across all repeats for each experimental scale, and successive data points are connected by a line that darkens as time progresses. t_1 denotes the first point displayed, which for the simulation occurs 400,000 time-steps after the slide contacts each measurement point, and for the laboratory data occurs 100 camera frames after contact; thus t_1 differs between x_1 and x_2 . Subsequent time intervals are displayed every 400,000 time-steps

or 100 camera frames respectively, until the final point is reached. For $\theta_W = 0^\circ$, 11 data points are provided at the channel sidewall at x_1 and at the channel centre at x_2 ; after the final data point at t_{11} , the slide tails have entered dilute regimes in the laboratory and simulations and the data is cut off for clarity. The behaviour of the slides between t_1 and t_{11} is the focus of Fig. 91. While the legend shows the colours of only t_1 and t_{11} for brevity, each data-point in between (t_2 to t_{10}) is expressed with darkening colour in Fig. 91; as time passes, the colour of each data line transitions from light to dark.

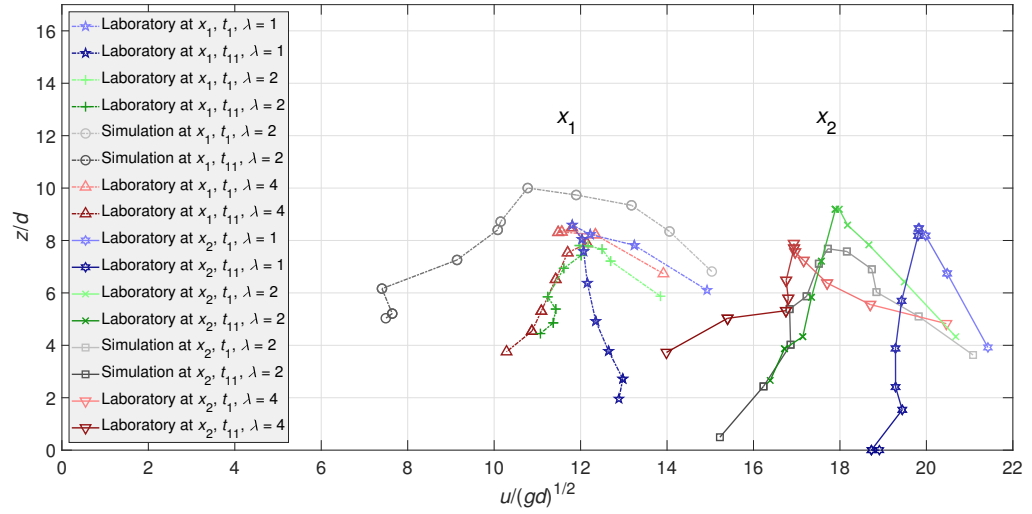


Figure 91 Laboratory (L1–L6, L18–L21, and L30–L37) and simulated (S4) non-dimensional slide surface velocity plotted against slide depth at 400,000 simulation time-step intervals, with t_1 starting 400,000 time-steps after the slide front contacts each measurement point, with $\theta_W = 0^\circ$

Overall, the variation of surface velocity and thickness matches better between the simulated and laboratory slides at the channel centre at x_2 than at the channel sidewall at x_1 . In Fig. 91, the sidewall surface velocity at x_1 rapidly diminishes as the front passes, briefly pausing at a peak thickness value before starting to rapidly diminish again. The timing and nature of this peak matches the laboratory data, but the laboratory slides diverge after this point, with the thickness reducing while the surface velocity at the sidewall varies only slightly over time. The simulated

4. RESULTS

surface velocity at this point corresponds well to the data seen in Fig. 81, which suggests an increase in shearing behaviour at the sidewalls is responsible for the differences between the simulated and laboratory results.

The small- and medium-scale experiments show a reduced surface velocity at t_1 compared to the large-scale experiments and the medium-scale simulation, followed by a roughly constant non-dimensional velocity of around 12. As the slide tail approaches x_1 , the surface velocity decreases at similar rates at $\lambda = 2$ and 4, while the surface velocity actually increases at $\lambda = 1$, highlighting the presence of a fluidisation mechanism that may develop in the laboratory as the scale increases. Meanwhile, the simulated velocity decreases rapidly, indicating that the influence of sidewall friction is reduced at x_1 in the laboratory experiments compared to the simulations. Meanwhile, looking at the corresponding data at the channel centre at x_2 , the differing rate of decrease of the surface velocity seen in the simulations is matched at all three experimental scales. However, the magnitude of the surface velocity varies drastically between these scales, corresponding to a faster rate of thickness decrease as the slide simply passes over the measurement point more quickly at the larger experimental scales. The simulated data achieves a much better fit, far from the influence of sidewall and basal friction.

While these patterns are clear in Fig. 91 for the experiments with $\theta_W = 0^\circ$, some notable differences can be seen in the experiments with $\theta_W = 15^\circ$ in Fig. 92. For $\theta_W = 15^\circ$, 12 data points are provided at the channel sidewall at x_1 and at the channel centre at x_2 , with 400,000 time-steps or 100 camera frames between each data point. After the final data point at t_{12} , the data is again cut off for clarity, with the behaviour between t_1 and t_{12} being the focus of Fig. 92. The extra data point provided is indicative of the longer runout time of the slides at $\theta_W = 15^\circ$. While the legend shows the colours of only t_1 and t_{12} for brevity, each data-point in between (t_2 to t_{11}) is again expressed with darkening colour in Fig. 92.

Looking first at the sidewall position at x_1 , the simulation arrives at a peak thickness at the same time as the laboratory slides, but with greater velocity. The velocity at peak thickness remains fairly constant in the laboratory slides for a while, before either decreasing at the smaller scales or increasing at the largest

scale. While the decrease in surface velocity and thickness as the slide tail approaches the sidewall position at x_1 is significant in the simulation, it is of lower magnitude and much less uniform in the laboratory data. This is particularly true for $\lambda = 1$ and 4, where the surface velocity increases about 3/4 of the way into the slide events. At $\lambda = 4$, the surface velocity reduces again after this point until the slide tail passes, while at $\lambda = 1$, the surface velocity seems to roughly stay constant. Meanwhile, at the channel centre at x_2 , some differences can be seen in Fig. 92 in how the laboratory surface velocity and thickness vary over time across all three experimental scales.

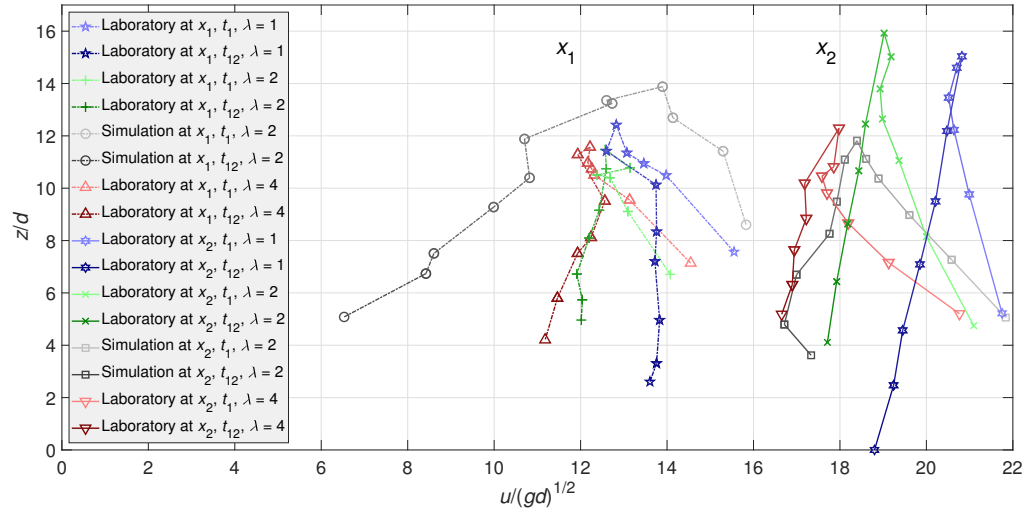


Figure 92 Laboratory (L13–L17, L26–L29, and L46–L53) and simulated (S6) non-dimensional slide surface velocity plotted against slide depth at 400,000 simulation time-step intervals, with t_1 starting 400,000 time-steps after the slide front contacts each measurement point, with $\theta_W = 15^\circ$

Overall, the slide thicknesses recorded at $\lambda = 1$ and 2 are significantly greater than those in the numerical simulations, to a similar degree as those seen in Fig. 91. However, while the simulation shows a similar triangular pattern where the surface velocity decreases consistently over time while the thickness increases and decreases over the slide event, the laboratory experiments show a more elongated peak that is consistent across all three experimental scales. In these cases, the

surface velocity decreases at a fairly constant rate until a moment briefly before the slide peak passes through the measurement point. At this moment, the slide velocity starts to increase again momentarily until the peak thickness is reached, after which the surface velocity and thickness decrease with time as seen in the data at x_2 in Fig. 92. This shows some differences in the relationship between slide thickness and velocity at the channel centre close to the transition curve as the release mass (and thus mean thickness) increases. The simulation data matches the laboratory data much better at the channel centre at x_2 (albeit with reduced thickness), but the surface velocity at peak thickness does not show the brief reversal seen in the laboratory data, suggesting the mechanism causing this behaviour is not modelled in the DEM.

4.3.6 Deposit dimensions and properties

Figure 93 provides a plan view of the deposits across the various laboratory conditions with images taken such that the deposits can be roughly compared in isolation of scale, with some clear trends being immediately visible. Firstly, the slide fronts and tails all displayed minor curvature at the sidewall regions, confirming that despite the wide channel selected for this study, sidewall friction effects still manifest across the entire channel width. Additionally, some minor ridge structures of increased thickness are visible close to the sidewalls, particularly at larger experimental scales and increased slide masses. Later measurements of the deposit thickness will confirm the magnitude of this phenomenon.

Another visible change is an increase in front dispersion with increasing λ matching the trend seen as the slide front progresses through the measurement points seen in Figs. 69 and 71. The deposit tails however remain discrete in contrast to those of the slide in motion; this is expected due to the tail particles colliding with the settling mass of the frontward slide particles and dissipating all of their energy as they come to rest. Finally, the deposit length increases overall with θ_W and decreases with increasing λ , with all three experimental scales showing different deposit positioning.

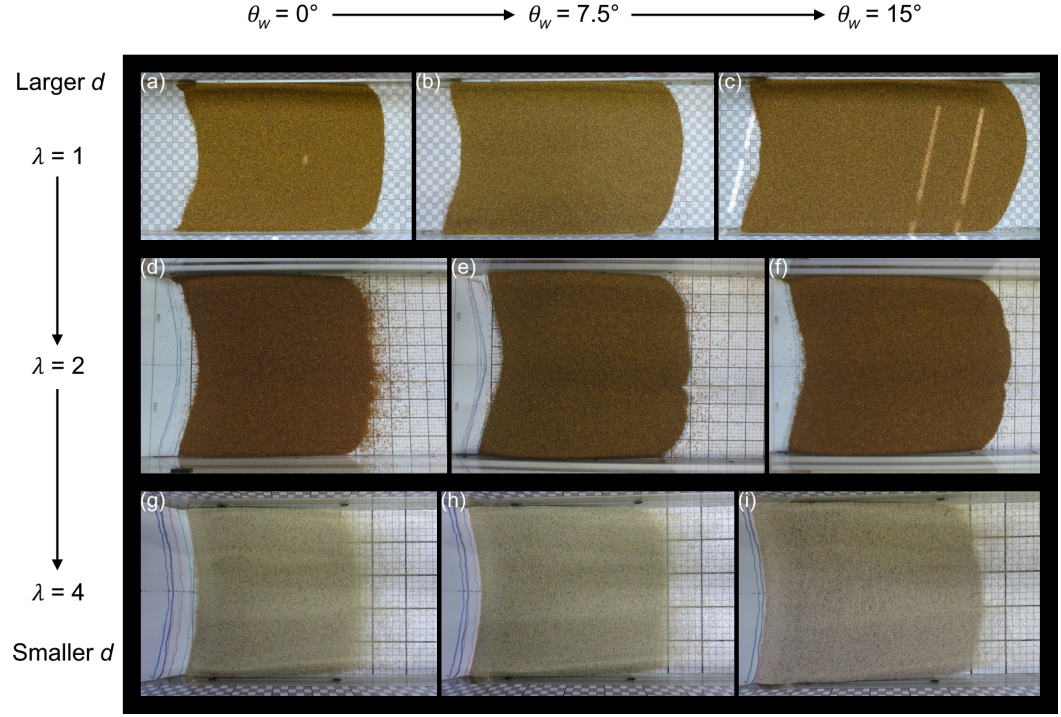


Figure 93 Plan view of laboratory slides of all conditions, with θ_W increasing from left to right and λ increasing from top to bottom. (a) L6, (b) L10, (c) L13, (d) L21, (e) L23, (f) L29, (g) L31, (h) L41, and (i) L48

Figures 94 to 96 compare these final deposits from laboratory experiments across all values of λ and θ_W to their respective simulations. The distances from the shutter release point and the height of the deposit surfaces above that of the flat runout area are non-dimensionalised with respect to the mean particle diameter at each experimental scale to allow direct comparison. In this case, the data points from each laboratory deposit surface are displayed individually, to display the variation and repeatability of producing granular slide deposits with the same initial conditions. In general, laboratory slides of identical initial conditions and scales showed relatively little variation from each other, with no correlation in variation being seen with experimental scale or initial release mass. However, there was some slight asymmetry recorded in the deposits, particularly those at $\lambda = 1$. As a result, the data is presented from both sides of the channel.

4. RESULTS

At $\theta_W = 0^\circ$, Fig. 94 shows that the laboratory slide deposits are all relatively flat and have all cleared the transition curve. Typically, the deposit rapidly increases in thickness as it becomes more distant from the transition curve until a peak thickness is reached, after which the thickness slowly declines until the slide front manifests as a disperse mono-layer of particles. The simulated deposit is positioned further into the transition curve, with the tail being placed roughly halfway up the transition curve. Additionally, the simulated slide front is somewhat closer to the transition curve than the laboratory slides at all scales, and the region immediately leading up to the front is much shallower, with a lateral ridge separating the frontal region from the rest of the deposit. These changes were seen across the channel width, indicating that although the surface velocity matched well between the simulated and laboratory slides at $\lambda = 2$, the final settlement behaviour is significantly different. As these changes were roughly uniform with width, this suggests that the disparity is likely due to the increased shear between the surface and base, as suggested by Fig. 81, rather than due to the additional shear seen at the sides, as seen in Figs. 91 and 92.

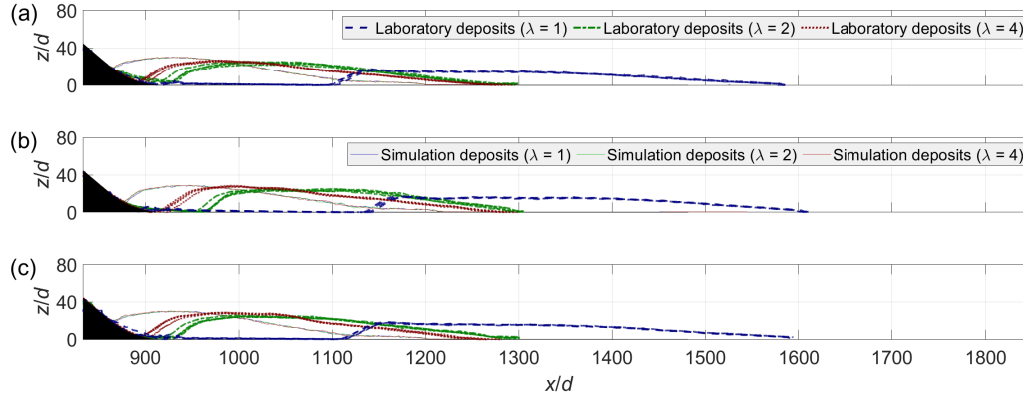


Figure 94 Comparison of laboratory (L1–L6, L18–L21, and L30–L37) and simulated (S1, S4, and S7) deposit surfaces with $\theta_W = 0^\circ$, at (a) 10% across, (b) 50% across, and (c) 90% across the channel width

Looking at the laboratory deposits at $\lambda = 4$, the front and tail positions are similar to those at $\lambda = 2$, but are placed closer to the transition curve, by approximately 30 particle diameters. Notably the deposit tails at this small experimental

scale settle much closer to the transition curve at the sidewall locations. The peak thickness seems to increase consistently with λ , with the simulated deposit showing the greatest thickness. Generally, the smallest laboratory deposits displayed more curved, convex surfaces than those at the larger scales, with the simulated deposit showing the most overall curvature. However, the largest differences can clearly be seen in the laboratory deposits at $\lambda = 1$, where the slide fronts extend past those of the respective simulation by almost 200 mean particle diameters at both the sidewall and central positions. The slide fronts also extend further ahead, by almost 225 mean particle diameters at the sidewall positions and almost 250 mean particle diameters at the central position. This is confirmed by the vastly increased slide surface velocity compared to the other slide data seen in Fig. 84.

The deposit surfaces at the largest scale are also much flatter in general, with a sharp increase in slide thickness at the tail producing a tail surface inclination roughly equivalent to the particle friction angle. This tail is then followed by a flat plateau region that extends for roughly half of the deposit length before the thickness starts to diminish again. This demonstrates that the increased slide velocity of the large-scale laboratory slides results in additional spreading and extension of the slide deposit, as well as a thinner, flatter deposit morphology. The mechanisms that cause this difference in behaviour may be related to the hypermobility phenomenon seen in real-world avalanches and landslides of volume $>10^6 \text{ m}^3$ (Parez and Aharonov, 2015; Johnson et al., 2016), or this may be an unrelated scale effect that has manifested due to the relatively reduced influence of interstitial airflow and turbulence, or due to different frictional interactions with the channel. Overall, the simulations showed no significant variation of deposit shapes with λ .

As θ_W increases, some notable differences can be seen in the deposit shape. Across all experimental scales and in both the simulation and laboratory results, Fig. 95 shows that the slide tail continues to recede towards the transition curve (even resting on it at the smallest experimental scale) and that the slide front continues to extend further beyond it. The non-linear changes seen in the deposit morphology necessitate including Fig. 95 in this section as opposed to Section C. Comparing the simulation and laboratory data at $\lambda = 2$, the disparity seen at

4. RESULTS

$\theta_W = 0^\circ$ is still highly apparent at $\theta_W = 15^\circ$, with the simulated front and tail remaining roughly $60 d$ behind the laboratory values. The increased tail curvature seen in Fig. 94 is still present but does not seem to have become more prominent with the increased release mass. However, the peak thickness of the simulated and laboratory deposits at $\lambda = 2$ matches well at the channel centre despite the significant difference in deposit placement. The laboratory deposits recorded at $\lambda = 4$ still lag behind at the front and tail locations by approximately $30 d$.

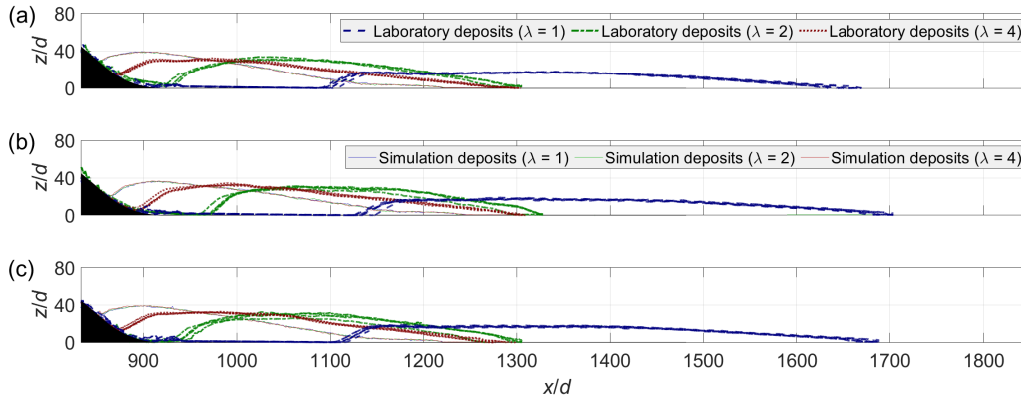


Figure 95 Comparison of laboratory (L7–L12, L22–L25, and L38–L45) and simulated (S2, S5, and S8) deposit surfaces with $\theta_W = 7.5^\circ$, at (a) 10% across, (b) 50% across, and (c) 90% across the channel width

Notably, the peak structure of the smallest experimental deposits has changed significantly, with relatively little difference in peak thickness between the channel sidewall and centre regions and the development of a flatter plateau structure similar to that seen with the largest deposits, particularly at the channel sidewalls. Meanwhile, the laboratory deposits recorded at $\lambda = 1$ remain positioned far ahead of the simulated deposit. The tails of these large-scale deposits still remain 250 particle diameters in front of those from the respective simulation, while the laboratory fronts also remain between 350–400 particle diameters ahead. Overall, the deposit shape at $\lambda = 1$ remains very similar to those with the lowest θ_W .

Figure 96 demonstrates the continuation of the trends seen in the laboratory experiments at $\lambda = 1$ and $\lambda = 4$ at the largest value of θ_W . For this slide configu-

ration, the simulated deposit tail is positioned at the back of the transition curve, with the tail almost touching the inclined ramp section at the sidewalls. While the simulated front distance from the curve continues to increase, this increase is slow compared to the laboratory experiments, with the difference reaching 50–60 particle diameters. These changes show that the extra particles placed in the tail region of the initial release wedge have resulted in extra particles mostly being positioned in the tail of the final deposit. Although the slide front extended at $\theta_W = 7.5^\circ$ compared to at $\theta_W = 0^\circ$, it appears that the overall increase in slide thickness (and thus deposit thickness) has reduced the degree of this extension at $\theta_W = 15^\circ$. This behaviour can also be seen to a degree in the laboratory data at $\lambda = 4$, where the deposit tail has built up significantly in the transition curve, resulting in the tail position being almost as elevated from the flat runout zone as the peak position.

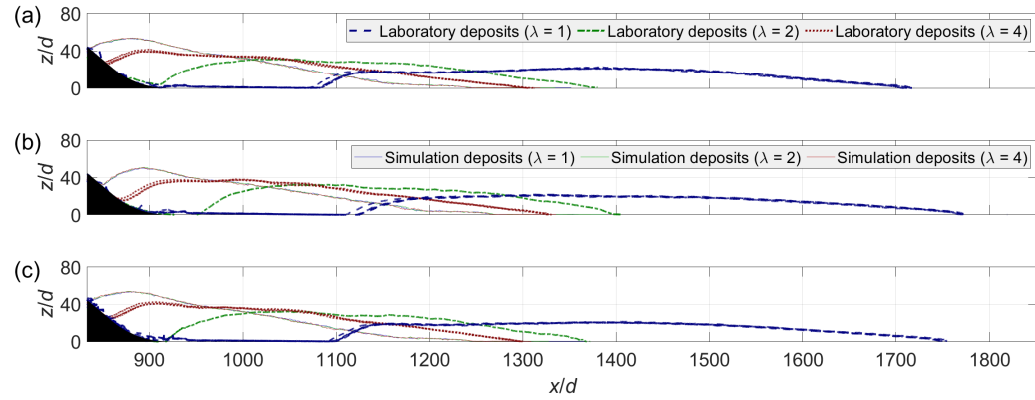


Figure 96 Comparison of laboratory (L13–L17, L26–L29, and L46–L53) and simulated (S3, S6, and S9) deposit surfaces with $\theta_W = 15^\circ$, at (a) 10% across, (b) 50% across, and (c) 90% across the channel width

In these laboratory deposits, the peak position at the sidewalls forms almost immediately after the slide tail as a noticeable ridge, before the thickness decreases slightly and a small plateau forms, after which the thickness slowly decreases until the deposit front is reached. However, this ridge is much smaller at the channel centre, and is followed by a second taller peak in the middle of the plateau region. Meanwhile, the front positions in the small-scale laboratory deposits have barely

4. RESULTS

moved, with only slight difference being seen at the channel centre. This implies that the mechanisms restraining the rear slide particles from extending the slide front in the laboratory have been captured well by the simulation. However, this trend does not carry over to the large-scale experiments at $\lambda = 1$, which shows almost the exact opposite behaviour to the laboratory deposits seen at $\lambda = 4$. Figure 96 demonstrates that the large-scale laboratory deposit tails at $\theta_W = 15^\circ$ have stayed in almost the same positions as those at $\theta_W = 7.5^\circ$, while the deposit fronts have extended further forward by almost 50 particle diameters at both the sidewall and central positions. This has been matched by an increase in peak deposit thickness of 15%.

Overall, the large-scale laboratory deposits still remain significantly flatter than those at the smaller scales, but more prominent slide peaks can be seen closer towards the slide front at the sidewall regions, compared to the relatively flat plateau seen at the channel centre. This shows that the reduced thickness of the spreading deposit has resulted in different interactions between the sidewall flows affected by wall friction and the unrestrained central slide core. The development of these thicker ridges on the channel sides is reminiscent of the phenomenon seen in Fig. 13 in Johnson et al. (2012), suggesting the development of additional slide depositional features after a certain value of λ is reached. Thus, the laboratory data seen in Figs. 94 to 96 suggests that the spreading behaviour of the slide deposit varies significantly with experimental scale, particularly once certain values of θ_W are reached.

Figure 97 provides further comparison of the slide front and tail positions recorded across the various experiments, again in comparison to the simulations. The deposit dimensions along the channel length and across the channel width have been non-dimensionalised, and the central 80% of the channel width has been displayed, as the scanned deposit meshes became slightly inconsistent close to the channel sidewalls. Overall, Fig. 97 confirms that the curvature of the deposit fronts and tails is gradual as the particle position moves from the sidewall to the channel centre. Furthermore, the variation in the laboratory experiments at each experimental scale can be seen more clearly with this comparison, with the

variation at $\lambda = 4$ decreasing with increasing θ_W , while the variation at $\lambda = 1$ and 2 increases for $\theta_W = 7.5^\circ$ before decreasing again at $\theta_W = 15^\circ$. This implies that there is no direct correlation between θ_W and laboratory variability. However, the variability is generally greater at larger experimental scales, when considering the results at all values of θ_W . This is counter-intuitive, considering that Re decreases with increasing size and thus the inherent randomness imposed by random particle motion should be diminished.

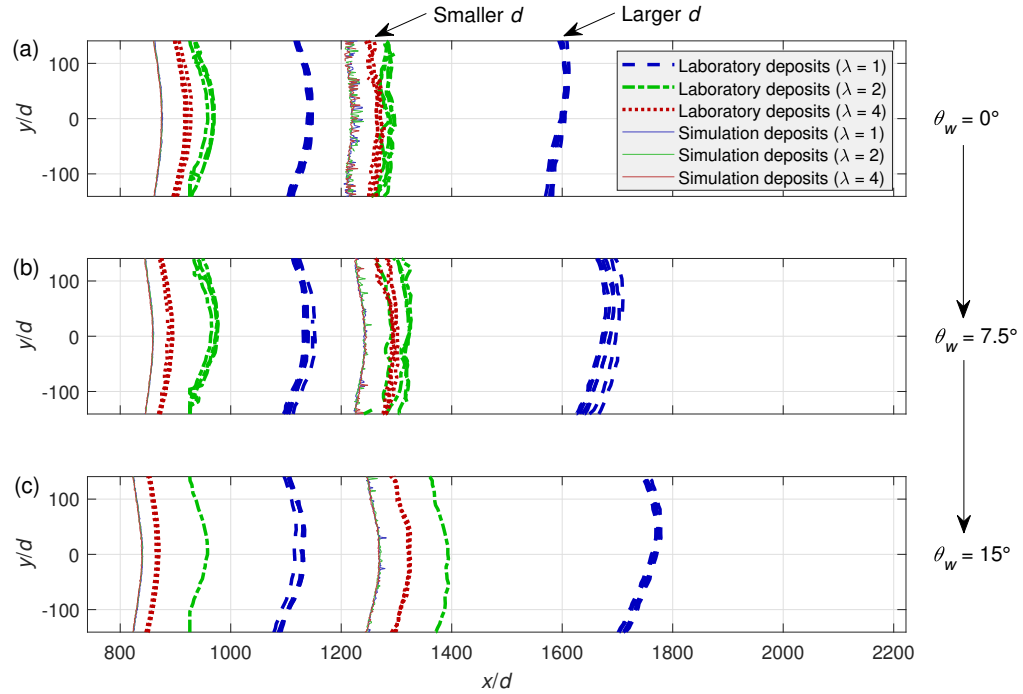


Figure 97 Comparison of laboratory and simulation deposit front and tail positions for (a) $\theta_W = 0^\circ$, (b) $\theta_W = 7.5^\circ$, and (c) $\theta_W = 15^\circ$

The simulation underpredicts the runout distance of both the slide front and tail at all values of λ by a significant degree. However, a dilute region of particles further from the slide front can still be found in the simulated deposits, which manifests to a similar degree in the laboratory deposits. This correlates with the behaviour seen in the cylinder collapse validation in Section 4.2, where free particles can detach themselves from the main slide mass and roll further than expected.

4. RESULTS

However, the shearing differences seen in the simulation seem to cause the bulk deposit mass to settle closer to the transition curve, despite the presence of this dilute frontal region.

This may be related to the lack of interlocking effects seen in the DEM due to the spherical particles used (Section 3.4), which may be important in driving the motion of a discrete slide front over a greater distance than seen in the current simulations. As the influence of this interlocking mechanism and the shear rate throughout the deposit is reduced overall in the cylinder-collapse context, these mechanisms only become apparent and influential to the slide deposit in the chute geometry simulations; an important conclusion for future validation exercises. Alternatively, this may be caused by other mechanics not captured by the DEM, particularly air interactions.

However, the laboratory data seen at $\lambda = 1$ still demonstrates increased spreading alongside increased runout distance compared to the respective simulation. In this case, the extreme difference in slide surface velocity compared to the smaller experimental scales, especially closer to the slide tail, may overcome these physical factors affecting spreading behaviour, resulting in a net increase in spreading of the discrete slide mass. In all cases, the trends in front and tail position seen in Fig. 93 and Figs. 94 to 96 are preserved across the whole channel and between experimental repeats. Smaller-scale slides receding further back towards the transition curve and larger-scale slides extending further into the runout zone, highlighting a clear scale effect. Additionally, the simulated deposit shows very little curvature in comparison to the laboratory deposits, particularly at the slide tail, matching expectations based on Figs. 94 to 96.

Table 7 summarises the key non-dimensionalised slide positions identified in Fig. 97, as well as the peak positions seen in Figs. 94 to 96. In particular, this table highlights the absolute and relative magnitude of these non-dimensional differences, quantifying the reported scale effects. Table 8 provides a comparison between the non-dimensional volumes of the simulated and laboratory deposits to identify any variation in deposit composition with scale. The porosities were also estimated by dividing the volume of the particles used in the experiment by the total volumes V_s and V_d of the initial and deposit slide volumes. The initial slide volume is constrained by the release wedge triangle in both the laboratory and simulations, while the deposit meshes provide accurate estimates of the deposit volume. In the simulation, the total particle volume is provided directly, while the laboratory values are based on weighing containers of particles as described in Section 3.2.2.

Table 7 Non-dimensionalised slide front, peak, and tail positions

Exp. no.	λ	θ_W	Position	Parameter	Simulation		Laboratory		Laboratory-simulation difference			
					x/d	z/d	x/d	z/d	x/d		z/d	
(-)	(-)	(°)	(-)	(-)	(-)	(-)	(-)	(-)	(-)	(%)	(-)	(%)
S1, L1–L6	1	0	Sidewall	Tail	857	-	1103	-	+246	+28.7	-	-
				Peak	926	24.9	1147	17.2	+221	+23.0	-7.7	-30.9
				Front	1185	-	1584	-	+399	+33.7	-	-
			Centre	Tail	875	-	1144	-	+269	+30.7	-	-
				Peak	947	28.7	1184	16.3	+237	+25.0	-12.4	-43.2
				Front	1220	-	1601	-	+381	+31.2	-	-
S2, L7–L12	1	7.5	Sidewall	Tail	843	-	1101	-	+258	+30.6	-	-
				Peak	917	33.3	1357	17.5	+440	+47.9	-15.8	-47.4
				Front	1207	-	1648	-	+441	+36.5	-	-
			Centre	Tail	860	-	1138	-	+278	+32.3	-	-
				Peak	915	36.3	1288	17.9	+373	+40.8	-18.4	-50.7
				Front	1247	-	1684	-	+437	+35.0	-	-
S3, L13–L17	1	15	Sidewall	Tail	820	-	1084	-	+264	+32.2	-	-
				Peak	906	43.9	1404	21.5	+498	+55.0	-22.4	-51.0
				Front	1221	-	1714	-	+493	+40.4	-	-
			Centre	Tail	841	-	1127	-	+286	+34.0	-	-
				Peak	908	47.5	1328	21.4	+420	+46.3	-26.1	-54.9
				Front	1274	-	1766	-	+492	+38.6	-	-

4. RESULTS

Table 7 Non-dimensionalised slide front, peak, and tail positions (continued)

Exp. no.	λ	θ_W	Position	Parameter	Simulation		Laboratory		Laboratory-simulation difference			
					x/d	z/d	x/d	z/d	x/d		z/d	
(-)	(-)	(°)	(-)	(-)	(-)	(-)	(-)	(-)	(-)	(%)	(-)	(%)
S4, L18–L21	2	0	Sidewall	Tail	857	-	886	-	+29	+3.4	-	-
				Peak	926	24.9	1016	24.3	+92	+9.9	-0.6	-2.4
				Front	1185	-	1250	-	+65	+5.5	-	-
			Centre	Tail	875	-	967	-	+92	+10.5	-	-
				Peak	947	28.7	1091	23.6	+144	+15.2	-5.1	-17.7
				Front	1220	-	1287	-	+67	+5.5	-	-
S5, L22–L25	2	7.5	Sidewall	Tail	843	-	925	-	+82	+9.7	-	-
				Peak	917	33.3	1044	29.7	+127	+13.8	-3.6	-10.8
				Front	1207	-	1262	-	+55	+4.6	-	-
			Centre	Tail	860	-	973	-	+113	+13.1	-	-
				Peak	915	36.3	1070	29.1	+155	+16.9	-7.2	-19.8
				Front	1247	-	1309	-	+62	+5.0	-	-
S6, L26–L29	2	15	Sidewall	Tail	820	-	905	-	+85	+10.4	-	-
				Peak	906	43.9	1020	31.7	+114	+12.6	-12.2	-27.8
				Front	1221	-	1364	-	+143	+11.7	-	-
			Centre	Tail	841	-	951	-	+110	+13.1	-	-
				Peak	908	47.5	1091	32.2	+183	+20.3	-15.3	-32.2
				Front	1274	-	1406	-	+132	+10.4	-	-
S7, L30–L37	4	0	Sidewall	Tail	857	-	897	-	+40	+4.7	-	-
				Peak	926	24.9	981	27.1	+55	+5.9	+2.2	+8.8
				Front	1185	-	1248	-	+63	+5.3	-	-
			Centre	Tail	875	-	923	-	+48	+5.5	-	-
				Peak	947	28.7	997	27.9	+50	+5.3	-0.8	-2.8
				Front	1220	-	1268	-	+48	+3.9	-	-
S8, L38–L45	4	7.5	Sidewall	Tail	843	-	866	-	+23	+2.7	-	-
				Peak	917	33.3	970	31.5	+53	+5.8	-1.8	-5.4
				Front	1207	-	1264	-	+57	+4.7	-	-
			Centre	Tail	860	-	892	-	+32	+3.7	-	-
				Peak	915	36.3	993	33.1	+78	+8.5	-3.2	-8.8
				Front	1247	-	1296	-	+49	+3.9	-	-
S9, L46–L53	4	15	Sidewall	Tail	820	-	845	-	+25	+3.0	-	-
				Peak	906	43.9	904	40.7	-2	-0.2	-3.2	-7.3
				Front	1221	-	1284	-	+63	+5.2	-	-
			Centre	Tail	841	-	869	-	+28	+3.3	-	-
				Peak	908	47.5	993	37.6	+85	+9.4	-9.9	-20.8
				Front	1274	-	1323	-	+49	+3.8	-	-

Table 8 Slide initial and deposit volumes and porosities

Exp. no.	Exp. type	λ	V_s	V_s/d^3	V_d	V_d/d^3	N_s	N_d
(-)	(-)	(-)	(m ³)	(-)	(m ³)	(-)	(-)	(-)
S1	Simulation	1	3.73×10^{-2}	1.89×10^6	4.12×10^{-2}	2.09×10^6	0.430	0.484
L1–L6	Laboratory	1	3.73×10^{-2}	1.89×10^6	4.15×10^{-2}	2.11×10^6	0.391	0.453
S2	Simulation	1	4.91×10^{-2}	2.49×10^6	5.37×10^{-2}	2.73×10^6	0.430	0.479
L7–L12	Laboratory	1	4.91×10^{-2}	2.49×10^6	5.40×10^{-2}	2.75×10^6	0.389	0.444
S3	Simulation	1	6.70×10^{-2}	3.40×10^6	7.22×10^{-2}	3.67×10^6	0.430	0.471
L13–L17	Laboratory	1	6.70×10^{-2}	3.40×10^6	7.35×10^{-2}	3.73×10^6	0.390	0.444
S4	Simulation	2	4.66×10^{-3}	1.89×10^6	5.15×10^{-3}	2.09×10^6	0.430	0.484
L18–L21	Laboratory	2	4.66×10^{-3}	1.89×10^6	5.42×10^{-3}	2.20×10^6	0.390	0.476
S5	Simulation	2	6.13×10^{-3}	2.49×10^6	6.70×10^{-3}	2.72×10^6	0.430	0.478
L22–L25	Laboratory	2	6.13×10^{-3}	2.49×10^6	7.22×10^{-3}	2.94×10^6	0.392	0.484
S6	Simulation	2	8.38×10^{-3}	3.40×10^6	9.00×10^{-3}	3.66×10^6	0.431	0.470
L26–L29	Laboratory	2	8.38×10^{-3}	3.40×10^6	9.48×10^{-3}	3.85×10^6	0.389	0.460
S7	Simulation	4	5.81×10^{-4}	1.89×10^6	6.43×10^{-4}	2.09×10^6	0.430	0.485
L30–L37	Laboratory	4	5.81×10^{-4}	1.89×10^6	7.12×10^{-4}	2.31×10^6	0.388	0.501
S8	Simulation	4	7.66×10^{-4}	2.49×10^6	8.28×10^{-4}	2.69×10^6	0.429	0.472
L38–L45	Laboratory	4	7.66×10^{-4}	2.49×10^6	9.62×10^{-4}	3.13×10^6	0.391	0.515
S9	Simulation	4	1.05×10^{-3}	3.40×10^6	1.12×10^{-3}	3.65×10^6	0.432	0.468
L46–L53	Laboratory	4	1.05×10^{-3}	3.40×10^6	1.22×10^{-3}	3.97×10^6	0.388	0.473

Generally, the simulated deposits took up slightly greater volumes than those of the initial slide masses, resulting in greater porosities. This increase in porosity decreases slightly as θ_W and thus the slide mass increases, suggesting that the increased mass acts to compress the final deposit into a tighter packing during the settlement phase. In the simulations, this trend did not depend on experimental scale. This contrasts with the laboratory data, where the initial wedge porosities were consistently lower than those of the simulations.

At $\lambda = 1$, the final volumes are in very good agreement with the simulations, with both systems appearing to behave in similar ways despite the initial difference in porosity. At $\lambda = 4$, the final laboratory volumes are significantly higher than

4. RESULTS

in the simulations, showcasing increased porosity that more than compensates for the initial reduced porosity. The dependence of N_d on θ_W also does not seem to be as clear in the laboratory experiments, but can still be seen at the largest experimental scale, to a similar degree of magnitude as that seen in the simulations. This implies that the decreased turbulence and Re encountered at in the smaller-scale laboratory experiments results in looser, less compacted final deposits due to the reduced turbulent damping of the mixing and fluctuating components of particle motion. Additionally, the dependence of N_d on θ_W in the simulations and the least turbulent laboratory experiments at $\lambda = 1$ implies that, after a certain scale threshold is reached, the extra mass and thickness of the depositing slide results in increased compaction, while this effect diminishes in comparison to turbulent mixing as λ increases.

These estimates of deposit porosity are relatively crude, being based on a mesh that encompasses the surface of the entire slide. While the margin of error for the position of photogrammetric reference points on the laboratory surface is within a particle diameter, the erratic volume measurements at $\lambda = 2$ seem to suggest that this method can break down depending on the positioning of cameras capturing the reference photos. To produce more accurate estimates for the porosity of the simulations, the cell-based method described in Section 3 was used to calculate the porosity on a more local basis. Figure 98 describes the porosity in cubic cells of 5 mm side length throughout simulation S4, with $\lambda = 2$ and $\theta_W = 0^\circ$, with (a) depicting the base layer of particles laying on the runout zone surface and each subsequent layer moving up one cell length until the slide peak is reached.

Several distinct features are captured by this more detailed analysis. Firstly, it can be seen that the porosity in the base layer of the slide deposit is typically greater than that seen in the upper layers, with the base porosity fluctuating around $N = 0.46 \pm 0.025$ compared to the mean porosity of around $N = 0.43 \pm 0.025$. These values are both lower than the estimates provided for simulation S4 in Table 8, which suggests that the surface-tight mesh used for those calculations, when analysed on isolation, overestimates the deposit volume. This makes sense as the mesh fitted to the deposit surface is not perfectly concave and may include

some of the air surrounding the deposit surface. It is expected that the base layer would demonstrate increased porosity, as it is impossible for particles to fill many of the gaps with centres below that of the minimum particle diameter. This increased porosity is similarly present at the channel sidewalls, although the zone of interest is much less prominent on Figs. 98 and 99, being only a pixel wide.

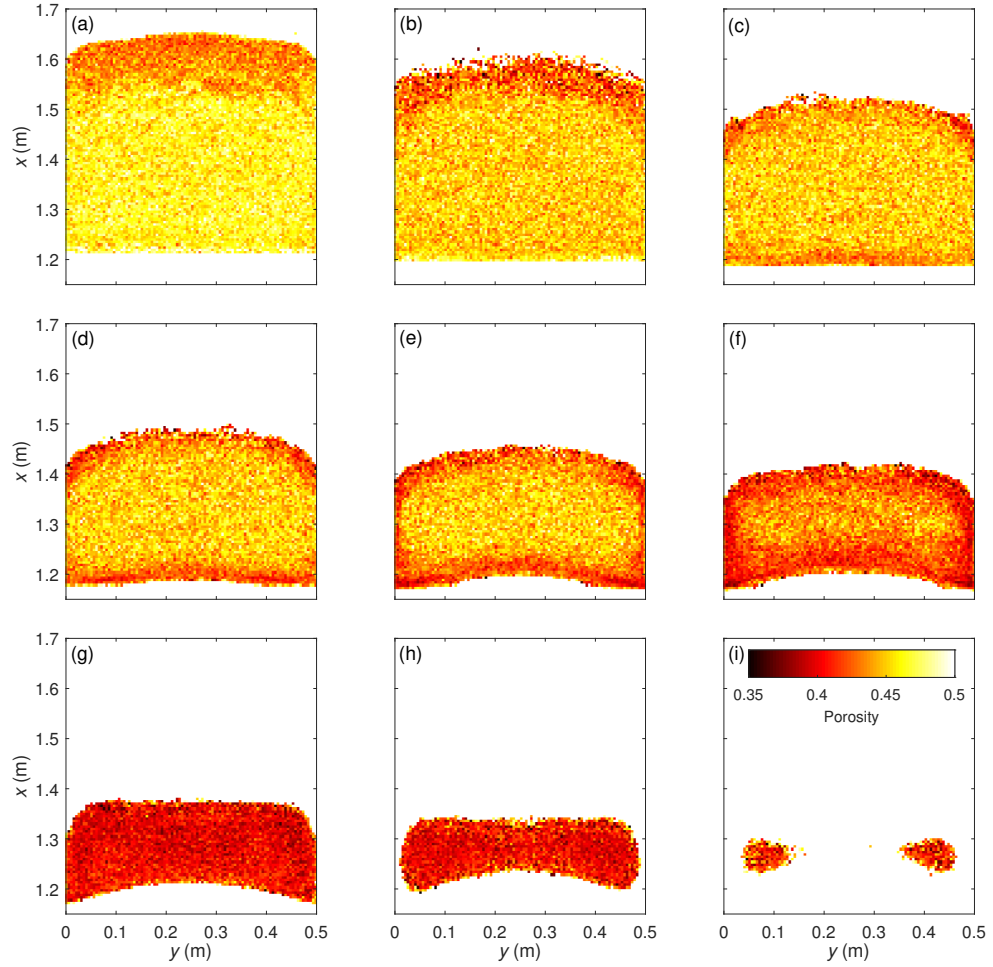


Figure 98 Local analysis of slide porosity for simulation S4, with $\lambda = 2$ and $\theta_W = 0^\circ$. (a) represents the first 5 mm away from the runout zone surface, with (b) to (i) moving up the deposit in 5 mm intervals

4. RESULTS

Overall, the deposit porosity away from base layer seems to stay constant until the deposit surface is encountered, at which point the porosity decreases to around $N = 0.41 \pm 0.025$. This again makes sense, as the particles at the top of the deposit surface are free to settle into gaps in the granular matrix without additional constraints from granular layers further down, resulting in tighter packing. The porosity also decreases noticeably towards the slide front, particularly on the base layer, which demonstrates porosity values close to the mean porosity of more elevated layers. This demonstrates that the deposit front varies considerably in composition from the rest of the deposit due to its settlement history and the potential segregation of particles during the slide event. Additionally, the deposit tail region is also considerably more compressed overall, with a thin strip being seen at the contact with the transition curve and extreme reduction in porosity to around $N = 0.40 \pm 0.025$, reduced even compared to the deposit surface in the flat runout zone.

Figure 99 provides further analysis of simulation S6, with $\lambda = 2$ and $\theta_W = 0^\circ$. Many of the features seen in Fig. 98 can also be seen in Fig. 99, such as reduced overall porosity compared to the initial estimates, increased porosity in the base layer and at the sidewalls, decreasing porosity with increasing height from the runout zone surface, and reduced porosity in close to the slide front and very close to the slide tail. In particular, the most drastic reduction of porosity at the slide tail is seen in the top three layers in Fig. 99(m)–(o), suggesting that this porosity-reducing mechanism is more related to the deposit surface than to the tail position. This confirms that the simulated slide porosity does not vary significantly with θ_W , and analysis of the simulations at different values of λ confirms that the simulation does not capture any porosity-related scale effects either.

The transition curve is clearly present as a horizontal cutoff at the base layers in Figs. 98 and 99. As the slide base and sidewall cells comprise of less of the total volume for higher values of θ_W , this corresponds to the slight decreases in porosity seen in the initial estimates in Table 8. While the simulation does not fully capture the shape effects seen from the angular particles in the laboratory experiments, it is likely that many of the features seen in Figs. 98 and 99 are also present in the

laboratory deposits due to the physical reasoning presented here. A similar analysis of the porosity of simulation S5 can be seen in Fig. 151 in Section D.

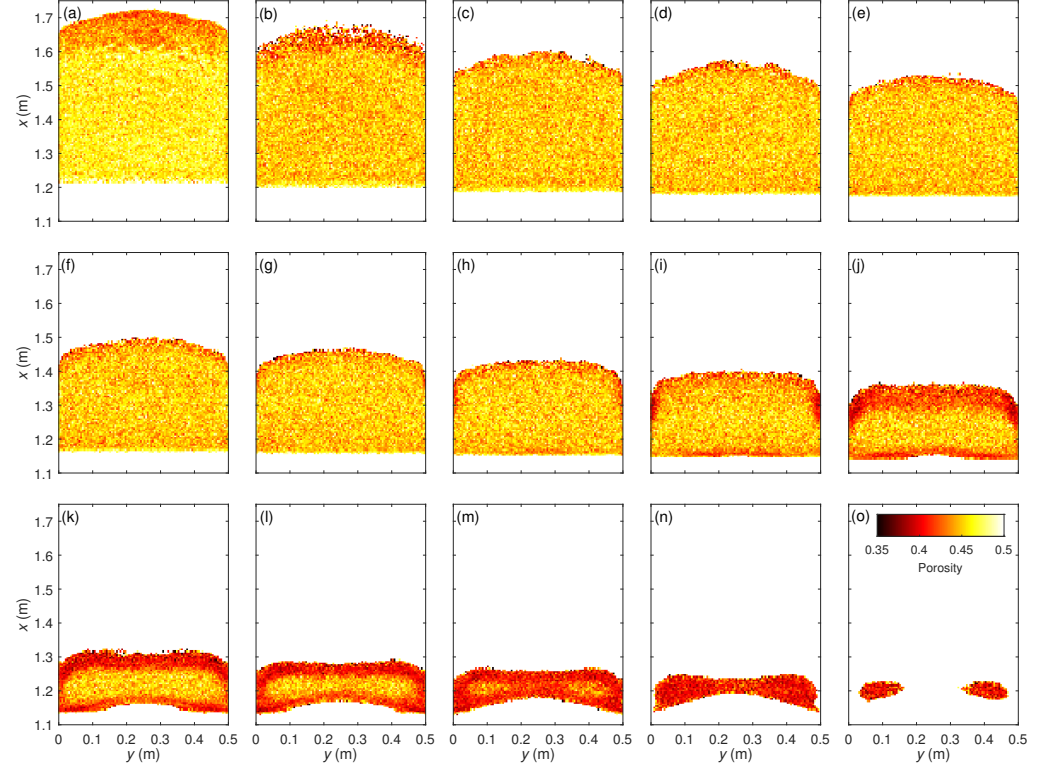


Figure 99 Local analysis of slide porosity for simulation S6, with $\lambda = 2$ and $\theta_W = 15^\circ$. (a) represents the first 5 mm away from the runout zone surface, with (b) to (o) moving up the deposit in 5 mm intervals

4.3.7 Simulated scale-series extrapolation

While many of the figures seen throughout Section 4.3 show that the simulation matches the behaviour of the medium-scale experiments at $\lambda = 2$ well in certain aspects, they also confirm that the simulations at $\lambda = 1$ and $\lambda = 4$ do not capture the laboratory experiments as well, showing an inability to reproduce scale effects. To further evaluate the capability of the DEM to model scale effects, additional simulations were performed using values of $\lambda = 0.2$ and $\lambda = 20$. The medium-scale

4. RESULTS

laboratory experiments were used as a baseline for comparison due to the relatively good match with the corresponding simulation.

Figures 100 and 101 highlight the position distributions of the slide events at $\lambda = 0.2$ and $\lambda = 20$ respectively. Meanwhile, Figs. 102 to 104 provide a visual comparison of the slide evolution from release to deposition of these three experimental scales, looking at quarter points in the duration of each slide after release. The initial slide tail and front positions are marked as $x_{t,0}$ and $x_{f,0}$ respectively. The physical dimensions of the slide are preserved to highlight the difference between the three experimental scales, and the images are taken from a top-down perspective looking over the runout area.

Overall, Figs. 100 to 104 show very similar relative slide behaviour at all points in the slide development at each scale, despite vast differences in slide mass and dimensions. Some interesting characteristics of the slide surface velocity can be seen in Figs. 102 to 104, such as the large amount of shearing at the sidewalls and the resulting staggering of the central and sidewall slide tails, being more-or-less equally present at all simulated scales. Some small changes can be seen in the front and tail positions of the final deposit, and to a lesser extent, during the latter phases of the slide evolution. The slide deposit tail position is about 3 particle diameters further from the transition curve at $\lambda = 20$ than at $\lambda = 0.2$, at both the channel sidewalls and centre. Meanwhile, the position of the discrete deposit front at $\lambda = 20$ exceeds that of $\lambda = 0.2$ by up to 12 particle diameters at the sidewalls, and up to 18 at the channel centre. Additionally, the central peak position is slightly delayed in Fig. 101 in comparison to Fig. 100, by a factor of roughly 2% where the distinct blue section near the moment of slide release disappears, while the corresponding peak at the sidewalls does not demonstrate this trend.

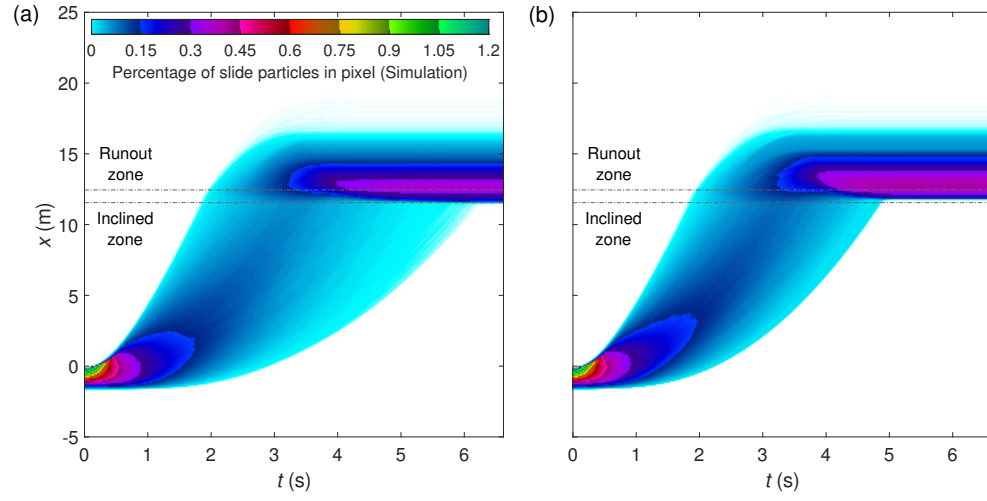


Figure 100 Position distribution over time for simulated slide S10, for $\lambda = 0.2$ and $\theta_W = 0^\circ$ at (a) channel sidewalls and (b) channel centre

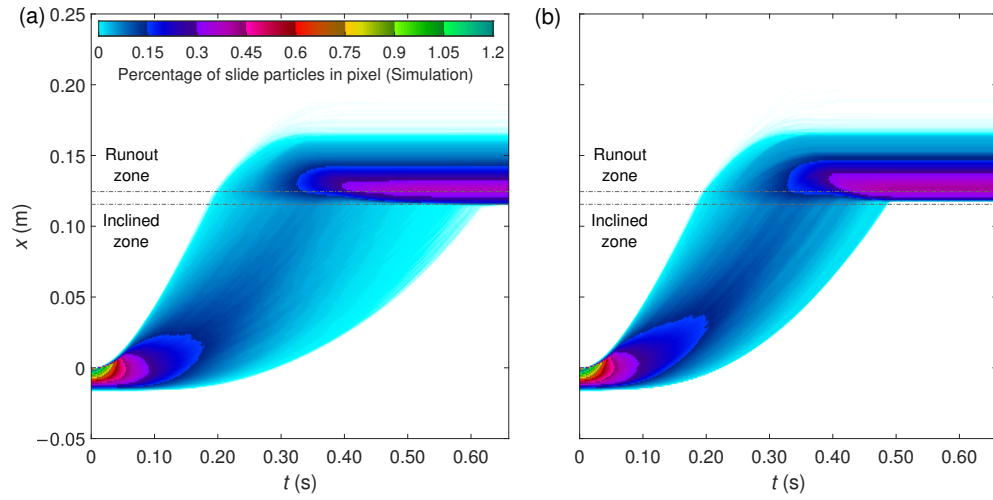


Figure 101 Position distribution over time for simulated slide S11, for $\lambda = 20$ and $\theta_W = 0^\circ$ at (a) channel sidewalls and (b) channel centre

4. RESULTS

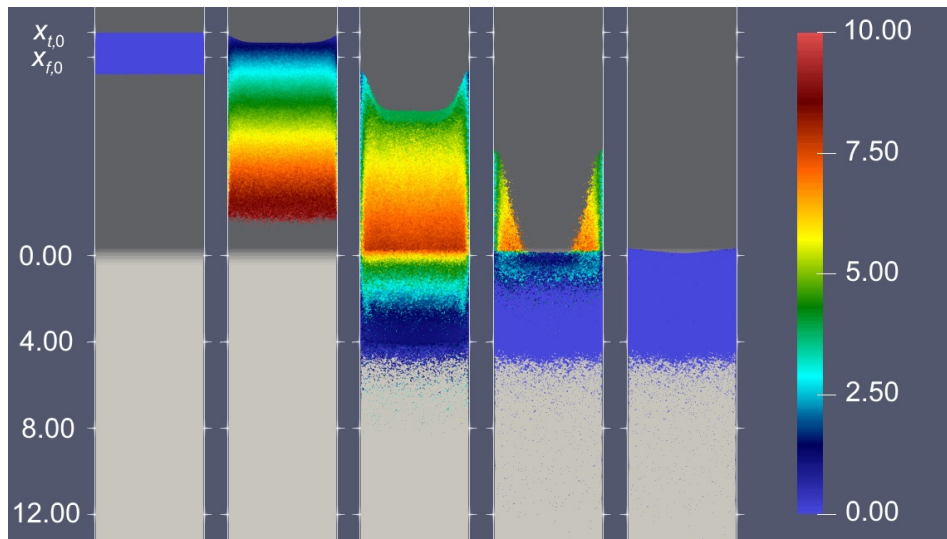


Figure 102 Plan view of slide position and velocity over time at $\lambda = 0.2$ (S11)

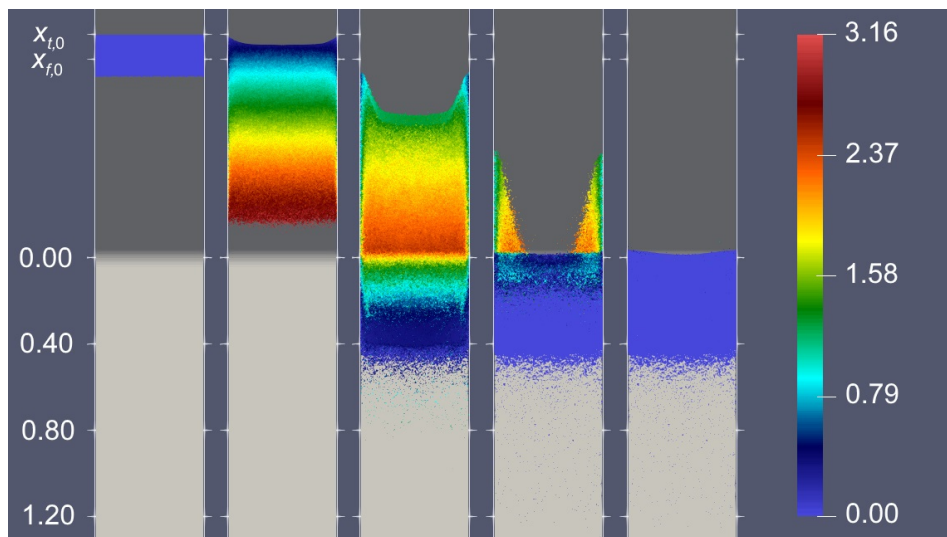


Figure 103 Plan view of slide position and velocity over time at $\lambda = 2$ (S4)

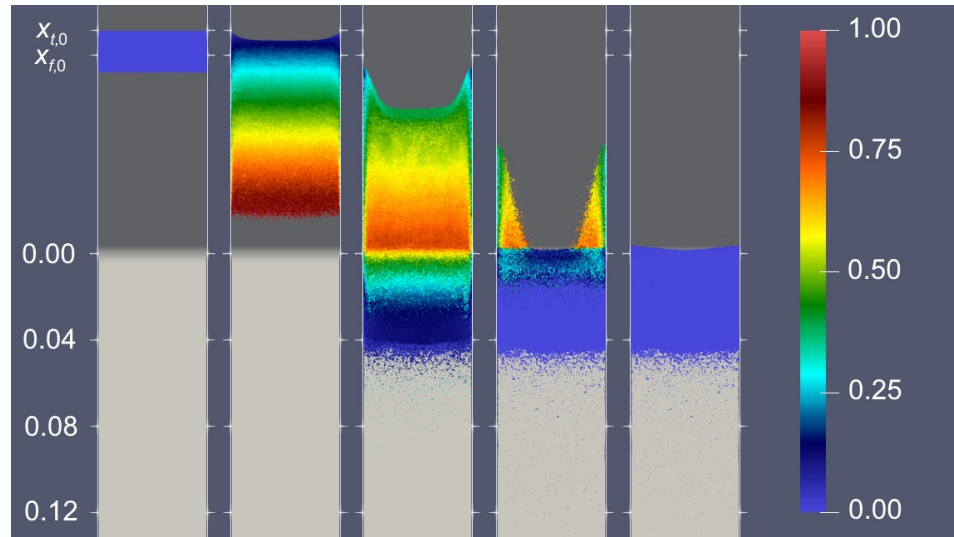


Figure 104 Plan view of slide position and velocity over time at $\lambda = 20$ (S10)

Additionally, Figs. 105 and 106 indicate that some subtle differences in velocity distribution across both slide events occur between $\lambda = 0.2$ to 20. In particular, the central blue cluster in Fig. 106 extends out 8% longer after the slide release before dissipating in comparison to the same cluster in Fig. 105, demonstrating reduced velocity of some particles at super-small scale. This suggests that scale effects start to become visible between simulations with a scale ratio of 100:1, with Fig. 79 showing that these trends are interpolated steadily as λ varies. These scale effects may manifest due to constant material stiffness causing differing Ca between the simulated slides.

This result is encouraging, showing that non-Re scale effects may be captured by the simulation, and that these differences in deposit position and velocity act in the direction seen the laboratory data, suggesting alignment with laboratory Re scale effects. However, the simulated scale effects remain insignificant within the main experimental range of $\lambda = 1$ to 4, due to the lack of representation of Re-related mechanisms in the DEM.

4. RESULTS

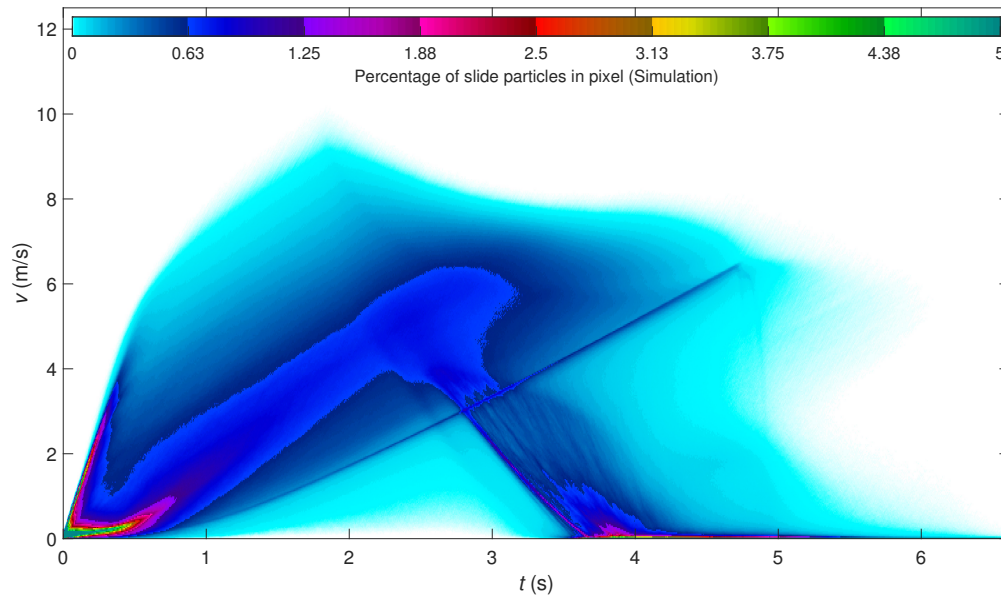


Figure 105 Velocity distribution for simulation S10, with $\lambda = 0.2$ and $\theta_W = 0^\circ$

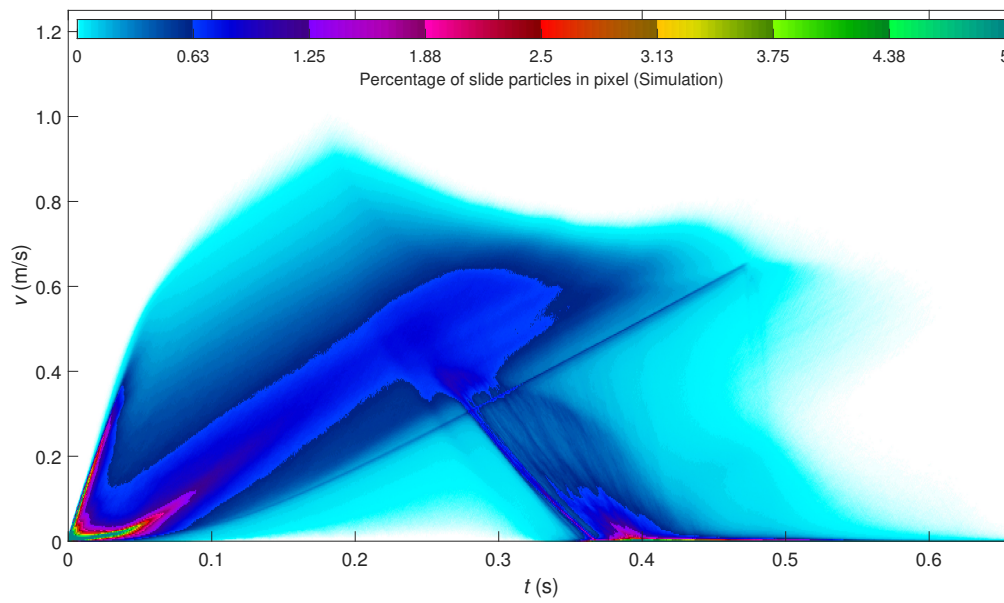


Figure 106 Velocity distribution for simulation S11, with $\lambda = 20$ and $\theta_W = 0^\circ$

4.4 Summary

Overall, clear scale effects were identified in the laboratory experiments, with the deposit position and shape depending heavily on λ and demonstrating increased runout distance with increasing size. This is matched by a clear increase of slide surface velocity with λ that can be seen at x_1 but becomes more pronounced further down the ramp at x_2 . The tail velocity showed particularly high dependence on scale and the large-scale deposits showed considerably greater spreading behaviour. Additionally, a "ridge" of peak thickness that depended strongly on θ_W could be identified from the laboratory data that was not present in the simulations, suggesting that the slide behaviour starts to vary significantly when its thickness passes a critical threshold. While this peak slide thickness does not seem to correlate directly with λ , the times at which these peak thicknesses pass over the measurement points correspond well to relative peaks in the slide surface velocities, suggesting that this phenomenon may still be linked to scale effects.

Generally the simulation showed a good match in surface velocity to the laboratory experiments, with values decreasing below the laboratory values at $\lambda = 2$ as the slide peak passed through the measurement points, tending towards the laboratory values at $\lambda = 1$ at the tail. However, despite this match in surface velocity, the sidewall surface velocity of the simulation greatly reduced over time compared to all of the laboratory slides. The simulation data and increased runout time of the simulated slide events highlights that the base velocity is also significantly reduced in the simulation compared to the laboratory slides; although no exact measurements of this velocity were taken, the impacts on the general slide dynamics are clear. These two changes seem to manifest in reduced overall runout length and deposit parameter positions in the simulations compared to the laboratory slides. However, the magnitude of these differences was not much greater than those caused by scale effects.

Additionally, the changes seen between laboratory slides of varying λ were mostly not replicated in the simulations of larger- and smaller-scale granular slides, with simulations with λ from 1 to 4 showing insignificant variation across all of

4. RESULTS

the key slide parameters. While simulations conducted at much larger and smaller scales in Section 4.3.7 showed some slight changes that depended on λ acting in the expected direction based on the discussion seen in Section 2, these changes were much smaller than those seen in the laboratory experiments. The differences between slides with different values of θ_W are generally replicated throughout experimental repeats and at different experimental scales, and correspond well to differences seen in simulations of varying θ_W . This highlights that the differences identified with varying λ are the result of scale effects. The causes and nature of these scale effects are further discussed in Section 5.

5 Discussion

5.1 Introduction

In this chapter, the experimental results will be discussed and analysed in the context of other studies, attempting to discover the causes of differences identified between granular slides of different experimental scales. The numerically simulated granular slides will also be analysed in more depth to identify whether physical processes identified in the laboratory slides and in the literature manifest in the DEM, and to direct ideas for further laboratory experimentation. In Section 5.2, the relative scale-invariance of the DEM compared to the laboratory experiments will be discussed relating to underlying physical mechanisms and their deployment within the model, for both Re and Ca scale effects. In Section 5.3, the slide velocity profile over the slide depth recorded in the simulations will be compared to the Bagnold-like profile.

In Section 5.4, various non-dimensionalised slide parameters from different experimental scales will be correlated, minimising the difference between subsets to produce estimates for how strongly the grain Reynolds number influences each parameter, and highlighting the differences in influence between parameters. Section 5.4.1 is focused on the slide surface velocity, while Section 5.4.2 is focused on physically validating the influence of Re scale effects in this context. Section 5.4.3 is focused on key deposit parameters, while Section 5.4.4 compares the slide runout data to that of other studies, and Section 5.4.5 is focused on the slide volumes and porosities. Finally, in Section 5.5, focus is placed on the model effect of constant surface roughness on the scale series of experiments in this study, and the difference from that seen in Pohlman et al. (2006) is highlighted.

5.2 Scale-invariance in DEM and secondary mechanisms

One of the main observations made when comparing the numerical DEM simulations to the laboratory experiments, was the comparative lack of scale effects seen with increasing scale in the DEM. While the simulations generally represented parameters such as the slide surface velocity, runout distance, and deposit morphology well, there were no significant differences seen between simulations of different scales. After non-dimensionalisation, all of the aforementioned key parameters remained roughly constant between the simulations at different scales. This demonstrates that the processes that lead to the most dominant scale effects in the laboratory experiments are not modelled adequately within the DEM. For example, the DEM does not capture the effects of air flow through the granules, particle fracture and subsequent dust generation, or acoustic fluidisation. The relative impact of these mechanisms on the laboratory experiments will be assessed.

Parez and Aharonov (2015) highlight two physical processes that would lead to increased runout with increasing scale in a purely granular model: either the friction of the slide is dependent on the slide volume, due to changes in shear rate and other related mechanisms, or grains spread further from the slide centre of mass as scale increases (as noted in Section 2.3.3). This presents a dichotomy of whether increasing runout with increasing scale is dominated by changes in overall friction (and thus the centre of mass of the slide runs out further to a similar degree as the slide front and tail) or by changes in spreading (and thus the slide front extends much further from the centre of mass).

Table 9 clarifies this dichotomy, and shows that the balance between centre-of-mass movement and longitudinal spreading behaviour is roughly balanced across the laboratory experiments of this study. L_s denotes the longitudinal spread or slide length, simply being $x_f - x_t$ in this case. The deposit longitudinal spread for the experiments at $\lambda = 1$, $\theta_W = 0$ is 35% higher on average than that of the corresponding experiments at $\lambda = 4$, with this percentage increasing to 36.2% at $\theta_W = 7.5^\circ$ and again to 42.2% at $\theta_W = 15^\circ$. Comparing the centre-of-mass movement between $\lambda = 1$ and $\lambda = 4$, x_c is placed 26.4% further from the shutter

release position at the larger scale at $\theta_W = 0^\circ$, increasing to 30% at $\theta_W = 7.5^\circ$ and to 33% at $\theta_W = 15^\circ$. Meanwhile, deposit spreading was reduced at $\lambda = 2$ compared to at $\lambda = 4$, but the slide centre-of-mass remained slightly further from the transition curve.

Table 9 Laboratory slide spreading and centre of mass movement

Exp. no.	λ	θ_W	x_t/d (side)	x_t/d (centre)	x_f/d (side)	x_f/d (centre)	L_s/d (side)	L_s/d (centre)	x_c/d
(-)	(-)	($^\circ$)	(-)	(-)	(-)	(-)	(-)	(-)	(-)
L1–L6	1	0	1103	1144	1584	1601	481	457	1330
L7–L12	1	7.5	1101	1138	1648	1684	547	546	1363
L13–L17	1	15	1084	1127	1714	1766	630	639	1394
L18–L21	2	0	886	967	1250	1287	364	320	1098
L22–L25	2	7.5	925	973	1262	1309	337	336	1107
L26–L29	2	15	915	958	1389	1407	474	449	1138
L30–L37	4	0	897	923	1248	1268	351	345	1052
L38–L45	4	7.5	866	892	1264	1296	398	404	1049
L46–L53	4	15	845	869	1284	1323	439	454	1048

This confirms that, across the entire scale series, both the deposit spreading and centre-of-mass movement tend to increase as smaller values of λ and larger experimental scales are approached. This suggests that the scale effects imposed on the granular slides may affect the effective friction at the base and the shearing behaviour of the top slide layer to similar degrees. However, scale effects that impact the slide runout may also be influenced by fluidisation, with fluidisation mechanisms such as acoustic, stiffness-related, and air fluidisation potentially having a strong influence on the basal slide motion while also facilitating increased shear with the material above it.

5.2.1 Influence of acoustic fluidisation

The acoustic energy density caused by vibrations at the channel base is strongest close to this basal region (Collins and Melosh, 2003; Chung, 2018), with airflow (Re) fluidisation becoming more dominant in the upper slide layers, imposing scale effects on slide velocity throughout the slide depth. Interestingly, while centre-of-mass movement was independent of θ_W at the smallest experimental scale, the influence of θ_W on this parameter seems to increase as λ decreases. Meanwhile, the deposit spread increases strongly with θ_W at all three scales, with this difference increasing only slightly more at higher values of θ_W . This highlights that the thickness-dependence of slide parameters such as the deposit centre-of-mass starts to increase with scale. Additionally, this suggests that the effects of mass-dependent mechanisms such as acoustic fluidisation are also subject to scale effects.

Melosh (1979) and Collins and Melosh (2003) suggest that acoustic fluidisation is characterised by high-frequency pressure variations that occur, in the context of this study, as the release wedge collapses and spreads over the ramp surface. These vibrations may then overcome the overburden stresses of the slide material at certain locations if they are strong enough, reducing the effective friction of the slide. These pressure variations differ from those caused by random particle collisions due to their scale relative to the slide mass; acoustic pressure variations are likely to influence large local areas of particles at once in similar ways. The response of the slide depends strongly on the dominant wavelengths of the vibrations, which may elucidate how scale effects could manifest via this mechanism. For particles of the same material, it may be that the dominant wavelengths do not scale linearly with the particle diameters. This could cause acoustic effects to relieve the overburden pressure in different ways at different scales, as the increasing thickness of the slides correspond to the dominant vibration wavelengths.

While the Rayleigh-wave-speed described in Section 3.4.6 varies in proportion to the particle diameter, this represents the wavelength of dispersive, random particle collisions, rather than the larger wavelengths representative of acoustic fluctuations. In both cases, these wavelengths do not conform to Froude scaling,

suggesting that acoustics could cause scale effects to manifest within a Froude scale series. The strength of these scale effects is difficult to quantify. Collins and Melosh (2003) suggest that the dominance of acoustic wavelengths over individual particle collisions in a slide would cause large groups of particles to move in unison with greatly reduced granular temperature, reducing the energy dissipation caused by particle collisions and thus allowing the slides to run out for longer and over greater distances. Laboratory measurement of the granular temperature throughout the depth of granular slides in a Froude scale series could further elucidate the strength of acoustic fluidisation relative to airflow fluidisation.

However, Collins and Melosh (2003) also suggest that the dominant wavelengths of acoustic fluidisation are likely within the order of 0.01 to 1 m. As the maximum slide thickness during flow approaches a maximum of 0.04 m at x_2 at $\lambda = 1$, it is unlikely that the slide thickness would exceed this wavelength apart from during the initial collapse of the release wedge, where the slide thickness reduces quickly from 0.25 m towards more representative values. This may cause laboratory experiments of the scales seen in this study to be unable to model the influence of acoustic fluidisation seen in slides thicker than one wavelength, and thus these scale effects may not be present in this study.

Johnson et al. (2016) also suggests that acoustic fluidisation is a dominant mechanism in driving the long runout of large natural events, fluidising slides even shortly after their initial release. Johnson et al. (2016) notes the presence of two dominant frequencies; one consistent with waves between the slide and basal surfaces and one of the order of $2d$ that acts in combination with the former to produce acoustic fluidisation. Johnson et al. (2016) describes the former to be problematic as a dominant influence in isolation, as it would suggest that slide viscosity would increase with slide thickness, when the opposite is found in nature. Furthermore, these simulations attempt to replicate acoustic fluidisation in large natural events with very large particles with diameters in the order of 1 m. In this context, the Rayleigh-wave speed is significantly different and the dominant wavelengths of 0.01 to 1 m seen in Collins and Melosh (2003) are present. Additionally, the simulations used in Johnson et al. (2016) to validate natural events are 2D in

nature and use discs rather than spheres, preventing lateral transmission of acoustic waves across the slide width. Overall, while there is evidence to suggest that acoustic fluidisation is relevant to scale effects in large granular slides of a natural scale, there is little evidence to suggest that the mechanism is impactful at the laboratory scale, where significant scale effects have still been observed.

5.2.2 Influence of material stiffness

The only slight scale effect seen in the simulations (see Tables 2 and 6 for key input parameters) was a slight increase in runout (in the order of 20 particle diameters) between $\lambda = 0.2$ and $\lambda = 20$, a scale difference of 100. This difference is insignificant compared to the runout difference seen in the laboratory experiments across a much smaller scale range (Table 7), and thus is not likely to be caused by the same physical mechanism. For such a large scale difference between these simulations, material parameters that remain constant across all scales (such as the particle stiffness) may start to impose additional, smaller effects. As discussed in Section 2.3, the grain Cauchy number (Ca) is a force ratio representing the balance between inertial and elastic forces, and was highlighted as a potential cause of scale effects. However, as the particle stiffness is extremely high and the stiffness of the chute surface covering polypropylene and underlying steel are also relatively high, the elastic forces acting on the slide are very low compared to the gravity force. This justifies why the differences in Ca only start to induce small effects at large scale differences in the simulations. While it is likely that these effects would also manifest in laboratory experiments of similar scale differences, it would be difficult to isolate these Ca scale effects from the more dominant Re scale effects, due to their extremely small magnitude and relative lack of influence.

Another factor that must be considered is the presence of apparently minor levels of particle fracture and dust generation in the laboratory experiments. While this was practically non-existent at $\lambda = 4$, at $\lambda = 1$ the channel became coated in a very thin layer of dust after the experiments were completed, suggesting that dust generation increases with size. This factor is likely related to Ca and

the particle Weibull modulus, as these numbers reflect the respective influence of compressibility and fracture behaviour on the granular slides. As the fracture of particles acts as a dissipative mechanism, reducing the energy of colliding particles, one might expect that the increase of particle fracture rate at increasing scale would reduce the slide velocity and deposit runout of granular slides. This may be counteracted by particle wear and abrasion removing asperities, reducing the particle friction coefficients to a greater degree. The build-up of dust could also impact the size distribution of the sliding particles (Einav, 2007) and cause a greater overall collision-rate throughout the slide due to the increase in particle count, potentially dissipating even more energy. This change in size distribution may also impact segregation behaviour, which can potentially be significant at the slide front and tails (Johnson et al., 2012; Gray, 2018). Furthermore, the generation of dust may impact airflow through the granular slide in complex ways.

However, even at $\lambda = 1$, the mass of dust generated in experiments was extremely low compared to the bulk slide mass, perhaps 0.01–0.1%. The energy dissipation caused by such a low fracture rate is extremely small compared to the kinetic energy of the slide and even the surrounding airflow, with the model effect of increasing fracture being far weaker than the scale effect of Re -dependence seen in this study. Due to the extremely low level of dust generation seen in the laboratory, the influence of the mechanisms described in this section are likely to be extremely minimal. While the relative influence of the particle-fracture model effect compared to that of using a scale-constant material stiffness is hard to quantify, it is clear from the laboratory data that the extremely low level of dust generation present is not the cause of the significant scale effects seen.

In conclusion, with acoustic and stiffness-related influences on scale effects also being ruled out as minimal in the laboratory experiments of this present study, this leaves air fluidisation as the remaining candidate for the key mechanism facilitating laboratory scale effects. The degree of influence that air fluidisation exerts over these scale effects will be evaluated in Section 5.4. Additionally, acoustics between particles are not captured by the DEM, and thus cannot be responsible for the small differences seen in the simulations in Section 4.3.7.

5.3 Power-law-similarity of simulated slide velocity profiles

This section investigates how similar the granular slides conducted in this study are to continuous granular flows with similar properties. If the unsteady granular slide was found to match the properties of a steady granular flow at specific moments in time, then scale-effects identified in this study may also be applicable to granular flows under specific circumstances. As the Bagnold model is typically representative of steady granular flows, comparing the granular slides to power-law models reminiscent of the Bagnold profile will highlight how steady the shearing behaviour in the granular slides is in different regions, such as the slide front, peak, centroid, and tail, throughout the slide events.

Figures 107 and 109 provide the velocity data from Figs. 82 and 83 normalised with respect to the maximum velocity and thickness at each time interval. Figures 108 and 110 attempt to map power law functions onto the variation of velocity throughout the slide depth seen in Figs. 107 and 109. This function is similar to the typical Bagnold velocity profile seen in Eq. (1) in Section 2.2.1, except the power of $3/2$ is replaced with β to provide the best fit to the underlying data. Furthermore, as the typical Bagnold profile defines a condition where the slip velocity is zero (such as a flow on a rough bed), this expression has been modified to fit $u(z)$ from the slip velocity $u(0)$ to the surface velocity $u(h)$. As the ramp angle θ remains constant in the experiments of this study, $A(\theta)$ also remains constant, so it can be ignored when comparing the relative difference between surface and base velocity. This results in the following expression:

$$u(z) = u(0) + [u(h) - u(0)] \left[1 - \left(\frac{h-z}{h} \right)^\beta \right]. \quad (48)$$

The powers of β seen in Figs. 108 and 110 were selected by minimising the mean residual r_{min} of the fit function to the simulation velocity data, with β and r_{min} being provided for the slides at $\theta_W = 0^\circ$ in Table 10 and at $\theta_W = 15^\circ$ in Table 11. Values of β close to 1.5 highlight that the slide behaves similarly to

a Bagnold-like flow, in that the slide velocity increases more and more quickly with the distance from the channel surface. Values of β closer to 1 highlight that the shear flow through the slide at the measurement point varies uniformly with depth, more closely resembling plug-like flow. The velocity profiles shown in Figs. 108 and 110 are normalised with the maximum slide velocity u_s (the surface velocity was consistently the highest velocity metric of the simulated slides) and the slide thickness h . The mean residuals are also normalised with respect to the maximum slide velocity u_s , and were generally largest during the middle phases of the slide and at the sidewall positions, increasing with θ_W at the central position.

Particles that have detached from the main slide body (typically by at least 2 mean particle diameters) have been excluded from this analysis, typically resembling about 1 to 2% of the data. At the time intervals where these velocity profiles are recorded, these excluded particles do not influence the bulk granular slide and are thus treated as outliers, to ensure that the β values and power-laws selected are as applicable to and representative of the bulk slide as possible. Overall, Figs. 108 and 110 show that the value of β fluctuates significantly as the slide enters and exits both the x_1 and x_2 measurement points (Fig. 44), at both the channel sidewall and centre. In Fig. 108 at the sidewalls, values typically fluctuate between 1.0–1.5, with values as low as 0.64 and as high as 2.03.

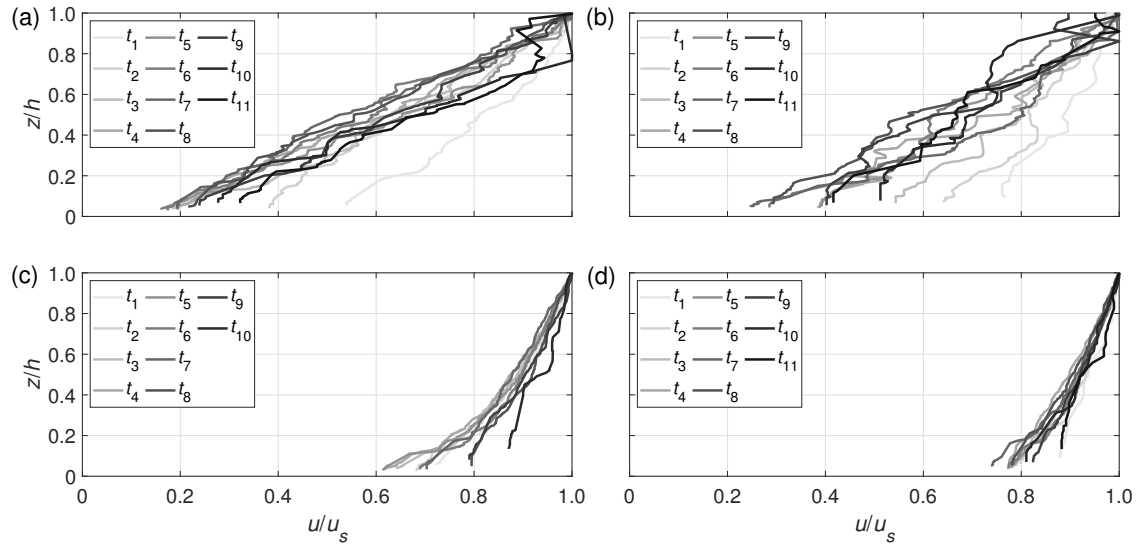


Figure 107 Simulated (S4) particle velocity data (Fig. 82) normalised to maximum velocity and thickness at (a,c) x_1 and (b,d) x_2 at (a,b) the channel sidewall and (c,d) the channel centre, with $\theta_W = 0^\circ$. Data plotted at 400,000 time-step intervals t_1 to t_{11} , with t_1 starting 400,000 time-steps after the front reaches the measurement point

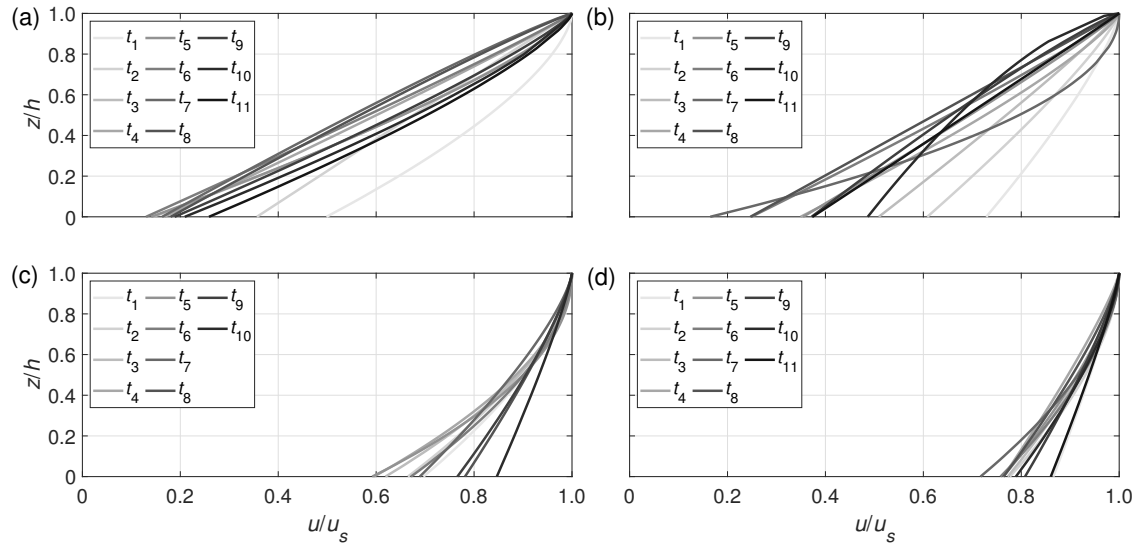


Figure 108 Fitting of power-law velocity profiles based on Eq. (48) over the slide depth of simulated (S4) particle velocity data (Fig. 107) at (a,c) x_1 and (b,d) x_2 at (a,b) the channel sidewall and (c,d) the channel centre, with $\theta_W = 0^\circ$. Fit-lines plotted at 400,000 time-step intervals t_1 to t_{11} , with t_1 starting 400,000 time-steps after the front reaches the measurement point

Table 10 β and r_{min} values for Fig. 108 with $\theta_W = 0^\circ$

Time-step	x_1 , sidewall		x_2 , sidewall		x_1 , centre		x_2 , centre	
	β	r_{min}	β	r_{min}	β	r_{min}	β	r_{min}
(-)	(-)	(%)	(-)	(%)	(-)	(%)	(-)	(%)
t_1	1.56	1.09	1.28	1.51	1.63	0.91	1.18	0.50
t_2	0.99	2.22	1.20	2.36	1.63	1.01	1.69	0.95
t_3	1.30	3.28	1.09	2.05	1.81	1.70	1.49	0.37
t_4	1.06	1.86	1.25	3.28	1.82	1.68	1.18	0.38
t_5	1.31	1.65	1.08	1.83	2.03	1.94	1.46	0.75
t_6	1.06	2.26	1.11	3.46	1.73	1.63	1.68	1.04
t_7	0.90	1.77	2.03	3.28	1.35	1.18	1.75	0.89
t_8	0.92	1.96	1.00	3.01	1.25	0.80	1.30	0.47
t_9	1.18	1.91	0.87	5.22	1.31	0.53	1.27	0.29
t_{10}	1.30	4.67	0.64	3.14	1.19	0.76	1.47	0.93
t_{11}	1.32	3.28	1.01	2.51	-	-	1.18	0.99

Meanwhile, at the channel centre, β values are typically higher and range from 1.18–2.03, indicating that the flow at the channel centre is more Bagnold-like while the flow at the channel sides is more plug like. β values are demonstrably greater at the channel centre, which alongside increased basal velocity implies significantly different flow conditions between the channel sidewalls and centre. In Fig. 110, the values of β produced at the sidewalls are very similar to those seen in Fig. 108 despite the increase in slide thickness. However, the β values at the channel centre are significantly increased in Fig. 110, with the minimum relative slip velocity also decreasing. This suggests that the additional overburden pressure applied by the thicker slide mass most strongly affects the basal velocity at the channel centre. This is supported by the consistent increase of β as the slide peak approaches, matched by a consistent decrease as the slide peak passes the measurement points.

At the channel sidewalls, the value of β often fluctuates between specific timesteps, suggesting that short-term movements of grains have a greater in-

fluence on the shear behaviour in the slide than long-term characteristics such as the slide history. This fluctuation is strongest when $\theta_W = 0$; this makes physical sense as the reduced overburden pressure allows individual grain movements on the base to disturb the surface layers of the slide to a greater extent. Additionally, the slip velocity is greatest as the slide fronts and tails pass the measurement points, decreasing to its lowest relative value roughly halfway during the slide's passing. This property holds true in both Fig. 108 and Fig. 110, with the slip velocity being greatest as the slide front passes at the sidewalls, and as the slide tail passes the channel centre, providing some insight into the longitudinal shear that may be occurring in the slide mass during this time. Additionally, combined with observations from Figs. 82 and 83, it can be seen that this variation of β is not necessarily correlated with the ratio of slip to surface velocity. β describes the rate at which the slip velocity transitions to the surface velocity, and is more representative of the relative depth of influence at which the channel friction starts to dissipate in the slide than of the overall frictional influence.

This behaviour is consistent for both values of θ_W presented. Comparing the data in Figs. 108 and 110 at the two measurement points, the slip velocity typically increases relative to the surface velocity at all time-steps at x_2 compared to x_1 . However, the differences in β values selected do not seem to show much correlation to θ_W . β values in (a) and (b) seeming to fluctuate around the same mean in both Fig. 108 and 110, suggesting that the shear flow for both initial conditions is fundamentally similar at the sidewalls, despite the differences in overall slide thickness. Overall, the strongest conclusion that can be drawn from Figs. 108 and 110 is that the linearity of the simulated slide velocity profiles with depth varies considerably, with fluctuations caused by individual particle movements having a stronger influence on thinner slides, while the spatial and temporal positioning of the slide have a stronger influence on thicker slides. This fluctuation may be diminished in the laboratory experiments where particle interlocking exerts more influence on the slide motion, but it may also be augmented by the more random contact dynamics caused by the irregular particle shapes.

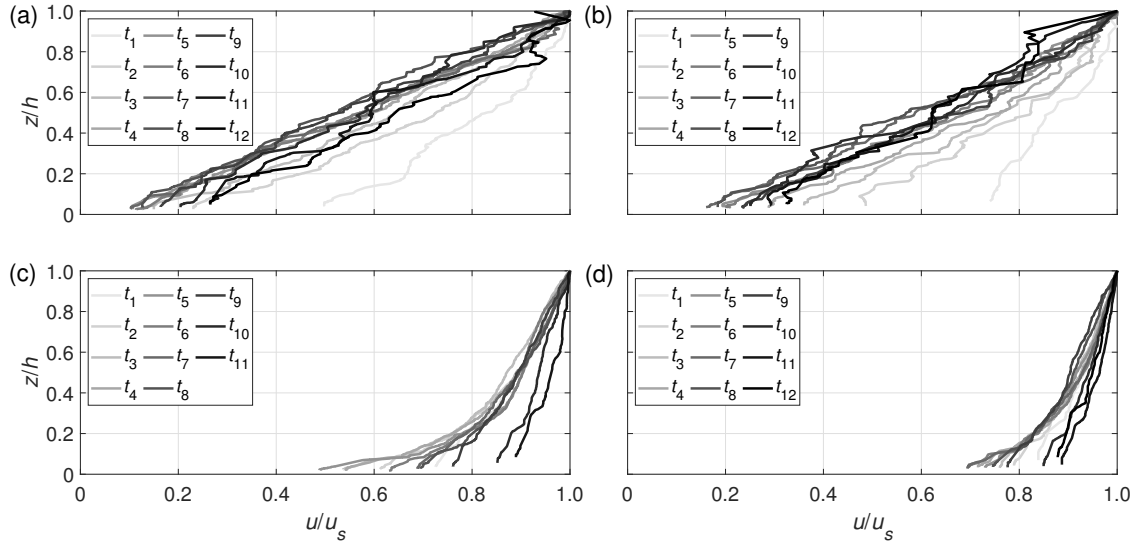


Figure 109 Simulated (S6) particle velocity data (Fig. 83) normalised to maximum velocity and thickness at (a,c) x_1 and (b,d) x_2 at (a,b) the channel sidewall and (c,d) the channel centre, with $\theta_W = 15^\circ$. Data plotted at 400,000 time-step intervals t_1 to t_{12} , with t_1 starting 400,000 time-steps after the front reaches the measurement point

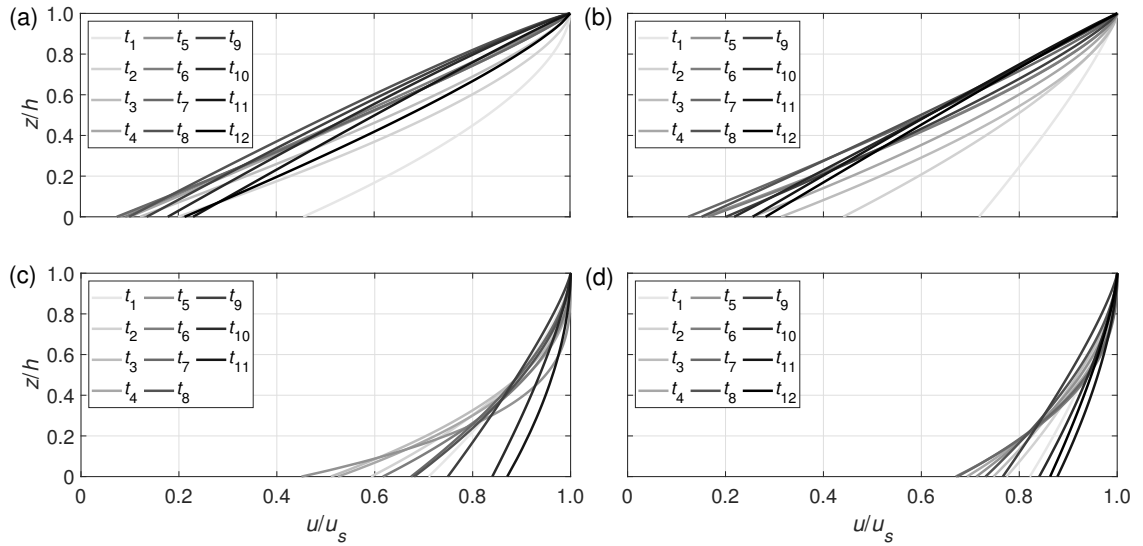


Figure 110 Fitting of power-law velocity profiles based on Eq. (48) over the slide depth of simulated (S6) particle velocity data (Fig. 109) at (a,c) x_1 and (b,d) x_2 at (a,b) the channel sidewall and (c,d) the channel centre, with $\theta_W = 15^\circ$. Fit-lines plotted at 400,000 time-step intervals t_1 to t_{12} , with t_1 starting 400,000 time-steps after the front reaches the measurement point

Table 11 β and r_{min} values for Fig. 110 with $\theta_W = 0^\circ$

Time-step	x_1 , sidewall		x_2 , sidewall		x_1 , centre		x_2 , centre	
	β	r_{min}	β	r_{min}	β	r_{min}	β	r_{min}
(-)	(-)	(%)	(-)	(%)	(-)	(%)	(-)	(%)
t_1	1.69	1.82	1.22	1.36	1.48	0.66	1.42	0.45
t_2	1.51	1.68	1.44	1.91	1.98	1.60	1.62	0.54
t_3	1.27	1.90	1.57	1.67	2.27	3.55	1.65	0.84
t_4	1.10	1.22	1.43	1.82	2.42	2.69	2.22	1.40
t_5	1.13	1.48	1.36	1.94	3.43	3.65	1.95	1.12
t_6	1.06	1.63	1.36	1.11	2.13	2.75	2.51	1.55
t_7	1.13	1.98	1.17	1.36	1.64	0.95	2.40	1.63
t_8	0.88	1.32	1.08	2.41	1.72	1.21	1.63	1.36
t_9	0.89	1.95	1.22	1.69	1.22	0.59	1.24	0.92
t_{10}	0.89	2.15	1.02	3.54	1.34	0.75	1.43	0.49
t_{11}	0.95	3.08	0.95	2.04	1.82	0.33	1.63	0.35
t_{12}	1.25	2.47	0.97	2.94	-	-	1.38	0.48

Schaefer and Bugnion (2013) describe a robust experimental methodology used to collect accurate slide velocity profiles at the channel sidewalls, featuring experiments with spherical ballotini in a range of sizes and frictional conditions. Velocity fields for the sidewall flow were constructed from high-speed camera footage in a similar manner to how the surface velocity fields in this study were calculated. Fig. 3(b) in Schaefer and Bugnion (2013) demonstrates similar velocity fields at the channel sidewall to those in Fig. 82 of this study, with their experiment showing slightly more curvature of the velocity profiles due to the additional friction with the rough channel surface. This highlights that the variation of slide velocity with depth fluctuates similarly in the numerically simulated and laboratory flows with spherical particles, suggesting that airflow through the slide does not significantly disrupt this depth-velocity gradient. This implies that it would be possible to identify scale effects in this velocity variation with a scale series of laboratory experiments conducted in a similar manner to Schaefer and Bugnion (2013).

5.4 Reynolds-dependency of key slide parameters

The main hypothesis presented in this study is that the differences in slide parameters such as slide surface velocity, slide thickness, and slide runout can be attributed to differences in the grain Reynolds number (Re) between experimental scales. The Froude scaling approach described in Section 2.3 ensures that the gravity force is accounted for correctly in the experimental scale series of this study. However, it also highlights differences in how the air-particle interaction influences the slide motion. To quantify the relative strength of Re on various slide parameters, power-fitting has been completed to identify the optimal fit of experimental data when multiplied by a power α of Re .

5.4.1 Reynolds-dependency of surface velocity

Figures 111 and 112 multiply the non-dimensional laboratory surface velocities highlighted in Figs. 84 and 85 by a power of Re at each moment in time as the slide passes through the x_1 and x_2 measurement points. While multiplying or dividing by Re without a power is not useful (Figs. 147 and 148 show this for the data with $\theta_W = 0$), a power α can be selected so that the experimental data at each scale collapses with minimal error and maximised R^2 values. This approach finds the extent to which the surface velocity is correlated to Re ; a value of $\alpha = -1$ (i.e. pure correlation) results in a parameter with d as the only variable and thus does not collapse the data effectively, so it is expected to find α values greater than -1 .

The fit-line to which the collapsed data-set is matched is a polynomial that starts when t_* , the non-dimensional time at which the slide front reaches the measurement point, equals 0. These polynomials follow the structure seen in Eq. (49); this structure was selected to capture the main features seen in the velocity profile, such as the sharp decrease in initial velocity levelling out as the majority of the slide passes. For example, T_4 and T_5 mostly fit to the tail passing.

$$t(d/g)^{1/2} = T_0 + T_1 t_* + T_2 t_*^2 + T_3 t_*^3 + T_4 t_*^4 + T_5 t_*^5 \quad (49)$$

Table 12 highlights the α and R^2 values of the Re-normalised data in Figs. 111 to 113 and compares them to the R^2 values of the unnormalised, original data. The coefficients T_0 to T_5 are also given for each data-set shown in Figs. 111 to 113. Slight improvement of data-fit with Re-normalisation is seen at x_1 , with greater improvement at x_2 .

Overall, Fig. 111 shows that the non-dimensional laboratory surface velocity collapses fairly neatly between experimental scales when multiplied by an appropriate power of Re, at least for the flat initial release wedge. The match is particularly good during the middle phase of the slide, after the front has passed and the peak thickness is reached but before the tail approaches and the thickness starts to decrease significantly. However, the timing difference seen when the slide fronts arrive at the measurement points at $\lambda = 4$ remain present, as do differences in the tail velocity decline at $\lambda = 1$. Notably, the value of α at x_2 is almost double that seen at x_1 , showing an overall improvement of the degree of fit to the experimental data. This demonstrates that the dependence of the slide surface velocity on Re increases further down the slide, i.e., faster slides become exponentially more dependent on Re. This makes sense as Re is proportional to the particle velocity; the difference in α between x_1 and x_2 is close to the square of the difference in slide velocity at a specific t_* between these measurement points.

Table 12 α and R^2 values of the original and Re-normalised slide surface velocity fitted to Eq. (49). Fit improvement refers to the improvement of fit between pure $u_s/(gd)^{1/2}$ scaling and combined $u_s/(gd)^{1/2} \times \text{Re}^\alpha$ scaling

Fig.	θ_W	Position	α	R^2	Fit imp.	T_0	T_1	T_2	T_3	T_4	T_5
(-)	(°)	(-)	(-)	(-)	(%)	(-)	(-)	(-)	(-)	(-)	(-)
Fig. 111	0	x_1	0	0.820	14.9	18.35	-2.8×10^{-1}	1.3×10^{-3}	1.4×10^{-4}	-2.6×10^{-6}	1.2×10^{-8}
			-0.029	0.847		14.58	-1.7×10^{-1}	-3.6×10^{-4}	1.4×10^{-4}	-2.5×10^{-6}	1.2×10^{-8}
		x_2	0	0.759	43.7	22.65	-1.6×10^{-1}	-4.3×10^{-3}	2.4×10^{-4}	-3.3×10^{-6}	1.4×10^{-8}
			-0.047	0.865		16.57	-5.2×10^{-2}	-5.6×10^{-3}	2.3×10^{-4}	-3.0×10^{-6}	1.3×10^{-8}
Fig. 149	7.5	x_1	0	0.804	17.4	19.03	-4.1×10^{-1}	1.2×10^{-2}	-1.7×10^{-4}	1.3×10^{-6}	-4.3×10^{-9}
			-0.029	0.838		14.89	-2.2×10^{-1}	5.4×10^{-3}	-5.8×10^{-5}	2.4×10^{-7}	-5.6×10^{-10}
		x_2	0	0.750	49.2	22.82	-1.9×10^{-1}	-1.3×10^{-3}	1.4×10^{-4}	-2.0×10^{-6}	8.1×10^{-9}
			-0.048	0.873		16.58	-7.8×10^{-2}	-2.7×10^{-3}	1.3×10^{-4}	-1.8×10^{-6}	7.3×10^{-9}
Fig. 112	15	x_1	0	0.835	21.9	18.86	-3.4×10^{-1}	9.3×10^{-3}	-1.3×10^{-4}	8.7×10^{-7}	-2.6×10^{-9}
			-0.028	0.871		15.76	-2.2×10^{-1}	5.0×10^{-3}	-5.2×10^{-5}	2.0×10^{-7}	-3.1×10^{-10}
		x_2	0	0.725	51.8	23.15	-2.3×10^{-1}	2.6×10^{-3}	3.6×10^{-5}	-8.2×10^{-7}	3.5×10^{-9}
			-0.049	0.867		16.95	-8.8×10^{-2}	-1.3×10^{-3}	8.0×10^{-5}	-1.0×10^{-6}	4.0×10^{-9}
Fig. 113	All	x_1	0	0.744	9.8	17.77	-2.9×10^{-1}	6.5×10^{-3}	-4.3×10^{-5}	-2.5×10^{-7}	2.4×10^{-9}
			-0.027	0.769		15.12	-2.0×10^{-1}	3.4×10^{-3}	9.5×10^{-6}	-6.7×10^{-7}	3.7×10^{-9}
		x_2	0	0.713	39.7	22.43	-2.2×10^{-1}	1.5×10^{-3}	8.0×10^{-5}	-1.5×10^{-6}	6.6×10^{-9}
			-0.048	0.827		16.74	-9.6×10^{-2}	-1.5×10^{-3}	1.0×10^{-4}	-1.4×10^{-6}	6.0×10^{-9}

5. DISCUSSION

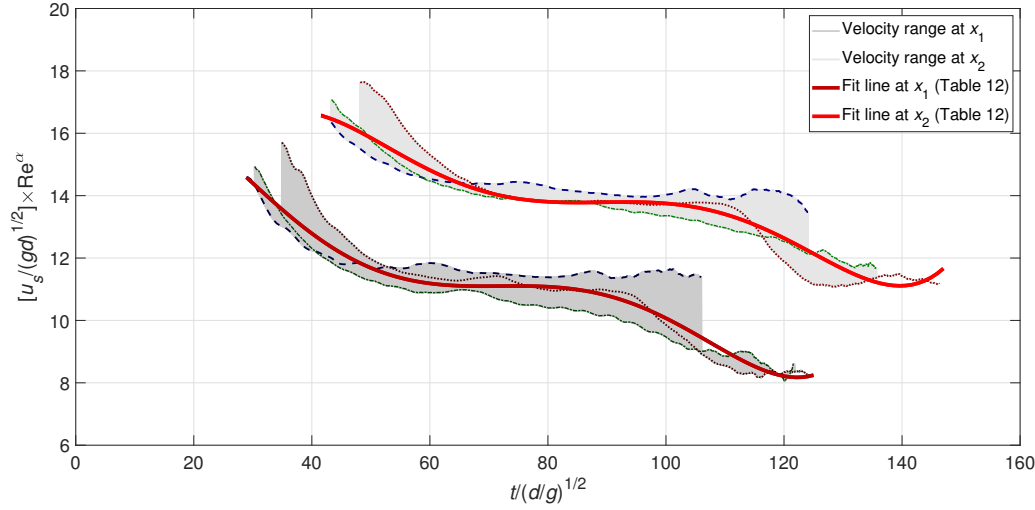


Figure 111 Comparison of Re-normalised slide surface velocity (data from Fig. 84) profiles over time with $\theta_W = 0^\circ$. Dotted data-lines are described by the legend of Fig. 84. $t_* = t/(d/g)^{1/2} - 28.93$ at x_1 and $t/(d/g)^{1/2} - 41.59$ at x_2

Figure 112 confirms that the values of α are also very close for increasing θ_W , showing that the surface velocity of the slides does not become significantly more dependent on Re with increasing slide thickness. This makes intuitive sense, as the slide surface is subject to similar surrounding airflow conditions after the front has passed and the slide thickness approaches the peak, regardless of the actual slide thickness. Meanwhile, Fig. 113 provides a broader comparison of the total data-set comprising of all θ_W values. Overall, the α values selected were similar to those selected for each individual θ_W value, confirming that the trends seen in Figs. 111 are generally applicable. While in Figs. 111 and 112, the data spread after Re-normalisation was roughly equal between x_1 and x_2 , the data spread of the unnormalised data was originally greater at x_2 , showing a greater degree of fit improvement at this location. Furthermore, normalising the data across all values of θ_W shows reduced effectiveness at x_1 and only slightly reduced effectiveness at x_2 in Fig. 113. This suggests that the initial slide mass and thickness exerts the greatest influence on slide velocity and its Re-dependence at x_1 , before dissipating at x_2 where the slide has spread out more thinly.

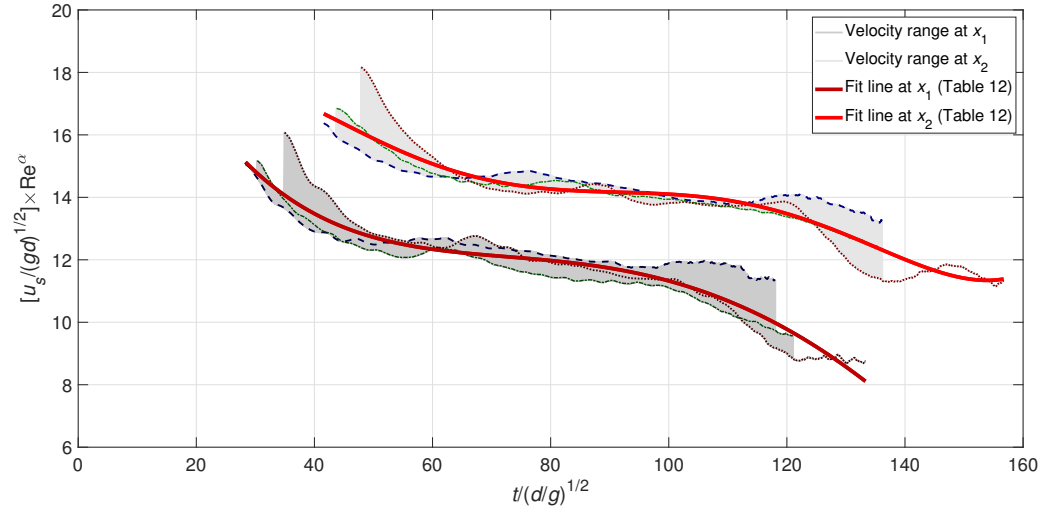


Figure 112 Comparison of Re-normalised slide surface velocity (data from Fig. 85) profiles over time with $\theta_W = 15^\circ$. Dotted data-lines are described by the legend of Fig. 85. $t_* = t/(d/g)^{1/2} - 28.33$ at x_1 and $t/(d/g)^{1/2} - 41.59$ at x_2

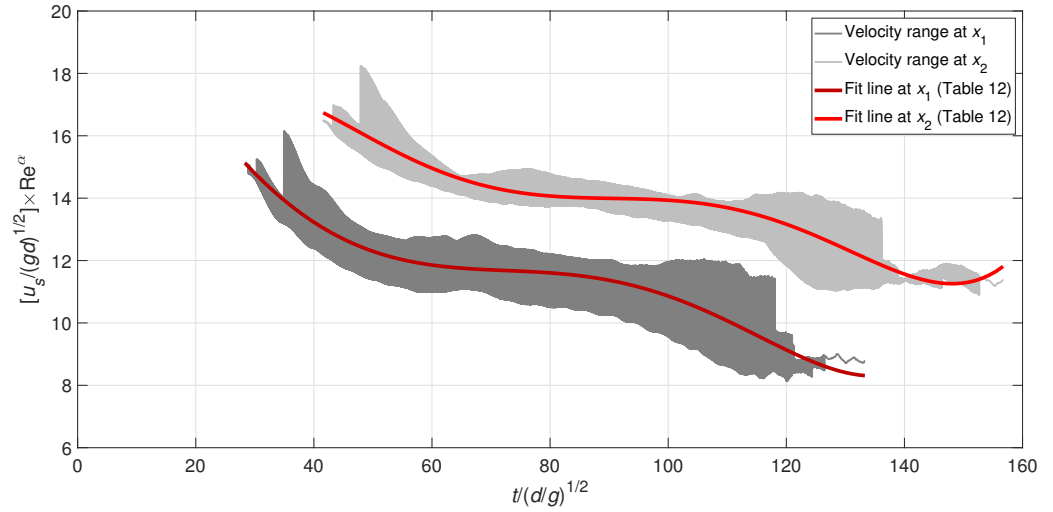


Figure 113 Comparison of Re-normalised slide surface velocity profiles over time across all θ_W values. $t_* = t/(d/g)^{1/2} - 28.33$ at x_1 and $t/(d/g)^{1/2} - 41.59$ at x_2

Looking more closely at the R^2 values in Table 12, it can also be seen that the fit improvement of the data via Re-normalisation also increases with θ_W . This improvement of data-fit is greater than the ratio of corresponding α values for each data-set, showing that fit improvement does not directly correlate with larger negative α values when comparing different values of θ_W . However, larger negative α values still seem to relate to greater fit improvement when compared between measurement points for experiments with the same θ_W . The data collapse was noticeably worse when data-sets with differing θ_W values were merged together, suggesting that normalising slides of different geometry is not particularly effective for this parameter. While constant values of α have been used for this fitting approach, it may be more appropriate to use a value of α that changes over time, which would highlight how the influence of Re scale effects on surface velocity changes over time. However, such a model has the potential to be over-fit to the laboratory data collected; a wider range of data would be needed to meaningfully validate such an approach.

5.4.2 Drag force normalisation of slide surface velocity

Overall, a good degree of fit improvement is seen using the Re normalisation approach on the slide surface velocity, but there is scope for further improvement to this methodology of evaluating scale effects. An alternative normalisation approach has been developed for this parameter based on the estimated drag force acting on isolated surface particles, to clarify the influence of this particular physical mechanism on the Re scale effects seen in this study. This approach takes the laboratory surface velocity data and estimates the terminal velocity of an average particle moving down the channel based on its shape and drag force coefficient. As the particle accelerates under the ramp-wise component of gravity, Re increases, impacting the instantaneous drag coefficient C_D acting on the particle and causing the terminal velocity to evolve over time. The ratio k_D of a particle's instantaneous velocity in a vacuum u_f (i.e. in isolation of the drag force) and its instantaneous drag-influenced velocity u_d can be determined numerically for all intermediate velocity values:

$$k_D(t) = \frac{u_f(t)}{u_d(t)}. \quad (50)$$

The surface velocity data can then be multiplied by this ratio to calibrate the data in an attempt to remove the influence of drag force on the surface velocity, to calculate the "drag-free" surface velocity. The fit improvement of this k_D calibrated data can then be compared to that of the Re^α normalised data, to identify the degree to which drag force is responsible for the Re scale effects observed.

The instantaneous velocity u_f at time t of a particle falling along a slope of angle θ in a vacuum is given by Eq. (51). In this model, the effect of sliding friction is ignored, as the surface particle is moving in isolation of the underlying slide.

$$u_f(t) = g t \sin \theta. \quad (51)$$

The instantaneous terminal velocity u_t of the particle experiencing drag force is given by Eq. (52), where \bar{A} is the mean cross-sectional area of the particle in the direction of motion. As the particle's orientation will fluctuate as it moves through the air, and C_D depends strongly on this orientation (Bagheri and Bonadonna, 2016), the use of a mean cross-sectional area provides a representative evolution of behaviour across all orientations.

$$u_t(t) = \sqrt{\frac{2mg \sin \theta}{\rho_s C_D(t) \bar{A}}}. \quad (52)$$

The instantaneous velocity u of the particle under drag force can then be calculated using u_t , and is given by Eq. (53). As C_D depends on Re , the grain Reynolds number of the particle Re is then calculated from u , as shown in Eq. (54), where

5. DISCUSSION

d is the particle diameter and ν_f is the kinematic viscosity of air.

$$u_d(t) = u_t(t) \tanh\left(\frac{u_f(t)}{u_t(t)}\right), \quad (53)$$

$$\text{Re}_d(t) = \frac{u_d(t)d}{\nu_f}. \quad (54)$$

With this information, the instantaneous drag coefficient C_D can be determined using Eq. (55) (Bagheri and Bonadonna, 2016). This value of C_D can then be fed into Eq. (52) at the next time-step $t + \delta t$ so that the process can be repeated numerically over time, from the start of the particle's motion to its final stable terminal velocity. This approach is accurate with a sufficiently small time-step.

$$C_D(t + \delta t) = \frac{24k_S}{\text{Re}_d(t) \left[1 + 0.125 (\text{Re}_d(t)k_N/k_S)^{2/3}\right]} + \frac{0.46k_N}{1 + (5330k_S/\text{Re}_d(t)k_N)}. \quad (55)$$

To evaluate the influence of particle shape effects on instantaneous drag force, the model of Bagheri and Bonadonna (2016) has been used to model a representative oblate spheroid with a major/minor axis ratio a/b of 1.55 (Section 2.2.4). k_N and k_S are shape-dependent parameters that account for particle behaviour at the Newton's (high) and Stokes' (low) Re thresholds, and are described by Eqs. (56) to (61), with ρ_s and ρ_f denoting the particle and fluid density, respectively.

$$\log(k_N) = \alpha_2 [-\log(F_N)]^{\beta_2}, \quad (56)$$

$$k_S = \frac{F_S^{1/3} + F_S^{-1/3}}{2}, \quad (57)$$

$$\alpha_2 = 0.45 + \frac{10}{\exp [2.5 \log (\rho_s / \rho_f)] + 30}, \quad (58)$$

$$\beta_2 = 1 - \frac{37}{\exp [3 \log (\rho_s / \rho_f)] + 100}, \quad (59)$$

$$F_N = \left(\frac{b}{a} \right)^2, \quad (60)$$

$$F_S = \frac{b}{a}. \quad (61)$$

Eqs. (60) and (61) are suitable for use with oblate spheroid particles, with Bagheri and Bonadonna (2016) providing more information on equations suitable for other particle shapes. Bagheri and Bonadonna (2016) validated this particle drag model against many different particle shapes in many different velocity regimes, making it suitable for use in this drag-force normalisation technique.

Figure 114 displays how u_f , u_t , and most importantly u_d vary over time for all experimental values of λ , using particles with corresponding d . As these particles are oblate spheroids, d represents the diameter of a sphere of equivalent mass; the dimensions of the oblate spheroid are used for all calculations. Overall, u_t starts low and approaches a constant value as u_d increases, with the rate at which this constant value is approached increasing as λ decreases. While u_d initially matches u_f , the rate of increase rapidly diminishes within the time-scale of the experiments of this study, leading to values of k_D significantly higher than unity. This suggests that, as the particles accelerate down the channel under gravity, the drag force becomes exponentially more influential over the slide dynamics until the transition curve is reached and the velocity decreases.

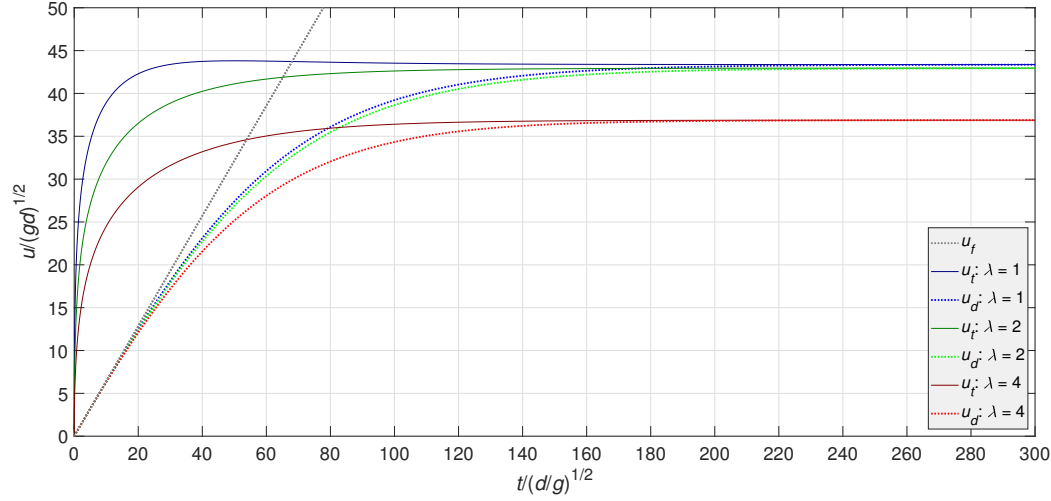


Figure 114 Comparison of dimensionless u_f , u_t , and u_d over dimensionless time

Notably, although u_t increases as λ decreases within this range, the final value of u_t at $\lambda = 1$ is only slightly larger than that at $\lambda = 2$, while the difference between the values at $\lambda = 2$ and 4 is much larger. At even smaller values of λ , u_t actually starts to decrease compared to larger λ values. Additionally, the final value of u_t approached at $\lambda = 1$ is lower than the maximum value of u_t seen at $t(d/g)^{1/2} = 50$. This is due to the behaviour of C_D within Newton's regime of Re being approached; while this threshold would not be reached for spherical particles with the regime of Re seen in this study (Fig. 16), the shape factors k_N and k_S cause the mean particle to enter this regime (Fig. 17). However, as u_f diverges only slightly from u_d during the period where u_t varies significantly between $\lambda = 1$ and 2, the result is similar values of u_d over time between $\lambda = 1$ and 2.

Figure 115 shows how the drag force calibration factor k_D varies with u_d across an experimentally reasonable range of values, such that the laboratory and simulation data from x_1 and x_2 falls within this range. Overall, the influence of drag force on particle velocity is strongest at $\lambda = 4$ where Re is the smallest and C_D is relatively high in the Stokes' regime. As λ decreases to 2, Re increases and C_D decreases, but at $\lambda = 1$, the decrease rate of C_D reduces due to entering Newton's drag regime. The result is that, within the experimental range, the laboratory

velocity data at $\lambda = 4$ is calibrated upwards much more than at $\lambda = 1$ and 2, where the magnitude of calibration is relatively similar.

Finally, corresponding values of k_D from Fig. 115 can be assigned to the laboratory velocity values to normalise the data. Figures 116 and 117 multiply the non-dimensional laboratory surface velocities highlighted in Figs. 84 and 85 by k_D at each moment in time as the slide passes through the x_1 and x_2 measurement points. Additionally, Table 13 highlights the α and R^2 values of the k_D -normalised data in Figs. 116 to 117 and compares them to both the values selected with Re normalisation and the unnormalised values.

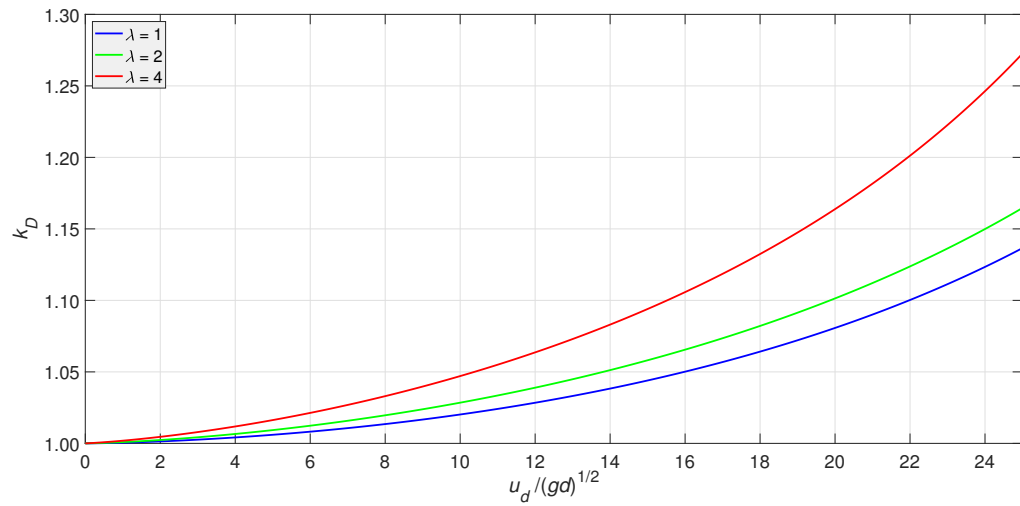


Figure 115 Comparison of k_D across experimental range of $u_d/(gd)^{1/2}$

5. DISCUSSION

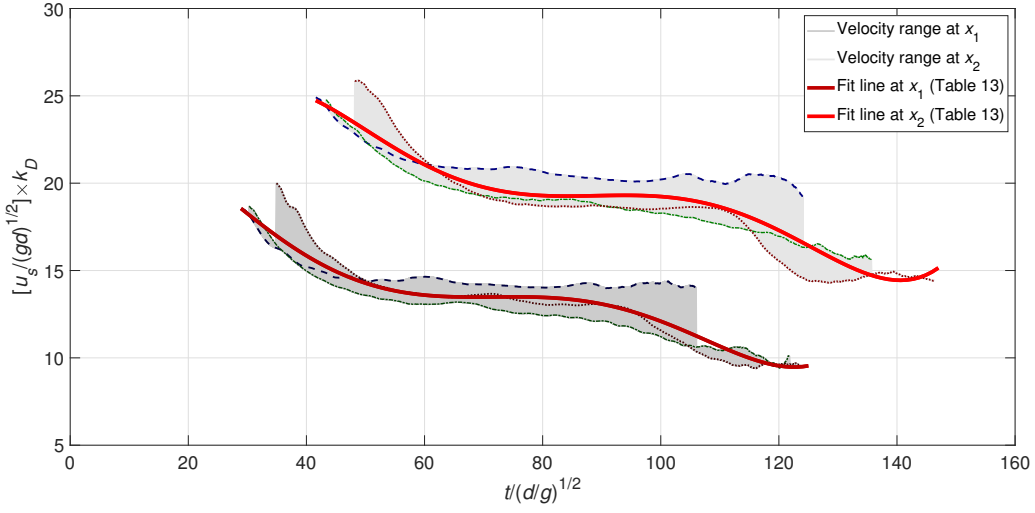


Figure 116 Comparison of k_D -normalised slide surface velocity (data from Fig. 84) profiles over time with $\theta_W = 0^\circ$. Dotted data-lines are described by the legend of Fig. 84. $t_* = t/(d/g)^{1/2} - 28.93$ at x_1 and $t/(d/g)^{1/2} - 41.59$ at x_2

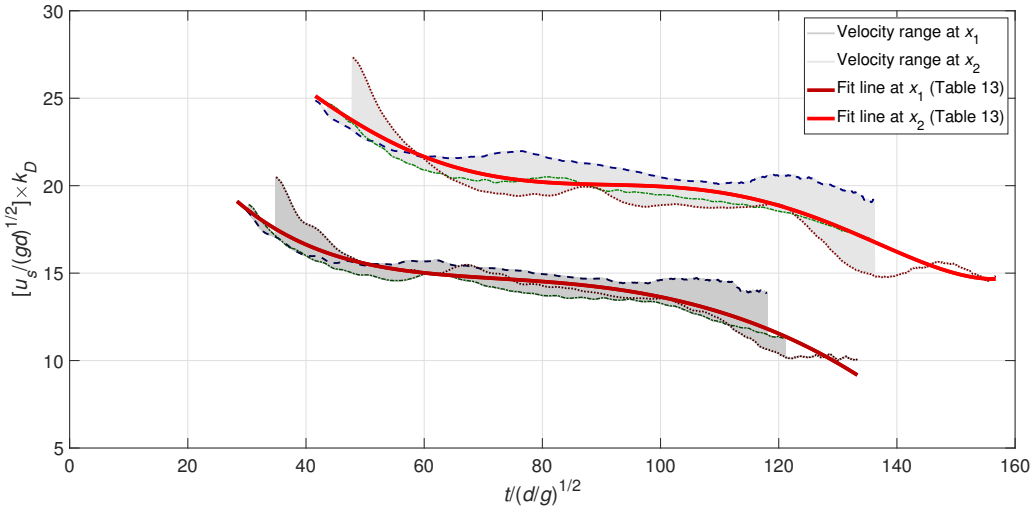


Figure 117 Comparison of k_D -normalised slide surface velocity (data from Fig. 85) profiles over time with $\theta_W = 15^\circ$. Dotted data-lines are described by the legend of Fig. 84. $t_* = t/(d/g)^{1/2} - 28.33$ at x_1 and $t/(d/g)^{1/2} - 41.59$ at x_2

Table 13 α , k_D , and R^2 values of the original and normalised slide surface velocities fitted to Eq. (49). Fit improvement refers to the improvement of fit between pure $u_s/(gd)^{1/2}$ scaling and combined $u_s/(gd)^{1/2} \times \text{Re}^\alpha$ or $u_s/(gd)^{1/2} \times k_D$ scaling

Fig.	θ_W	Position	Normalisation	R^2	Fit imp.	T_0	T_1	T_2	T_3	T_4	T_5
(-)	(°)	(-)	(-)	(-)	(%)	(-)	(-)	(-)	(-)	(-)	(-)
Fig. 116	0	x_1	None	0.820		18.35	-2.8×10^{-1}	1.3×10^{-3}	1.4×10^{-4}	-2.6×10^{-6}	1.2×10^{-8}
			$\alpha = -0.029$	0.847	14.9	14.58	-1.7×10^{-1}	-3.6×10^{-4}	1.4×10^{-4}	-2.5×10^{-6}	1.2×10^{-8}
			k_D	0.828	4.4	18.55	-2.7×10^{-1}	1.0×10^{-3}	1.7×10^{-4}	-3.2×10^{-6}	1.6×10^{-8}
		x_2	None	0.759		22.65	-1.6×10^{-1}	-4.3×10^{-3}	2.4×10^{-4}	-3.3×10^{-6}	1.4×10^{-8}
			$\alpha = -0.047$	0.865	43.7	16.57	-5.2×10^{-2}	-5.6×10^{-3}	2.3×10^{-4}	-3.0×10^{-6}	1.3×10^{-8}
			k_D	0.818	24.2	24.73	-1.6×10^{-1}	-6.8×10^{-3}	3.4×10^{-4}	-4.7×10^{-6}	2.0×10^{-8}
Fig. 150	7.5	x_1	None	0.804		19.03	-4.1×10^{-1}	1.2×10^{-2}	-1.7×10^{-4}	1.3×10^{-6}	-4.3×10^{-9}
			$\alpha = -0.029$	0.838	17.4	14.89	-2.2×10^{-1}	5.4×10^{-3}	-5.8×10^{-5}	2.4×10^{-7}	-5.6×10^{-10}
			k_D	0.818	6.9	18.86	-3.4×10^{-1}	9.0×10^{-3}	-1.1×10^{-4}	-6.8×10^{-7}	-2.1×10^{-9}
		x_2	None	0.750		22.82	-1.9×10^{-1}	-1.3×10^{-3}	1.4×10^{-4}	-2.0×10^{-6}	8.1×10^{-9}
			$\alpha = -0.048$	0.873	49.2	16.58	-7.8×10^{-2}	-2.7×10^{-3}	1.3×10^{-4}	-1.8×10^{-6}	7.3×10^{-9}
			k_D	0.822	28.5	24.72	-2.0×10^{-1}	-2.2×10^{-3}	1.9×10^{-4}	-2.7×10^{-6}	1.2×10^{-8}
Fig. 117	15	x_1	None	0.835		18.86	-3.4×10^{-1}	9.3×10^{-3}	-1.3×10^{-4}	8.7×10^{-7}	-2.6×10^{-9}
			$\alpha = -0.028$	0.871	21.9	15.76	-2.2×10^{-1}	5.0×10^{-3}	-5.2×10^{-5}	2.0×10^{-7}	-3.1×10^{-10}
			k_D	0.850	9.0	19.10	-2.9×10^{-1}	7.4×10^{-3}	-9.3×10^{-5}	5.1×10^{-7}	-1.3×10^{-9}
		x_2	None	0.725		23.15	-2.3×10^{-1}	2.6×10^{-3}	3.6×10^{-5}	-8.2×10^{-7}	3.5×10^{-9}
			$\alpha = -0.049$	0.867	51.8	16.95	-8.8×10^{-2}	-1.3×10^{-3}	8.0×10^{-5}	-1.0×10^{-6}	4.0×10^{-9}
			k_D	0.807	29.7	25.12	-2.4×10^{-1}	1.6×10^{-3}	7.2×10^{-5}	-1.3×10^{-6}	5.6×10^{-9}

5. DISCUSSION

Overall, a smaller degree of fit improvement is observed with the k_D -normalisation compared to the Re^α normalisation of surface velocity, reaching 29.5% of the Re^α normalisation fit improvement at x_1 and 55.4% at x_2 , respectively for $\theta_W = 0^\circ$. These respective ratios improve to 39.6% and 57.9% at $\theta_W = 7.5^\circ$ and to 41.1% and 57.3% at $\theta_W = 15^\circ$. This suggests that the particle drag force has a greater influence on the scale effects seen in the surface velocity further down the ramp where the slide velocity is higher, which is expected due to the greater C_D seen at this position. The fit improvement with the k_D normalisation approach also improves as θ_W increases, particularly at x_1 , but is curtailed to a maximum value compared to the fit improvement of the Re^α normalisation. This suggests that the surface velocity is more representative of the mean slide velocity of thicker laboratory slides, and thus the drag force becomes more relevant in this context. This is supported to an extent by the simulation data seen in Tables 10 and 11, showing that the central velocity profile curvature (represented by the approximating power β) increases at both x_1 and x_2 at the channel centre, weighting the mean slide velocity more closely to the surface velocity.

Additionally, this suggests that regardless of the slide thickness, the degree to which scale effects in surface velocity are influenced by the drag force on individual particles is limited. This implies other mechanisms are present to contribute further to these scale effects, particularly at lower particle velocities. Air on the macro-scale granular system may exert a particularly strong influence; changes in particle drag caused by changes in slide velocity may affect granular temperature and thus energy dissipation. Furthermore, air fluidisation may reduce the effective friction angle of the slide, imposing additional scale effects. This highlights the wide range of physical mechanisms that can influence Re scale effects.

In both normalisation approaches, the data fit is best during the quasi-constant phase of slide velocity seen as the bulk of the slide passes through the measurement points. The fit improvement is noticeably worse as the slide fronts and tails pass through the points, as seen in Figs. 111, 112, 116, and 117. This suggests that mechanisms unrelated to Re influence scale effects more strongly in these regions, where the slide starts to become dilute.

5.4.3 Reynolds-dependency of key deposit parameters

Tables 14 to 17 show the results of multiplying the slide front, peak, mass centroid, and tail runout distances by a power α of Re . R_s denotes the horizontal distance between the shutter release point and the corresponding location on the flat runout surface, and is ensemble-averaged between all experiments conducted with the same parameters. As the slide deposits are stationary, the grain Reynolds number at t_1 (400,000 time-steps from the front contacting the x_2 measurement point) is used as a reference value for the power-fitting, as this is sufficiently close to the maximum surface velocity during the slide event and could be easily measured in both the simulation and laboratory experiments in this study.

Table 14 Re-dependency of laboratory slide deposit front positions

θ_W	Exp. no.	λ	R_s/d	RMSE	$Re(t_1)$	α	$R_s/d \times Re^\alpha$	RMSE	Fit imp.
(°)	(-)	(-)	(-)	(-)	(-)	(-)	(-)	(-)	(%)
0	L1–L6	1	1382		655.1		557.4		
	L18–L21	2	1074	0.221	226.6	−0.140	502.8	0.027	87.8
	L30–L37	4	1027		78.7		557.1		
7.5	L7–L12	1	1465		651.6		568.8		
	L22–L25	2	1153	0.220	222.4	−0.146	523.8	0.018	91.7
	L38–L45	4	1080		80.2		569.6		
15	L13–L17	1	1544		654.4		543.5		
	L26–L29	2	1177	0.271	225.9	−0.161	491.8	0.027	90.0
	L46–L53	4	1107		81.9		544.5		

Overall, the laboratory data from all values of θ_W converge towards a single point after this Re -normalisation. To minimise the relative mean-squared error (RMSE), this typically results in one data-set outlying from the others. This highlights that the data does not fit perfectly via Re -normalisation and that other factors, such as the granular nature of the system, may also impact the deposit dimensions. As the value of Re used for the normalisation of these deposit parameters is the grain Reynolds number, and does not represent the slide as a whole,

5. DISCUSSION

using a Reynolds number that accounts for the thickness of the slide may be more appropriate. However, the current fit is extremely close in comparison to the fit of the surface velocity seen in Section 5.4.1, and is good enough to conclude that Re is the major contributor to the deposit morphology and how it varies with scale.

Table 15 Re -dependency of laboratory slide deposit peak positions

θ_W	Exp. no.	λ	R_s/d	RMSE	$Re(t_1)$	α	$R_s/d \times Re^\alpha$	RMSE	Fit imp.
(°)	(-)	(-)	(-)	(-)	(-)	(-)	(-)	(-)	(%)
0	L1–L6	1	976		655.1	−0.101	507.1		97.8
	L18–L21	2	891	0.091	226.6		515.4	0.002	
	L30–L37	4	789		78.7		507.7		
7.5	L7–L12	1	1077		651.6	−0.150	407.6		94.6
	L22–L25	2	859	0.221	222.4		381.6	0.012	
	L38–L45	4	788		80.2		408.1		
15	L13–L17	1	1123		654.4	−0.171	370.7		93.8
	L26–L29	2	812	0.275	225.9		321.4	0.017	
	L46–L53	4	789		81.9		371.2		

Table 16 Re -dependency of laboratory slide deposit mass centroid positions

θ_W	Exp. no.	λ	R_s/d	RMSE	$Re(t_1)$	α	$R_s/d \times Re^\alpha$	RMSE	Fit imp.
(°)	(-)	(-)	(-)	(-)	(-)	(-)	(-)	(-)	(%)
0	L1–L6	1	1122		655.1	−0.137	464.1		89.2
	L18–L21	2	890	0.223	226.6		421.1	0.024	
	L30–L37	4	844		78.7		460.1		
7.5	L7–L12	1	1155		651.6	−0.156	424.2		93.1
	L22–L25	2	899	0.289	222.4		387.9	0.020	
	L38–L45	4	841		80.2		420.3		
15	L13–L17	1	1186		654.4	−0.169	398.9		95.3
	L26–L29	2	930	0.236	248.9		365.1	0.011	
	L46–L53	4	840		81.9		397.3		

Table 17 Re-dependency of laboratory slide deposit tail positions

θ_W	Exp. no.	λ	R_s/d	RMSE	$\text{Re}(t_1)$	α	$R_s/d \times \text{Re}^\alpha$	RMSE	Fit imp.
(°)	(-)	(-)	(-)	(-)	(-)	(-)	(-)	(-)	(%)
0	L1–L6	1	934		655.1		391.5		
	L18–L21	2	754	0.202	226.6	−0.134	364.7	0.015	92.5
	L30–L37	4	707		78.7		393.7		
7.5	L7–L12	1	926		651.6		352.6		
	L22–L25	2	759	0.226	222.4	−0.149	339.1	0.005	97.8
	L38–L45	4	680		80.2		353.7		
15	L13–L17	1	913		654.4		329.7		
	L26–L29	2	746	0.223	225.9	−0.157	318.6	0.003	98.5
	L46–L53	4	659		81.9		330.0		

Tables 14 to 17 also contain the RMSE values of the raw data for comparison. Typically, the fit between deposit parameters of various scales was better than the fit of surface velocity, corresponding to the higher optimal α values selected. θ_W did not have a significant influence on the fit improvement with Re-normalisation, but the deposit peak and tail positions showed better fit improvement compared to the deposit front and mass centroid positions. As the deposit front, peak, centroids, and tail runout distances seen in Tables 14 to 17 are normalised by the particle diameter before further normalisation by Re, the values of α shown in these tables are directly comparable to those seen in Figs. 111 to 113. This demonstrates that the slide deposit dimensions depend more greatly on the grain Reynolds number than the slide surface velocity as it traverses the inclined portion of the ramp.

This suggests that the Re scale effects seen in this study manifest most strongly after the slide traverses the transition curve and enters its settlement phase. As α correlates to the slide velocity and distance from the shutter release in Figs. 111 to 113, it is intuitive that the highest values of α would be seen in the deposit dimensions, where the scale effects have influenced the slide for the longest duration, and the slide has built up significant additional velocity to be dissipated at larger scales. The α values for the deposit front and tail positions are relatively easy to compare, as they both represent boundaries at which the slide thickness becomes

zero, with the front position not being influenced by the rest of the deposit morphology. The α values at the deposit front and mass centroid are typically greater than those of the slide tail, with the data at $\theta_W = 7.5^\circ$ being the exception by a small degree. This suggests that the front and mass centroid are slightly more influenced by the grain Reynolds number, and thus the additional mobilisation of the slide by the surrounding airflow, than the slide peak and tail.

The values of α seen in Tables 14 to 17 increase consistently with θ_W , showing that increasing the slide mass and mean thickness increase the Re-dependency as the slide starts to settle fully. This holds true for the slide fronts, peaks, and tails, with the runout distance of the peak showing a much stronger dependency. This makes intuitive sense, as Figs. 94 to 96 show that the deposit thickness increases with θ_W more quickly close to the slide front than the slide tail, shifting the thickest deposit zone closer to the slide front. Overall, this consistent increasing Reynolds-dependency with θ_W contrasts with the velocity profiles seen in Figs. 111 to 113, where the surface velocity remains equally Re-dependent across all values of θ_W .

This suggests a few possibilities; one is that as the slide thickness increases, Re-based fluidisation influences the base velocity more than the surface velocity. This would result in relatively decreased shear flow for larger values of θ_W , resulting in farther runout and significant changes in the deposit settlement process and final dimensions that could not be identified from analysing the surface velocity alone. Another possibility is that these thickness-dependent Re scale effects start to manifest as the slide starts to settle; airflow interaction in the transition curve may be more complex than that in the inclined region preceding it, and could change significantly as the in-flowing slide thickness increases in comparison to the curve radius. These hypotheses highlight the need for additional laboratory velocity measurements of the base velocity during the inclined region, and velocity measurements in general of the settling slide in the runout zone.

5.4.4 Comparison of slide runout data to other studies

As the slide front position (i.e. total runout) is the parameter least affected by the rest of the deposit morphology and settlement process, further analysis was conducted on the Reynolds-dependency of the total runout in particular. Figure 118 compares the volume-normalised total runout R_t/h^* with the volume-normalised fall height H_c/h^* , where h^* is the cube-root of the slide volume V_s . This comparison includes the experiments conducted in this study, as well as the experiments conducted by Davies and McSaveney (1999), which investigated the relationship between fall height and runout distance for a range of slide sizes and dimensions.

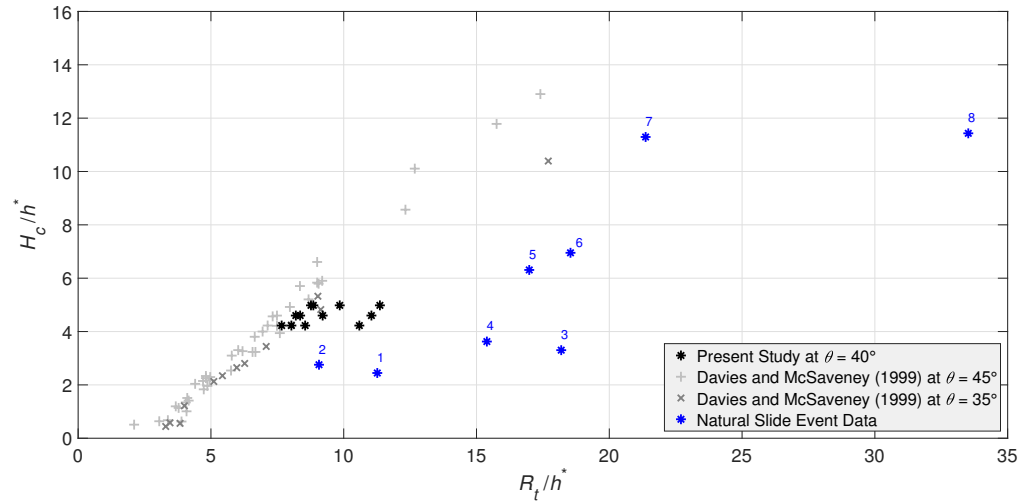


Figure 118 Comparison of volume-normalised slide runout and fall height (see Table 18 for raw data)

While the experiments from Davies and McSaveney (1999) do not precisely follow a Froude scale series (the particle diameters and initial slide geometry are mostly not scaled, for instance), they provide a large range of slide geometries for which the slide Reynolds-dependency can be evaluated, with ramp angles close to θ used in the present study. The front velocity of these slides was estimated via conservation of energy, using Eq. (21), with $\mu = 29^\circ$ and values of θ including 35° and 45° as described in Fig. 118. Additionally, many natural slide events have been included in this comparison, displaying similar conditions to these laboratory ex-

5. DISCUSSION

periments such as channelised sliding, relatively low moisture content, insignificant entrainment, and composition of many small particles.

The relevant physical parameters of these natural slides are described in Table 18; Fig. 118 refers to these slides as "Other Data". Overall, this data shows a considerable amount of spread, with higher fall heights generally correlating with larger runout distances. The laboratory data from the present study segregates into horizontal bands based on θ_W ; the flat release wedge has the lowest value of H_c , which increases with θ_W . Meanwhile, R_t/h^* increases as λ decreases, with the smallest laboratory-scale data matching reasonably well with the data from Davies and McSaveney (1999). Normalising the total set of runout data with Re in Fig. 119 leads to a tighter fit, with many of the natural slides falling in line with the rest of the data as a result.

Table 18 Important physical parameters of natural granular slides seen in Fig. 118. (1) Cruden and Hungr (1986). (2) McKinnon (2010). (3) Shugar and Clague (2011). (4) Moore (1976). (5) McSaveney (2002). (6) Lipovsky et al. (2008). (7) Sosio et al. (2008). (8) Evans et al. (2001)

Slide	R_t	H_c	V_s	h^*	u_s	d_{50}	R_t/h^*	H_c/h^*	Re
(-)	(m)	(m)	(m ³)	(-)	(m/s)	(mm)	(-)	(-)	(-)
Frank ¹ (1903)	1800	760	30×10 ⁶	311	45	2	5.79	2.45	5960
Elm ² (1881)	2017	613	11×10 ⁶	222	83.5	5	9.07	2.76	27400
Sherman Glacier ³ (1964)	5950	1080	35×10 ⁶	327	67	4	18.19	3.30	17700
Rubble Creek ⁴ (1855)	4500	1060	25×10 ⁶	292	30	0.8	15.39	3.63	1590
Mount Cook ⁵ (1991)	7000	2600	70×10 ⁶	412	60	5	16.99	6.31	19900
Mount Steele ⁶ (2007)	5760	2160	30×10 ⁶	311	65	2	18.54	6.95	8600
Thurweiser ⁷ (2004)	2800	1480	2.25×10 ⁶	131	67	6	21.37	11.30	24900
Mount Cayley ⁸ (1984)	3460	1180	1.1×10 ⁶	103	70	0.8	33.53	11.43	3710

Notably, the laboratory experiments from the experiments of the present study fall in line with those of Davies and McSaveney (1999) for $\alpha = -0.091$, while the majority of the natural slides also align with the laboratory data for this value. The fit improves by 61.3% with this Re-normalisation. Some of the natural events are

outliers in this comparison, with the Mount Cayley, Rubble Creek, and Sherman Glacier slides still displaying increased runout distances after this Re-normalisation. This highlights that other physical factors may have been present in these events that facilitated even further increased runout. Additionally, the most relevant characteristic particle length used for the Re-normalisation is not fixed; d_{50} was selected as it represents the mean particle diameter and can be directly compared between experiments, but smaller or larger particles may be more representative depending on the slide size distribution and other factors.

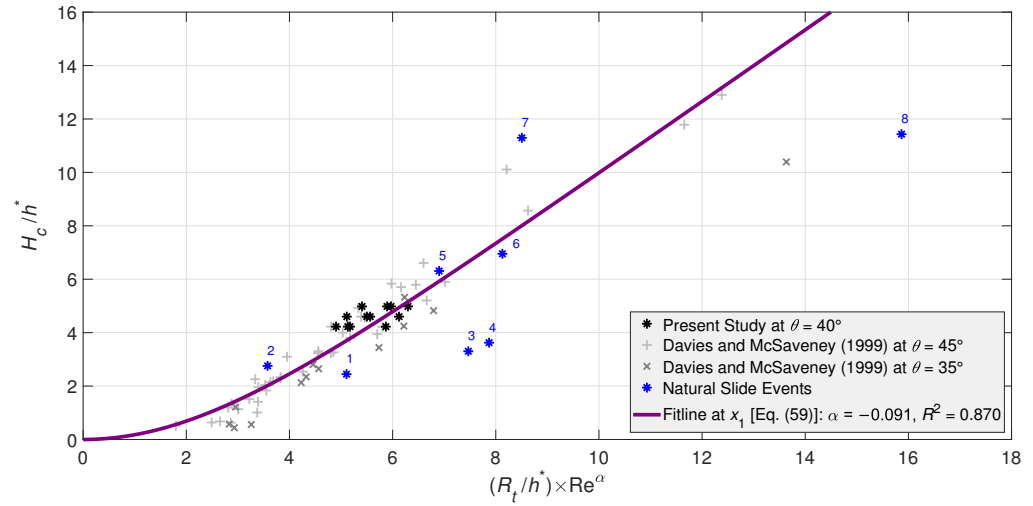


Figure 119 Re-normalisation of slide runout data from Fig. 118

The fit-line in Fig. 119 is described by Eq. (62), and tends towards a linear relationship between Re-normalised runout distance and fall height.

$$H_c/h^* = 5.0 \ln \{ \cosh(0.27 R_t/h^* \times \text{Re}^\alpha) \} \quad (62)$$

The α value selected including these additional data is significantly lower than those seen in Table 14, suggesting that other physical factors start to increase in relative influence compared to Re-dependent fluidisation at geophysical scales. These may include the secondary mechanisms discussed in Section 2.2, such as

5. DISCUSSION

acoustic fluidisation, frictional melting, and fragmentation. The Sherman Glacier slide in particular (3) contained large amounts of snow and ice, which may have melted and fluidised during the slide event before re-solidifying in the deposits analysed in Shugar and Clague (2011).

5.4.5 Reynolds-dependency of other deposit parameters

In Sections 5.4.1 and 5.4.3, the differences in surface velocity and deposit dimensions respectively between experiments of different scales could be reduced by normalising the data to Re , with the deposit dimensions being more strongly influenced than the surface velocity. However, other slide parameters are not normalised effectively by this method. In particular, the peak slide thickness as it crosses the measurement points (as seen in Figs. 87 to 90) does not vary much with scale, suggesting that this parameter is not strongly influenced by scale effects in general, as well as Re -related scale effects in particular. Instead, the rate at which the slide thickness decreases is more scale dependent, due to the changes in slide velocity described in Section 4.3.4. Re -normalisation was also conducted on the deposit volumes and porosities in Table 8, resulting in Tables 19 and 20 respectively.

Table 19 Re -dependency of slide deposit volumes

θ_W	Exp. no.	λ	V_d/d^3	RMSE	$Re(t_1)$	α	$V_d/d^3 \times Re^\alpha$	RMSE	Fit imp.
(°)	(-)	(-)	(-)	(-)	(-)	(-)	(-)	(-)	(%)
0	L1–L6	1	2.11×10^6		655.1		2.77×10^6		
	L18–L21	2	2.20×10^6	0.029	226.6	0.044	2.85×10^6	0.009	69.0
	L30–L37	4	2.31×10^6		78.7		2.80×10^6		
7.5	L7–L12	1	2.75×10^6		651.6		4.12×10^6		
	L22–L25	2	2.94×10^6	0.049	222.4	0.062	4.15×10^6	0.007	86.5
	L38–L45	4	3.13×10^6		80.2		4.05×10^6		
15	L13–L17	1	3.73×10^6		654.4		4.52×10^6		
	L26–L29	2	3.85×10^6	0.009	225.9	0.030	4.60×10^6	0.001	84.7
	L46–L53	4	3.97×10^6		81.9		4.49×10^6		

Overall, the volume and porosity show an inverse correlation with Re compared to the slide surface velocity and deposit position; larger scale deposits were typically slightly more compact and less porous. While the slide volume consistently decreased as λ decreased, the data did not collapse perfectly with Re -normalisation, with the normalised volume typically being greatest at $\lambda = 2$ for the optimal value of α . This suggests that other non- Re scale effects also manifest in the settlement porosity and corresponding volume of the slide deposits.

Notably, the selected α values in Tables 19 to 20 are significantly less than those in Tables 14 to 17, suggesting that Re scale effects influence the deposit volume and porosity less strongly than its shape and position. α also does not increase consistently with θ_W , with the deposits at $\theta_W = 15^\circ$ being significantly less Re -dependent than the others. As these deposits have significantly reduced thickness due to their increased spreading and overall lateral movement, this suggests that the deposit porosity becomes less influenced by Re , where frictional processes start to exert more influence in the final settlement phases. Behaviours based purely on particle geometry, such as basal dilation of the slide mass during the slide, may thus become more relevant as λ decreases.

Table 20 Re -dependency of slide deposit porosities

θ_W	Exp. no.	λ	N_d	RMSE	$Re(t_1)$	α	$N_d \times Re^\alpha$	RMSE	Fit imp.
($^\circ$)	(-)	(-)	(-)	(-)	(-)	(-)	(-)	(-)	(%)
0	L1–L6	1	0.453		655.1		0.617		
	L18–L21	2	0.476	0.038	226.6	0.048	0.616	0.011	67.7
	L30–L37	4	0.501		78.7		0.618		
7.5	L7–L12	1	0.444		651.6		0.699		
	L22–L25	2	0.484	0.061	222.4	0.070	0.706	0.008	87.1
	L38–L45	4	0.515		80.2		0.700		
15	L13–L17	1	0.444		654.4		0.543		
	L26–L29	2	0.460	0.010	225.9	0.031	0.546	0.002	81.0
	L46–L53	4	0.473		81.9		0.543		

This data suggests that the deposits at $\lambda = 1$ and 2 are more dilutant, not reaching a fully compact state due to their settlement in the transition curve and a relative lack of shearing (and thus eventual compaction) at $\lambda = 4$. Re scale effects do not seem to be fully responsible for this settlement behaviour. The wide range of α values selected for different slide and deposit parameters across the experimental scale series suggests that scale effects act on granular slides in a heterogeneous manner. Some characteristics of the slide are greatly influenced by differences in scale and the resulting differences in physical interactions, while others are influenced more subtly and others may not be influenced at all. Interestingly, the deposit volume and porosity show a reverse correlation with Re when compared to the slide velocity and deposit dimensions, highlighting the complexity of scale effect interactions on dry granular slides.

5.5 Influence of channel surface roughness

While the scale series of laboratory experiments conducted in this study has been completed with as few model effects as possible, some model effects were inevitable due to the choice of materials used for the experiments. In particular, the same materials were used to line the channel surface and form the channel sidewalls respectively at each experimental scale (Section 3). These materials have the same stiffness, but as described in Section 5.2, the stiffness of all materials involved in this study was high enough to prevent any stiffness-related model effects from significantly influencing the granular slides. Furthermore, the materials were selected to provide smooth surfaces, such that the roughness length would be sufficiently low at all experimental scales to prevent any significant influence. The basal friction angle was also confirmed to match for the materials at all experimental scales (Section 3.2.2). This section will briefly discuss the impact of varying channel roughness on a laboratory scale series, to help minimise this issue in any future studies, particularly those that might involve rougher channel materials.

In general, conducting a scale series with rough channel materials would necessitate the roughness length of the material (the distance at which roughness


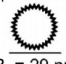
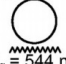
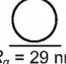
elements protrude from the channel base) to vary proportionally to the particle diameter. One case where this would be particularly easy is to simply attach particles from the main slide to interchangeable channel surfaces. However, in other cases, a regular material of different properties may be required, which may not be economical to scale for each experiment in a scale series. The simulations in this study were conducted modelling the acrylic and polypropylene surfaces of the laboratory chute as perfectly smooth interfaces, and demonstrate a significant non-zero slip velocity at the channel base and at the sidewalls, despite the influence of sidewall and basal friction on the granular slides. Noor et al. (2010) suggest that the roughness length of laser-cut acrylic lies within the order of $0.5 \mu\text{m}$, 0.1% of the smallest particle diameter in this study, which applies to the channel sidewalls. Meanwhile, the datasheets from the polypropylene manufacturers suggest that the roughness length of the channel base is within the order of $15 \mu\text{m}$, which is 3% of the smallest particle diameter. Clearly, this suggests that the basal roughness length is more likely to impose model effects on the study than the sidewall roughness length.

Pohlman et al. (2006) describes how the frictional properties of materials change as the particle and surface roughness are varied, analysing both cases where the particle and surface roughness are similar and those where one is significantly rougher than the other. Figure 120(a) shows that the coefficient of friction of a rough particle on a surface increases as the roughness length R_q of the surface decreases, for various different values of normal force applied to the contact. Figure 120(b) expands on this by measuring the coefficient of sliding friction of glued tripods of particles sliding down the surface, confirming that the friction coefficient and intensity increase consistently as the surface becomes relatively smoother.

Pohlman et al. (2006) suggest that this increase in friction intensity is caused by the reduction of asperities between the particle and boundary surfaces, causing more of the normal force applied by the overburden pressure to be dissipated via friction. Particle diameters of 2–3 mm were used, matching the particles used at $\lambda = 1$ in the present study well. In the present study, with the base roughness length being up to 3% of the particle diameter at maximum, this is likely to cause a slight reduction in overall friction angle and increase the runout of the labora-

5. DISCUSSION

tory slides in comparison to laboratory experiments conducted on an infinitesimally smooth surface. It is tempting to compare this to the simulations with their perfectly smooth channel surfaces, but as the particle roughness is not modelled in these simulations either, the results of this comparison would be misleading. As the sidewall material is much smoother than the base material, this may cause the effects of sidewall friction to be diminished in the laboratory experiments in comparison to the basal friction. The impact on the coefficient of friction from surface roughness in this study may be to that seen in Pohlman et al. (2006), as the difference between particle and surface roughness lengths approaches that in Fig. 120. However, the basal friction angles measured for each material have already been shown to match between experiments of different scales, within the margins of error seen in Fig. 120.

(a)	Surface Condition	Normal Force (mN)	Coefficient of Friction (μ)	Friction Intensity
	$R_q = 235 \text{ nm}$	49	0.22 ± 0.03	
		147	0.19 ± 0.03	
	$R_q = 544 \text{ nm}$	245	0.15 ± 0.01	
	$R_q = 235 \text{ nm}$	49	0.26 ± 0.05	
		147	0.23 ± 0.03	
	$R_q = 29 \text{ nm}$	245	0.28 ± 0.07	
	$R_q = 56 \text{ nm}$	49	0.11 ± 0.01	
		147	0.12 ± 0.01	
	$R_q = 544 \text{ nm}$	245	0.11 ± 0.01	
	$R_q = 56 \text{ nm}$	49	0.27 ± 0.02	
		147	0.44 ± 0.03	
	$R_q = 29 \text{ nm}$	245	0.48 ± 0.03	

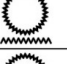


(b)	Surface Condition	Coefficient of Friction (μ)	Friction Intensity
	$R_q = 235 \text{ nm}$ $R_q = 304 \text{ nm}$	0.16 ± 0.02	
	$R_q = 235 \text{ nm}$ $R_q = 23 \text{ nm}$	0.35 ± 0.07	
	$R_q = 235 \text{ nm}$ $R_q = \text{N/A}$	0.44 ± 0.02	
	$R_q = 56 \text{ nm}$ $R_q = 304 \text{ nm}$	0.14 ± 0.01	
	$R_q = 56 \text{ nm}$ $R_q = 23 \text{ nm}$	0.25 ± 0.02	
	$R_q = 56 \text{ nm}$ $R_q = \text{N/A}$	0.35 ± 0.07	

Figure 120 (a) Mean coefficient of friction for single particles pressed against a surface. (b) Mean coefficient of friction for particle tripods sliding down a flat surface. Friction intensity is a graphical representation of the friction coefficient

The largest ratio of particle-to-surface roughness in Fig. 120 is roughly 10:1, while that of the smallest particles at $\lambda = 4$ (estimating a roughness length of 0.125 mm due to particle asphericity) is roughly 8.3:1. This ratio increases with scale, and as such the friction coefficients would tend towards their maximum values at the larger experimental scales. However, the laboratory experiments con-

sistently show increasing runout with scale, suggesting that the influence of surface roughness on runout length is much less than the influence of scale effects such as Re -fluidisation, and that the influence of surface roughness on friction coefficient in the experiments of the present study is much less than that seen in Pohlman et al. (2006). Furthermore, as these differences in friction coefficient did not manifest in the initial measurements of the material friction angles (Section 3.3), this suggests that the effect of basal surface roughness on the granular slides in this study is not as significant as in Pohlman et al. (2006). It is possible that the vastly increased ratios of particle diameter to surface roughness length in the present study (roughly 33.3:1 compared to 10000:1 and even greater in Pohlman et al. (2006)) prevent these differences from manifesting.

5.6 Summary

The laboratory slide experiments conducted in this study show the influence of Re scale effects in a variety of ways. In particular, the slide surface velocity becomes increasingly dependent on Re as the slide travels further down the slope, suggesting that this scale effect becomes exponentially stronger for larger and larger slides. This manifests in much stronger Re -dependence of the slide deposit parameters, such as the slide front, peak, centroid, and tail positions, which are more strongly influenced by Re due to their dependence on the maximum slide velocity achieved before settlement, and the shearing behaviour of the slide as it enters and leaves the transition curve.

However, comparing the Reynolds-normalised runout positions of the experiments in this study to those in other studies and in nature confirms that other physical factors such as fragmentation and moisture content remain relevant and relatively unexplored causes of model effects. Other slide parameters such as the slide volume and porosity seem to show a weaker inverse dependence on Re . This highlights that Re exerts varying influence on the various characteristics of dry granular slides, relative to physical mechanisms inherent to the granular system.

Meanwhile, the simulations show that the shearing behaviour in the slides of this study fluctuates significantly and does not strictly follow a Bagnold-like velocity profile, with the variation of velocity with depth fluctuating between linear and Bagnold-like profiles. Further laboratory analysis of the base velocity across the channel and of the velocity-depth profile at the sidewalls would be valuable for assessing the influence of scale effects on this shearing behaviour. This may support the hypothesis that the base velocity varies to a greater extent than the surface velocity with scale, being subject to stronger airflow fluidisation effects.

The effects of surface roughness not being scaled with the particle diameter also do not seem to be significant, despite Pohlman et al. (2006) suggesting that differences in roughness lengths much smaller than the particle diameter can lead to large differences in applied friction coefficients. This precedent highlights the importance of correctly scaling surface roughness in studies involving smooth or spherical particles. However, the friction coefficient measurements from this present study suggests the mechanisms that cause this frictional difference with surface roughness do not necessarily apply to sufficiently aspherical particles.

Additionally, calibrating the laboratory surface velocity data in attempts to isolate and remove the influence of drag force acting on individual particles in the slide also results in fit improvement. This shows that a significant portion of the Re scale effects seen in the surface velocity are caused by the particle drag force, but other physical factors such as the influence of drag on the macro-scale granular system and the reduction of effective friction angle may be responsible for the rest of these scale effects. This drag force normalisation adds some physical validation to the use of a power law normalisation approach based on Re^α , but shows there is still considerable room to improve understanding of the scale effects present.

Comparisons of the laboratory runout data to slides from Davies and McSaveney (1999) and natural events (Table 18) further confirm the strong influence of Re scale effects within a large range of slide parameters. Importantly, Eq. 62 and Fig. 119 show that laboratory-scale results can be effectively calibrated to model natural phenomena via Re -normalisation. This significantly expands the utility of laboratory modelling for hazard prediction and mitigation of dry granular slides.

6 Conclusions and Outlook

6.1 Conclusions

The main aim of this study was to identify scale effects in dry granular slides, through the application of a scale series of laboratory experiments based on Froude similarity. A further aim was to directly quantify the influence of these scale effects on key parameters of the granular slides, and to evaluate which physical factors were responsible for these scale effects. To achieve these aims, a versatile laboratory set-up was designed and constructed to conduct geometrically similar dry granular slides at different scales. This set-up consisted of a smooth inclined channel section, circular transition curves, a flat runout section, and channel sidewalls that could be positioned to produce similar chute geometries at the desired scales.

Froude scaling was applied to a scale series experiments in this study to ensure that resultant differences between parameters of geometrically similar experiments could be solely attributed to non-Froude number scale effects. The ratio of a characteristic slide length dimension from the largest experiment to the smallest experiment (λ) was 4, with λ values of 1, 2, and 4 being assessed in the scale series. For each value of λ , three different initial slide release conditions were assessed, with the angle of the release wedge surface from the horizontal θ_W being assessed at 0, 7.5, and 15°. Angular sand particles were used to provide insight on scale effects that may manifest in natural slides, with parameters and size-distributions being scaled to fit the geometries of the scale series (Section 3.2.2). Experiments were repeated in identical conditions to isolate and mitigate any potential errors, with measured parameters given in this study being ensemble averages from each set of experimental repeats.

This laboratory set-up was designed so that the slide surface velocity and slide thickness could be measured at two locations on the inclined channel section, while the final deposit dimensions could be measured once the slide events had finished. The slide surface velocity was measured in an area around the measurement point using particle image velocimetry (PIV), which produced measurements across one

6. CONCLUSIONS AND OUTLOOK

half of the channel. This proved to be sufficient as the slides conducted in the present study were highly symmetrical, as seen in both digital camera footage of the slide events in progress and in the final deposit dimensions. Meanwhile, the slide thickness was measured at the corresponding channel sidewall and the channel centre using laser trigonometry. Although the precision of the technique was reduced relative to the PIV measurements, the technique was sufficient for accurately capturing the variation in slide thickness over time at these measurement points. Finally, the deposit dimensions were measured using photogrammetry to produce accurate 3D meshes of the complete deposit mass, with the meshes having sufficient precision and accuracy for the accurate extraction of slide front, peak, mass centroid, and rear positions, as well as estimates for the slide volume and porosity.

The laboratory experiments conducted in this study successfully identified clear differences in dry granular slide behaviour between experimental scale factors of $\lambda = 1$ to 4. In particular, the surface velocity of slides as they traversed the inclined channel sections increased by up to 20% as the scale increased, while the slide runout distance increased by up to 40%. The deposit volume and porosity also decreased by over 10% as the scale increased, while properties such as the maximum slide thickness as it traversed the inclined channel section did not vary consistently with scale. The repeatability of the slide release, the resulting slide behaviour, and the measurement of key slide parameters was verified, establishing that the model and measurement effects from the set-up were insignificant and that any relative differences between similar experiments of different scales were essentially caused by scale effects.

Additionally, discrete element modelling (DEM) simulations were completed that replicated the geometry of the laboratory experiments, as well as significantly larger and smaller slides at $\lambda = 0.2$ and $\lambda = 20$ respectively. The parameters of the DEM and validity of the modelling approach (particularly the use of a rolling-resistance coefficient with spherical particles to model asphericity) were validated by modelling an axisymmetric column collapse and an experiment from Hutter et al. (1995). The axisymmetric column collapse verified that the DEM did a

good job at modelling the general granular physics of the laboratory experiments and particles, while the simulation of experiment #117 from Hutter et al. (1995) showed that the DEM captured the position distribution of a slide over time well for a typical chute geometry.

The use of a rolling-resistance method to simulate the asphericity of rough, angular sand grains with spherical DEM particles was largely successful in representing key slide parameters such as the slide velocity and settlement behaviour. The simulation also provided further insight on the physics of the laboratory slide, particularly in the variation of slide velocity with depth. While the laboratory experiments only captured the surface velocity, the velocity-depth profiles of the DEM could be extracted easily, showing that the slide fluctuates between Bagnold-like and plug-like velocity profiles as it passes over fixed points on the inclined channel section. This highlights the transient nature of the granular slides in comparison to the steady granular flows more commonly studied in the technical literature (Pouliquen, 1999; Artoni et al., 2012).

When simulating the experimental geometries of the present study, the DEM modelled the laboratory experiments at $\lambda = 2$ reasonably well. However, dilute regions such as the slide front and tail proved more difficult to represent accurately using this approach. More importantly, the DEM was not seen to capture scale effects, with many key slide parameters being scale-invariant and only very small increases in runout distance being observed for extremely large differences in scale, in the order of 1:100. This difference seems to be a Ca scale effect based on the material stiffness not varying across the scale series. The DEM also did not model particle fracture processes that became increasingly important at large scales in the laboratory, which could also affect key slide parameters. It is clear that while the DEM describes many of the most important processes in a granular slide well, the mechanisms that cause scale effects in the laboratory experiments are not captured.

The extensive data collected from the laboratory experiments in this study proved sufficient for the quantification of scale effects, clarifying how factors such as the experiment scale and initial slide release geometry affect the influence of

scale effects on the key slide parameters measured. Power-law normalisation of the laboratory data to the grain Reynolds number Re significantly improves the fit of the majority of these parameters across differing experimental scales, as well as the fit to many natural events. This confirms that Re -related effects such as airflow fluidisation contribute the most to the scale effects seen in the laboratory experiments. The optimal choice of power α of Re for each normalised slide parameter reflects the relative influence of Re , with values of α ranging from -0.17 to 0.07 . Negative values of α highlight parameters that increase with scale and Re , such as slide surface velocity and runout distance, while positive values reflect parameters that decrease as scale increases, such as deposit volume and porosity. Additional normalisation of the slide surface velocity based on the drag force acting on individual particles shows that this Re normalisation method has physical basis for this parameter, with the particle drag force being responsible for 29.5% to 57.9% of the fit improvement seen with Re normalisation.

The optimal values of α found in this study suggest that the deposit runout distance and morphology are the parameters most strongly affected by Re scale effects, with the influence being lower on the slide surface velocity but increasing as the slide approaches its maximum velocity. Additionally, many slide runout parameters show increasing Re influences on scale effects with increasing slide mass, in this case governed by the release wedge steepness θ_W . As these differences do not manifest in the α values selected when looking at the slide surface velocity, this suggests that Re scale effects exert the strongest influence during the slide's settlement behaviour, and that the strength of these scale effects depends on the thickness of the slide as it starts to settle. The relative strength of Re scale effects seen in the laboratory scale series justifies the lack of scale effects seen in the corresponding simulations, which were conducted in isolation of Re -dependent mechanisms such as surrounding and interstitial airflow.

The strong influence of Re scale effects on dry granular slide runout distances in particular is further confirmed within a large range of slide parameters by comparisons of the laboratory data to slides from Davies and McSaveney (1999) and natural events (see Table 18 for references). Eq. 62 and Fig. 119 demonstrate that

laboratory-scale results can be effectively calibrated to model natural phenomena via Re-normalisation. This significantly expands the utility of laboratory modelling for hazard prediction and mitigation in the context of dry granular slides.

6.2 Outlook

Overall, the laboratory set-up and numerical model established in this study provide a suitable framework for further analysis of scale effects in dry granular slides in the future. This section provides several potential expansion routes to further investigate scale effects in dry granular slides, both in terms of improving the laboratory set-up and using it to investigate a wider range of conditions, and in terms of improving the DEM to more accurately model these physical slides.

Section 5.3 highlights the significant variation of slide velocity with depth in the simulations, and suggests this variation is also significant in the laboratory experiments. To quantify this, the laboratory set-up could be adapted to allow a more comprehensive range of velocity measurements. Replacing the inclined channel surface with another section of transparent acrylic would allow the base velocity to be recorded via PIV. This would allow the influence of scale effects to be determined throughout the slide depth, to validate the hypothesis that Re-based scale effects influence the shear flow in the slide and exert more influence on the base velocity than the surface velocity, due to the base being more directly fluidised. PIV analysis could also be conducted through the acrylic sidewalls of the slide with additional cameras, providing more evidence of any scale effects in this shear flow at the sidewalls instead of at the channel base. Section 5.5 suggests that the variation of surface roughness should not cause model effects with the existing materials, but care should be taken if experiments are conducted with smooth, spherical particles using this approach.

The simulations also highlight the complex nature of slide settlement in the flat runout zone, while the most significant scale effects observed in the laboratory can be seen in the deposit parameters within this zone. Accordingly, future laboratory

experiments should provide more comprehensive measurement and coverage of the slide velocity and thickness in the runout zone. This would provide a more complete image of the slide behaviour and further clarify the interaction of scale effects during this critical phase of slide settlement. Elevating the entire laboratory set-up would allow for a transparent runout zone, which would allow camera footage to further elucidate the settlement behaviour of the laboratory slides and provide insight into the base velocity profile during settlement via PIV.

The power-law normalisation in Section 5.4 highlights the necessity of capturing Re scale effects in numerical models. Future simulations that attempt to capture the scale effects seen in laboratory experiments must be capable of capturing the mechanisms seen in the laboratory. In particular, coupling the DEM with computational fluid dynamics (CFD) is crucial for attempting to represent the Re scale effects imposed by airflow fluidisation. While other secondary mechanisms exist in the laboratory experiment that may be difficult to implement into a numerical model, such as particle fracture and acoustic fluidisation, these mechanisms were seen to exert much less influence on the laboratory experiments than Re scale effects. CFD-coupling is thus the highest priority in attempting to improve the representation of scale effects in even dry granular slides in a numerical context. Additionally, further investigation into how the minor simulated scale effects seen for very large differences in λ correlate to Ca may be useful, as this could inform further study on the strength of these effects in the laboratory. This would be particularly relevant in a context free of laboratory particle fracture, such as a slide consisting of steel ball-bearings, and may be more relevant to industrial contexts than natural slide events.

The drag force normalisation of the slide surface velocity seen in Section 5.4.2 shows that the particle drag force reduces the velocity of fine particles significantly more than for larger ones. Not only has the drag force been shown to contribute significantly to Re scale effects seen in this parameter, but it also has the potential to impact polydisperse slides heterogeneously. The normalisation conducted in Section 5.4.2 was completed using a mean representative particle, but in actuality both the particle size and shape varied significantly within the slides for each

experimental condition. The role of particle drag force on scale effects in granular slides could be further elucidated by a scale series of laboratory experiments conducted in a vacuum, in isolation of Re influences. Additionally, while CFD remains a powerful tool for capturing air interactions in granular slides, the existing DEM could be modified to apply resisting drag forces based on the method seen in Section 5.4.2 between time-steps. This method could simulate the effects of particle drag more closely while not necessarily requiring coupling with a CFD model.

The laboratory set-up from this study can additionally be adapted to evaluate a wider range of initial slide conditions and geometries in the future, to further identify the influence of scale effects on dry granular slides. The channel material can be coated in a layer of rough particles, scaled to those of the granular slide, to investigate scale effects that manifest in slides with non-slip boundary conditions. Different shutter designs could also be implemented to identify scale effects in unconfined granular slides, such as in their lateral spreading or potentially self-channelisation. More detailed analysis of the local deposit porosity in the laboratory may also elucidate further scale effects, as significant local variations could be seen in the DEM. Additionally, the volume of dust generated by experiments could also be examined, to potentially quantify the scale-dependence of particle fracture and identify the secondary effects this imposes on the slides during motion, in combination with more comprehensive velocity measurement techniques.

Finally, it would be fairly straightforward to investigate wet or moist granular slides using this setup. Care would need to be taken to ensure that the modular sidewalls and rotating shutter are waterproof at their connection to the channel surface, to prevent any leakage of water or disruption to the slide bulk after its release. However, the investigation of scale effects in moist granular slides would have a large impact, potentially being applicable to a much larger range of natural events and scenarios. Fluid properties such as surface tension and viscosity would also need to be calibrated at each scale investigated.

A Additional slide position distribution data

In this section, further laboratory-numerical comparisons are provided for the position distribution data corresponding to $\theta_W = 7.5^\circ$ (S2 and L7–L12, and S5 and L22–L25, respectively). Position distribution data is also provided for the simulation data at $\lambda = 4$ for all values of θ_W (S7 to S9), in addition to the simulation data at $\lambda = 0.2$ and $\lambda = 20$ for $\theta_W = 0^\circ$ (S10 and S11). Figures 121 to 125 were omitted from Section 4.3.2 as the data showed trends and patterns that were already apparent from the data at $\theta_W = 0^\circ$ and 15° . The data is included here for further comparison and reference. Additionally, Figs. 126 to 131 showcase the spread of data from individual laboratory experiments compared to the simulation data corresponding to Figs. 75 to 78 and Figs. 121 to 122, which is faded to emphasise the laboratory data spread. Generally, this spread was very minor, and was thus omitted from Section 4.3.2 to emphasise the simulation data.

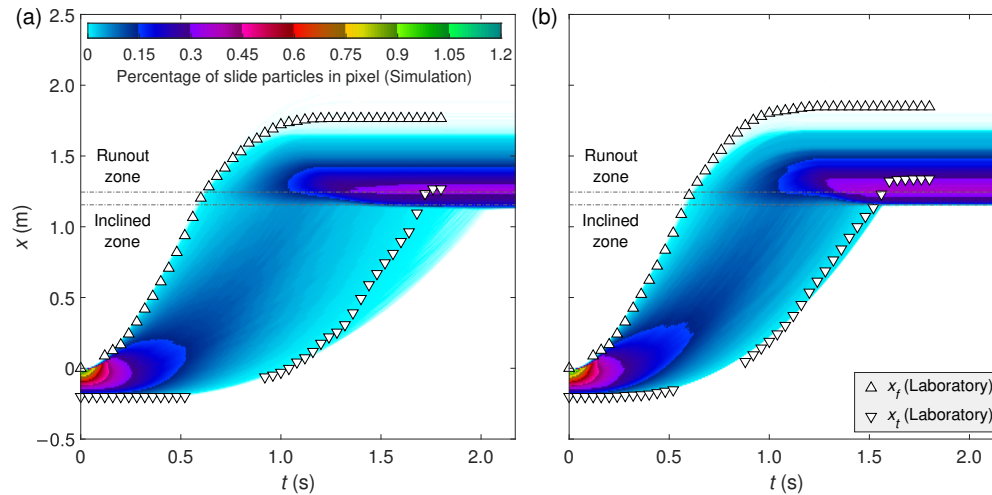


Figure 121 Comparison of position distribution over time between laboratory (L22–L25) and simulation (S5) slides, for $\lambda = 2$ and $\theta_W = 7.5^\circ$ at (a) channel sidewalls and (b) channel centre

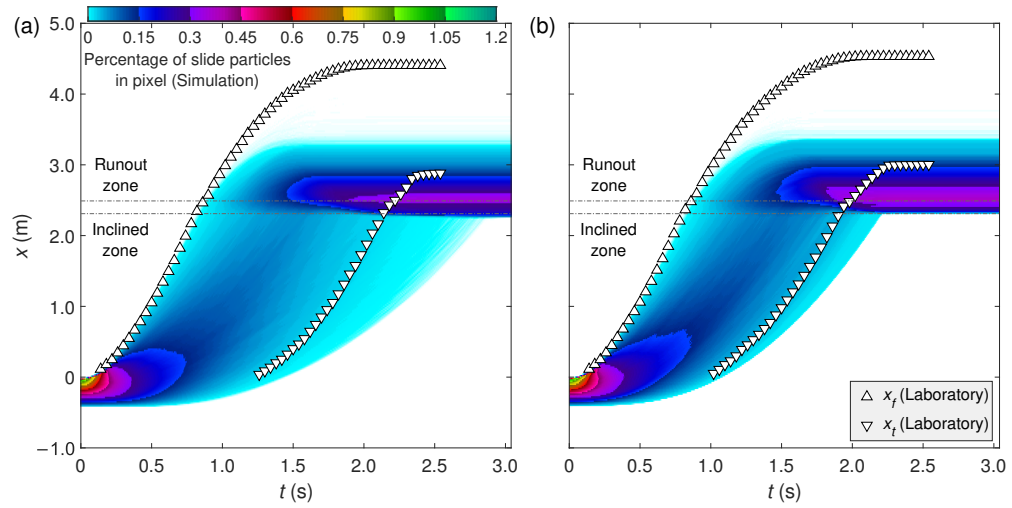


Figure 122 Comparison of position distribution over time between laboratory (L7–L12) and simulation (S2) slides, for $\lambda = 1$ and $\theta_W = 7.5^\circ$ at (a) channel sidewalls and (b) channel centre

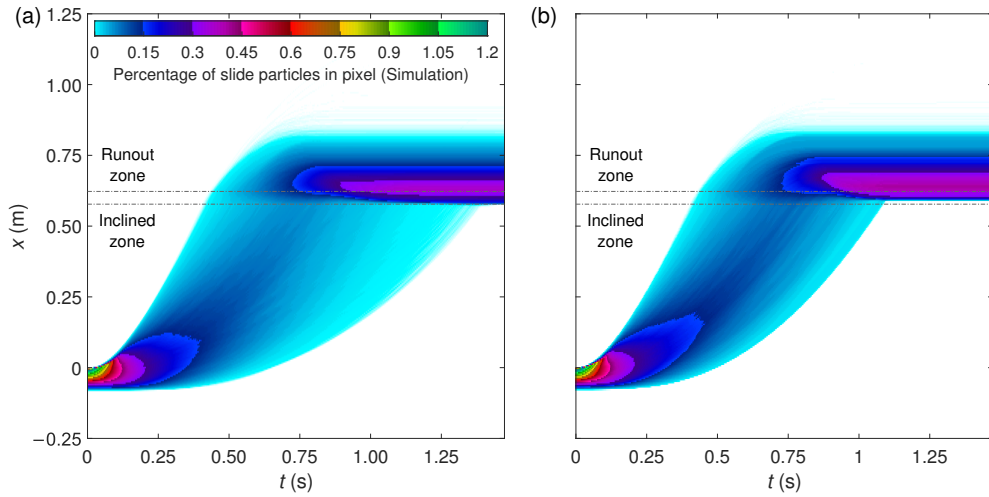


Figure 123 Position distribution over time for simulated slide S7, for $\lambda = 4$ and $\theta_W = 0^\circ$ at (a) channel sidewalls and (b) channel centre

A. ADDITIONAL SLIDE POSITION DISTRIBUTION DATA

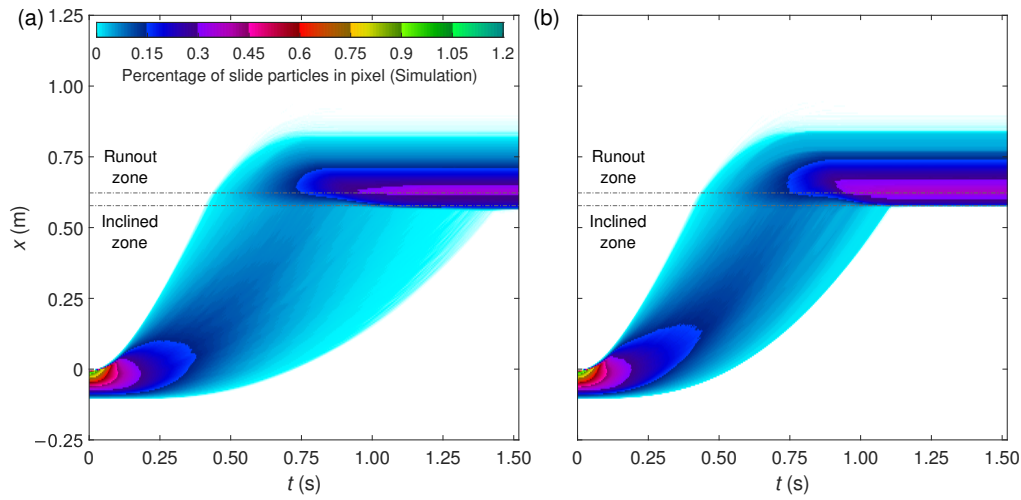


Figure 124 Position distribution over time for simulated slide S8, for $\lambda = 4$ and $\theta_W = 7.5^\circ$ at (a) channel sidewalls and (b) channel centre

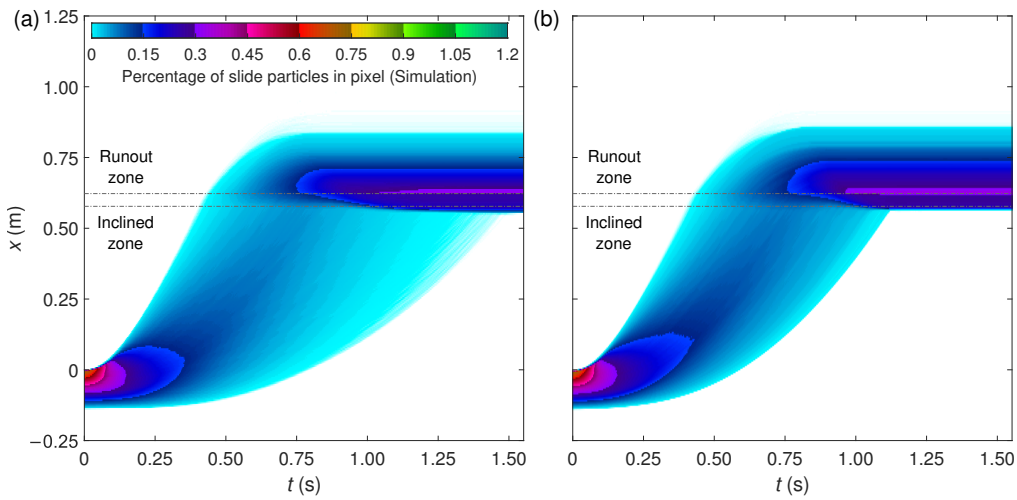


Figure 125 Position distribution over time for simulated slide S9, for $\lambda = 4$ and $\theta_W = 15^\circ$ at (a) channel sidewalls and (b) channel centre

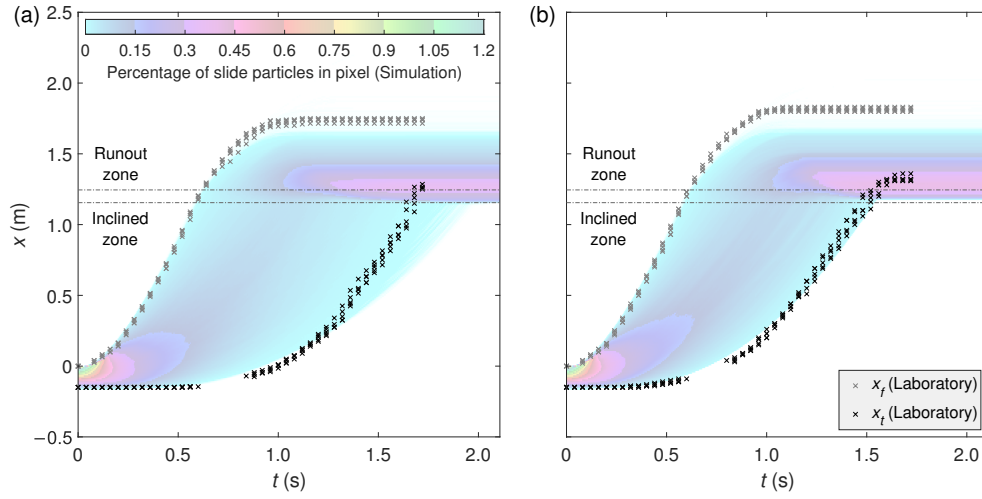


Figure 126 Comparison of position distribution over time between individual laboratory (L18–L21) and simulation (S4) slides, for $\lambda = 2$ and $\theta_W = 0^\circ$ at (a) channel sidewalls and (b) channel centre

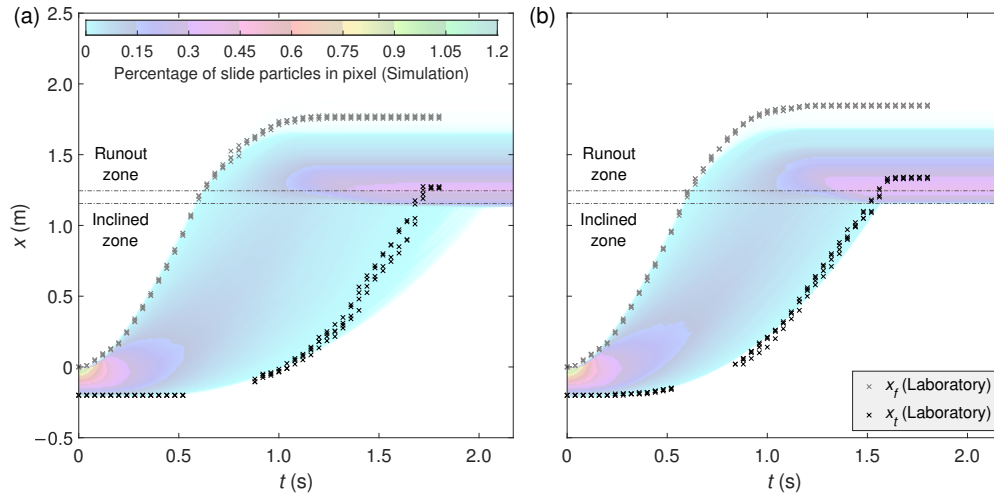


Figure 127 Comparison of position distribution over time between individual laboratory (L22–L25) and simulation (S5) slides, for $\lambda = 2$ and $\theta_W = 7.5^\circ$ at (a) channel sidewalls and (b) channel centre

A. ADDITIONAL SLIDE POSITION DISTRIBUTION DATA

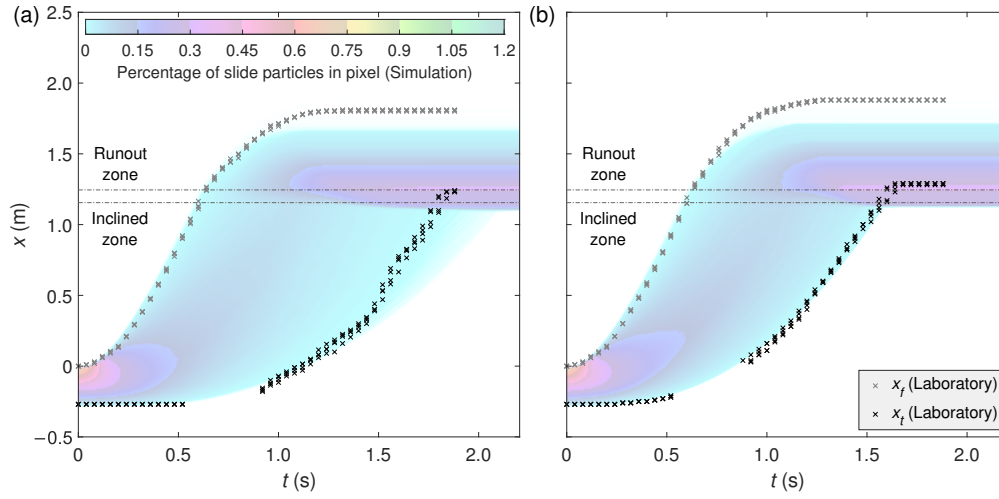


Figure 128 Comparison of position distribution over time between individual laboratory (L26–L29) and simulation (S6) slides, for $\lambda = 2$ and $\theta_W = 15^\circ$ at (a) channel sidewalls and (b) channel centre

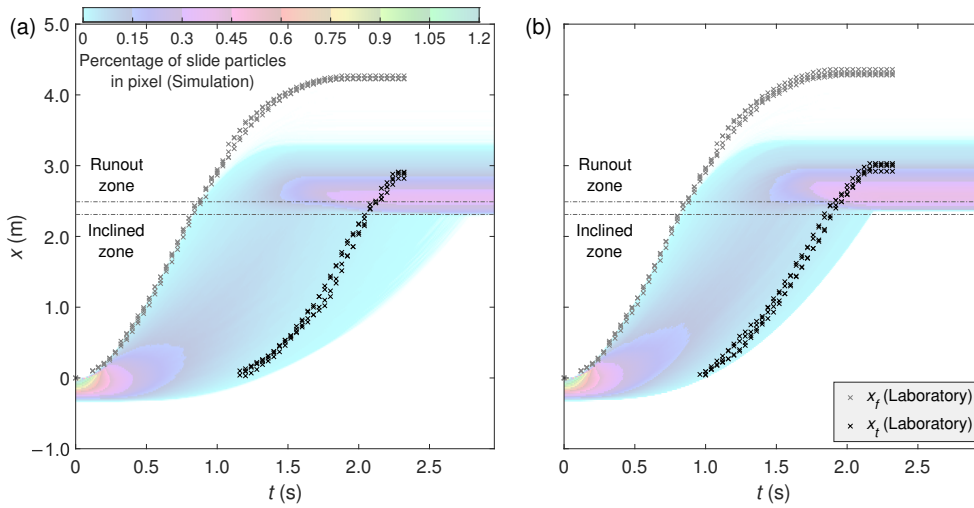


Figure 129 Comparison of position distribution over time between individual laboratory (L1–L6) and simulation (S1) slides, for $\lambda = 1$ and $\theta_W = 0^\circ$ at (a) channel sidewalls and (b) channel centre

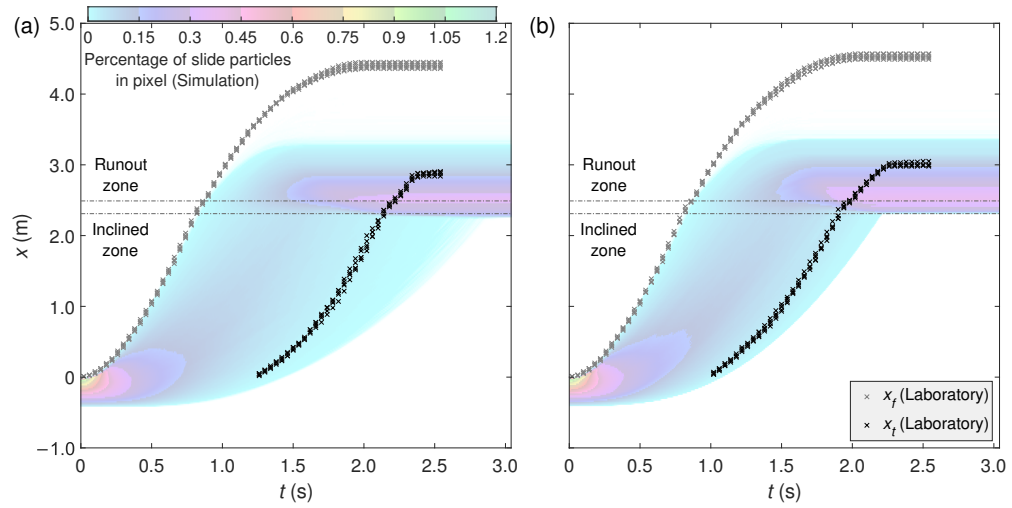


Figure 130 Comparison of position distribution over time between individual laboratory (L7–L12) and simulation (S2) slides, for $\lambda = 1$ and $\theta_W = 7.5^\circ$ at (a) channel sidewalls and (b) channel centre

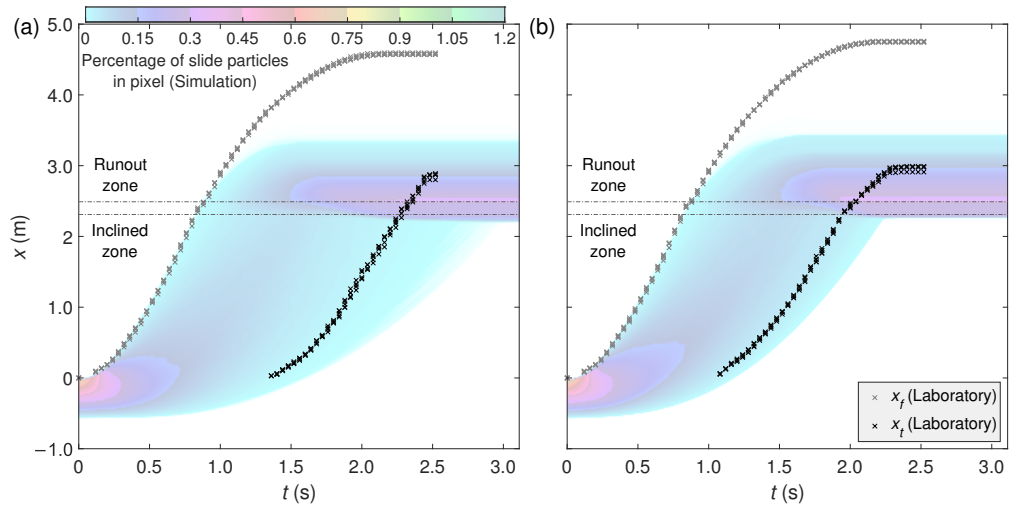


Figure 131 Comparison of position distribution over time between individual laboratory (L13–L19) and simulation (S3) slides, for $\lambda = 1$ and $\theta_W = 15^\circ$ at (a) channel sidewalls and (b) channel centre

B Additional simulated velocity distribution data

In this section, additional simulated slide velocity distribution data is provided for the simulation at $\lambda = 2$ and $\theta_W = 7.5^\circ$ (S5), as well as for the simulations at $\lambda = 1$ (S1–S3) and $\lambda = 4$ (S7–S9) for all values of θ_W , and the simulations at $\lambda = 0.2$ (S10) and $\lambda = 20$ (S11) for $\theta_W = 0^\circ$. Figures 132 to 138 were omitted from Section 4.3.3 as the data again showed trends and patterns that were already apparent from the data presented in that section. Overall, the data show in Sections A and B further demonstrate the relative lack of scale effects seen in simulations of λ within the laboratory range. However, the differences can be seen clearly as interpolations of the significantly larger differences seen between Figs. 106 and 105 in Section 4.3.7. This further highlights that these minor simulation scale effects are consistent across multiple values of λ and should not be attributed to random simulation noise.

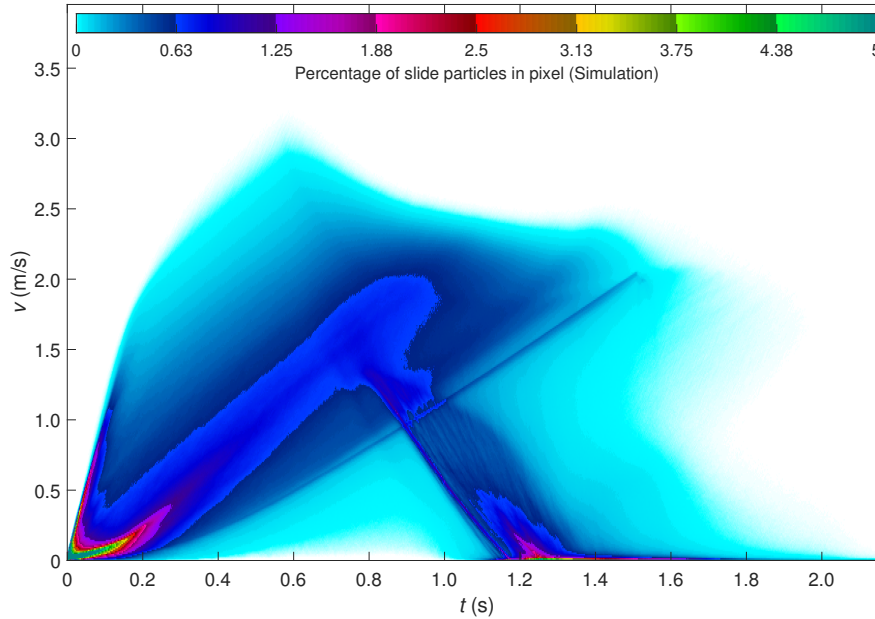


Figure 132 Velocity distribution for simulation S5, with $\lambda = 2$ and $\theta_W = 7.5^\circ$

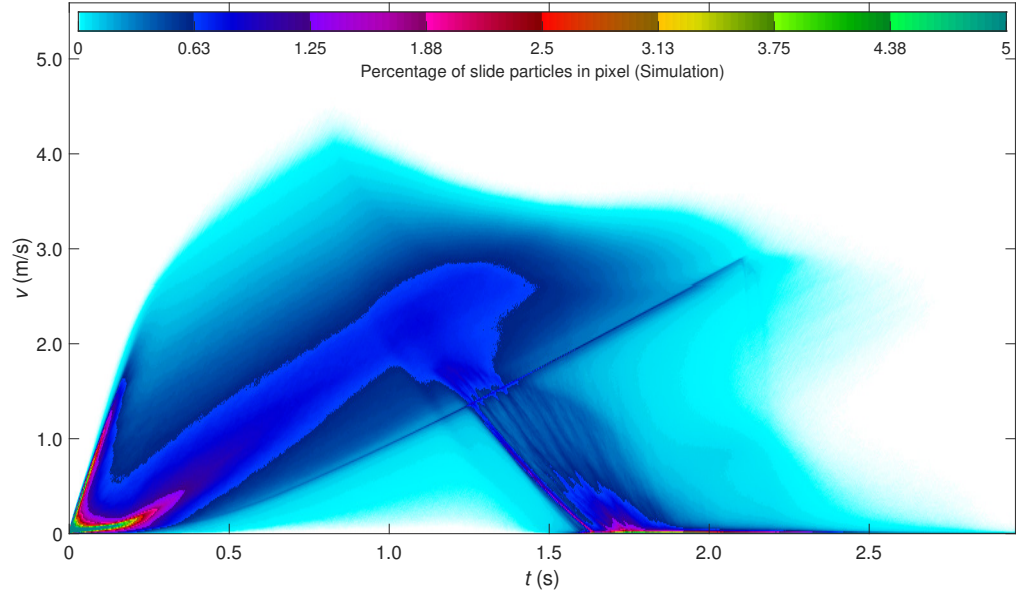


Figure 133 Velocity distribution for simulation S1, with $\lambda = 1$ and $\theta_W = 0^\circ$

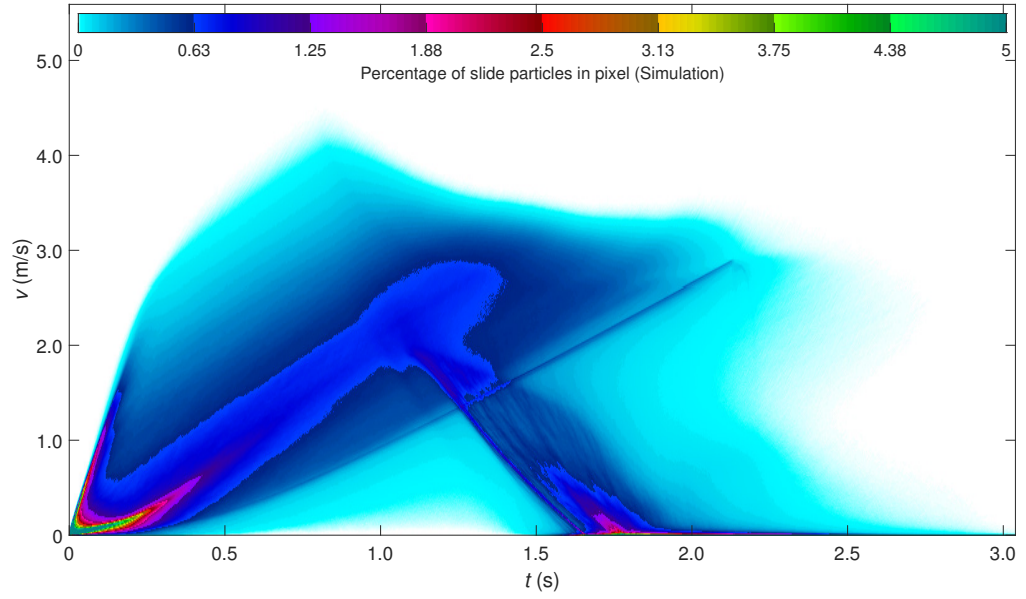


Figure 134 Velocity distribution for simulation S2, with $\lambda = 1$ and $\theta_W = 7.5^\circ$

B. ADDITIONAL SIMULATED VELOCITY DISTRIBUTION DATA

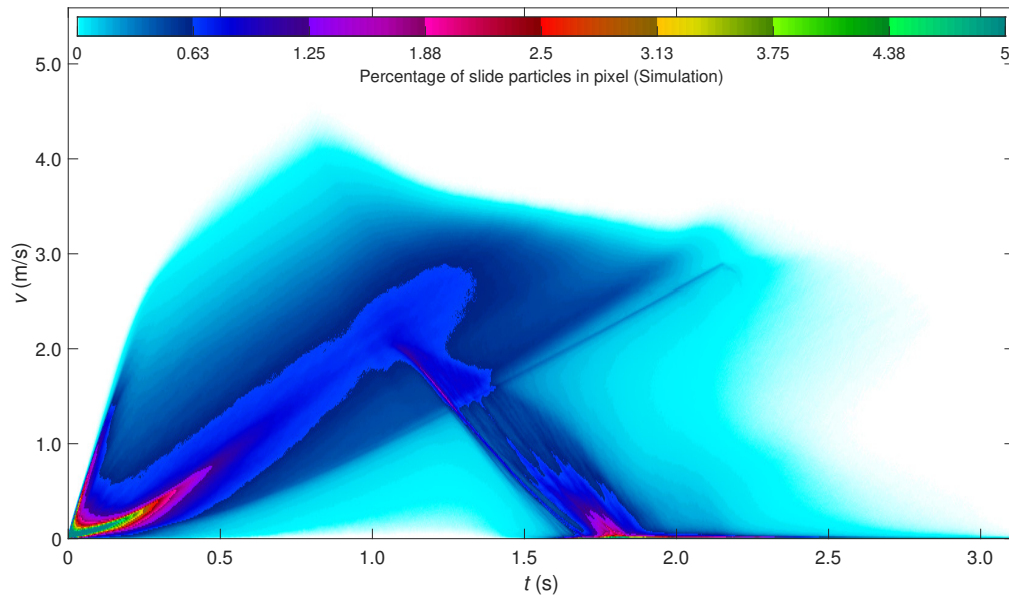


Figure 135 Velocity distribution for simulation S3, with $\lambda = 1$ and $\theta_W = 15^\circ$

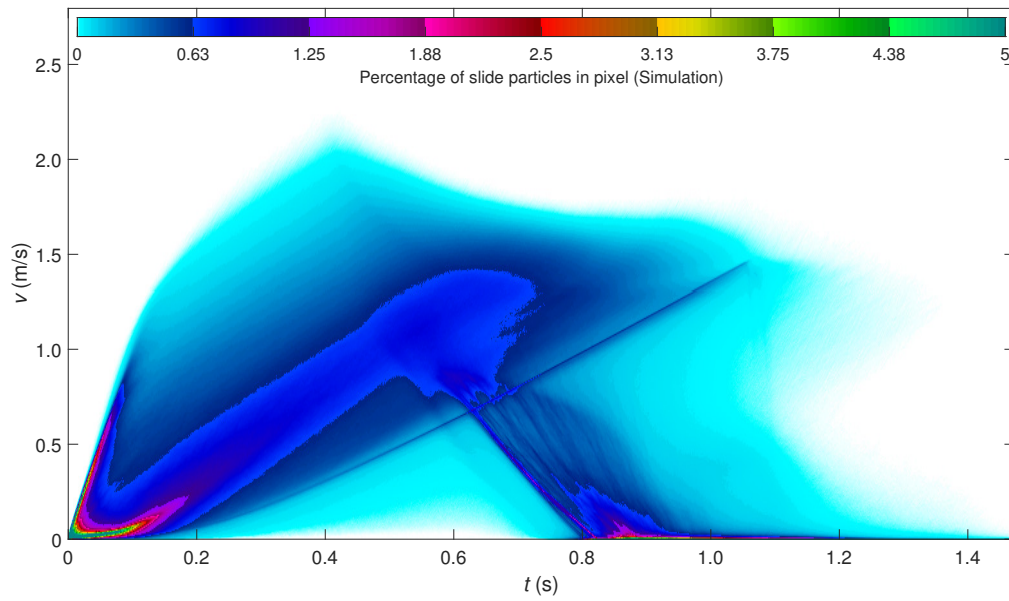


Figure 136 Velocity distribution for simulation S7, with $\lambda = 4$ and $\theta_W = 0^\circ$

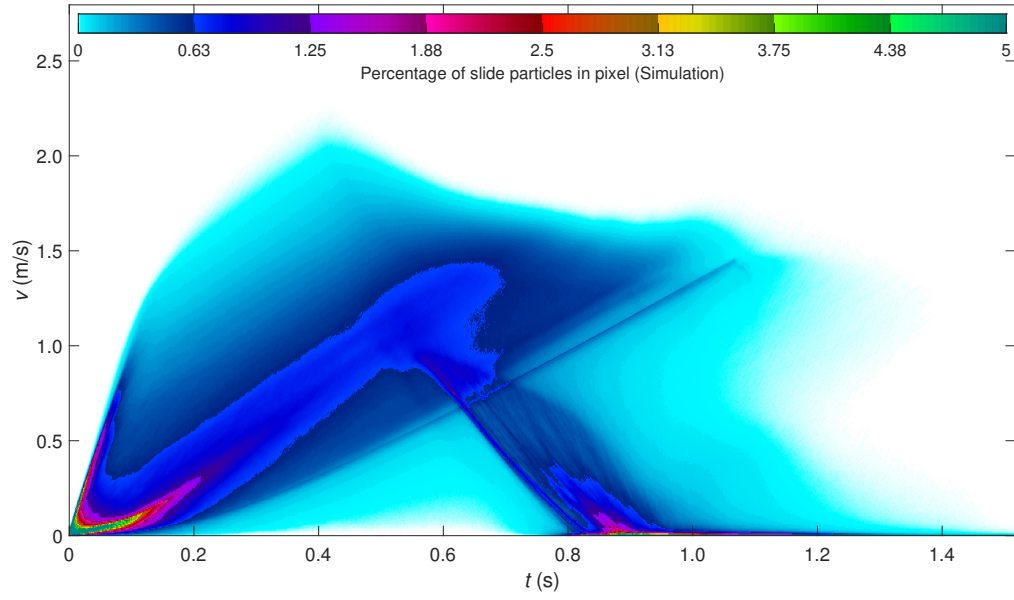


Figure 137 Velocity distribution for simulation S8, with $\lambda = 4$ and $\theta_W = 7.5^\circ$

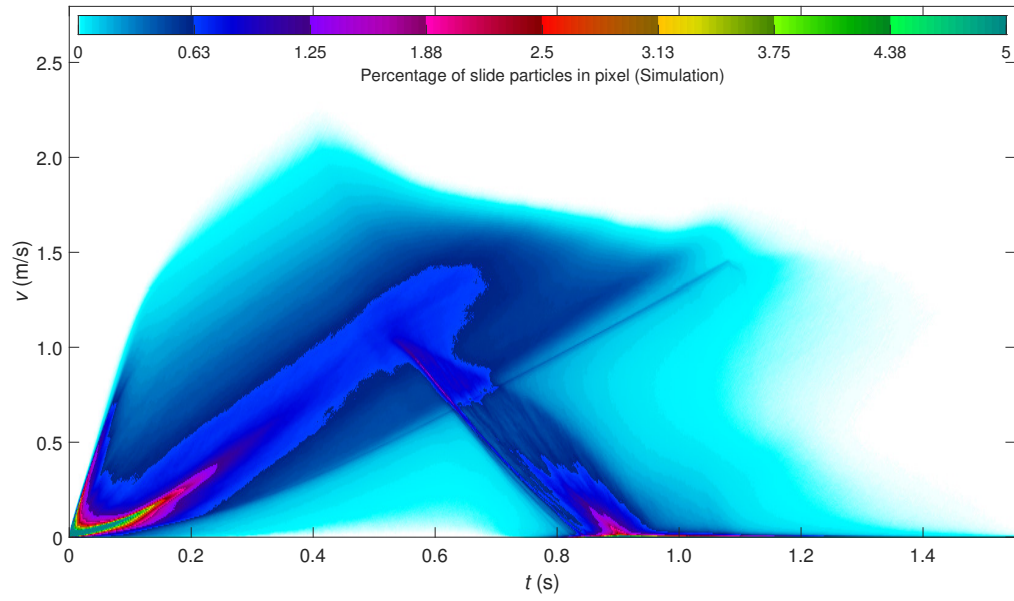


Figure 138 Velocity distribution for simulation S9, with $\lambda = 4$ and $\theta_W = 15^\circ$

B. ADDITIONAL SIMULATED VELOCITY DISTRIBUTION DATA

Additionally, Fig. 139 highlights the simulated slide velocity profiles at $\lambda = 2$ and $\theta_W = 7.5^\circ$, in a similar manner to Figs. 82 and 83 in Section 4.3.4. Fig. 140 normalises this data with respect to the maximum velocity and thickness at each time-step, while Fig. 141 fits power laws to these normalised velocity profiles in a similar manner to Figs. 108 and 110 in Section 5.3, reinforcing the conclusions from those sections. Table 21 provides the powers β and normalised residuals of these curves. Finally, Figs. 142 and 143 highlight the slide velocity profiles from the scale-series extrapolation, further supporting the conclusions of Section 4.3.7 and highlighting slight differences in the base velocity between $\lambda = 0.2$ and 20.

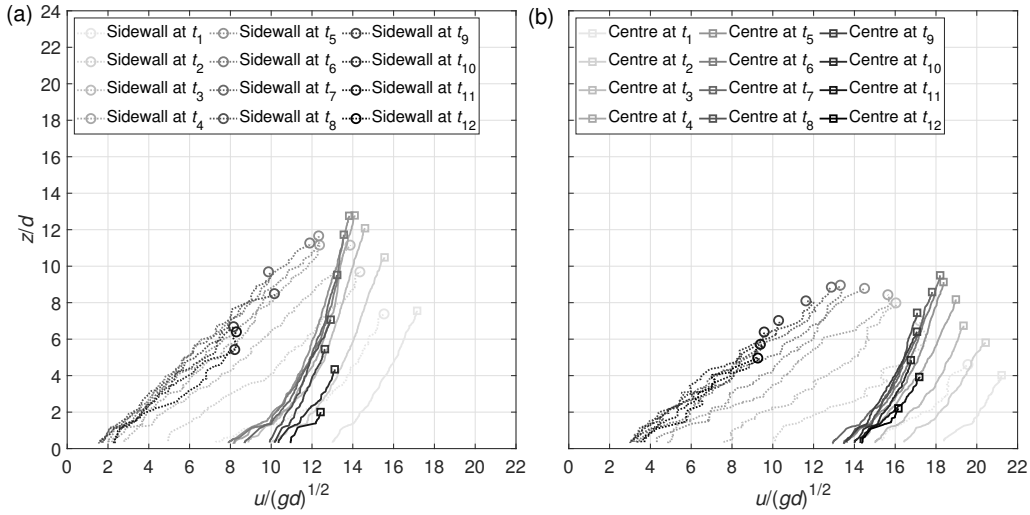


Figure 139 Simulated (S5) non-dimensional mean slide velocity plotted against slide depth at 400,000 time-step intervals, with t_1 starting 400,000 time-steps after the slide front contacts the (a) x_1 and (b) x_2 measurement points, with $\theta_W = 7.5^\circ$. Circles denote sidewall surface velocities while squares denote central surface velocities

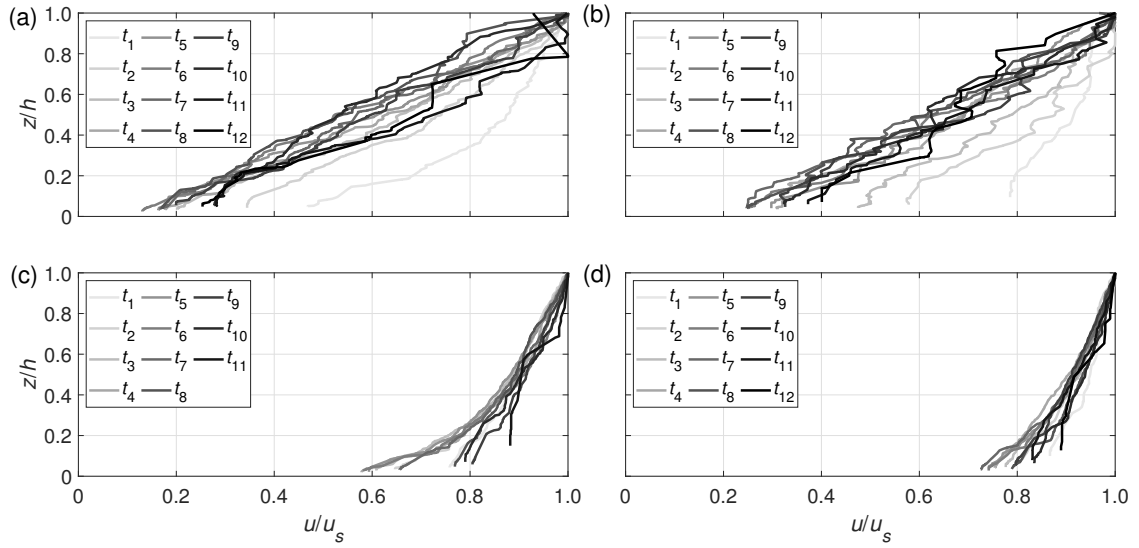


Figure 140 Simulated (S5) particle velocity data (Fig. 139) normalised to maximum velocity and thickness at (a,c) x_1 and (b,d) x_2 at (a,b) the channel sidewall and (c,d) the channel centre, with $\theta_W = 0^\circ$. Data plotted at 400,000 time-step intervals t_1 to t_{12} , with t_1 starting 400,000 time-steps after the front reaches the measurement point

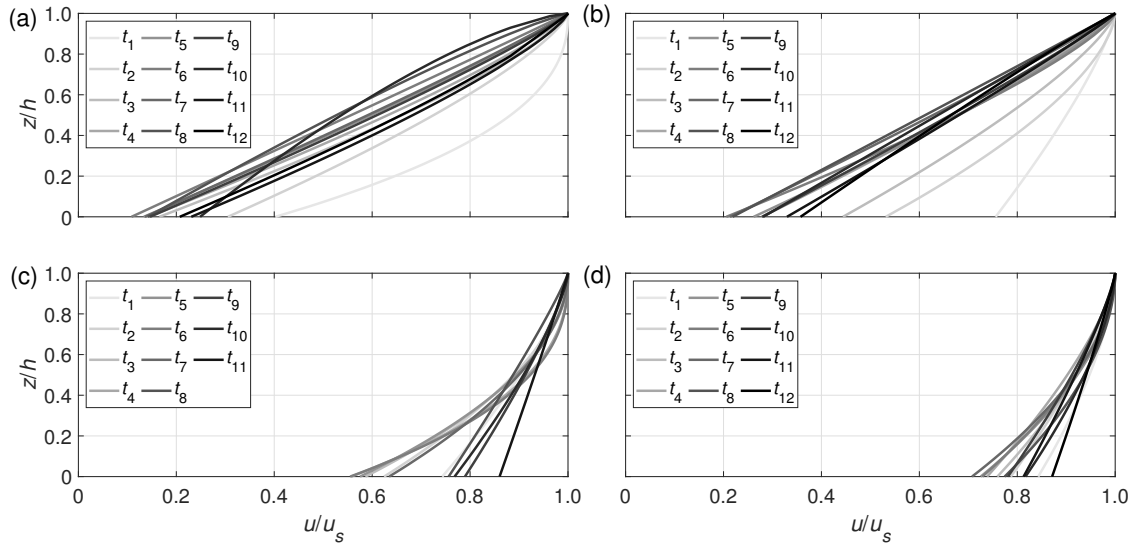


Figure 141 Fitting of power-law velocity profiles based on Eq. (48) over the slide depth of simulated (S5) particle velocity data (Fig. 140) at (a,c) x_1 and (b,d) x_2 at (a,b) the channel sidewall and (c,d) the channel centre, with $\theta_W = 0^\circ$. Fit-lines plotted at 400,000 time-step intervals t_1 to t_{12} , with t_1 starting 400,000 time-steps after the front reaches the measurement point

Table 21 β and r_{min} values for Fig. 108 with $\theta_W = 0^\circ$

Time-step	x_1 , sidewall		x_2 , sidewall		x_1 , centre		x_2 , centre	
	β	r_{min}	β	r_{min}	β	r_{min}	β	r_{min}
(-)	(-)	(%)	(-)	(%)	(-)	(%)	(-)	(%)
t_1	2.35	2.47	1.29	1.32	1.39	0.67	1.58	0.62
t_2	1.34	1.72	1.61	2.29	1.76	2.18	1.39	0.77
t_3	1.30	1.04	1.33	2.03	1.96	2.02	1.61	0.56
t_4	1.22	1.32	1.16	3.02	2.43	2.64	1.42	0.35
t_5	1.11	1.82	1.21	2.66	2.00	2.23	1.83	0.97
t_6	1.01	1.64	1.30	2.05	2.53	1.87	1.73	1.06
t_7	1.08	1.78	1.08	2.69	1.86	1.49	1.83	1.07
t_8	0.86	1.97	1.01	1.86	1.12	0.55	1.86	0.91
t_9	1.13	2.46	1.10	3.71	1.27	0.48	1.31	0.62
t_{10}	0.70	1.42	0.99	2.71	1.35	0.64	1.54	0.49
t_{11}	1.28	4.89	1.07	2.34	1.04	1.41	1.21	0.73
t_{12}	1.22	3.78	0.94	4.50	-	-	1.12	1.13

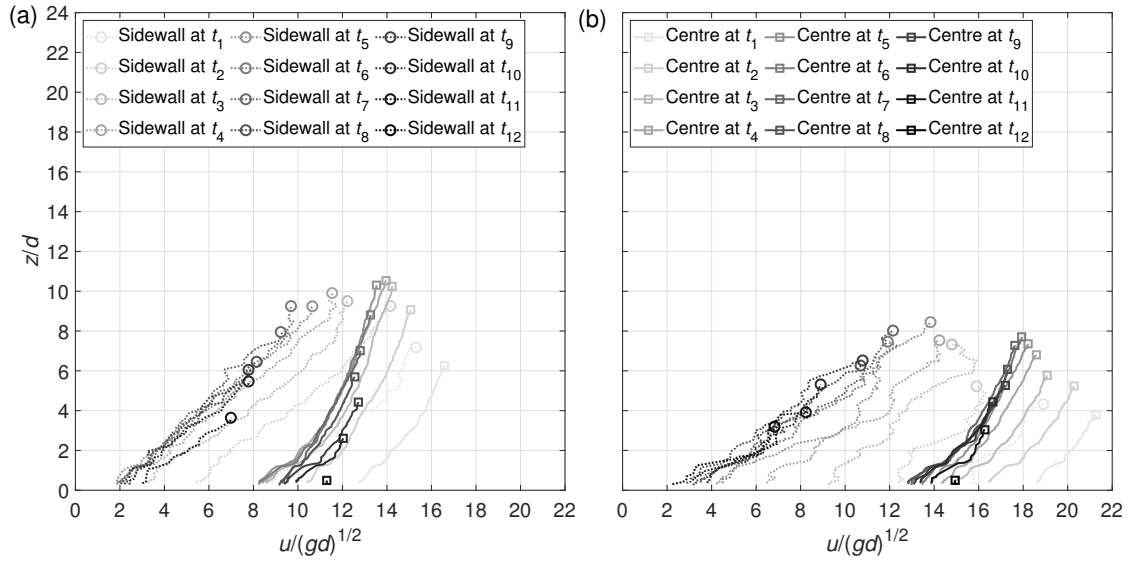


Figure 142 Simulated (S10) non-dimensional mean slide velocity plotted against slide depth at 126,500 time-step intervals, with t_1 starting 126,500 time-steps after the slide front contacts the (a) x_1 and (b) x_2 measurement points, with $\lambda = 0.2$ and $\theta_W = 0^\circ$. Circles denote sidewall surface velocities while squares denote central surface velocities

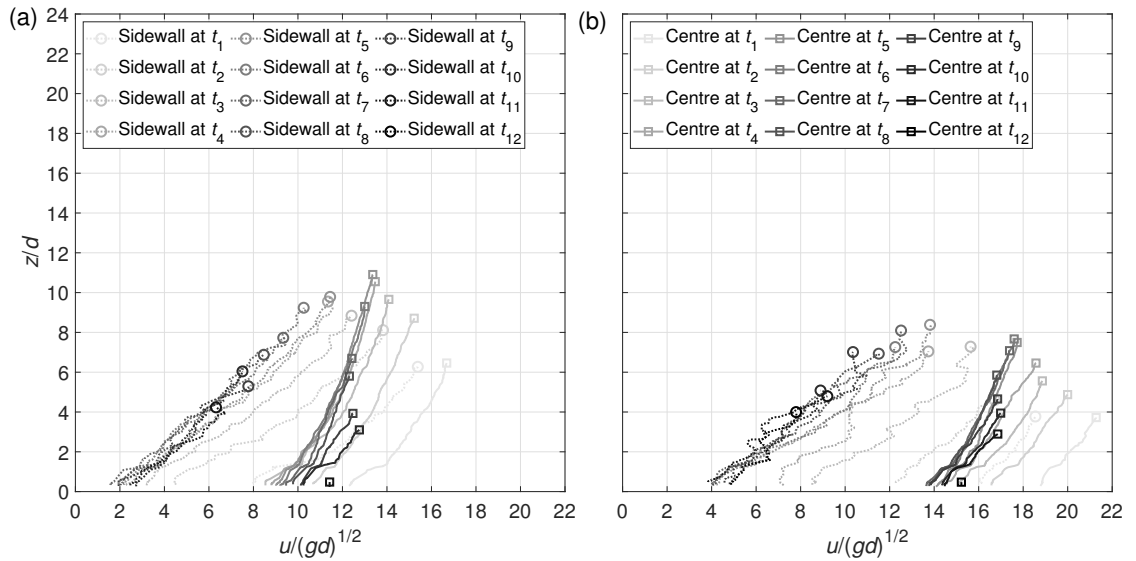


Figure 143 Simulated (S11) non-dimensional mean slide velocity plotted against slide depth at 1,265,000 time-step intervals, with t_1 starting 1,265,000 time-steps after the slide front contacts the (a) x_1 and (b) x_2 measurement points, with $\lambda = 20$ and $\theta_W = 0^\circ$. Circles denote sidewall surface velocities while squares denote central surface velocities

C Additional laboratory-simulation comparisons

In this section, additional laboratory-simulation comparisons are provided for $\theta_W = 7.5^\circ$, with simulation data corresponding to $\lambda = 2$ (S5). Figures 144 to 149 demonstrate that the trends and patterns seen at $\theta_W = 0^\circ$ and 15° in Sections 4.3.4 to 5.4.1 continue in an approximately linear manner through $\theta_W = 7.5^\circ$, with expected behaviour upon Re-normalisation. Figures 147 and 148 also showcase how the Re-normalisation seen in Section 5.4 is not useful without proper selection of a power α by which Re is modified. Finally, Fig. 150 provides the k_D -normalised velocity data for $\theta_W = 7.5^\circ$.

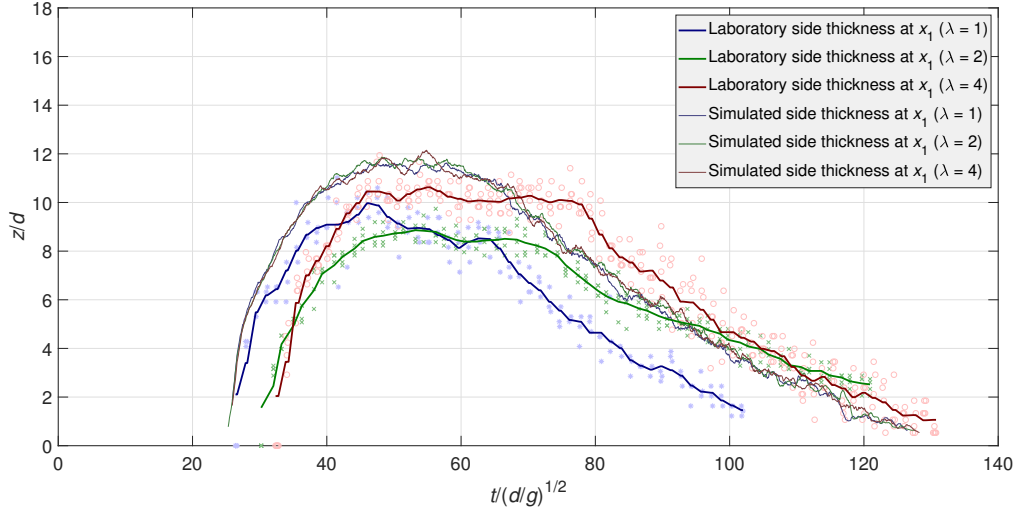


Figure 144 Comparison of laboratory (L7–L12, L22–L25, and L38–L45) and simulated (S2, S5, and S8) slide thickness profiles at the channel sidewall position at x_1 , with $\theta_W = 7.5^\circ$

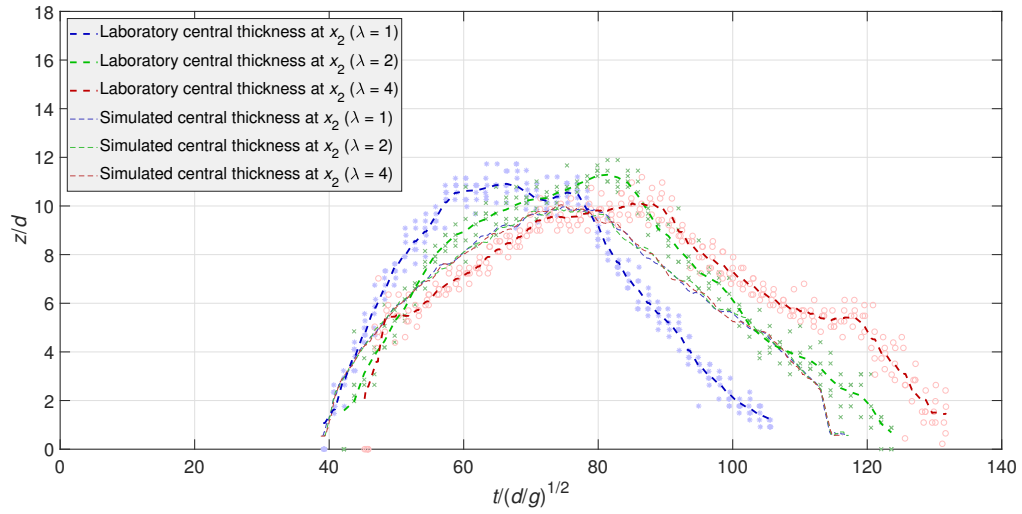


Figure 145 Comparison of laboratory (L7–L12, L22–L25, and L38–L45) and simulated (S2, S5, and S8) slide thickness profiles at the channel centre position at x_2 , with $\theta_W = 7.5^\circ$

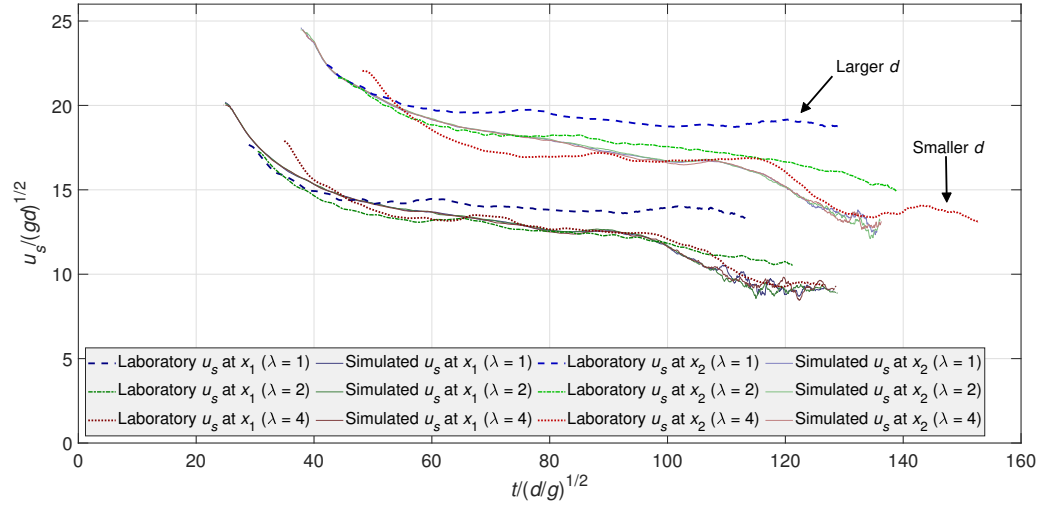


Figure 146 Comparison of ensemble-averaged slide surface velocity profiles at x_1 and x_2 . Laboratory (L7–L12, L22–L25, and L38–L45) and simulated (S2, S5, and S8) velocity measurements with $\theta_W = 7.5^\circ$

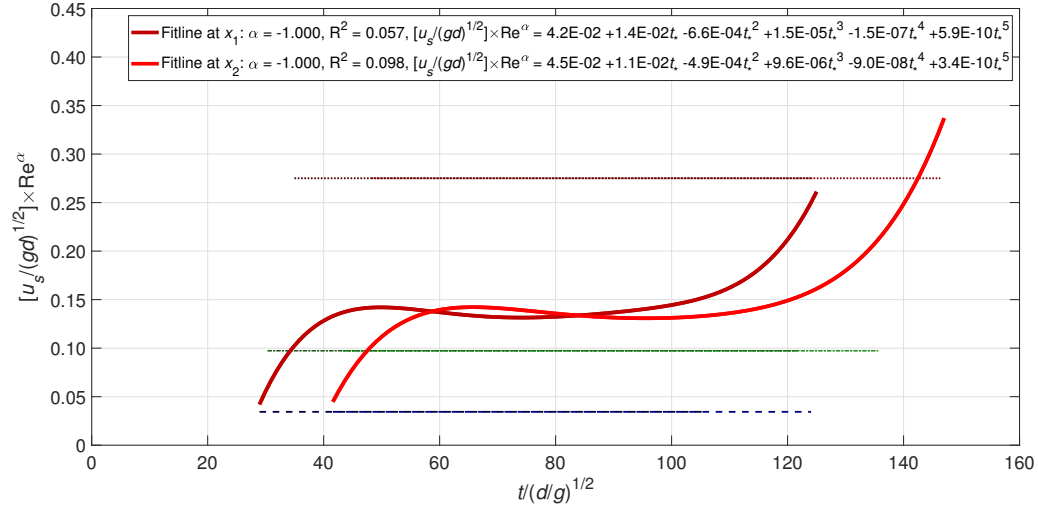


Figure 147 Comparison of Re-normalised slide surface velocity (data from Fig. 84) profiles over time with $\theta_W = 0^\circ$ and $\alpha = -1$. Dotted data-lines are described by the legend of Fig. 84. $t_* = t/(d/g)^{1/2} - 28.93$ at x_1 and $t/(d/g)^{1/2} - 41.59$ at x_2

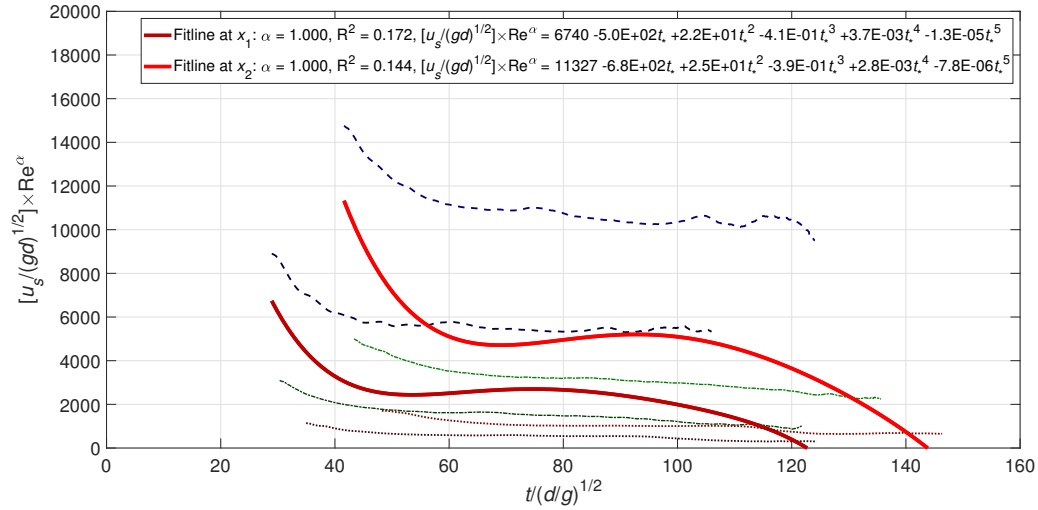


Figure 148 Comparison of Re-normalised slide surface velocity (data from Fig. 84) profiles over time with $\theta_W = 0^\circ$ and $\alpha = 1$. Dotted data-lines are described by the legend of Fig. 84. $t_* = t/(d/g)^{1/2} - 28.93$ at x_1 and $t/(d/g)^{1/2} - 41.59$ at x_2

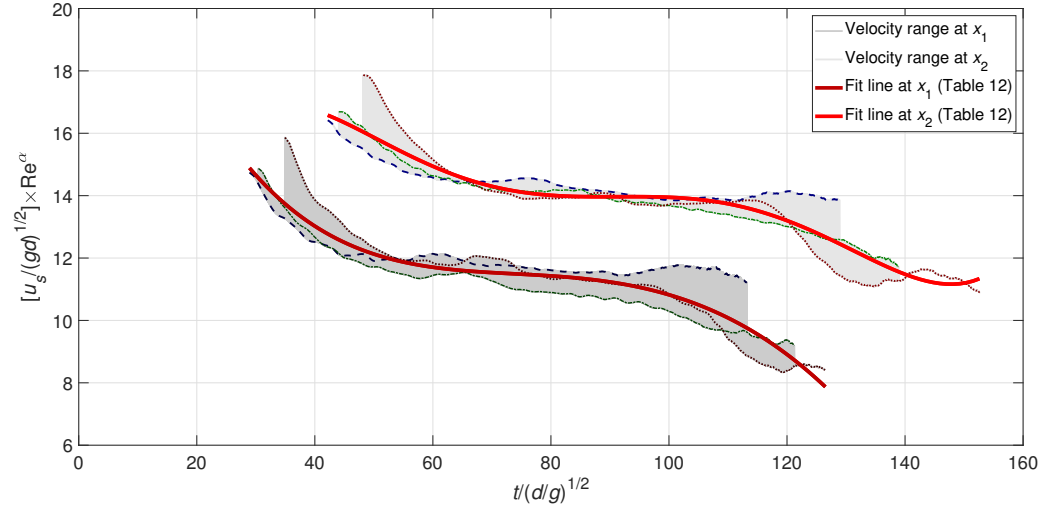


Figure 149 Comparison of Re-normalised surface velocity (data from Fig. 146) profiles over time with $\theta_W = 7.5^\circ$. Dotted data-lines are described by the legend of Fig. 146. $t_* = t/(d/g)^{1/2} - 28.93$ at x_1 and $t/(d/g)^{1/2} - 42.19$ at x_2

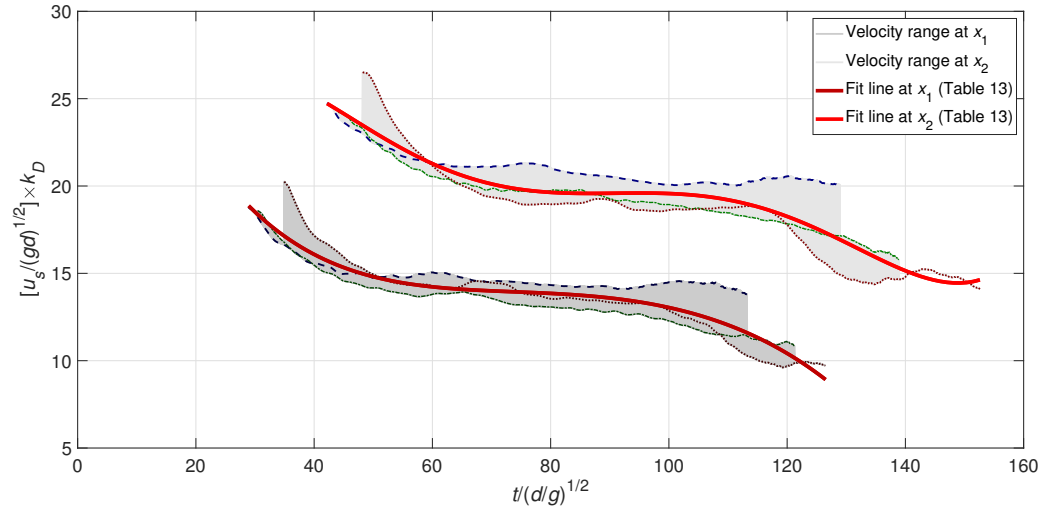


Figure 150 Comparison of k_D -normalised surface velocity (data from Fig. 146) profiles over time with $\theta_W = 7.5^\circ$. Dotted data-lines are described by the legend of Fig. 146. $t_* = t/(d/g)^{1/2} - 28.93$ at x_1 and $t/(d/g)^{1/2} - 42.19$ at x_2

D Additional porosity data

In this section, data from a local porosity analysis of the simulated deposit at $\lambda = 2$ and $\theta_W = 7.5^\circ$ (S5) is provided in Fig. 151. This data can be compared to Figs. 98 and 99 in Section 4.3.6, and provides an interpolation of the behaviours and patterns seen in the deposit local porosity distribution as θ_W increases. Figure 151 was omitted from Section 4.3.6 as the additional data did not provide any further direct insight into scale effects in the simulations. However, the data is included for reference here as it confirms the linear development of behaviours with increasing θ_W that could be monitored in future laboratory experiments.

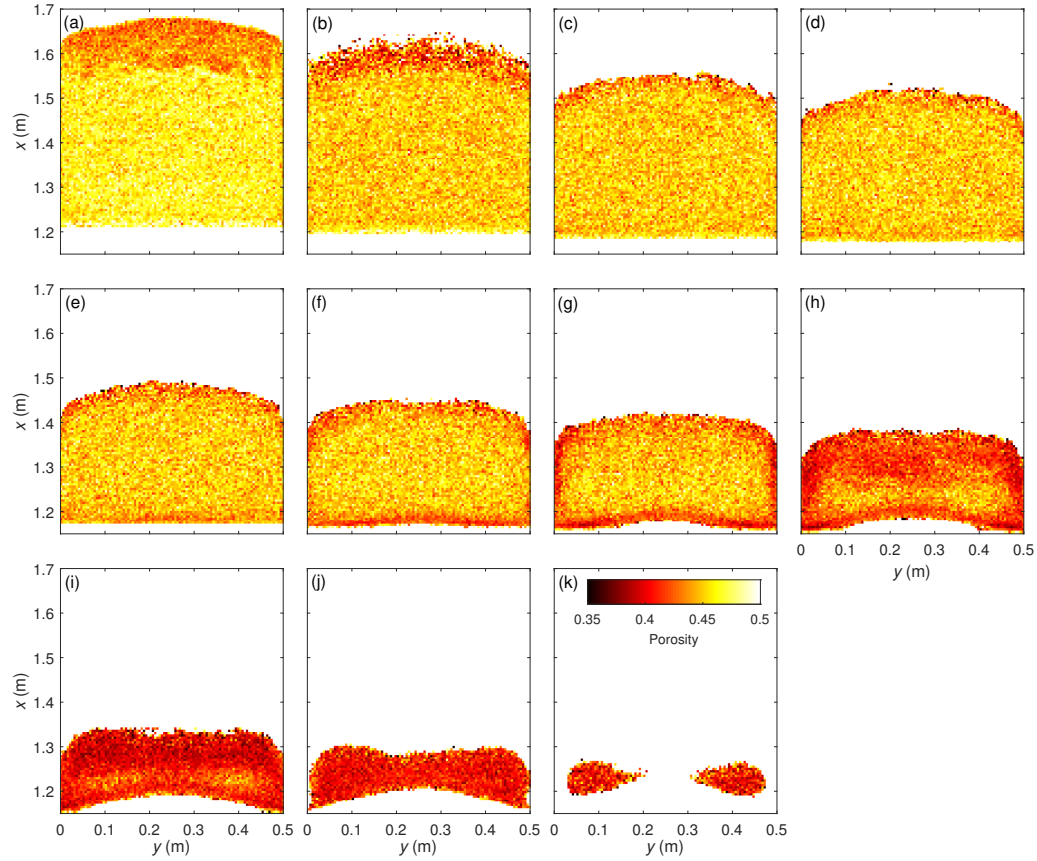


Figure 151 Local analysis of slide porosity for simulation S5, with $\lambda = 2$ and $\theta_W = 7.5^\circ$. (a) represents the first 5 mm away from the runout zone surface, with (b) to (k) moving up the deposit in 5 mm intervals

E Laboratory measurement error assessment

This section will more rigorously summarise and assess the measurement errors seen in the laboratory measurement of key slide parameters from Section 4.3. Many of these parameters were only subject to one source of error, and as such errors did not typically compound to produce increased uncertainty in raw measurements. Ensemble-averaging the data from repeats of laboratory experiments under identical conditions divides all of these uncertainties by a factor of $\sqrt{N_r}$, where N_r is the number of experimental repeats. This process was completed for all parameters displayed in Section 4.3, unless individual experiments are highlighted, such as in Figs. 94 to 96. $N_r = 4$ for laboratory experiments with $\lambda = 2$. $N_r = 5$ for laboratory experiments with $\lambda = 1$ and $\theta_W = 15^\circ$, while $N_r = 6$ for other laboratory experiments with $\lambda = 1$. Finally, $N_r = 7$ for laboratory experiments with $\lambda = 4$.

Deposit front and tail positions through the slide events were measured from digital camera footage, as seen in Figs. 75 to 78, and in Figs. 121 and 122. The uncertainty on the timing of the data points in these figures is ± 0.017 s, due to the frame rate of the digital camera footage being 30 Hz. The uncertainty on the position of the data points in these figures is ± 0.01 m, due to the resolution of the digital camera footage. Data points that exceeded this value of uncertainty were omitted. The laboratory position data corresponding to Figs. 123 to 125 were similarly omitted due to camera footage issues preventing accurate measurement of the front and tail positions at $\lambda = 4$.

Slide surface velocities were measured via PIV from the high-speed camera footage, as seen in Figs. 84, 85, and 146. As the parameters of the PIV analysis were well-suited to the high-speed camera footage, the uncertainty of velocity measurements at specific timesteps is estimated at $\pm 2.5\%$. The uncertainty of timing of the velocity measurements is estimated at ± 1 camera frame at each scale (Table 2) due to interpreting the shutter release from an LED switching off in the camera frame. The LED consistently switched off in synchronisation with the electromagnets, resulting in low uncertainty in this parameter.

Slide thicknesses were measured via laser trigonometry from the high-speed camera footage, as seen in Figs. 87 to 90, and in Figs. 144 and 145. As noted in Section 3.3, uncertainty in the accuracy of the ramp co-ordinates ($\pm 2.5\%$) and in the accuracy of the thickness measurement due to interference ($\pm 10\%$) compounds to a total uncertainty of $\pm 10.3\%$. Additionally, the incidence angle θ_i was calculated with an uncertainty of $\pm 5\%$, which leads to a final total uncertainty of thickness $\pm 11.2\%$, taking $\theta_i = 30^\circ$ as the mean value. This reflects the experimental scatter seen in Figs. 87 to 90 and in Figs. 144 and 145 well.

Deposit positions were measured from the photogrammetric meshes, seen in Figs. 94 to 97 and Table 7. The uncertainty in individual position measurements is ± 0.5 mm across all three experimental scales, due to the resolution of the measurement grids in the images captured for photogrammetry, and due to the precision of the point clouds generated in the photogrammetry process. This corresponds to relatively low uncertainty on the deposit front and tail positions, as well as the x -coordinate of the peak positions, but higher uncertainty in the y -coordinate, as well as the deposit thicknesses.

Deposit volumes and porosities were measured from the photogrammetric meshes, seen in Table 8. The measurement uncertainty for volume is the product of uncertainties in measurement of all three of the slide dimensions. The calculation of exact volume uncertainties is difficult due to the complex deposit shapes, but estimates can be made. At $\lambda = 1$ and $\theta_W = 0^\circ$, the measurement error of a deposit dimension equals $0.741d$. Assuming a deposit length of $370d$, a deposit width of $370d$, and deposit mean thickness of $20d$, this leads to respective relative uncertainties of 0.20%, 0.20%, and 3.70%. These compound into a relative uncertainty of volume of 3.71%, demonstrating that only relative uncertainty in the thickness measurement is significant in the volume calculations for these specific deposit geometries.

As the uncertainty is independent of particle diameter, this uncertainty estimate reduces linearly with λ . The mean non-dimensional deposit thickness also decreases as λ decreases, mitigating the improvement of uncertainty with decreasing λ , but the increase in particle size results in all deposits of lower λ having greater absolute

thickness, resulting in 3.71% being a conservative estimate across the data-set. The measurement uncertainty of the deposit porosity is simply that of the deposit volume multiplied by $\sqrt{2}$, as the volume of the particles is divided by the volume surrounding the slide. This results in a porosity errors of 5.25% in the previous example.

Finally, it should be noted that the mean particle diameter is an estimate based on the data-sheets provided by Garside Sands. As a result, the uncertainty in mean particle diameter across the whole slide mass is assumed to be negligible due to the extremely large particle counts. This means that the uncertainty in key dimensionless parameters such as u/\sqrt{gd} , $t/\sqrt{d/g}$ and Re is expected to be similar to that of the remaining fundamental parameters, in this case being the uncertainty in u , t , and u , respectively.

References

- AgiSoft-LLC (2016). Agisoft Photoscan Professional (Version 1.2.6). Retrieved from <http://www.agisoft.com/downloads/installer/>. Accessed: 13-06-2017.
- Ai, J., Chen, J.-F., Rotter, J., and Ooi, J. (2011). Assessment of rolling resistance models in discrete element simulations. *Powder Technology*, 206(3):269–282.
- Andreotti, B., Forterre, Y., and Pouliquen, O. (2013). *Granular media: Between Fluid and Solid*. Cambridge University Press, New York.
- Aradian, A., Raphael, E., and de Gennes, P.-G. (2002). Surface flows of granular materials: A short introduction to some recent models. *Comptes Rendus Physique*, 3(2):187–196.
- Armanini, A. (2013). Granular flows driven by gravity. *Journal of Hydraulic Research*, 51(2):111–120.
- Armstrong, B. and Williams, K. (1986). *The Avalanche Book*. Fulcrum Golden, Colorado.
- Artoni, R., Santomaso, A., Go, M., and Canu, P. (2012). Scaling laws for the slip velocity in dense granular flows. *Physical Review Letters*, 108(23):1–4.
- AZoM (2001). Silica - Silicon Dioxide (SiO₂). Retrieved from <https://www.azom.com/properties.aspx?ArticleID=1114>. Accessed: 17-09-2019.
- Bagheri, G. and Bonadonna, C. (2016). On the drag of freely falling non-spherical particles. *Powder Technology*, 301:526–544.
- Bagnold, R. (1954). Experiments on a gravity-free dispersion of large solid spheres in a Newtonian fluid under shear. *Proceedings of the Royal Society A*, 225(1160):49–63.
- Baird, W., Caldwell, J., Edge, W., Magoon, O., and Treadwell, D. (1980). Report on the damages to the Sines Breakwater, Portugal. In *Proceedings of the 17th International Coastal Engineering Conference*, pages 3063–3077, Sydney. ASCE.

- Baker, J., Barker, T., and Gray, J. (2016a). A two-dimensional depth-averaged $\mu(l)$ -rheology for dense granular avalanches. *Journal of Fluid Mechanics*, 787:367–395.
- Baker, J., Johnson, C., and Gray, J. (2016b). Segregation-induced finger formation in granular free-surface flows. *Journal of Fluid Mechanics*, 809:168–212.
- Banton, J., Villard, P., Jongmans, D., and Scavia, C. (2009). Two-dimensional discrete element models of debris avalanches: Parameterization and the reproducibility of experimental results. *J. Geophys. Res.*, 114(F04013):1–15.
- Baranau, V. and Tallarek, U. (2014). Random-close packing limits for monodisperse and polydisperse hard spheres. *Soft Matter*, 10:3826–3841.
- Barenblatt, G. (1996). *Scaling, self-similarity, and intermediate asymptotics*. Cambridge University Press, Cambridge.
- Berti, M., Genevois, R., Simoni, A., and Tecca, P. (1999). Field observations of a debris flow event in the Dolomites. *Geomorphology*, 29:265–274.
- Börzsönyi, T., Ecke, R., and McElwaine, J. (2009). Patterns in flowing sand: Understanding the physics of granular flow. *Physical Review Letters*, 103(178302):1–4.
- Bowman, E., Laue, J., Imre, B., and Springman, S. (2010). Experimental modelling of debris flow behaviour using a geotechnical centrifuge. *Canadian Geotechnical Journal*, 47(7):742–762.
- Bowman, E. and Take, W. (2015). The runout of chalk cliff collapses in england and france — case studies and physical model experiments. *Landslides*, 12(2):225–239.
- Brilliantov, N. and Pöschel, T. (2004). *Kinetic theory of granular gases*. Oxford University Press.
- Brodu, N., Delannay, R., Valance, A., and Richard, P. (2015). New patterns in high-speed granular flows. *Journal of Fluid Mechanics*, 769:218–228.

- Bryant, S., Take, W., and Bowman, E. (2014). Observations of grain-scale interactions and simulation of dry granular flows in a large-scale flume. *Canadian Geotechnical Journal*, 52(5):638–655.
- Bryant, S., Take, W., Bowman, E., and Millen, M. (2015). Physical and numerical modelling of dry granular flows under coriolis conditions. *Geotechnique*, 65(3):188–200.
- Brzesowsky, R., Spiers, C., Peach, C., and Hangx, S. (2011). Failure behavior of single sand grains: Theory versus experiment. *Journal of Geophysical Research*, 116(B06025):1–13.
- Bui, H., Fukagawa, R., Sako, K., and Wells, J. (2011). Slope stability analysis and discontinuous slope failure simulation by elasto-plastic smoothed particle hydrodynamics (SPH). *Géotechnique*, 61(7):565–574.
- Burns, S. and Hanley, K. (2017). Establishing stable time-steps for DEM simulations of non-collinear planar collisions with linear contact laws. *International Journal for Numerical Methods in Engineering*, 110(2):186–200.
- Campbell, C. (2006). Granular material flows – An overview. *Powder Technology*, 162(3):208–229.
- Campbell, C. (2011). Elastic granular flows of ellipsoidal particles. *Physics of Fluids*, 23(1):1–11.
- Campbell, C., Cleary, P., and Hopkins, M. (1995). Large-scale landslide simulations: Global deformation, velocities and basal friction. *Journal of Geophysical Research*, 100(B5):8267–8293.
- Chang, D., Zhang, L., Xu, Y., and Huang, R. (2011). Field testing of erodibility of two landslide dams triggered by the 12 May Wenchuan earthquake. *Landslides*, 8(3):321–332.
- Choi, C., Ng, C., Au-Yeung, S., and Goodwin, G. (2015). Froude characteristics of both dense granular and water flows in Froude modelling. *Landslides*, 12(6):1197–1205.

- Chung, M. (2018). Acoustic fluidisation in granular flows. Master's thesis, Department of Civil Engineering, University of Nottingham.
- Cleary, P. and Campbell, C. (1993). Self-lubrication for long runout landslides: Examination by computer simulation. *Journal of Geophysical Research*, 98(B12):21,911–21,924.
- Cleary, P. and Frank, M. (2006). Three-dimensional discrete element simulations of axi-symmetric collapses of granular columns. Technical Report 44710. Technische Universitat Kaiserslautern.
- Cleary, P. and Sawley, M. (2002). DEM modelling of industrial granular flows: 3D case studies and the effect of particle shape on hopper discharge. *Applied Mathematical Modelling*, 26(2):89–111.
- Coetzee, C. (2017). Review: Calibration of the discrete element method. *Powder Technology*, 310:104–142.
- Colagrossi, A. and Landrini, M. (2003). Numerical simulation of interfacial flows by smoothed particle hydrodynamics. *Journal of Computational Physics*, 191(2):448–475.
- Collins, G. and Melosh, H. (2003). Acoustic fluidization and the extraordinary mobility of sturzstroms. *Journal of Geophysical Research*, 108(B10):1–14.
- Cruden, D. and Hungr, O. (1986). The debris of the Frank Slide and theories of rockslide-avalanche mobility. *Canadian Journal of Earth Sciences*, 23(3):425–432.
- Cundall, P. and Strack, O. (1979). A discrete numerical model for granular assemblies. *Géotechnique*, 29(1):47–65.
- Dade, W. and Huppert, H. (1998). Long-runout landslides. *Geology*, 26(9):803–806.
- Daerr, A. and Douady, S. (1999). Sensitivity of granular surface flows to preparation. *Europhysics Letters*, 47(3):324–330.

- Dalziel, S. (2009). Digiflow User Guide, Dalziel Research Partners. Retrieved from <http://www.dalzielresearch.com/digiflow/digiflow.htm/>. Accessed 27-06-2017.
- Davies, T. and McSaveney, M. (1999). Runout of dry granular avalanches. *Canadian Geotechnical Journal*, 36(2):313–320.
- Davies, T., McSaveney, M., and Hodgson, K. (1999). A fragmentation-spreading model for long-runout rock avalanches. *Canadian Geotechnical Journal*, 36(6):1096–1110.
- De Blasio, F. and Crosta, G. (2014). Simple physical model for the fragmentation of rock avalanches. *Acta Mechanica*, 225(1):243–252.
- de Blasio, F. and Elverhøi, A. (2008). A model for frictional melt production beneath large rock avalanches. *Journal of Geophysical Research*, 113(F02014):1–13.
- De Haas, T., Braat, L., Leuven, J., Lokhorst, I., and Kleinhans, M. (2015). Effects of debris flow composition on runout, depositional mechanisms, and deposit morphology in laboratory experiments. *Journal of Geophysical Research: Earth Surface*, 120(9):1949–1972.
- Denlinger, R. and Iverson, R. (2004). Granular avalanches across irregular three-dimensional terrain: 1. Theory and computation. *Journal of Geophysical Research*, 109(F1):1–14.
- Dullien, F. (1991). *Porous Media*. Academic Press, San Diego, CA.
- Eckart, W., Gray, J., and Hutter, K. (2003). *Particle image velocimetry (PIV) for granular avalanches on inclined planes*. Springer-Verlag Berlin Heidelberg.
- EDEM (2018). DEM Solutions Limited, Edinburgh, UK. <https://www.edemsimulation.com/software/>.
- Einav, I. (2007). Fracture propagation in brittle granular matter. *Proceedings of the Royal Society A*, 463:3021–3035.

- Erismann, T. (1986). Flowing, rolling, bouncing, sliding: Synopsis of basic mechanisms. *Acta Mechanica*, 64(1):101–110.
- Ettema, R., Kirkil, G., and Muste, M. (2006). Similitude of large-scale turbulence in experiments on local scour at cylinders. *Journal of Hydraulic Engineering*, 132(1):33–40.
- Evans, S., Bishop, N., Smoll, L., Murillo, P., Delaney, K., and Oliver-Smith, A. (2009). A re-examination of the mechanism and human impact of catastrophic mass flows originating on Nevado Huascarán, Cordillera Blanca, Peru in 1962 and 1970. *Engineering Geology*, 108(1–2):96–118.
- Evans, S., Hungr, O., and Clague, J. (2001). Dynamics of the 1984 rock avalanche and associated distal debris flow on Mount Cayley, British Columbia, Canada; implications for landslide hazard assessment on dissected volcanoes. *Engineering Geology*, 61(1):29–51.
- Forterre, Y. and Pouliquen, O. (2008). Flows of dense granular media. *Annual Review of Fluid Mechanics*, 40:1–24.
- Furuichi, M. and Nishiura, D. (2017). Iterative load-balancing method with multi-grid level relaxation for particle simulation with short-range interactions. *Computer Physics Communications*, 219:135–148.
- Gariano, S. and Guzzetti, F. (2016). Landslides in a changing climate. *Earth-Science Reviews*, 162:227–252.
- G.D.R. MiDi (2004). On dense granular flows. *European Physical Journal E*, 14(4):341–365.
- Gingold, R. and Monaghan, J. (1977). Smoothed particle hydrodynamics: Theory and application to non-spherical stars. *Monthly Notices of the Royal Astronomical Society*, 181(3):375–389.
- Glasser, B. and Goldhirsch, I. (2001). Scale dependence, correlations, and fluctuations of stresses in rapid granular flows. *Physics of Fluids*, 13(2):407–420.

- Glimsdal, S., L'Heureux, J.-S., Harbitz, C., and Løvholt, F. (2016). The 29th January 2014 submarine landslide at Statland, Norway—landslide dynamics, tsunami generation, and run-up. *Landslides*, 13(6):1435–1444.
- Goel, A., Wadley, H., and Deshpande, V. (2018). Impact of granular slugs on rigid targets: Effect of grain shape and fracture. *European Journal of Mechanics / A Solids*, 71:64–76.
- Goldhirsch, I. (2003). Rapid granular flows. *Annual Review of Fluid Mechanics*, 35:267–293.
- Goldhirsch, I. (2010). Stress, stress asymmetry and couple stress: From discrete particles to continuous fields. *Granular Matter*, 12(3):239–252.
- Gollin, D., Brevis, W., Bowman, E., and Shepley, P. (2017). Performance of PIV and PTV for granular flow measurements. *Granular Matter*, 19(3):42–57.
- Goren, L. and Aharanov, E. (2007). Long runout landslides: The role of frictional heating and hydraulic diffusivity. *Geophysical Research Letters*, 34(7301):1–7.
- Gray, J. (2018). Particle segregation in dense granular flows. *Annual Review of Fluid Mechanics*, 50:407–433.
- Gray, J. and Edwards, A. (2014). A depth-averaged $\mu(I)$ -rheology for shallow granular free-surface flows. *Journal of Fluid Mechanics*, 755:503–534.
- Gray, J., Gajjar, P., and Kokelaar, P. (2015). Particle-size segregation in dense granular avalanches. *Comptes Rendus Physique*, 16:73–85.
- Gray, J., Wieland, M., and Hutter, K. (1999). Gravity-driven free surface flow of granular avalanches over complex basal topography. *Proceedings of the Royal Society of London A: Mathematical, Physical and Engineering Sciences*, 455(1985):1841–1874.
- Greve, R., Koch, T., and Hutter, K. (1994). Unconfined flow of granular avalanches along a partly curved surface. I. Theory. *Proceedings of the Royal Society of London A: Mathematical, Physical and Engineering Sciences*, 445(1924):399–413.

- Grima, A. and Wypych, P. (2011). Development and validation of calibration methods for discrete element modelling. *Granular Matter*, 13(2):127–132.
- Hanes, D. and Walton, O. (2000). Simulations and physical measurements of glass spheres flowing down a bumpy incline. *Powder Technology*, 109(1–3):133–144.
- Haque, U., Blum, P., and da Silva, P. (2016). Fatal landslides in Europe. *Landslides*, 13(6):1545–1554.
- Haug, Ø., Rosenau, M., Leever, K., and Oncken, O. (2016). On the energy budgets of fragmenting rockfalls and rockslides: Insights from experiments. *Journal of Geophysical Research: Earth Surface*, 121(7):1310–1327.
- Haustein, M., Gladkyy, A., and Schwarze, R. (2017). Discrete element modeling of deformable particles in YADE. *SoftwareX*, 6:118–123.
- Heller, V. (2011). Scale effects in physical hydraulic engineering models. *Journal of Hydraulic Research*, 49(3):293–306.
- Heller, V. (2017). Self-similarity and Reynolds number invariance in Froude modelling. *Journal of Hydraulic Research*, 55(3):293–309.
- Heller, V. and Hager, W. (2010). Impulse product parameter in landslide generated impulse waves. *Journal of Waterway, Port, Coastal, and Ocean Engineering*, 136(3):145–155.
- Heller, V., Hager, W., and Minor, H. (2008). Scale effects in subaerial landslide generated impulse waves. *Experiments in Fluids*, 44:691–703.
- Heller, V. and Spinneken, J. (2015). On the effect of the water body geometry on landslide-tsunamis: Physical insight from laboratory tests and 2D to 3D wave parameter transformation. *Coastal Engineering*, 104:113–134.
- Holyoake, A. and McElwaine, J. (2012). High-speed granular chute flows. *Journal of Fluid Mechanics*, 710:35–71.
- Huang, X., Hanley, K., O’Sullivan, C., and Kwok, F. (2014). Effect of sample size on the response of DEM samples with a realistic grading. *Particuology*, 15:107–115.

- Hungr, O., Leroueil, S., and Picarelli, L. (2013). The Varnes classification of landslide types, an update. *Landslides*, 11(2):167–194.
- Hutter, K. and Greve, R. (1993). Motion of a granular avalanche in an convex and concave curved chute: experiments and theoretical predictions. *Philosophical Transactions of the Royal Society of London A: Mathematical, Physical and Engineering Sciences*, 342(1666):573–600.
- Hutter, K. and Koch, T. (1991). Motion of a granular avalanche in an exponentially curved chute: experiments and theoretical predictions. *Philosophical Transactions of the Royal Society of London A: Mathematical, Physical and Engineering Sciences*, 334(1633):93–138.
- Hutter, K., Koch, T., Plüss, C., and Savage, S. (1995). The dynamics of avalanches of granular materials from initiation to runout. Part II. Experiments. *Acta Mechanica*, 109(1–4):127–165.
- Hutter, K., Siegel, M., Savage, S., and Nohguchi, Y. (1993). Two-dimensional spreading of a granular avalanche down an inclined plane. Part I. Theory. *Acta Mechanica*, 100(1–2):37–68.
- Imre, B., Laue, J., and Springman, S. (2010). Fractal fragmentation of rocks within sturzstroms: insight derived from physical experiments within the ETH geotechnical drum centrifuge. *Granular Matter*, 12:267–285.
- Iverson, R. (1997). The physics of debris flows. *Reviews of Geophysics*, 35(3):245–296.
- Iverson, R. (2015). Scaling and design of landslide and debris-flow experiments. *Journal of Geophysical Research*, 244:9–20.
- Iverson, R., Logan, M., LaHusen, R., and Berti, M. (2010). The perfect debris flow? Aggregated results from 28 large-scale experiments. *Geomorphology*, 115(F3):1–29.
- Jackson, A. (2014). *Scaling for lobe and cleft patterns in particle-laden gravity currents*. PhD thesis, University of Nottingham.

- Jaeger, H. and Nagel, S. (1996). Granular solids, liquids, and gases. *Review of Modern Physics*, 68(4):1259–1273.
- Jenkins, J. and Zhang, C. (2002). Kinetic theory for identical, frictional, nearly elastic spheres. *Physics of Fluids*, 14(3):1228–1235.
- Jensen, R., Plesha, M., Edil, T., Bosscher, P., and Kahla, N. (2001). DEM simulation of particle damage in granular media—Structure interfaces. *International Journal of Geomechanics*, 1(1):21–39.
- Jerier, J.-F., Richefeu, V., Imbault, D., and Donzé, F.-V. (2010). Packing spherical discrete elements for large scale simulations. *Computer Methods in Applied Mechanics and Engineering*, 199(25–28):1668–1676.
- Johnson, B., Campbell, C., and Melosh, H. (2016). The reduction of friction in long runout landslides as an emergent phenomenon. *Journal of Geophysical Research: Earth Surface*, 121(5):881–889.
- Johnson, C., Kokelaar, B., Iverson, R., Logan, M., LaHusen, R., and Gray, J. (2012). Grain-size segregation and levee formation in geophysical mass flows. *Journal of Geophysical Research*, 117(F1):1–23.
- Jop, P. (2015). Rheological properties of dense granular flows. *Comptes Rendus Physique*, 16(1):62–72.
- Jop, P., Forterre, Y., and Pouliquen, O. (2005). Crucial role of side walls for granular surface flows: consequences for the rheology. *Journal of Fluid Mechanics*, 541:167–192.
- Jop, P., Forterre, Y., and Pouliquen, O. (2006). A constitutive law for dense granular flows. *Nature*, 441:727–730.
- Juanico, D., Longjas, A., Batac, R., and Monterola, C. (2008). Avalanche statistics of driven granular slides in a miniature mound. *Geophysical Research Letters*, 35(19403):1–4.
- Kamphuis, J. (1974). Practical scaling of coastal models. In *Proc. 14th Coastal engineering conference*, pages 2086–2101, Copenhagen. ASCE, New York.

- Kloss, C., Goniva, C., Hager, A., Amberger, S., and Pirker, S. (2012). Models, algorithms and validation for opensource DEM and CFD-DEM. *Progress in Computational Fluid Dynamics*, 12(2/3):140–152.
- Kokelaar, B., Bahia, R., Joy, K., Virouelt, S., and Gray, J. (2017). Granular avalanches on the moon: Mass-wasting conditions, processes, and features. *Journal of Geophysical Research: Planets*, 122(9):1893–1925.
- Krugger-Emden, H., Rickelt, S., Wirtz, S., and Scherer, V. (2008). A study on the validity of the multi-sphere discrete element method. *Powder Technology*, 188(2):153–165.
- Lajeunesse, E., Mangeney, A., and Vilotte, J.-P. (2004). Spreading of a granular mass on a horizontal plane. *Physics of Fluids*, 16(7):2371–2381.
- Latham, J.-P. and Munjiza, A. (2004). The modelling of particle systems with real shapes. *Philosophical Transactions of the Royal Society of London A: Mathematical, Physical and Engineering Sciences*, 362(1822):1953–1972.
- Lee, C. and Huang, C. (2012). Kinetic-theory-based model of dense granular flows down inclined planes. *Physics of Fluids*, 24(073303):1–18.
- Legros, F. (2002). The mobility of long runout landslides. *Engineering Geology*, 63:301–331.
- LIGGGHTS (2016). gran model hertz model. DCS Computing GmbH, JKU Linz and Sandia Corporation. Retrieved from https://www.cfdem.com/media/DEM/docu/gran_model_hertz.html. Accessed: 26-06-2017.
- Lipovsky, P., Evans, S., Clague, J., Hopkinson, C., Couture, R., Bobrowsky, P., Ekström, G., Demuth, M., Delaney, K., Roberts, N., Clarke, G., and Schaeffer, A. (2008). The July 2007 rock and ice avalanches at Mount Steele, St. Elias Mountains, Yukon, Canada. *Landslides*, 5(4):445–455.
- Liu, L. (2003). Simulation of microstructural evolution during isostatic compaction of monosized spheres. *Journal of Physics D: Applied Physics*, 36(15):1881–1889.

- Liu, L., Zhang, S., and Yu, A. (1999). Dynamic simulation of the centripetal packing of mono-sized spheres. *Physica A*, 268:433–453.
- Liu, W., He, S., Li, X., and Xu, Q. (2016). Two-dimensional landslide dynamic simulation based on a velocity-weakening friction law. *Landslides*, 13(5):957–965.
- Lo, C., Bolton, M., and Cheng, Y. (2010). Velocity fields of granular flows down a rough incline: a DEM investigation. *Granular Matter*, 12(5):477–482.
- Loth, E. (2007). Drag of non-spherical solid particles of regular and irregular shape. *Powder Technology*, 182(3):342–353.
- Lube, G., Huppert, H., Sparks, R., and Hallworth, M. (2004). Axisymmetric collapses of granular columns. *Journal of Fluid Mechanics*, 508:175–199.
- Lucas, A., Mangeney, A., and Ampuero, J. (2014). Frictional velocity-weakening in landslides on earth and on other planetary bodies. *Nature Communications*, 5(3417):1–9.
- Luhmann, T., Robson, S., Kyle, S., and Harley, I. (2006). *Close Range Photogrammetry*. Whittles, Scotland.
- Lynn Highland Graphics (2004). USGS Fact Sheet 2004–3072: Landslide Types and Processes. U.S. Department of the Interior, U.S. Geological Survey. <https://pubs.usgs.gov/fs/2004/3072/pdf/fs2004-3072.pdf>.
- Markauskas, D. and Kačianauskas, R. (2011). Investigation of rice grain flow by multi-sphere particle model with rolling resistance. *Granular Matter*, 13(2):143–148.
- Markauskas, D., Kačianauskas, R., Džiugys, A., and Navakas, R. (2010). Investigation of adequacy of multi-sphere approximation of elliptical particles for DEM simulations. *Granular Matter*, 12(1):107–123.
- Matsushima, T. and Saomoto, H. (1978). Discrete element modeling for irregularly shaped sand grains. In *Proceedings of NUMGE2002: Numerical methods in geotechnical engineering*, pages 239–246.

- McArdell, B., Bartelt, P., and Kowalski, J. (2007). Field observations of basal forces and fluid pore pressure in a debris flow. *Geophysical Research Letters*, 34(7406):1–4.
- McElwaine, J. and Nishimura, K. (2001). *Ping-pong ball avalanche experiments*. Blackwell Publishing Ltd., UK.
- McFall, B., Mohammed, F., Fritz, H., and Liu, Y. (2018). Laboratory experiments on three-dimensional deformable granular landslides on planar and conical slopes. *Landslides*, 15(9):1713–1730.
- McKinnon, M. (2010). *Landslide Runout, Statistical Analysis of Physical Characteristics and Model Parameters*. PhD thesis, University of British Columbia (Vancouver).
- McSaveney, M. (2002). *Recent rockfalls and rock avalanches in Mount Cook National Park, New Zealand*. Geological Society of America.
- Melosh, H. (1979). Acoustic fluidization: A new geologic process? *Journal of Geophysical Research*, 84(B13):7513–7520.
- Miller, D. (1960). Giant waves in Lituya Bay Alaska. Geological survey, Professional paper 354-C. US Government Printing Office, Washington DC.
- Miller, G. and Pursey, H. (1955). On the partition of energy between elastic waves in a semi-infinite solid. *Proceedings of the Royal Society A*, 233(1192):55–69.
- Minh, N. and Cheng, Y. (2013). A DEM investigation of the effect of particle-size distribution on one-dimensional compression. *Géotechnique*, 63(1):44–53.
- Mirghasemi, A., Rothenburg, L., and Matyas, E. (1997). Numerical simulations of assemblies of two-dimensional polygon-shaped particles and effects of confining pressure on shear strength. *Soils and Foundations*, 37(3):43–52.
- Mollanouri Shamsi, M. and Mirghasemi, A. (2012). Numerical simulation of 3D semi-real-shaped granular particle assembly. *Powder Technology*, 221:431–446.

- Mollon, G. and Zhao, J. (2013). Generating realistic 3D sand particles using Fourier descriptors. *Granular Matter*, 15(1):95–108.
- Montrasio, L., Schilirò, L., and Terrone, A. (2016). Physical and numerical modelling of shallow landslides. *Landslides*, 13(5):873–883.
- Moore, D. (1976). The Rubble Creek landslide, Garibaldi, British Columbia. Master's thesis, Department of Geological Sciences, University of British Columbia.
- Moriwaki, H., Inokuchi, T., Hattanji, T., Sassa, K., Ochiai, H., and Wang, G. (2004). Failure processes in a full-scale landslide experiment using a rainfall simulator. *Landslides*, 1(4):277–288.
- Nguyen, C., Nguyen, C., Bui, H., Nguyen, G., and Fukugawa, R. (2017). A new SPH-based approach to simulation of granular flows using viscous damping and stress regularisation. *Landslides*, 14(1):69–81.
- Noor, M., Kadirgama, K., and Rahman, M. (2010). Analysis of surface roughness for laser cutting on acrylic sheets using response surface method. In *National Conference in Mechanical Engineering Research and Postgraduate Students*, pages 24–31, Panang, Malaysia. University Malaysia Panang.
- Ogawa, S. (2002). Multitemperature theory of granular materials. In *Proceedings of the U.S.-Japan Seminar on Continuum Mechanical and Statistical Approaches in the Mechanics of Granular Materials*, pages 208–217, Tokyo. Gakujutsu Bunken Fukyu-kai.
- Okura, Y., Kitahara, H., and Sammori, T. (2000a). Fluidization in dry landslides. *Engineering Geology*, 56:347–360.
- Okura, Y., Kitahara, H., Sammori, T., and Kawanami, A. (2000b). The effects of rockfall volume on runout distance. *Engineering Geology*, 58:109–124.
- Otsubo, M., O'Sullivan, C., and Shire, T. (2017). Empirical assessment of the critical time increment in explicit particulate discrete element method simulations. *Computers and Geotechnics*, 86:67–79.

- Ouadfel, H. (1998). *Numerical simulation of granular assemblies with three-dimensional ellipsoid-shaped particles*. PhD thesis, Department of Civil Engineering, Waterloo University, Ontario.
- Oumeraci, H. (1984). Scale effects in coastal hydraulic models. In *Symp. Scale effects in modelling hydraulic structures 7(10)*, pages 1–7, Esslingen. H. Kobus ed. Technische Akademie.
- Parez, S. and Aharonov, E. (2015). Long runout landslides: a solution from granular mechanics. *Frontiers in Physics*, 3(80):1–10.
- Pasha, M., Hare, C., Ghadiri, M., Gunadi, A., and Piccione, P. (2016). Effect of particle shape on flow in discrete element method simulation of a rotary batch seed coater. *Powder Technology*, 296:29–36.
- PFC 5.0 (2018). Itasca Consulting Group, Inc., Minneapolis, MN. <https://www.itascacg.com/software/pfc>, Accessed: 24-07-2018.
- Podlozhnyuk, A., Pirker, S., and Kloss, C. (2017). Efficient implementation of superquadric particles in discrete element method within an open-source framework. *Computational Particle Mechanics*, 4(1):101–118.
- Pohlman, N., Severson, B., Ottino, J., and Lueptow, R. (2006). Surface roughness effects in granular matter: Influence on angle of repose and the angle of segregation. *Physical Review E*, 73(3):1–9.
- Pouliquen, O. (1999). Scaling laws in granular flows down rough inclined planes. *Physics of Fluids*, 11(3):542–548.
- Pouliquen, O. and Forterre, Y. (2009). A non-local rheology for dense granular flows. *Philosophical Transactions of the Royal Society of London A: Mathematical, Physical and Engineering Sciences*, 367(1909):5091–5107.
- Pudasaini, S., Hsiau, S.-S., Wang, Y., and Hutter, K. (2005). Velocity measurements in dry granular avalanches using particle image velocimetry technique and comparison with theoretical predictions. *Physics of Fluids*, 17(9):1–10.

- Pudasaini, S. and Hutter, K. (2010). *Avalanche dynamics: Dynamics of rapid flows of dense granular avalanches*. Springer-Verlag Berlin Heidelberg.
- Pudasaini, S. and Miller, S. (2013). The hypermobility of huge landslides and avalanches. *Engineering Geology*, 157:124–132.
- Pudasaini, S., Wang, Y., Sheng, L.-T., Hsiau, S.-S., Hutter, K., and Katzenbach, R. (2008). Avalanching granular flows down curved and twisted channels: Theoretical and experimental results. *Physics of Fluids*, 20(7):1–11.
- Rabczuk, T. and Eibl, J. (2003). Simulation of high velocity concrete fragmentation using SPH/MLSPH. *International Journal for Numerical Methods in Engineering*, 56(10):1421–1444.
- Ranieri, G. (2007). The surf zone distortion of beach profiles in small-scale coastal models. *Journal of Hydraulic Research*, 45(2):261–269.
- Rombi, J., Pooley, E., and Bowman, E. (2006). Factors influencing granular debris flow behaviour: an experimental investigation. In *Proc. 6th International Conference on Physical Modelling in Geotechnics*, pages 379–384, Kowloon. Taylor and Francis, Rotterdam.
- Saingier, G., Deboeuf, S., and Lagrée, P.-Y. (2016). On the front shape of an inertial granular flow down a rough incline. *Physics of Fluids*, 28(5):1–15.
- Santivale, N. and Bowman, E. (2012). Internal imaging of saturated granular free-surface flows. *International Journal of Physical Modelling in Geotechnics*, 12(4):129–142.
- Santivale, N. and Bowman, E. (2017). Visualization of dominant stress-transfer mechanisms in experimental debris flows of different particle-size distribution. *Canadian Geotechnical Journal*, 54(2):258–269.
- Savage, S. and Hutter, K. (1989). The motion of a finite mass of granular material down a rough incline. *Journal of Fluid Mechanics*, 199(1):177–215.

- Schaefer, M. and Bugnion, L. (2013). Velocity profile variations in granular flows with changing boundary conditions: Insights from experiments. *Physics of Fluids*, 25(063303).
- Schaefer, M., Bugnion, L., Kern, M., and Bartelt, P. (2010). Position dependent velocity profiles in granular avalanches. *Granular Matter*, 12(3):1–15.
- Scheidegger, A. (1973). On the prediction of the reach and velocity of catastrophic landslides. *Rock Mechanics and Rock Engineering*, 5:231–236.
- Shan, T. and Zhao, J. (2014). A coupled CFD-DEM analysis of granular flow impacting on a water reservoir. *Acta Mechanica*, 225(8):2449–2470.
- Shugar, D. and Clague, J. (2011). The sedimentology and geomorphology of rock avalanche deposits on glaciers. *Sedimentology*, 58(7):1762–1783.
- Silbert, L., Ertas, D., Grest, G., Halsey, T., and Levine, D. (2002a). Geometry of frictionless and frictional sphere packings. *Physical Review E*, 65(3):1–6.
- Silbert, L., Grest, G., Plimpton, S., and Levine, D. (2002b). Boundary effects and self-organization in dense granular flows. *Physics of Fluids*, 14(8):2637–2645.
- Silbert, L., Landry, J., and Grest, G. (2003). Granular flow down a rough inclined plane: Transition between thin and thick piles. *Physics of Fluids*, 15(1):1–9.
- Singh, V. (1996). *Hydrology of Disasters*. Springer Netherlands.
- Slonaker, J., Motley, D., Zhang, Q., Townsend, S., Senatore, C., Iagnemma, K., and Kamrin, K. (2017). General scaling relations for locomotion in granular media. *Physical Review E*, 95(5):1–8.
- Smilauer, V. and Chareyre, B. (2015). DEM formulation. In *Yade Documentation 2nd ed*, pages 1–22. doi:10.5281/zenodo.34044. <http://yade-dem.org>, Accessed: 24-07-2018.
- Song, Y., Turton, R., and Kayihan, F. (2006). Contact detection algorithms for DEM simulations of tablet-shaped particles. *Powder Technology*, 161(1):32–40.

- Sosio, R., Crosta, G., and Hungr, O. (2008). Complete dynamic modeling calibration for the Thurwieser rock avalanche (Italian Central Alps). *Engineering Geology*, 100(1–2):11–26.
- Sovilla, B., Burlando, P., and Bartelt, P. (2006). Field experiments and numerical modeling of mass entrainment in snow avalanches. *Journal of Geophysical Research*, 111(F3):1–16.
- Staron, L. and Lajeunesse, E. (2009). Understanding how volume affects the mobility of dry debris flows. *Geophysical Research Letters*, 36(12402):1–4.
- Sukumaran, B. and Ashmawy, A. (2001). Quantitative characterisation of the geometry of discrete particles. *Géotechnique*, 51(0):1–9.
- Tagaki, D., McElwaine, J., and Huppert, H. (2011). Shallow granular flows. *Physical Review E*, 83(3):1–9.
- Thielicke, W. and Stamhuis, E. (2014). PIVlab: Towards User-friendly, Affordable and Accurate Digital Particle Image Velocimetry in MATLAB. *Journal of Open Research Software*, 2(1):1–10.
- Thompson, E. and Huppert, H. (2007). Granular column collapses: further experimental results. *Journal of Fluid Mechanics*, 575:177–186.
- Thornton, C. (2015). *Granular dynamics, contact mechanics and particle system simulations*. Springer International Publishing, Switzerland.
- Tsuzuki, S. and Aoki, T. (2016). Effective dynamic load balance using space-filling curves for large-scale SPH simulations on GPU-rich supercomputers. In *Proceedings of the 7th Workshop on Latest Advances in Scalable Algorithms for Large-Scale Systems*, pages 1–8, Salt Lake City. IEEE.
- Turnbull, B. (2011). Scaling laws for melting ice avalanches. *Physical Review Letters*, 107(25):1–4.
- Valentino, R., Barla, G., and Montrasio, L. (2008). Experimental analysis and micromechanical modelling of dry granular flow and impacts in laboratory flume tests. *Rock Mechanics and Rock Engineering*, 41(1):153–177.

- Vangla, P., Roy, N., and Gali, M. (2018). Image based shape characterization of granular materials and its effect on kinematics of particle motion. *Granular Matter*, 20(6):1–19.
- Ventisette, C., Gigli, G., Bonini, M., Corti, G., Montanari, D., Santoro, S., Sani, F., Fanti, R., and Casagli, N. (2015). Insights from analogue modelling into the deformation mechanism of the Vaiont landslide. *Geomorphology*, 228:52–59.
- Verlet, L. (1967). Computer "experiments" on classical fluids. Part I. Thermodynamical properties of Lennard-Jones molecules. *Physical Review*, 159(1):98–103.
- Wadell, H. (1932). Volume, shape, and roundness of rock particles. *Journal of Geology*, 40(5):443–451.
- Walton, O. (1982). Discrete element analysis of granular materials. In *Proceedings of the 4th International Conference of Numerical Methods in Geomechanics*, pages 1799–1803, Rotterdam. Balkema.
- Warnett, J., Denissenko, P., Thomas, P., Kiraci, E., and Williams, M. (2014). Scalings of axisymmetric granular column collapse. *Granular Matter*, 16(1):115–124.
- Weatherley, D., Boros, V., Hancock, W., and Abe, S. (2010). Scaling Benchmark of ESyS-Particle for Elastic Wave Propagation Simulations. In *Sixth IEEE International Conference on e-Science*, pages 1–7.
- Weatherley, D., Hancock, W., and Boros, V. (2014). ESyS-Particle Tutorial and User's Guide Version 2.3. Retrieved from <https://www.scribd.com/document/238628978/ESyS-Particle-Tutorial/>. Accessed: 24-07-2018.
- Wensrich, C. and Katterfeld, A. (2012). Rolling friction as a technique for modelling particle shape in DEM. *Powder Technology*, 217:409–417.
- Wensrich, C., Katterfeld, A., and Sugo, D. (2014). Characterisation of the effects of particle shape using a normalised contact eccentricity. *Granular Matter*, 16(3):327–337.

- Wu, C.-Y. and Cocks, A. (2006). Numerical and experimental investigations of the flow of powder into a confined space. *Mechanics of Materials*, 38(4):304–324.
- Wu, F., Fan, Y., Liang, L., and Wang, C. (2016). Numerical simulation of dry granular flow impacting a rigid wall using the discrete element method. *PLOS ONE*, 11(8):1–17.
- Xing, A., Yuan, X., Xu, Q., Zhao, Q., Huang, H., and Cheng, Q. (2017). Characteristics and numerical runout modelling of a catastrophic rock avalanche triggered by the Wenchuan earthquake in the Wenjia valley, Mianzhu, Sichuan, China. *Landslides*, 14(1):83–98.
- Xu, C., Xu, X., Yao, X., and Dai, F. (2014). Three (nearly) complete inventories of landslides triggered by the May 12, 2008 Wenchuan Mw 7.9 earthquake of China and their spatial distribution statistical analysis. *Landslides*, 11(3):441–461.
- Yan, B. and Regueiro, R. (2018). A comprehensive study of MPI parallelism in three-dimensional discrete element method (DEM) simulation of complex-shaped granular particles. *Computational Particle Mechanics*, 5(4):553–577.
- Yang, W., Zhou, Z., Pinson, D., and Yu, A. (2014). Periodic boundary conditions for discrete element method simulation of particle flow in cylindrical vessels. *Industrial and Engineering Chemistry Research*, 53(19):8245–8256.
- Yavari-Ramshe, S. and Ataie-Ashtiani, B. (2016). Numerical modelling of subaerial and submarine landslide-generated tsunami waves—recent advances and future challenges. *Landslides*, 13(6):1325–1368.
- Yu, A., An, X., Zou, R., Yang, R., and Kendall, K. (2006). Self-assembly of particles for densest packing by mechanical vibration. *Physical Review Letters*, 97(26):1–8.
- Zarn, B. (1992). Local river expansion: A measure to stabilize the bed of emme river at utzendorf. In *VAW Mitteilung 118.*, Zürich. D. Vischer ed. ETH Zürich.
- Zhang, H. and Makse, H. (2005). Jamming transition in emulsions and granular materials. *Physical Review E*, 72(1):1–11.

- Zhang, X. and Vu-Quoc, L. (2000). Simulation of chute flow of soybeans using an improved tangential force–displacement model. *Mechanics of Materials*, 32(2):115–129.
- Zhang, Z., Liu, L., Yuan, Y., and Yu, A. (2001). A simulation study of the effects of dynamic variables on the packing of spheres. *Powder Technology*, 116(1):23–32.
- Zhao, T. (2015). Coupled DEM-CFD Investigation of Granular Transport in a Fluid Channel. In *IOP Conference Series: Earth and Environmental Science 26*, pages 1–7.
- Zhao, T., Crosta, G., Utili, S., and de Blasio, F. (2017). Investigation of rock fragmentation during rockfalls and rock avalanches via 3-D discrete element analyses. *Journal of Geophysical Research: Earth Surface*, 122(3):678–695.
- Zheng, J. and Hryciw, R. (2017). An image based clump library for DEM simulations. *Granular Matter*, 19(2):1–15.
- Zheng, K., Du, C., Li, J., Qiu, B., Fu, L., and Dong, J. (2015). Numerical simulation of the impact-breakage behaviour of non-spherical agglomerates. *Powder Technology*, 286:582–591.
- Zhou, Y., Xu, B., Zou, B., Yu, A., and Zulli, P. (2003). Stress distribution in a sandpile formed on a deflected base. *Advanced Powder Technology*, 14(4):401–410.
- Zhu, H., Zhou, Z., Yang, R., and Yu, A. (2008). Discrete particle simulation of particulate systems: A review of major applications and findings. *Chemical Engineering Science*, 63(23):5728–5770.